THERMOMECHANICAL FATIGUE CRACK FORMATION IN A SINGLE CRYSTAL NI-BASE SUPERALLOY

A Dissertation
Presented to
The Academic Faculty

By

Robert Lewis Amaro

In Partial Fulfillment
Of the Requirements for the Degree
Doctor of Philosophy in the
George W. Woodruff School of Mechanical Engineering

Georgia Institute of Technology

December, 2010

THERMOMECHANICAL FATIGUE CRACK FORMATION IN A SINGLE CRYSTAL NI-BASE SUPERALLOY

Approved by:

Dr. Stephen D. Antolovich, Co-Advisor
School of Materials Science and Engineering,
George W. Woodruff School of Mechanical Engineering
Georgia Institute of Technology

Dr. Richard W. Neu, Co-Advisor
George W. Woodruff School of Mechanical Engineering,
School of Materials Science and Engineering
Georgia Institute of Technology

Dr. David L. McDowell
George W. Woodruff School of Mechanical Engineering,
School of Materials Science and Engineering
Georgia Institute of Technology

Dr. W. Steve Johnson
School of Materials Science and Engineering,
George W. Woodruff School of Mechanical Engineering
Georgia Institute of Technology

Dr. Preet M, Singh
School of Materials Science and Engineering,
Georgia Institute of Technology

Date Approved: December XX, 2010

ACKNOWLEDGEMENTS

First and foremost, I would like to acknowledge my wife, Erika Stinson, for her patience and support during this arduous process; and for putting so much faith into a high school dropout. Thank you.

I am also grateful to my advisers Dr. Richard Neu and Dr. Stephen Antolovich for their vital guidance and dedicated mentorship. Furthermore, I am greatly appreciative of my dissertation reading committee Dr. David McDowell, Dr. W. Steve Johnson and Dr. Preet Singh who have provided experimental and technical support; without which this work would not have been possible.

I would like to acknowledge Pratt & Whitney for their financial support of this research. I am particularly grateful to Raymond Keith Kersey and Dr. Alexander Staroselsky of Pratt & Whitney for their technical support.

Dr. Blaine Reely, P.E., my professional mentor, has invested countless hours of his time to ensuring my success. I will be forever grateful for his guidance and friendship. Moreover, to name just a few of my academic mentors who were there long before this doctoral journey began, and without whom I would never have come so far in my studies: Dr. Ken Cunefare of Georgia Tech, and Professor Julie Tarr from Pima Community College in Tucson, AZ. Thank you for believing in me.

Finally, I would be remiss to not acknowledge my fellow researchers and associates at the Georgia Institute of Technology who have provided help, input or general support with regard to either my personal development or the development of this work: Mike Hirsch, Patxi Fernandez-Zelaia, Rob Kopkovits, Ben Beck, Nick Earnhart,

Matt Stone, Trey Parker, Jamie Wilson, Jason Mewes, Kevin Smith, Nico Hempel and Rick Brown.

TABLE OF CONTENTS

LIST OF TABLES

LIST OF FIGURES

SUMMARY

This research establishes a physics-based life model for the second-generation single crystal superalloy PWA 1484 experiencing out-of-phase (OP) thermomechanical fatigue (TMF). Degradation due to fatigue and a coupling between environmental attack and fatigue are the primary concerns under this loading. Both conventional TMF and special Bithermal Fatigue (BiF) experiments were conducted to isolate and therefore better understand the interactions between these damage mechanisms. The influence of crystallographic orientation, applied mechanical strain range, cycle maximum temperature and high temperature hold times were assessed. In addition, special experiments were used to establish the evolution of surface slip band spacing occurring at lower temperatures and isothermal non-stressed oxidation tests were used to establish the oxidation kinetics active at higher temperatures.

Several physics-inspired models were developed to describe the degradation observed in these experiments and ultimately predict cycles to failure. First, a model for stress-assisted γ' depletion was established from non-stressed γ' depletion studies, as well as TMF and BiF tests. Second, a model was established that correlates the slip band spacing to the applied inelastic strain and test temperature. Finally, a new physics-inspired life estimation model for OP TMF was established which accurately predicts the number of cycles to crack initiation as a function of crystal orientation, applied strain amplitude and stresses, temperature, cycle time including dwells, and surface roughness.

CHAPTER 1. INTRODUCTION

1.1 **Research Motivation**

The use of single crystal superalloys in the hot section of turbines has enabled higher turbine temperatures, thereby increasing efficiency and decreasing pollution [1, 2]. In addition to high temperatures, turbine blades experience relatively high strains induced by centrifugal forces coupled with thermal and mechanical strain transients brought on by geometric stress risers, vibrational mis-tuning, start-up and shut-down cycling as well as irregular load demands. When a component experiences this type of fatigue temperature interaction, i.e. temperature and mechanical strains varying simultaneously in a repetitious manner, it is called thermo-mechanical fatigue (TMF). In order to design a component to withstand these load conditions, the material deformation response to each of these conditions with respect to the material's anisotropy must be fully understood. Furthermore, and probably most importantly, the likely coupling effect that these load conditions have upon the material's deformation response must be understood [1]. Complicating matters is the fact that single crystal superalloys exhibit different damage mechanisms at different temperature regimes, load rates and applied load orientation [1, 3]. To date studies have been conducted which characterize single crystal superalloy response to low cycle fatigue (LCF) [4-6], TMF [3, 7-11], creep [7, 12, 13], and orientation [3, 6, 12, 14-16], though this is by no means an extensive list of the studies conducted in these areas. Due to the fact that turbine blades are always cast having the [001] crystallographic axis aligned with the longitudinal blade direction, only a small portion of the aforementioned studies took material orientation into account. The

orientation of applied load is of utmost importance at notches and cooling holes, as the direction of maximum stress is not as straightforward as in the bulk of the blade.

There is currently a gap in the knowledge base regarding the coupling of fatigue-environment-microstructure interaction upon the single crystal superalloy material response to TMF loading. As turbine blades experience TMF loading on each start-up/shut-down cycle in an oxidation prone environment, the knowledge of these interactions would enable the proposal of a robust physics-inspired life prediction model applicable to turbine blade components. When properly employed, such a model would enable the removal of blades based upon a "retirement for a cause" life management scheme rather than the currently employed "safe-life" calculations [1]; or in the very least, help to determine appropriate component inspection intervals.

1.2 **Research Objectives**

This research aims to establish a physics-inspired life determination model for the second generation single crystal superalloy PWA 1484. The life model was developed as a result of a combination of critical mechanical tests, dominant damage characterization and utilization of well-established literature. The resulting life model improves life prediction over currently employed methods and provides for extrapolation into yet unutilized operating regimes. Particularly, the proposed deformation model accounts for the materials' coupled fatigue-environment-microstructure response to TMF loading. Because the proposed model is be based upon the underlying deformation physics, the model is robust enough to be easily modified for other single crystal superalloys having similar microstructure. Future use of this model for turbine life estimation calculations would be based upon the actual deformation experienced by the turbine blade, thereby

enabling turbine maintenance scheduling based upon on a "retirement for a cause" life management scheme rather than the currently employed "safe-life" calculations. This advancement has the ability to greatly reduce maintenance costs to the turbine end-user since turbine blades would be removed from service for practical and justifiable reasons. Further, the utilization of such a model would reduce costs to the turbine manufacturer as this model will reduce the necessity of extensive preliminary testing protocols currently employed on new material and component development. Additionally this work will enable a rethinking of the warranty period, thereby decreasing warranty related replacements. Finally, this research provides a more thorough understanding of the deformation mechanisms present in loading situations that combine fatigue-environment-microstructure effects. This in turn may provide a building block for further research that attempts to add independent damage mechanisms such as severe creep.

1.3 **Overview of Dissertation**

This work is formatted such that each chapter may be a stand-alone document, subsequent to minimal modifications. The second chapter is comprised of a literature review focusing upon single crystal superalloy applications, damage mechanisms as well as current life prediction methodologies. The third chapter details the thermomechanical test procedures and results for this work. The fourth chapter is intended to be a standalone chapter on oxidation. This chapter details experimental procedures and results for all high-temperature material degradation studies performed during the course of this work. The fifth chapter details experimental results on slip band spacing studies performed for this work. The life modeling exercises completed for this work are

compiled in chapter six. Conclusions and recommendations are at the end of this dissertation.

CHAPTER 2. LITERATURE REVIEW

2.1 Introduction

Superalloys are a class of metals which exhibit excellent phase stability when loads are applied at temperatures up to 85% of the materials melting point [17]. This class of metal was developed for use in aero and power generation turbines where gas temperatures reach well over 1500° C and blades can see temperatures up to, and exceeding, 1100° C. Superalloys are typically nickel-base, iron-nickel-base or cobalt-base, and are most commonly used in one of three crystalline forms: i) polycrystalline, ii) directionally solidified, or iii) single crystal. The nickel-base superalloy microstructure, shown in Figure 2-1, is comprised of small, typically coherent, Ni_3Al $L1_2$ (FCC-like) precipitates (γ'), embedded in an FCC solid solution (γ), called the matrix, in which nickel is the primary element, but which also contains substitutional elements such as Mo, Cr, Re, etc. [18]. The precipitate size and volume fraction vary according to composition and heat treatment and are tailored for service loading and temperature conditions. Single crystal superalloys are cast by either using a grain selector method or a seed crystal, with the former being most prevalent due to its low(er) cost. The grain selector method produces a crystal with a longitudinal axis coincident with [001] (within 10°), while the other two axis are oriented randomly [3]. The crystals [001] growth is due to this orientations' favorable thermodynamic cooling process. Due to their slender geometry, turbine blades are cast so that their long axes is coincident with the crystal growth direction, which is fortunate given that the [001] orientation exhibits the lowest modulus and highest thermal stress resistance [4-7].

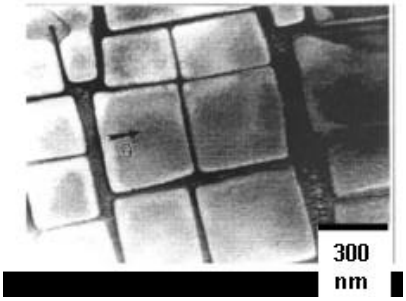

Figure 2-1: Typical Two Phase Superalloy Microstructure [19]

"Hot section" aero turbine blades are nearly exclusively made from single crystal superalloys due the material's desirable primary crystal orientation and resulting deformation response, as well as their superior creep response owing to the lack of grain boundaries [2]. Single crystal superalloys are designated by generation, with each subsequent generation marked by improved mechanical and/or high temperature response. The first generation alloys were developed to increase creep rupture response over their directionally solidified (DS) precursors, while the second generation alloys are marked by a 3 w/o % increase in Re which is thought to reduce lattice mismatch and mass diffusion, thereby improving creep capabilities [2, 17, 20]. Third generation alloys have up to 6 w/o % Re, which is thought to enhance lattice stability at temperatures up to 1160° C [2, 17]. Second generation single crystal superalloys are the most frequently used in modern aero engines [21]. Table 2-1a lists the nominal chemical composition for the four generations of single crystal superalloys, compared to the first generation. Table 2-1b provides a general overview of the roles that alloying elements play in superalloys.

Table 2-1: a) Nominal Chemical Composition of Superalloys by Generation (top) [2]; b) Role of Alloying Elements (bottom) [2, 21]

Chemical Composition (weight %)

SXSA Generation	Cr	Co	Mo	Re	Ru	W	Al	Ti	Ta	Nb	V	Hf	Others
Gen I	~9	~6	~2	N/A	N/A	~8	~5	~2	~5	N/A	N/A	N/A	N/A
Relative Change of Alloying Elements													
Gen II (WRT Gen I)	↓	↑	-	ADD	-	↓	-	-	-	-	DEL	-	-
Gen III (WRT Gen II)	↓	-	-	↑	-	-	-	-	-	-	DEL	-	ADD
Gen IV (WRT Gen III)	-	-	↑	-	ADD	-	-	-	-	DEL	DEL	-	-

Key	↓	↑	-	ADD	DEL
	Reduce	Increase	No Δ	ADD	DELETE

Role of alloying elements in superalloys

Effects	Alloying elements
Solid Solution Strengthening	Co, Cr, Mo, W, Ta, Re
Formation of γ'	Al, Ti
Raises solvus temperature of γ'	Co
Oxydation resistance	Al, Cr
Formation of γ''	Nb
Sulfidation resistance	Cr, Co
Retards γ' rafting	Re
Formation of topologicaly closed packed phases	Co, Mo, W, Re, Cr

Superalloys were developed for use as turbine components due to the extreme temperatures and loading conditions resulting form normal turbine operation. A schematic of a turbojet turbine is provided in Figure 2-2. This Schematic shows the relative locations for the four primary turbine regions. The compressor acts to compress the incoming air thereby increasing its pressure. When the compressed air reaches the combustor, it is mixed with fuel and the gas mixture is ignited. The resulting hot gasses expand and escape through the turbine, which extracts the mechanical work by spinning a shaft connected to the compressor blades.

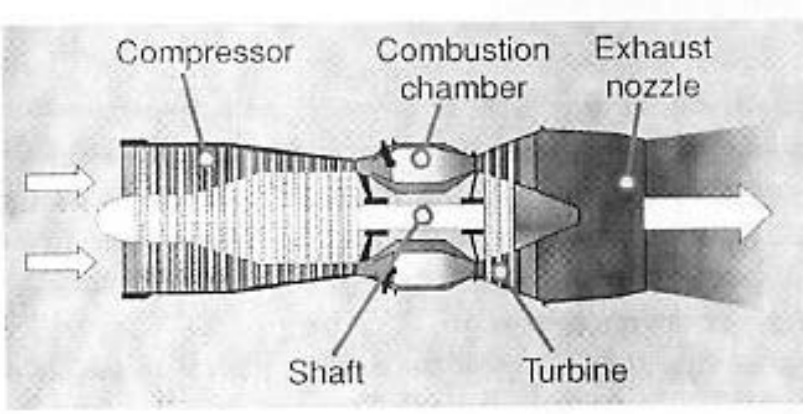

Figure 2-2: Schematic of a Basic Turbojet Gas Turbine Engine [2]

As gas turbines are heat engines, the primary way in which turbine efficiency is increased is through increased operating temperatures [1, 2]. The turbine operating temperature is characterized by the turbine entry temperature (TET). Historically the TET, and therefore the turbine efficiency, has been limited by the alloys used in the turbine. Figure 2-3 depicts the historic development for both superalloy material temperature capabilities and take-off TET temperatures for Rolls Royce civil aero engines. Take-off TET temperatures have increased as a function of time, owing to superalloy development.

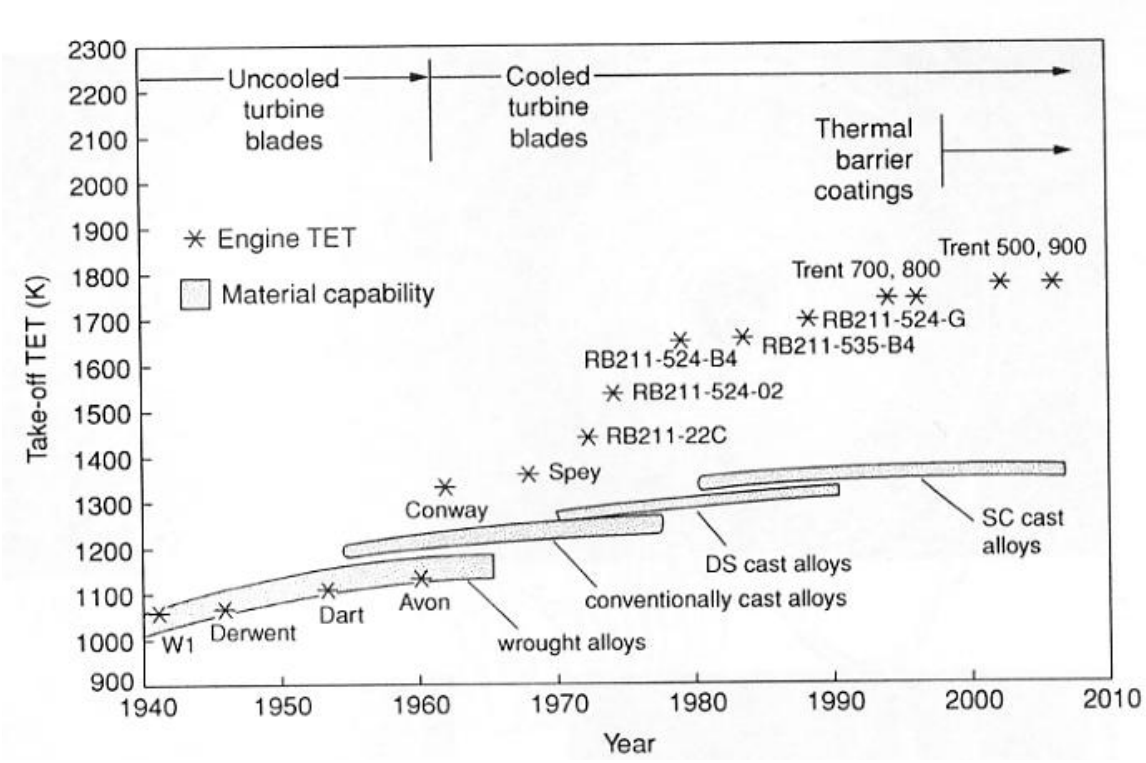

Figure 2-3: Evolution of Take-Off TET Capability for Rolls-Royce Civil Aero Engines [2]

Figure 2-4 offers a more stringent qualification for superalloy operating temperature capabilities, namely the temperature for 1000 hour creep life when loaded to 137 MPa (~20 ksi). Furthermore, Fig 2-4 provides a bit more clarity to the evolution of superalloys in that it shows the creep response of specific alloys as a function of time.

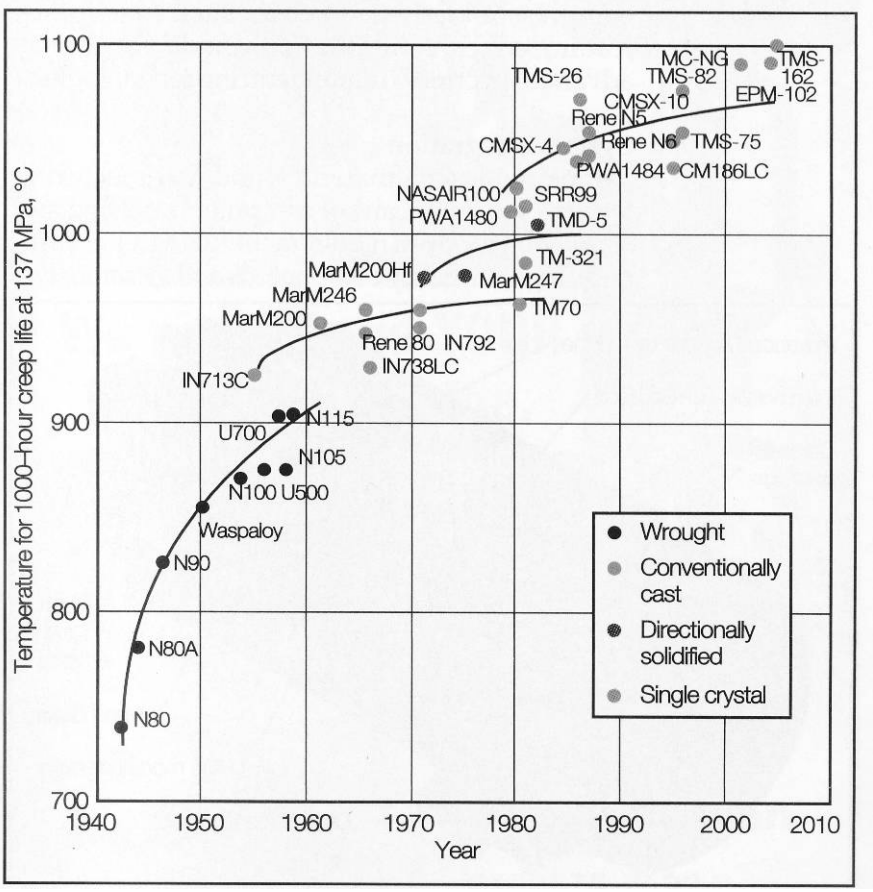

Figure 2-4: Superalloy Creep Response as a Function of Year. Originally from [2]

Superalloys are typically made in four forms: wrought, conventionally cast (polycrystalline), directionally solidified and single crystal; with the latter three being most prevalent. Figure 2-5 provides a schematic illustration of the three most commonly used crystalline forms in which superalloys are found

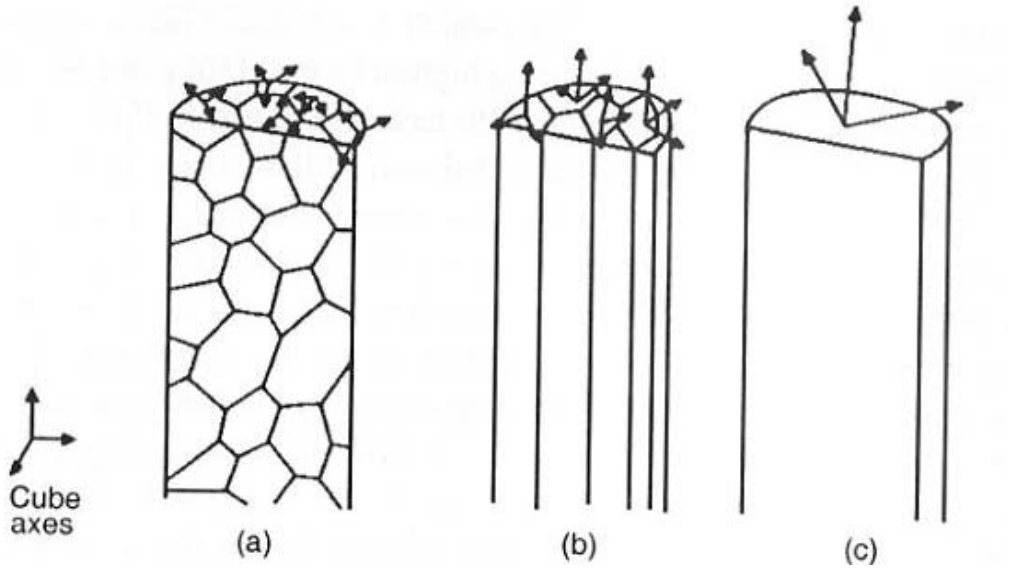

Figure 2-5: (a) Illustration of Equiaxed Polycrystalline, (b) Directionally Solidified, and (c) Single Crystal Alloys Used for Turbine Blade Airfoils [2]

Decreasing the number of grains, and therefore number of grain boundaries, in turbine materials has a primary effect upon diffusion and diffusion-based processes. It is well known that grain boundaries promote diffusion of oxygen and chemical constituents at a higher rate than the bulk material. Furthermore they also promote deformation by grain boundary sliding. The differential in grain boundary to bulk diffusion leads to increase creep rate as well as processes such as short circuit diffusion of oxygen, resulting in non-parabolic oxidation kinetics, [22] among other things. The effects of material structure on the creep strength, thermal fatigue (TF) resistance and corrosion resistance of superalloys is shown schematically in Figure 2-6

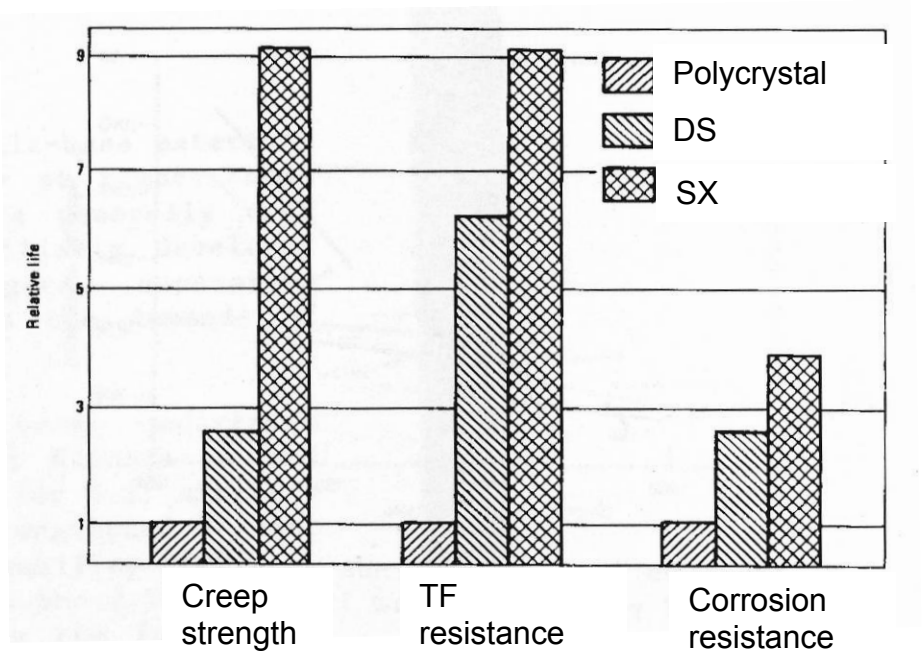

Figure 2-6: Superalloy Material Properties as a Function of Crystalline Structure [17]

Due to the different material property characteristics exhibited by the three forms in which superalloys are made, each type has found dominant use in different sections of turbines, depending upon the temperature in the turbine region of interest as well as turbine end-use, i.e. land based or aero. Polycrystalline superalloys are predominantly used as rotor material due to: a) the rotor experiences the lowest temperatures of all components in each turbine section, b) the centripetal acceleration experienced at the rotor has far less magnitude than that experienced by the blades, c) they are far less expensive to manufacture, and d) they have better high cycle fatigue properties. Directionally solidified (DS) superalloys are employed as vane and blade materials, where temperatures are far higher than those experienced at the disk, in both power generation and aero turbines. The decrease in, and alignment of grain boundaries enables the DS form of the alloy to withstand higher temperatures and centripetal accelerations than the polycrystalline form; this is due to the fact that there are fewer boundaries to

accommodate diffusion, grain boundary sliding and triple points. Due to the increase in cost of casting, single crystal superalloys are typically used as vanes and blades in the hot section of aero turbines, where the turbomachinery is pushed to the extremes of material capabilities. They are used to a lesser extent in power generation turbines [2, 17].

2.2 Description of PWA 1484

PWA 1484 is a second generation single crystal superalloy developed by Pratt & Whitney in the late 1980's. This material was developed to improve upon the creep resistance, strength, oxidation resistance and fatigue resistance of the first generation single crystal superalloy PWA 1480. The nominal chemical composition of the two alloys is compared in Table 2-2.

Table 2-2: Nominal Chemical Composition of PWA 1480 and PWA 1484 (wt %) [7]

	Ni	Cr	Ti	Mo	W	Re	Ta	Al	Co	Hf
PWA 1480	58.5	10	1.5	-	4	4	12	5	5	-
PWA 1484	59.6	5	-	2	6	3	8.7	5.6	10	0.1

Components made of PWA 1484 undergo a three-step heat treatment. The first step, a 1315°C solution heat treatment for 4 hours. Subsequent cooling results in the γ' precipitation into a uniform array of fine cuboidal particles (side length < 0.3μm). The next step is a 1080°C heat treatment for four hours which provides optimum γ' size distribution. Finally a 704°C heat treat at 24 hours produces fine γ' particles (side length < 0.1μm) between the larger particles, resulting in enhanced "intermediate temperature" yield strength [2, 7]. Each step in the heat treat process is followed by a controlled cooling period in order to ensure desired precipitate shape and size results. The service-

condition alloy has a γ' particle size between 0.25 and 0.35μm, a γ' volume fraction of approximately 63%, a density of 8.94 x 10^{-3} kg/cm^3, an incipient melting temperature of 1338° C and γ' solvus temperature of 1299° C [7].

2.3 General Plasticity and Slip Band Spacing

2.3.1 Fundamentals of Inelastic Deformation

The application of an inelastic shear strain in metals manifests as the movement of dislocations. Dislocations typically traverse close packed planes since the atoms of these planes are closer together, thereby providing a "smoother" surface for the dislocation movement [23, 24]. The combination of an easy-slip plane and easy-slip direction is termed a slip system. Each crystal structure has an associated set of slip systems. Figure 2-7 depicts the slip planes and directions of a face centered cubic (FCC) crystal structure. The activation of a particular slip system is dependent upon the crystal orientation with respect to the axis of loading. Under simple uniaxial loading the resolved shear stress (τ) on each slip system in the crystal structure is given by,

$$\tau = \sigma \bullet \cos(\varphi) \bullet \sin(\lambda) \qquad \textbf{(2-1)}$$

where σ is the applied uniaxial stress, λ the angle between the loading direction and the normal to the slip plane of interest and φ the angle between the loading direction and the slip direction of interest. The slip system with the largest values of τ will likely be activated first. Results from just such an analysis performed for FCC crystals loading in several directions are provided in Figure 2-8. The loading directions of interest are plotted on the standard stereographic triangle and shown in Figure 2-9.

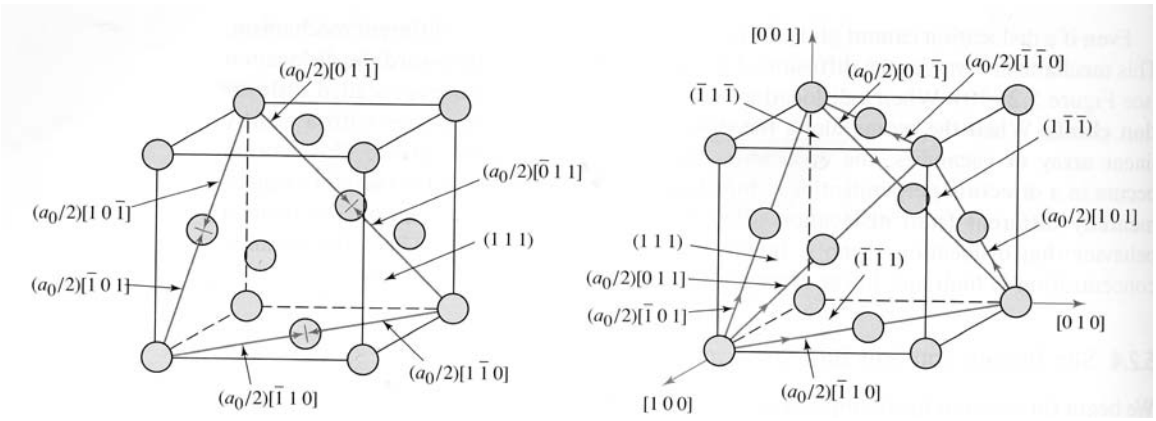

Figure 2-7 Slip Systems for FCC Crystal- Single Slip Plane Left, Tetrahedron Created by Four {111} Planes [23]

Loaded in (001)

Slip System	Schmid Factor
(111)[01-1]	0.408
(111)[10-1]	0.408
(111)[-110]	0
(1-11)[01-1]	0.408
(1-11)[-10-1]	0.408
(1-11)[-1-10]	0
(-111)[10-1]	0.408
(-111)[0-1-1]	0.408
(-111)[-1-10]	0
(-1-11)[0-1-1]	0.408
(-1-11)[-10-1]	0.408
(-1-11)[-110]	0

Loaded in (011)

Slip System	Schmid Factor
(111)[01-1]	0
(111)[10-1]	0.408
(111)[-110]	0.408
(1-11)[01-1]	0
(1-11)[-10-1]	0.408
(1-11)[-1-10]	0.408
(-111)[10-1]	0
(-111)[0-1-1]	0
(-111)[-1-10]	0
(-1-11)[0-1-1]	0
(-1-11)[-10-1]	0
(-1-11)[-110]	0

Loaded in (111)

Slip System	Schmid Factor
(111)[01-1]	0
(111)[10-1]	0
(111)[-110]	0
(1-11)[01-1]	0
(1-11)[-10-1]	0.272
(1-11)[-1-10]	0.272
(-111)[10-1]	0
(-111)[0-1-1]	0.272
(-111)[-1-10]	0.272
(-1-11)[0-1-1]	0.272
(-1-11)[-10-1]	0.272
(-1-11)[-110]	0

Loaded in (123)

Slip System	Schmid Factor
(111)[01-1]	0.175
(111)[10-1]	0.350
(111)[-110]	0.175
(1-11)[01-1]	0.117
(1-11)[-10-1]	0.467
(1-11)[-1-10]	0.350
(-111)[10-1]	0.117
(-111)[0-1-1]	0.292
(-111)[-1-10]	0.175
(-1-11)[0-1-1]	0.000
(-1-11)[-10-1]	0.000
(-1-11)[-110]	0.000

Figure 2-8 Schmid Analysis for FCC Crystal for Different Loading Directions: <001> Top Left, <011> Top Right, <111> Bottom Left and <123> Bottom Right

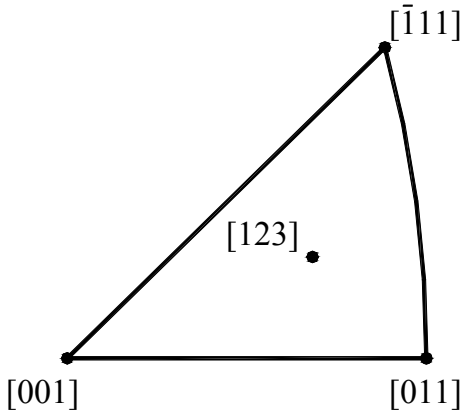

Figure 2-9 Loading Direction of Interest Plotted on Standard Stereographic Triangle

The results of the Schmid analysis provided in Fig 2-8 indicate that eight octahedral slip systems will be activated for an FCC crystal loaded in the <001> direction, four slip systems for <011> loading, six slip systems for <111> and a single slip system activated for <123> loading.

Dislocations are created in a crystal by "accidents" during the initial solidification of the crystal, internal stresses due to other defects in the crystal or by interactions between existing dislocations during inelastic deformation [23]. Dislocations introduced during solidification can result from the insertion of a partial atomic plane in the crystal to minimize energy (edge dislocation) or shifting of one atomic plane with respect to it's neighbor (screw dislocation). An increase in inelastic deformation leads to an increase in the number of dislocations, ultimately resulting in an increase in crystal strength, since an extra amount of work is required to move a given dislocation's stress field through the combined stress fields of the other dislocations in the crystal [23]. Hence, one expects more interactions and greater strain hardening in crystals where several slip systems are simultaneously activated. For FCC crystals [001] orientations would lead to multiple simultaneously activated slip systems, whereas [123] would have a single slip system

activated. Inelastic deformation in crystals is typically confined to planar regions of intense plastic deformation called slip bands. Slip bands are composed of a great number of identical parallel slip systems and are separated by material with relatively little dislocation accumulation. When a slip band intersects the free surface of a material, steps are formed, comprised of many small slip steps from each of the impinging slip systems [24].

2.3.2 Classical Plasticity Rate Equations

Low temperature plasticity is controlled by dislocation glide. The rate of dislocation glide is obstacle limited. There are two types of obstacles normally encountered. 1) discrete obstacles which are either bypassed by moving dislocations (in the case of weak obstacles), or cut by the dislocations (in the case of strong obstacles). 2) Extended diffuse barriers to dislocation movement which must be overcome collectively, such as lattice friction. Of interest to this work is the rate equation for plasticity limited by discrete obstacles [25],

$$\dot{\gamma} = \dot{\gamma}_0 \exp\left[-\frac{\Delta F}{kT}\left(1-\frac{\tau_s}{\hat{\tau}}\right)\right], \text{ where } \dot{\gamma}_0 = \frac{\alpha}{b}\left(\frac{\tau_s}{\mu}\right)^2 \beta b \nu \qquad \textbf{(2-2)}$$

where ΔF is the intrinsic activation energy of the barrier, k the Boltzmann constant, T the temperature, τ_s the shear stress, $\hat{\tau}$ the flow strength at 0 K, α is a constant, β is a dimensionless constant, b the Burgers vector, μ the shear modulus, and ν is the dislocation velocity.

Alloying of a material has primary effects on dislocation glide. If alloying produces weak particles, the solutes introduce friction-like resistance to dislocation glide. In this case Eq. 2-3 above would be utilized to describe the rate of plasticity, given that a larger value of $\hat{\tau}$ and higher value of ΔF were used. If alloying produces strong particles, these particles introduce independent barriers to dislocation movement. A second-phase particle such as the γ' found in superalloys is just such a particle. Gliding dislocations can only move through a strong particle array by cutting or bowing between, and in turn bypassing the particles. Particle cutting occurs at lower temperatures and bowing occurs at higher temperatures. This bowing leads to an increase in flow strength as the number of dislocations has been increased as a result of the bowing process. Of note is that the flow strength scales with the inverse of particle spacing [25]. The activation energy for obstacle bypass by bowing is very high. As such Eq. 2-3 is modified prior to use in this instance. Specifically one must substitute $\hat{\tau} \sim 2\mu b / l$ and $\Delta F \geq 2\mu b^3$. The large activation energy for bowing leads to a nearly athermal flow strength. Finally, obstacles may lead to precipitate cutting if the obstacles are finely dispersed and coherent. In general, the materials flow strength is proportional to the particle density. Frost and Ashby [25] note that "If the precipitate is allowed to coarsen it behaves like a dispersion of strong particles." In which case one may use Eq. 2-3 without modification.

For completeness, a short introduction to the rate equation governing low(er)-temperature creep is provided next. High temperature plasticity is often associated with power law creep. This is not strictly correct since secondary creep (power law creep) is just one of three possible creep regimes, depending upon temperature. The likely reason for this is due to the fact that power law creep has dominant effects over a considerable

time and temperature range. Above 0.3 T_m to 0.4 T_m, where T_m is the materials melting temperature, a pure metals flow strength is increasingly dependent upon strain rate, as governed by [25]

$$\dot{\gamma} \sim \left(\frac{\tau_s}{\mu} \right)^n \qquad \textbf{(2-3)}$$

where $\dot{\gamma}$ is the strain rate, τ_s the shear stress and μ is the shear modulus. The exponent n typically has a value between 3 and 10 for this creep regime. The climb mechanism typically sets in at temperatures above 0.6 Tm.

2.3.3 Slip Band Spacing

Many researchers have conducted studies on the effects of dislocation accumulation in crystalline materials as a function of applied strain. When "surface plasticity was apparent" i.e. slip bands or slip steps appear on the surface, the average spacing between slip bands is a good indication of the heterogeneity of the deformation within the material. One study determined that an increase in applied inelastic strain yields deformation homogenization by decreasing slip band spacing (therefore an increase in the number of slip bands) and the activation of multiple slip systems [26]. Diederich et al. [27] determined from experiments that the slip band spacing, C, of Waspaloy cycled isothermally at room temperature had the following functional form

$$C = A * \left(\Delta \varepsilon^{in} \right)^{-1/2} \qquad \textbf{(2-4)}$$

where $\Delta\varepsilon^{in}$ is the inelastic strain range of fully reversed tests, in this case. Venkataraman et al. [28] derived an energy-based relationship for slip band spacing in polycrystalline materials.

$$w^2 = 0.93ah\frac{\Delta\sigma - 2\sigma_F}{\mu}\frac{1}{M^2\varepsilon_p} \quad \textbf{(2-5)}$$

where w is the slip band spacing, a the grain size, h the slip band width, $\Delta\sigma$ the applied stress range, σ_F a lattice frictional stress, μ is the shear modulus, M is the reciprocal of the Schmid factor and ε_p is the inelastic strain. This relationship infers that "the spacing between the bands in the minimum energy configuration varies as the inverse square root of the plastic strain amplitude", thereby supporting the results of Diederich et al. The authors point out that the model is "strictly inapplicable" to single crystals as the derivation for the model assumed that the grain boundaries were primary internal obstacles. The results of work performed by Shyam et al. [26], Thomson et al. [29], Margolin et al. [30] and Harvey et al. [22] found that slip band spacing followed the general form

$$C = A * \left(\varepsilon^{in}\right)^{-n} \quad \textbf{(2-6)}$$

where C is the slip band spacing, A and n are constants and ε^{in} is the applied inelastic strain. This general relationship was shown to be appropriate for both monotonic loading as well as cyclic loading with cyclic strain ratio values of both zero and negative one.

Three independent studies performed on slip band spacing are of particular importance to the work presented here. First, Shyam and Milligan [31] established a model for slip irreversibility and its effect on fatigue crack propagation in the coarse

grained polycrystalline Ni-base superalloy KMA. Uniaxial compression tests were performed at three temperatures (25° C, 550° C and 650° C) at strains ranging from 3% to 25% at a strain rate of 0.1 s^{-1}. The authors concluded that, for all temperatures tested, once the dislocation density within existing slip bands saturates, additional inelastic deformation can only be accommodated by the nucleation of new slip bands. When looking at macroscopic effects, the authors also determined that an increase in temperature leads to crack tip blunting as well as crack tip oxidation. The oxidation at the crack tip enhances slip irreversibility, or the number of dislocations exiting the material through the free surface. This phenomena results in slip steps which are likely crack initiation locations.

The grain size also influences slip band spacing [29, 30]. Slip spacing studies on β-Titanium alloy with grain sizes of 49 μm, 65 μm, 94 μm and 200 μm suggest that the strain exponent becomes increasingly negative as the grain size increases [30]. Studies on aluminum brass and copper of different grain sizes [29] indicate a similar trend, as shown by the results for polycrystalline copper in Fig 2-10

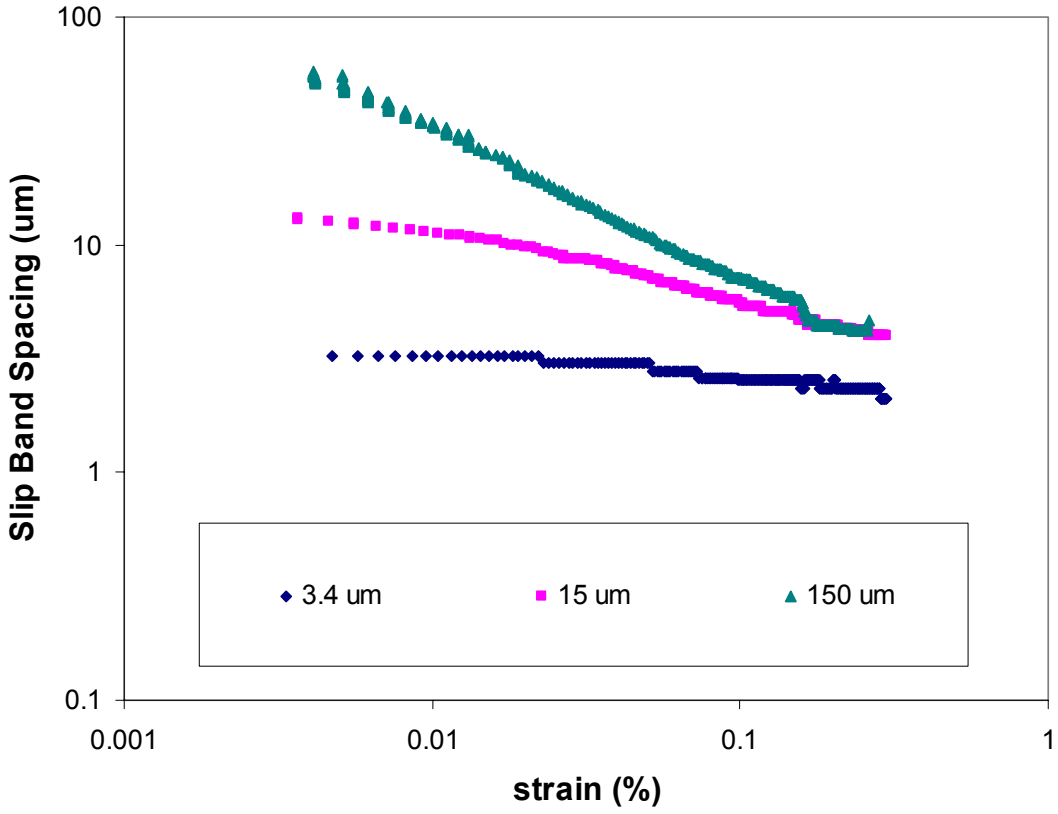

Figure 2-10 Dependence of Slip Band Spacing on Grain Size for Polycrystalline Copper [29]

2.4 Deformation Mechanisms

There are numerous studies which report the deformation characteristics of superalloys with respect to loading conditions. To report on all of them would be inappropriate, as different alloy compositions, loading conditions, environmental conditions, etc. all affect the deformation characteristics of the alloy in question. This work will focus on the turbine hot-section component material, primarily single crystal superalloys. Though a portion of the discussion will be applicable only to single crystals, a large amount will be valid for directionally solidified superalloys and to a lesser extent, to polycrystalline superalloys.

2.4.1 γ-γ' Interaction- influence of γ' precipitates on deformation

The most common superalloy microstructure is comprised of small coherent $L1_2$ (FCC-like) precipitates (γ') embedded in an FCC (γ) matrix. The γ' precipitates generally strengthen the composite system while the matrix allows for ductility. As a result, tensile properties are significantly controlled by the size and composition of the γ' phase [2, 5]. Second generation single crystal nickel-base superalloys have a γ' volume fraction of approximately 60%. Figure 2-11 shows the strength of alloys having varying γ' volume fractions as a function of temperature.

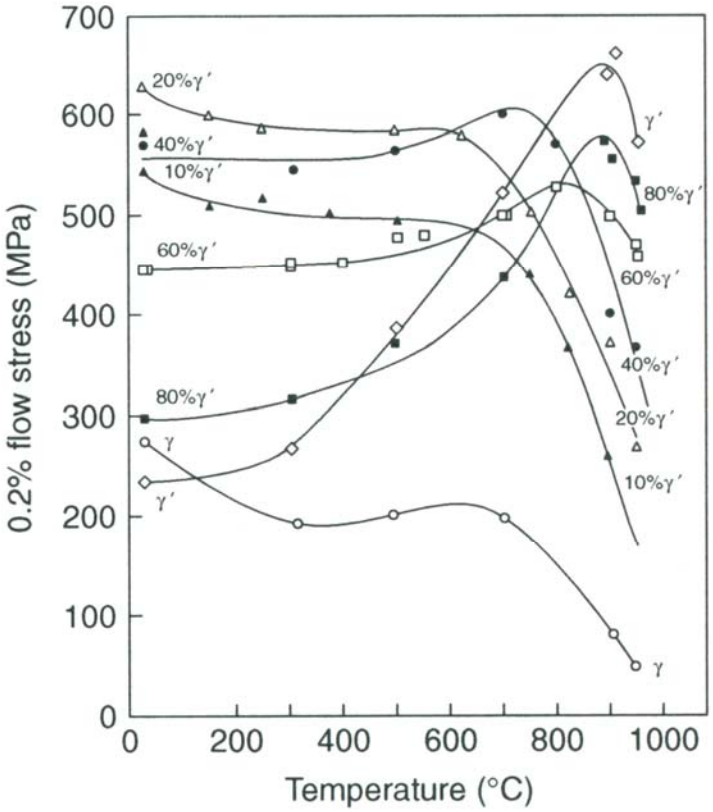

Figure 2-11: Yield Stress as a Function of Temperature and γ' Volume Fraction (%) in Ni-Cr-Al Ternary Alloys [2]

Well controlled and tailored values of γ' size and volume fraction are vital for optimum material properties. Creep properties are optimized by a γ' volume fraction of ~70% [2] as indicated in Figure 2-12.

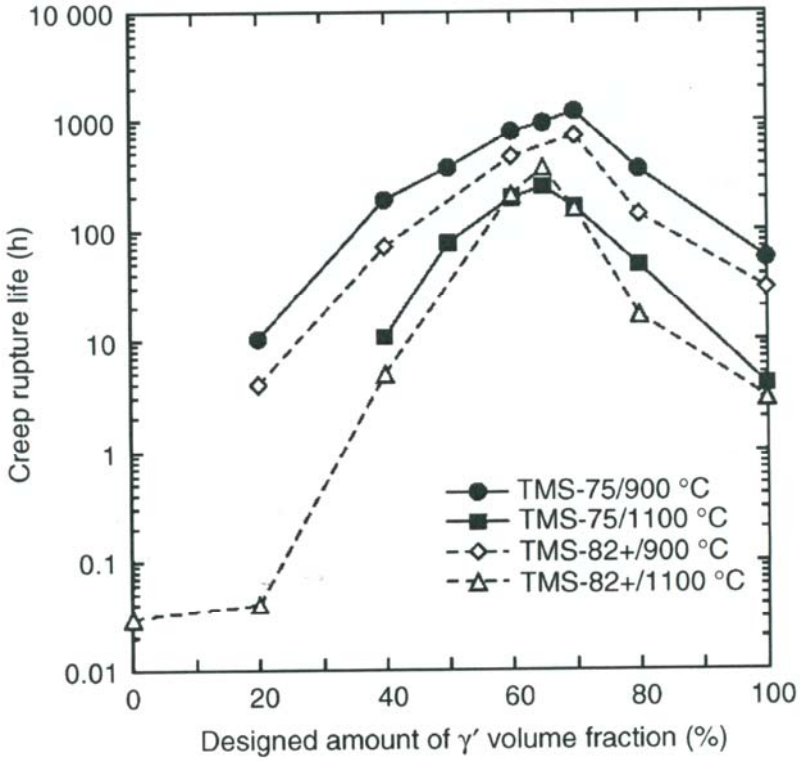

Figure 2-12 Creep Rupture Life of a representative Superalloy as a Function of γ' Volume Fraction (%) for a Fixed γ' Size [2]

An optimum value of γ' particle size ensures that the composite strength of the material is controlled by particle cutting, rather than the much weaker process of dislocation looping as indicated by Figures 2-13 and 2-14. Often the microstructure is tailored to obtain two or three distributions if γ' particles sizes, with coarse particles providing high temperature strength and ultra-fine particles providing intermediate temperature strength [2]. Figure 2-15 shows the variation in second phase particle size for PWA 1484.

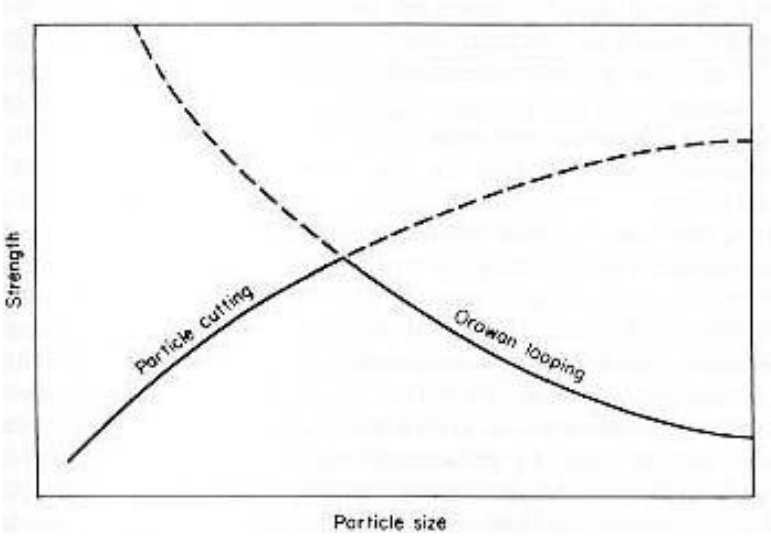

Figure 2-13 Theoretical Relationship Between γ' Particle Size and Alloy Strength [32]

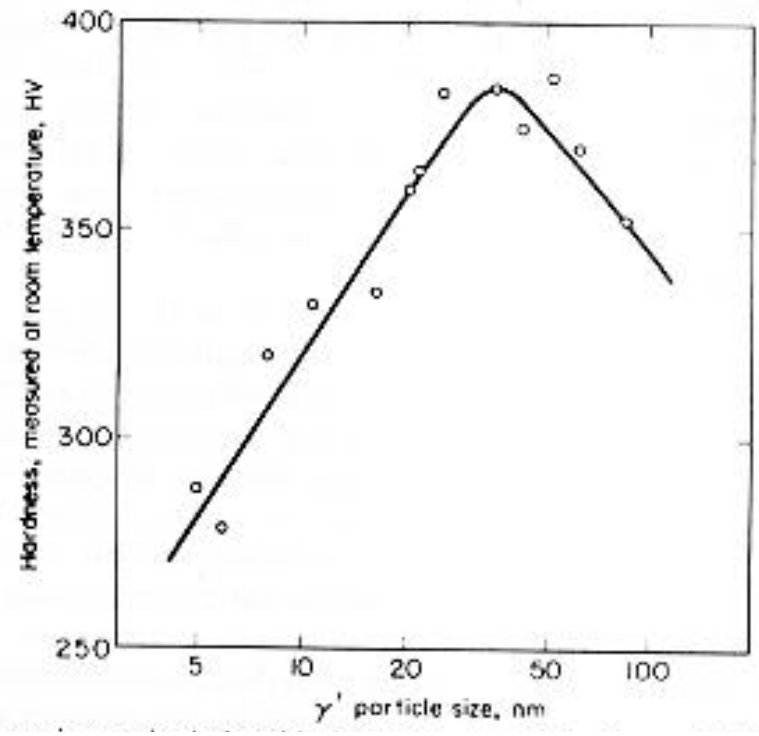

Figure 2-14 Experimental Relationship Between Particle Size and Alloy Strength in a Ni- 20% Cr Base Alloy [32]

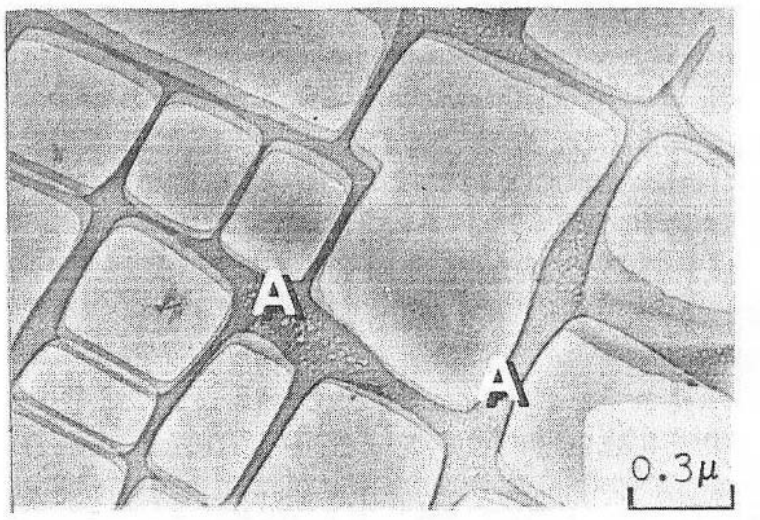

Figure 2-15 Variation in γ' Particles Size for PWA 1484 in Full Heat Treat Condition: Primary and ultra fine (A) γ' [7]

The result of the two-phase microstructure is that deformation may be confined to the γ phase or to both phases, depending upon test conditions. Milligan and Antolovich [33] determined that lower temperature monotonic tensile loading of PWA 1480 resulted in γ' shearing by pairs of a/2<110> dislocation in octahedral planes. At higher temperatures this alloy exhibited two-part deformation: bypass of the γ' occurred in the initial stages of loading followed by γ' shearing only after a significant increase in matrix dislocation density and considerable strain hardening had occurred. Another study found that the deformation was confined to the γ phase during high temperature LCF tests (temperatures above 950° C) having compressive hold times [34].

2.4.2 Orientation effects- anisotropic behavior of single crystal superalloys

Due to the nature of the FCC crystal structure, single crystal superalloys exhibit highly anisotropic material properties. The material anisotropy is manifested in elastic, inelastic and time dependant material deformations. The most predominant manifestation

of the materials asymmetry is the dependence of Young's modulus and yield strength on crystallographic orientation. Figure 2-16 shows the modulus of PWA 1480 plotted on a standard stereographic triangle. The critical resolved shear stress (τ_{RSS}) of the γ' precipitates increases with temperature to approximately 1000K. Furthermore, the γ' phase exhibits considerable tension-compression asymmetry. The asymmetry in the resolved shear stress when loaded in the <001> orientation is most prevalent at intermediate temperatures as shown in Fig 2-17.

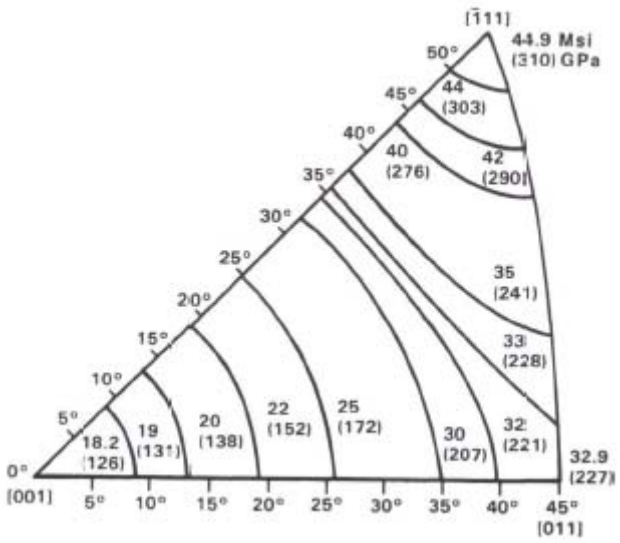

Figure 2-16: Elastic Modulus as a Function of Crystallographic Orientation for PWA 1480 [35]

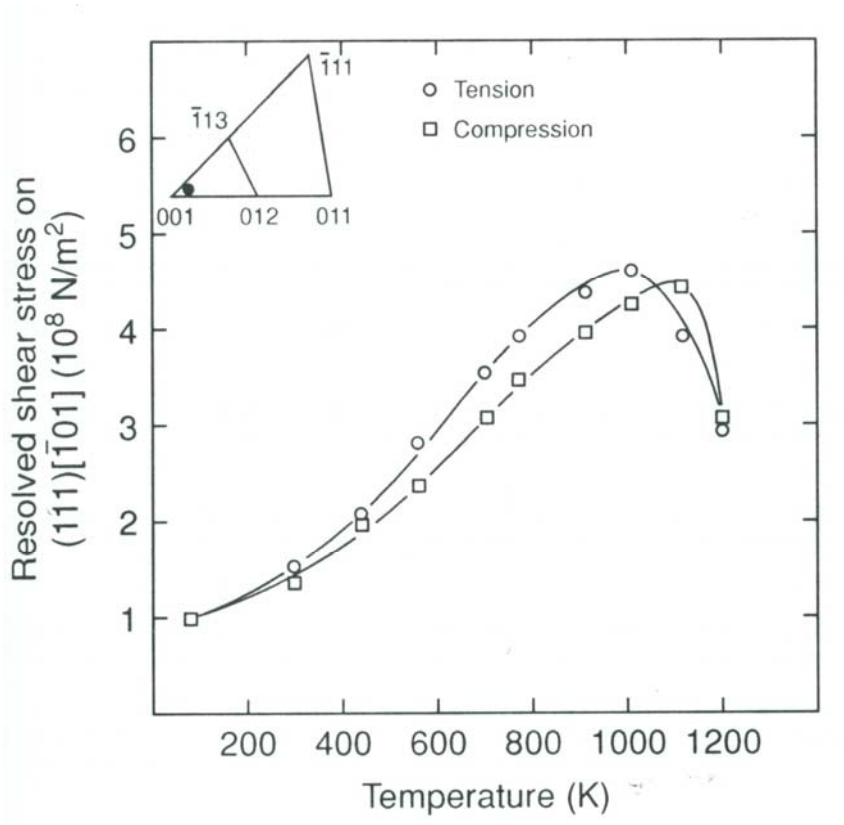

Figure 2-17 Variations with Temperature of Critical Resolved Shear Stress for γ' Single Crystals [2]

Single crystal superalloy asymmetry plays a large role in the amount of plasticity, stress relaxation (during strain dwells), creep response, as well as fatigue life [36]. In general, the [001] orientation has the highest ductility, the [110] orientation has the lowest yield strength, and the [111] orientation has the highest yield strength but the lowest ductility [11, 14, 16]. Due to the FCC cubic symmetry, inelastic deformation can easily be predicted using a Schmid analysis. A material which follows the Schmid law would be said to have "Schmid effects", whereas a material or orientation which doesn't behave according to the Schmid law would be said to have "non-Schmid" behavior. Numerous studies have been conducted to determine the validity of the Schmid-predicted slip system activation. Orientation plays a key role in determining which slip systems are

currently, as well as concurrently, activated at any time [37]. From a simple Schmid analysis one can determine that the number of concurrently activated octahedral slip systems ranging from eight for loading in the [001] orientation to one active slip system for loading in the [123] orientation. Results of a Schmid analysis for FCC crystals load in the <001> direction are provided in Table 2-3 with general conclusions provided in Table 2-4.

Table 2-3: Schmid Analysis for FCC Crystal Loaded in [001] Direction

Slip System	Schmid Factor
(111)[01-1]	0.408
(111)[10-1]	0.408
(111)[-110]	0
(1-11)[01-1]	0.408
(1-11)[-10-1]	0.408
(1-11)[-1-10]	0
(-111)[10-1]	0.408
(-111)[0-1-1]	0.408
(-111)[-1-10]	0
(-1-11)[0-1-1]	0.408
(-1-11)[-10-1]	0.408
(-1-11)[-110]	0

Table 2-4: Schmid Analysis for FCC Crystals- Active Slip Systems

Orientation	Primary Slip System	Number of Slip Systems Active
[001]	Octahedral	8 Oct.
[011]	Octahedral	4 Oct.
[111]	Octahedral	6 Oct.+3 Cube
[123]	Octahedral	1 Oct.

One study reported that PWA 1480, loaded in the [001] direction, deformed due to octahedral slip on the close packed planes, which confirms the Schmid analysis results [5]. Another study on Rene N4 found that the Schmid law works well for temperatures

greater than 800˚ C for all of the crystal orientation tested except for [111] [38]. For the [111] orientation the specimens exhibited "macroscopic cube slip", which was later determined to be multiple cross slip of two equally stressed {111} planes manifesting in a macroscopic fracture surface of [110] orientation, as shown in Fig 2-18 [38]. This phenomena was also observed by researchers working on fatigue of the single crystal SC16 [39]. Though the fracture surface initially appeared to be a cube plane leading the researchers to believe that considerable deformation had occurred on these planes prior to crack propagation, these studies found that the octahedral planes are in fact the primary carriers of plastic deformation in superalloys, and that the cube planes play a minimal role, if any.

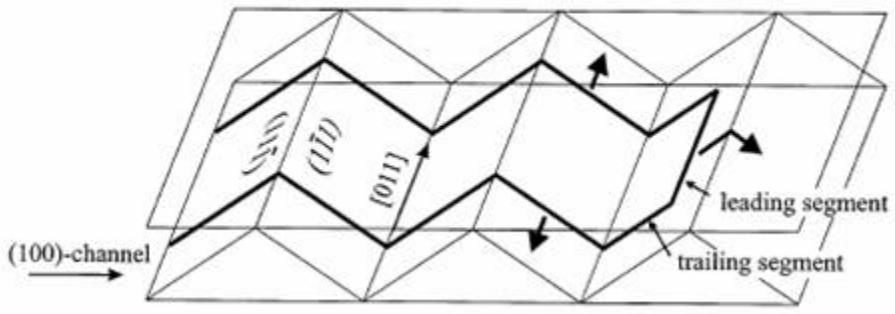

Figure 2-18 Sketch of Macroscopic "Cube" Slip composed of Cross Slip on Octahedral Planes [39]

These researchers found that the relationship proposed by Miner et el. [15] performed well when determining yield behavior for the "macroscopic" Schmid effect. The relationship, is simply an extension of the Schmid law with added parameters to fit experimental data,

$$\frac{1}{\sigma_y} = b_1 S_1 + b\ S_2 + \delta b_3 S_3 \qquad \textbf{(2-7)}$$

where σ_y is the yield strength, S_1, S_2, and S_3 are the Schmid factors for primary octahedral slip, cube cross slip and partial constriction, repectively. The terms b_1, b_2, and b_3 are fitting parameters and δ=+1 for tensile loading and -1 for compressive loading. A simple Schmid analysis has also been used to collapse strain-life trends for specimens having different primary crystallographic orientation. In one study the LCF lives of the superalloy PWA 1480 were compared for specimens having different loading orientations [6]. The researchers plotted life versus different fatigue indicator parameters, including those by Kandil et al.[40], Socie et al.[41], Fatemi and Socie [42] as well as Smith Watson and Topper [43]. It was found that the traditional fatigue indicator parameters did a poor job of correlating life for crystals having different loading orientations. When plotting the inelastic strain range on the slip system having the highest Schmid factor versus life, however, the life data for crystals of all orientations tested collapsed to a single relationship, albeit with significant dispersion of the results, as shown in Figure 2-19.

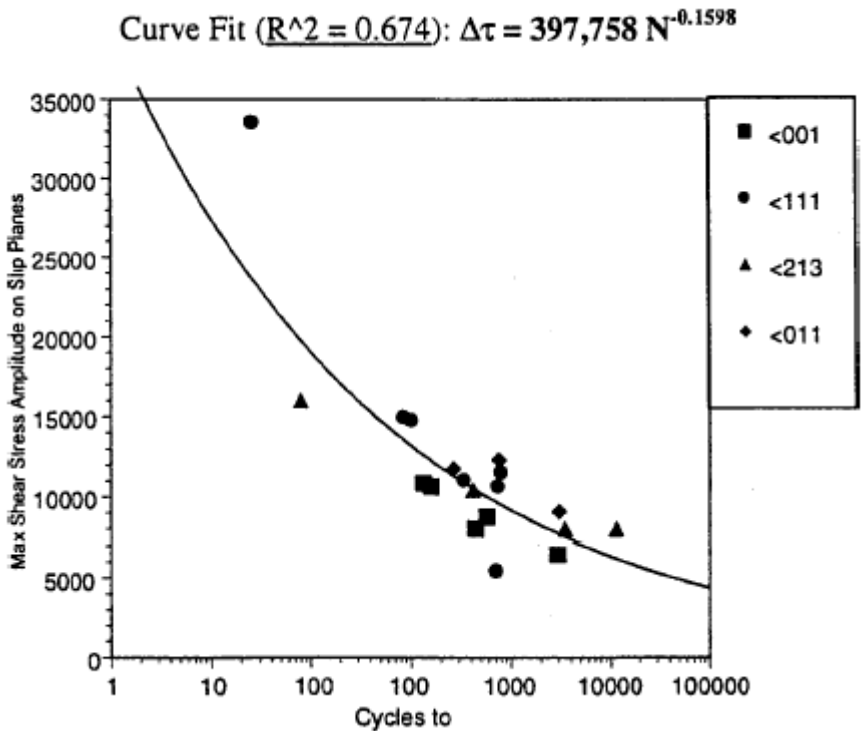

Figure 2-19 PWA 1493 649 ° C LCF Data: Resolved Shear Stress Range on Most Active Slip System versus Cycles to Failure [5]

Secondary material orientation has been shown to play a major role in crack growth beyond microcrack length [6]. Finally, orientation plays a large role in the number of cycles to failure for TMF tests. Tests conducted by Fleury et al. [44] showed that the [001] orientation had the longest TMF lives of all orientations tested, most likely due to the orientations' low modulus. This same study found that TMF lives were reduced by up to 4000 percent for orientations away from the primary growth axis.

2.4.3 Strain amplitude and strain rate effects

Single crystal superalloys also exhibit strain amplitude dependent deformation mechanisms when subjected to cyclic loading. One study, reporting on the LCF behavior of SC16, describes the representative superalloys' strain dependant fatigue behavior [45].

The authors found that for "lower" strain amplitude LCF testing at 950°C, the material exhibited deformation in the matrix channels, with dislocation glide occurring in the γ channels only. The dislocations became pinned at the γ/γ' interfaces where they subsequently formed networks. Strain softening also occurs in the lower strain amplitude tests. At "higher" strain amplitudes and similar temperatures the matrix dislocations were capable of shearing the γ' precipitates leading to stacking fault formation. Furthermore, studies of monotonic deformation in single crystal superalloys indicate a coupling between strain rate and temperature. Milligan and Antolovich [33], while performing a characterization study on PWA 1480, found that below 750˚C the material exhibited no strain rate effect. At lower strain rates, strength decreased at temperatures above 760˚C, while at higher strain rates the strength didn't decrease until temperatures were above 815˚C.

2.4.4 Temperature Effects

To fully understand TMF, the influence of temperature on the deformation mechanisms is critical. Temperature dependent effects manifest as strengthening mechanisms, ductility response, cyclic deformation mechanisms, oxidation and creep. The general trends for single crystal superalloy deformation response as a function of temperature is provided in Table 2-5.

Table 2-5: SXSA Temperature-Deformation Response [1, 3, 7, 17]

T<~400 C	Octehedral slip exhibiting dislocation movement through the matrix via glide
~400 C <T<~750 C	Dislocation movement through matrix via glide and climb
	Material exhibits non-Schmid effect
T>~750 C	Low strain rate: Dislocation movement through matrix via glide and climb
	High strain rate: dislocation shear of γ' precipitates
	Follows Schmid's law for all orientations except near [111]
	Primary creep occurs regardless of stress amplitude

Arakere and Orozco [5] found that the cyclic deformation mechanisms manifesting in PWA 1480 are divided into three temperature regimes:

- From room temperature to about 427˚C the material primarily experienced deformation on the octahedral slip systems.
- Above 427˚C thermally activated cross slip was observed and fracture surfaces exhibited crystallographic facets.
- Near 900˚C the deformation becomes more homogenous exhibiting less pronounced crystallographic facets on the failure surface.

Another study on the superalloy SC16 supports the high temperature observations above, and postulates that the ability to shear the γ' precipitates must be temperature dependent "as it is assumed to be related to stacking fault energy" [45]. Bettge and Osterle [39] performed a set of high temperature fatigue experiments on SC16 in order to characterize the damage mechanisms at both 750˚C and 850˚C. At 750˚C the dislocation pairs observed on the slip planes were capable of shearing the γ' particles. At 850˚C the dislocation moved from their slip planes at will and circumvented the γ' particles by climb. Results from a study conducted on PWA 1484 include tensile properties as a

function of temperature, shown in Figure 2-20. The yield response as a function of temperature is typical of most single crystal superalloys and is attributed to the γ' phase [2]. Particularly, the increasing yield strength with increasing temperature is due to cross-slip pinning of dislocation pairs in the γ' phase coupled by antiphase boundaries (APBs) [38]. The temperature dependent strengthening increases until dislocation climb becomes dominant, at which point the yield strength falls precipitously with increasing temperature. Particularly, the cross slip of dislocations from octahedral planes to cube planes account for the increase in yield strength as a function of temperature. This cross slip is ultimately the cause of Kear-Wilsdorf locks. Whereas the softening above the critical temperature is a result of thermally activated slip on cube planes [2].

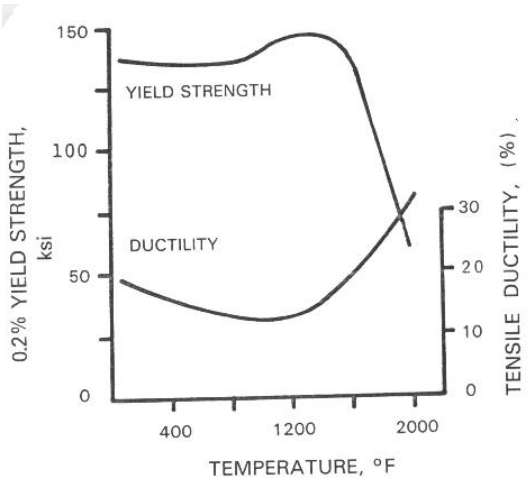

Figure 2-20: Tensile Yield Strength and Ductility as a Function of Temperature in PWA 1484 Loaded in [001] Direction [7]

The creep response of single crystal superalloys is also temperature dependent. Matan et al. [12] found that CMSX-4 experienced primary and secondary creep at 750˚C while at 950˚C the material exhibited tertiary creep. The authors note that at temperatures above 850˚C "all known superalloy single crystals exhibit logarithmic strain

softening behavior consistent with tertiary creep". Lukas et al. [46] found that the creep response of CMSX-4 was highly material-orientation dependent, with <001> being the "strongest" orientation at high stress and <011> the weakest for all tests performed. The creep results of Arakere and Orozco [5] on PWA 1480 support these findings. These authors found that creep behavior is extremely sensitive to crystal orientation as well as γ' precipitate size at temperatures between 750˚C and 850˚C. One study looking at the effects of creep and creep fatigue on single crystal superalloys determined that creep-fatigue tests with compressive holds exhibited dislocations in the γ phase only resulting in damage accumulation in the matrix only. Tensile holds, on the other hand, resulted in screw dislocations shearing the γ' precipitates and crack extension by creep deformation, i.e. coalescence of internal creep voids. Finally, this study determined that the interaction of creep-fatigue mechanisms was far more damaging than creep, or fatigue alone [4].

2.4.5 Influence of Coatings

Due to the operating temperatures in the hot section of turbines, Ni-base superalloys are typically treated with a coating to improve their environmental degradation properties. Superalloy coatings come in one of three forms: diffusion coatings, overlay coatings and thermal barrier coatings (TBC). Diffusion coatings consist of either an aluminum layer deposited by chemical vapor deposition, or a platinum layer deposited by electrodeposition followed by a layer of aluminum. Diffusion coatings form a protective alumina scale when exposed to high temperatures, thereby decreasing ingress of oxygen to the base material and reducing the amount of aluminum diffusing from the base material (i.e. reduces γ' depletion). Overlay coatings of MCrAlX-type are applied

by either air or vacuum plasma spraying or electron beam physical vapor deposition. Overlay coatings perform better than diffusion coatings, but at a higher cost. Overlay coatings advantage over diffusion coatings comes from the flexibility of chemical composition, and therefore the ability to manipulate coating physical properties. Thermal barrier coatings consist of a ceramic layer which provides thermal insulation, sometimes proceeded by a diffusion or overlay coated bond coat. The combination of the bond coat, which hinders diffusion, and the TBC ceramic layer, which provides thermal insulation, makes this coating scheme the most efficient, and most expensive. The three common coating systems are compared on the basis of service temperature and coating life in Fig 2-21.

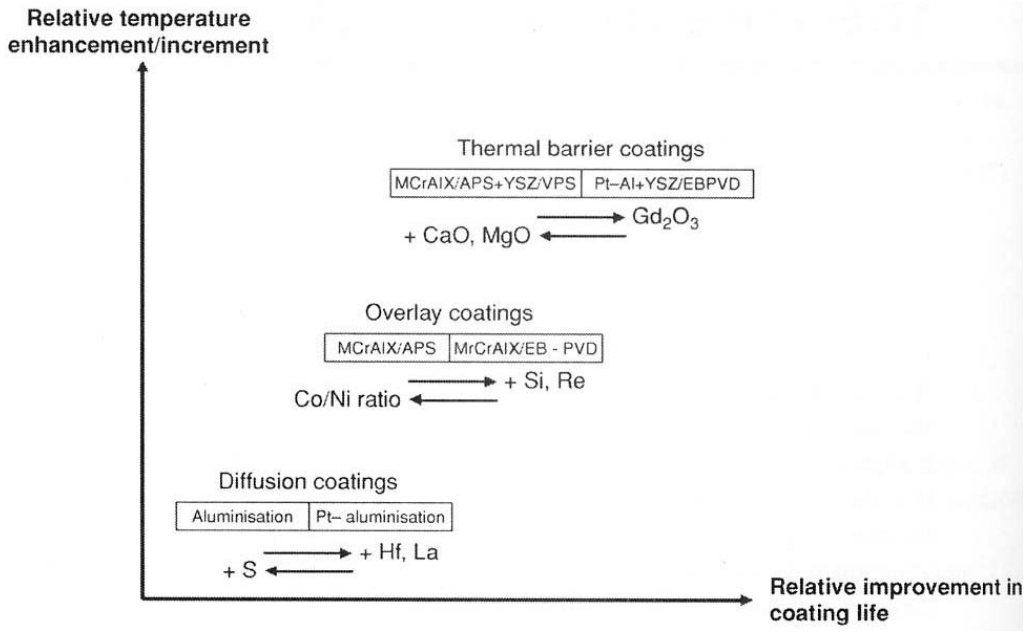

Figure 2-21 Comparison of Superalloy Coatings: Temperature Range vs. Life [2]

Due to the mismatch in coefficients of thermal expansion between the substrate alloy and coating, as well as the mechanical properties of the coatings at operating temperatures, superalloy coatings have a tendency to crack and spall within a relatively

short period of operation [2]. Furthermore a crack of the coating layer acts as a base-material fatigue crack initiation site due to the localized corrosion and oxidation attack occurring there. Additionally, cracks that initiate in the coating can easily propagate into the base material due to the local stress intensity at the crack tip leading to increased crack propagation rate in the base alloy [47]. An example of crack propagation from the Pt-modified diffusion coating into the alloy is shown in Figure 2-22.

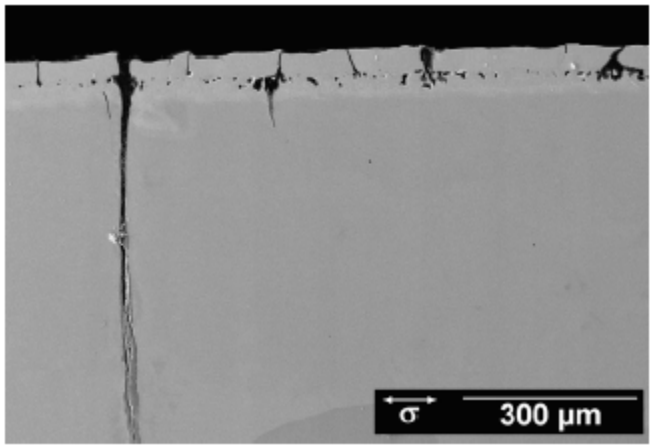

Figure 2-22 SEM Image of Coating Cracks in Pt-Modified NiAl Diffusion Coated PWA 1484 [47]

One study on fatigue life of the polycrystalline superalloy IN 738, having a CoNiCrAlY overlay-coating followed by an aluminum diffusion coating, subjected to LCF, HCF and TMF cycles determined that these coatings increase HCF life; decrease LCF life, especially when tensile loads are applied; and decrease TMF lives, especially OP TMF cycles [48]. Another study conducted on aluminide diffusion coated single crystal Rene N4 determined that the coating had no effect on life for IP BiF, but was detrimental for LCF and OP BiF. Furthermore, LCF coated specimens had longer lives at low(er) temps, while the coating had no effect at low(er) strain ranges when specimens were subjected to OP BiF. In general, this study found that bare as well as coated OP BiF

specimens experienced crack initiation at the material surface [49]. A study of the fatigue effects of NiCoCrAlY overlay coated single crystal superalloy PWA 1480 crack initiation determined that cracks initiated in the coatings of the specimens tested in LCF at 650° C early on, thereby significantly reducing life. Furthermore, this research found that cracks formed in the coating regardless of environment (air or vacuum), as such coating cracking is assumed to be a pure fatigue phenomena [8]. When tested in OP BiF between 650° C and 870° C, early coating failure led to coated specimens having significantly lower life. This study determined that, relative to <001> oriented superalloy specimens, the overlay coatings have greater coefficients of thermal expansion, higher elastic moduli, lower flow stress (particularly at high temperatures) and better ductility at higher temperatures. The authors summed up their research with the following conclusion: "Coating cracks are promoted in areas cycled into tension at low temps and may propagate into the superalloy. The greater coefficient of thermal expansion for the coating adds to this problem, since it places the coating in tension upon cooling from high temp." [8] This coupling of damage interactions would be most damaging in an OP TMF or BiF cycle.

2.5 Oxidation of Ni-base Superalloys

2.5.1 Introduction

The alloying composition of nickel-base superalloys is typically dominated by, in descending order of wt %, Co, Cr, Al, and Ta; with the remainder being made up of nickel. The presence of aluminum is promising for oxidation kinetics, as one would hope that a protective alumina scale would form, thereby decreasing oxidation kinetics. As

Giggins and Pettit [50] point out, thermodynamic considerations indicate that Al_2O_3 and Cr_2O_3 should be the stable oxide phases formed on Ni-Al and Ni-Cr alloys, respectively. Additionally, the small equilibrium constant for the following reaction

$$\mathbf{Al_2O_3 + 2Cr\ (alloy) = Cr_2O_3 + 2Al\ (alloy)} \qquad \textbf{(2-8)}$$

indicates that Al_2O_3 should be the stable phase on Ni-Cr-Al alloys. The addition of the many other alloying elements, as well as the dynamics between kinetics and thermodynamics, however, create oxidation scenarios in superalloys that are far more complicated.

Superalloys can form oxides having one of four scale morphologies. The common manifestation of high-temperature exposure among all superalloys, however, is the presence of a γ'-depleted zone near the surface. The γ'-depleted zone is a result of the aluminum in the γ' phase either diffusing out to create one of several Al-rich oxides or coalescing to form subsurface Al particles within the γ' depleted region. As the γ'-phase in superalloys provides the a strengthening mechanism at higher temperatures, the absence of this phase in the γ-depleted zone leaves a more ductile matrix, thereby allowing the dislocations to more-easily exit the alloy at the surface. Dislocation egress under cyclic loading typically leads to crack initiation due to the creation of intrusions and extrusions [20, 21, 51], though this is certainly not the only cause of crack initiation. Due to the dislocation density on the slip planes creating the intrusions and extrusions, these sites experience short circuit diffusion and can ultimately lead to crack initiation [22]. It should be noted that the rate of γ'-depletion should be intrinsically linked to the oxidation kinetics of an Al-rich oxide. As such, one can easily see that there exists an

interaction between oxidation and fatigue mechanisms. In fact, the γ' depletion depth is intrinsically linked to the oxidation rate constant k_p of the material, as shown in Fig 2-23 [52]. Where the rate constant is defined as

$$k_p = A\exp\left(\frac{-Q}{RT}\right) \quad \textbf{(2-9)}$$

where A is a material and temperature dependent constant, Q is the activation energy for the oxidation process and therefore may be temperature dependent, R the universal gas constant and T the temperature.

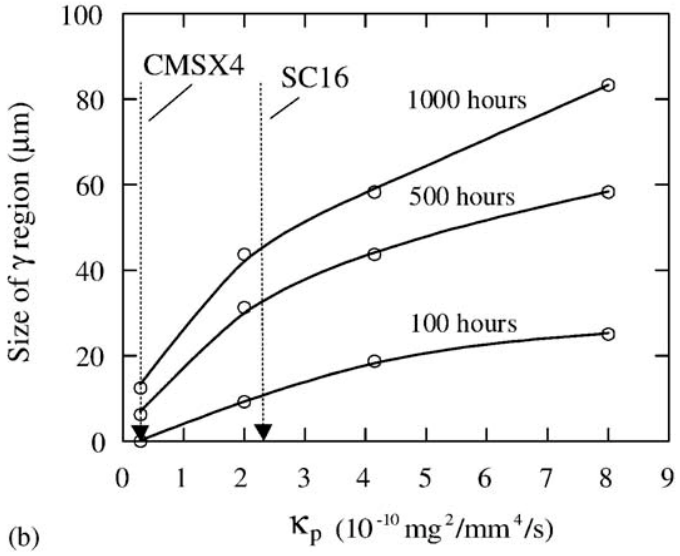

Figure 2-23 Effect of Oxidation Rate Constant, K_p, on the Growth of the γ Region [52]

As single crystal superalloys are predominantly utilized in aero turbine blades, and turbine blades experience the most severe conditions of all components within a turbine, the literature review presented here is primarily on single crystal superalloys, except where overlap occurs in oxidation behavior for polycrystalline and directionally-solidified superalloys. Furthermore, given that single crystal superalloy blades are

typically treated with a thermal barrier coating, one must address why base material oxidation kinetics are of interest. Without needlessly consuming space on a separate issue, Akhtar et al. [51] summed up the situation well when they wrote: *"... these coatings also degrade in service, thus exposing the bare superalloy itself directly to the environment of the gas stream. Therefore, the mechanisms of oxidation and/or corrosion are of the greatest importance not only for the coating, but also for the bare superalloys."* The effect of coatings on LCF and TMF life was addressed in Section 2.4.5.

2.5.2 General Superalloy Oxidation

The oxidation behavior of nickel-base superalloys is complicated by the inclusion of a large number of alloying elements. As Akhtar et al. [51] put it: *"... a (coupled thermodynamic-kinetic) model of oxidation capable of taking into consideration the ten or more alloying elements present in the single crystal superalloys (*Table 2-6*) and incorporating the partitioning of the elements into its two phase (γ+γ') microstructure remains yet to be developed*" [51].

Table 2-6 Nominal Chemical Composition (in Weight Percent) of Representative Single Crystal Superalloys [51]

Superalloy	Al	Co	Cr	Hf	Mo	Ni	Re	Ta	Ti	W	Y
CMSX-4	5.6	10.0	6.0	0.10	0.6	62.3	3.0	6.0	1.0	6.0	-
RENE-N5	6.2	7.5	7.0	0.15	1.5	63.6	3.0	6.5	-	6.0	0.01
PWA 1484	5.6	10.0	5.0	0.10	2.0	61.6	3.0	8.7	-	6.0	-
CMSX-10*	5.7	3.0	2.0	0.03	0.4	70.1	6.0	8.0	0.2	5.0	-
RENE-N6*	6.0	12.5	4.5	0.15	1.1	58.1	5.4	7.5	-	5.8	0.01

* Indicates third generation superalloy, the remaining being second generation

The majority of the superalloy oxidation studies to date are predicated upon the findings of Giggens and Pettit [50], who looked at the isothermal oxidation of nickel-

chromium-aluminum ternary alloys. This study focused on the three key alloying elements that have the highest impact during oxidation. In this seminal work the authors looked at 23 alloys having differing weight fractions of elements, from Ni-5Cr and Ni-3Al to Ni-30Cr-6Al, and various combinations between. Moreover, the alloys had varying microstructures, including single-phase γ, two-phase γ+ γ' as well as three-phase γ+ γ'+αCr. All of the alloys studied had an initial transient oxidation period lasting up to an hour, during which oxidation kinetics did not follow a simple rate law. The transient period was characterized by rapid conversion of surface layers to oxides, where the morphology and composition of the oxide layers changed with time. Once the oxide stabilized, the alloys studied fell into one of the 4 following categories: (refer to schematic shown in Fig 2-24)

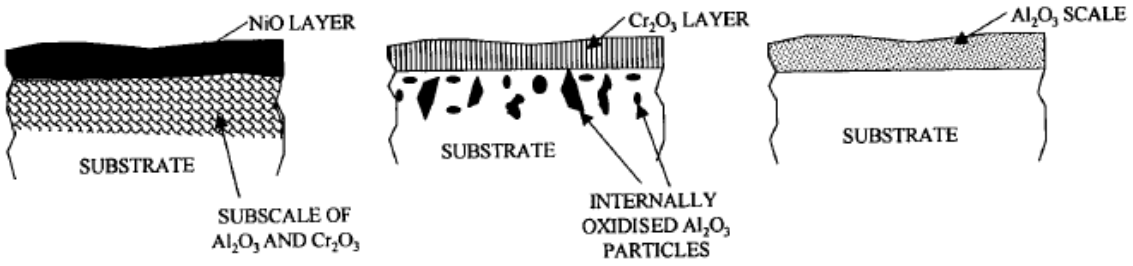

Figure 2-24 Schematic Diagram of Oxides Formed on Ni-Cr-Al Ternary Alloys. (a) Group I, (b) Group II and (c) Group III [50]

- Group I alloys
  - Typically followed parabolic rate laws.
  - Transient period typically short.
  - K_p for this group is consistently approximately an order of magnitude larger than that of pure Ni under the same conditions.
  - Characterized by a dense external NiO scale and an inner scale having a mixture of Cr_2O_3, Al_2O_3 and $Ni(Cr,Al)_2O_4$.

- Oxidation rates controlled by oxygen transport through the NiO scale

- Group II alloys
  - Typically followed parabolic rate laws, however there were deviations. Some deviation due to external oxide cracking while other alloys exhibited a continuously decreasing instantaneous rate constant.
  - Specimens with continuously decreasing instantaneous rate constants had "semi continuous" Al_2O_3 scales beneath an outer Cr_2O_3 layer. The authors assert that the near-continuous alumina inner scale most likely controlled kinetics in these cases.
  - These alloys are characterized by a dense outer Cr_2O_3 scale and an inner Al_2O_3 scale
  - Oxidation rate controlled by the diffusion of oxygen through the aluminum-doped Cr_2O_3 scale

- Group III alloys
  - Obeyed parabolic rate law almost immediately.
  - Lowest rate constants of all three groups.
  - Characterized by external Al_2O_3 scale only.
  - Oxidation rate controlled by diffusion through the external Al_2O_3 scale.

- Transition alloys
  - This group of alloys remained "transient" for the entire duration of tests.
  - Kinetics did not obey any simple rate law.
  - Structure of oxide scale changed with oxidation time.

- Exhibited Group I and Group III, Group II and Group III and Group I and Group II combined oxidation on single surface.
- Found that Al_2O_3 particles can coarsen and grow laterally.

The authors concluded that alloy composition determines which particular mechanism will prevail beyond the transient period; specifically the combined volume fraction of Cr_2O_3 and Al_2O_3 precipitated within the alloy. The authors found that chromium allows a continuous external Al_2O_3 layer to be formed at lower aluminum concentration than would be necessary if the chromium were not present. Further, aluminum plays a similar role in the formation of Cr_2O_3.

A study conducted on the isothermal oxidation behavior of directionally solidified superalloy CM247LC at 1100°C concluded that the material exhibited a long transition period (20 hours) during which time the oxide was characterized as Group I, followed by a transition to Group II [53]. This study determined that the oxidation kinetics for this material followed a parabolic rate law once the transition period ended. Furthermore, the oxidation of this alloy produced a sizeable γ'-depleted zone near the surface whenever an aluminum-bearing oxide formed. Oxidation resistance of this alloy degrades substantially at temperatures above 1000° C, culminating in virtually no weight gain at 1200° C due to complete oxide spallation. The authors also looked at the cyclic oxidation resistance of the alloy. For room temperature-1000° C cycling the alloy produces an oxide consisting of an outer spinel ($NiAl_2O_4$) and an inner alumina Al_2O_3 layer; for room temperature-1100° C cyclic oxidation in air the oxide is comprised of an outer layer consisting primarily of $NiAl_2O_4$ and NiO with the spinel dominating at long

times; while room temperature-1200° C cyclic oxidation leads to an outer layer predominantly consisting of spinel ($NiAl_2O_4$) and NiO where the NiO dominates at longer times. For reference, a spinel is any metal oxide having the general chemical composition AB_2O_4. The material tested at room temperature-1200° C, under cyclic temperature conditions, produced regions of Group I oxidation directly adjacent to Group II oxidation, as shown in Figure 2-25. Whereas the authors generally place this particular superalloy in the class of Group I and Group II, for both isothermal and cyclic oxidation, one can readily see that the oxide formed over long time periods is temperature dependent. This causes difficulty in determination of a singular oxidation kinetics relationship for the material over the entire temperature range that the material is intended to experience. Levy et al. [54, 55] looked at the oxidation kinetics of a superalloy having similar composition to CM247LC. This oxidation study on the alloy MAR-M200 between 704°C and 1093°C determined that the material behaves as a transition alloy for the first 20 hours of high temperature exposure followed by the formation of a stable alumina scale, similarly to the findings of Das et al. [53].

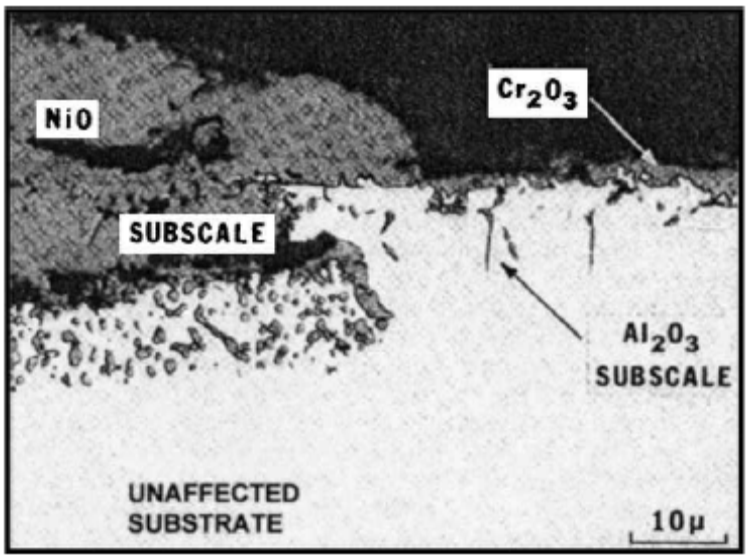

Figure 2-25 Example of "Transition Alloy" oxidation, presented in [53] at higher quality, originally from [50]

Bouhanek at al. [56] found similar oxidation results for the six commercial single crystal superalloys they studied. Specifically, the authors determined that all of the alloys in the study exhibited a transient "fast growth" period lasting up to 2 hours. Upon completion of the transient period, the materials exhibited differing oxidation dependent upon the isothermal oxidation temperature. At 900° C the oxide consisted of an outer layer of NiO and spinel ((Ni, Co)Cr_2O_4) and the inner layer consisted primarily of rutile ($CrTaO_4$); of note is that there were no aluminum-containing oxides detected at this temperature. At 900°C all materials studied generally behaved as Group I alloys. At 1100° C none of the alloys produced an adherent scale, resulting in considerable oxide spallation. The authors determined that wedging was the primary spallation mechanism. Nychka et al. [57] found that oxide spallation was time, surface preparation and sulfur content dependent in a representative 2nd generation single crystal superalloy; such that increasing any of these variables increases amount of spallation. This study concluded that the surface preparation had a large effect upon oxide spallation due to the ability of

the oxide to bond to the base alloy. These phenomena would lead to an increased oxidation rate as it would take longer for the system to reach steady state. Yet another series of isothermal oxidation studies performed on single crystal superalloys concluded that oxidation kinetics at 800 and 900° C was sub-parabolic (time exponent <0.5), having time exponents of 0.16 and 0.10 respectively [58, 59]. This alloy produced an internal Al-rich oxide scale (though not alumina) below an outer NiO scale at 800° C. The scale at this temperature was not uniform in thickness. At 900° C, however, the alloy produced a layered scale of relatively constant thickness consisting of NiO at the gas interface, below which was a spinel-rich sublayer, a $CrTaO_4$-rich layer, followed by an inner-most α-Al_2O_3 layer, resulting in a Group I-type oxidation.

These authors also looked at the difference in oxide formation between the dendritic and interdendritic regions. The authors report that superalloy composition is chemically segregated between these two regions; with the interdendritic regions being Al, Ti and Ta rich and W, Mo and Cr depleted, compared to the dendritic region. This no doubt explains the observation that the dendritic regions produced a course(r)-grained oxide while the interdendritic regions produced a fine(r)-grained oxide. It has been established that oxide crystal size plays a dominant role in oxidation kinetics in Nickel alloys [60, 61] and may explain a portion of the transient growth period exhibited by these alloys. At temperatures above 1000° C, this alloy exhibited parabolic oxidation kinetics with scale composition being temperature dependent. At 1000° C the alloy experienced a long transition period of approximately 100 hours where NiO and CoO dominated within the dendritic regions and α-Al_2O_3 primarily formed in the interdendritic regions. The most common oxide morphology for the high temperature range (1000-

1150°C) consisted of four layers: an outer layer of spinel, followed by sublayer of mainly Al_2O_3 with small amounts of spinel, then a thin layer of $CrTaO_4$-rich oxide, with an inner most layer of Al_2O_3. Not surprisingly the authors determined that oxidation kinetics was dominated by diffusion through the inner α-Al_2O_3 layer.

A very detailed study of several 2nd and 3rd generation single crystal superalloys revealed that a phase transformation occurs in nickel-base superalloys as a result of the existence of an external NiO scale [51]. The authors state that *"This transformation, which is the precursor to internal oxidation, creates a β phase (NiAl) first, followed by the δ phase (Ni_2Al_3) prior to the formation of the spinel $Ni(Cr,Al)_2O_4$ and Al_2O_3 in succession"*. The β phase is subsequently converted to the internally oxidized zone (γ'-depleted zone). This phase transformation occurred at 900°C for the alloys studied. Moreover these authors found that many 2nd and 3rd generation superalloys had mass gains at temperatures below 1000°C which were higher than mass gains above this temperature. This was attributed to the formation of an α-alumina scale at the higher temperatures that did not form at the lower temperatures. In conclusion, the authors believe that the reduced oxidation rate near 1000° C is attributed to the presence of the δ-phase (Ni_2Al_3) at this temperature. However, this inter-metallic compound is only effective at limiting oxidation below approximately 1130°C, as the compound is thermodynamically unstable at higher temperatures.

2.5.3 γ' Depletion

As mentioned in the previous section, aluminum-rich oxides that form on Ni-base superalloys create a subsurface region which is depleted of γ'. This occurs by one of two

processes. Either aluminum diffuses to the surface of the alloy to create an Al-rich surface oxide, or oxygen diffuses into the alloy creating subsurface alumina particles. Further exposure at high temperature aids diffusion in the latter case, enabling the internal alumina particles to grow [50, 62]. High temperature induced γ' depletion has been reported for nearly every superalloy studied [50-53, 56, 62-67]. The depletion of aluminum from the region below the material surface results in a weakened γ microstructure at elevated temperatures. Figure 2-11 of section 2.4.1 depicts the flow stress of the γ and γ' phases as a function of temperature. The figure clearly shows that as temperature increases above ~150° C, the γ' phase is increasingly stronger than the γ phase. This weakened microstructure results in stress redistribution near notches at higher temperatures [52, 66]. Furthermore the lower yield stress of the γ phase results in higher inelastic strains, for a given mechanical strain range. This phenomena was studied by Zhao and others [52, 66, 68, 69]. These researchers implicitly modeled the effect of γ'-depletion upon material response and crack initiation at smooth and sharp notches. Figure 2-26 shows their finite element results for material response to monotonic loading and fatigue loading as a function of γ' volume fraction.

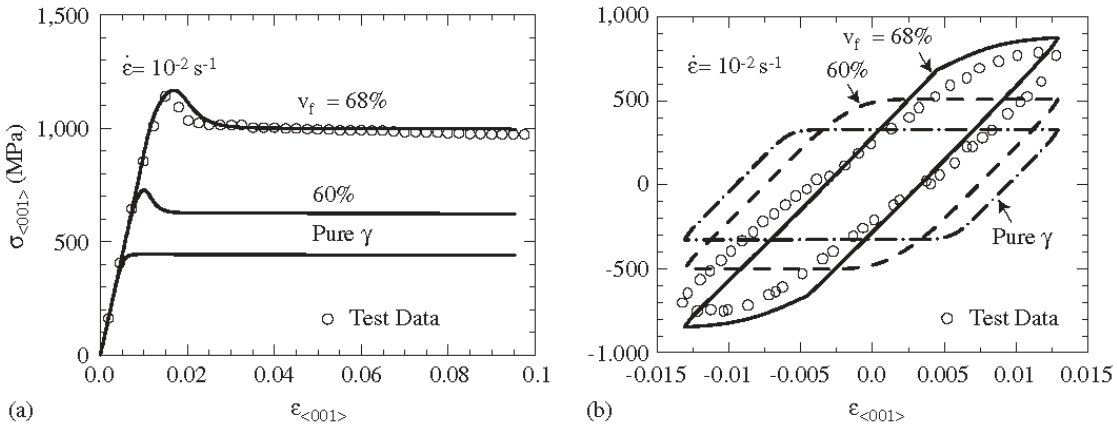

(a) **(b)**

Figure 2-26 Effect of γ' Volume Fraction on (a) Monotonic and (b) Cyclic Response at 950° C [52]

Note that in Fig 2-26b the amount of inelastic strain for γ-only microstructure is approximately 3-times greater than for a microstructure having 68% volume fraction of γ'. The results of Zhao et al.'s notch analysis are shown in Figure 2-27.

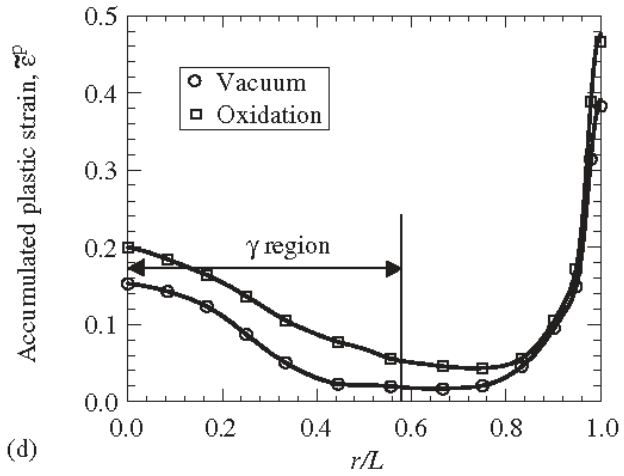

Figure 2-27 Comparison of Accumulated Inelastic Strain With and Without Oxidation After 400 hr at 950 °C [52]

One can clearly see in Figure 2-27 that the oxidation assisted γ' depleted zone experiences greater inelastic strains near the notch root.

Several researchers have debated whether to use oxidation or γ' depletion kinetics as the high temperature degradation mechanism of importance in their life estimation algorithms. Wright [65] concluded that oxidation kinetics were more appropriate for crack initiation estimation "since initiation is primarily a surface phenomenon". This argument, however, neglects the fact that the load carrying capabilities of the subsurface material are diminished by γ' depletion, and therefore have a strong influence on crack initiation. Zhao [52, 68] and Dumoulin [66], on the other hand, utilized the γ' depletion kinetics in their material deformation and life estimation schemes. Others have utilized both oxidation and γ' depletion kinetics [39-41]. The distinction between the two

damage mechanisms, however, may not be necessary. Though Wright [65] found a difference in kinetics between the two mechanisms in Rene N4, Kupkovits [67], Sehitoglu and Boismier [70] and Gordon et al. [62] found very similar kinetic relationships between oxidation and γ' depletion for the superalloys that they studied. The fact that some researchers have found that oxidation and γ' depletion kinetics are similar should not be surprising, given that the two processes are inextricably linked via the diffusion of aluminum [50, 52], as mentioned above.

2.5.4 Fatigue-Oxidation Interaction

Several studies have investigated the effects of an applied mechanical strain upon the oxidation kinetics of superalloys. One such study on the polycrystalline superalloy IN 738 LC found that the material preferentially oxidized in interdendritic and intergranular regions due to short-circuit diffusion [64] when subjected to TMF. This same study found that when subjected to TMF tests, the oxide growth on this material exhibited linear growth kinetics; as opposed to the parabolic kinetics exhibited for non-stressed oxidation tests. The oxide thickness as well as the γ'-depletion kinetics were linked to applied mechanical strain through a power law relationship, $t_h = A * \Delta\varepsilon_{mech}^{b}$, where t_h is either the oxidation or the γ' depletion depth and A & b are presumably material-dependent constants. The relationship held whether hold times were present in the cycle or not, though cycle parameters certainly affected the parameter values. In general, TMF tests having lower strain ranges had long enough lives to allow time for an oxidation process. In these cases increasing inelastic strain tends to increase oxidation kinetics. Where Esmaeili [64] found a power law relationship between oxidation kinetics

and applied strain, Reuchet and Remy [71] determined a linear relationship. Reuchet et al. [71] determined that oxidation kinetics was affected by applied strain through the following relationship: $t_h=C*t^{1/2}$, where t_h is the oxidation thickness, $C=C^0(1+K_m*\Delta\varepsilon^{PL}/2)$ and t is time, C^0 and K_m are material constants and $\Delta\varepsilon^{PL}$ is the inelastic strain range. Wright [65] found that the isothermal low cycle fatigue lives of a representative 2nd generation single crystal superalloy, Rene N4, was highly dependent upon the environment oxygen partial pressure, with increased oxygen partial pressure leading to an increase in oxidation kinetics. The author notes that the fatigue accelerated the oxidation kinetics considerably. Fleury and Remy [44] found that oxide scales cracked perpendicular to the TMF loading axis, leading them to the conclusion that both low and high temperature mechanisms are superimposed. When analyzing the TMF life results from the study, these researchers concluded that there is no interaction between fatigue and oxidation in the shorter life regime, whereas in the longer life regime, "there is a strong synergy between oxidation and fatigue which can only be accounted for by complex modeling". Simply put, these researchers confirmed that a minimum amount of time at high temperatures is required for significant oxidation to occur. If there isn't enough time to oxidize, the material will fail by fatigue mechanisms; whereas environmental-fatigue mechanisms dominate if a critical amount of oxide is produced. The effect of fatigue-environmental interactions is captured in Figure 2-28, where cracks have initiated at oxide spikes in René N4.

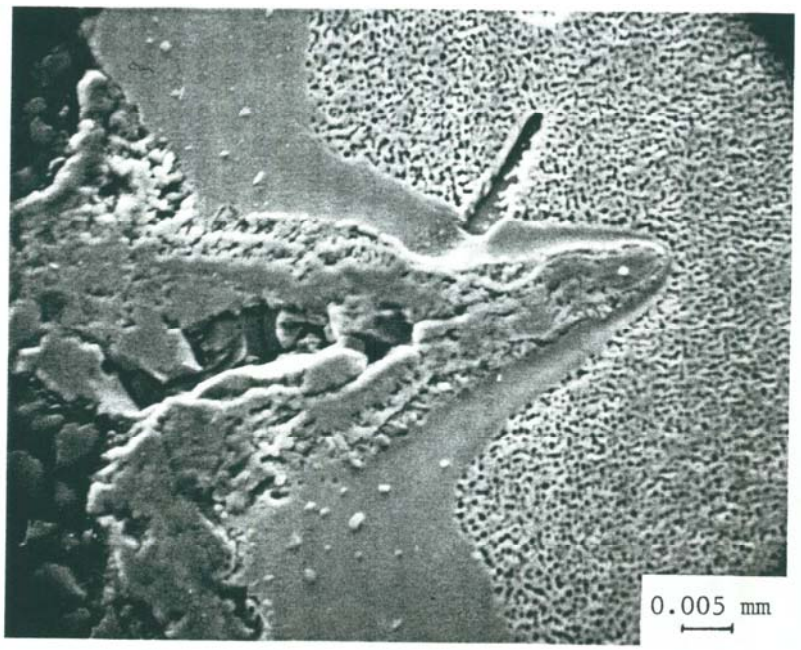

Figure 2-28 Fatigue Crack Initiation From Oxide Pits in Uncoated René N4 [65]

2.6 Gamma-prime (γ') Coarsening and Rafting

When exposed to high temperatures and/or strains for long periods of time, the γ' particles increase in size (coarsen) while the volume fraction remains unchanged. One proposed relationship for the average spacing between second phase particles (λ_p) states that the spacing is proportional to the particle size, for a given volume fraction [72],

$$\lambda_p = r_t\left(\left[\frac{4\pi}{3\varphi_p}\right]^{1/3} - 2\right) \qquad \textbf{(2-10)}$$

where r_t is the current average particle radius and φ_p is the particle volume fraction. When coarsening occurs, the average particle size and the distance between second phase particles increases. Coarsening has a significant effect upon creep rate when the rate is dominated by dislocation glide obstructed by γ' particles. Specifically, the creep strain rate in this case is derived as proportional to sinh(l), where l is the dislocation pinning

distance [72]. In short, the rate increases as the particle size and/or the particle spacing increases.

Classical particle coarsening kinetics were first determined by Wagner [73] as well as Lifshitz and Slyzov[74]. The classical coarsening equation, derived from first principles, follows

$$\left[r_t^3 - r_0^3\right]^{1/3} = k \bullet t^{1/3} \qquad \textbf{(2-11)}$$

where r_t is the particle radius as a function of time; r_0 is the initial particle size; t is time and k is a function of the diffusion coefficient, precipitate-matrix interfacial energy, mole fraction and molar volume of the matrix and precipitate respectively, and temperature. Solving for the particle size at time t gives

$$r_t = \left(k^3 t + r_0^{\ 3}\right)^{1/3} \qquad \textbf{(2-12)}$$

Manonukul et al.[72] fit the coarsening results of Betteridge and Heslop [32] for a Nimonic superalloy as

$$r_t = \dot{r}_t t^{1/3} + r_0 \textbf{, where } \dot{r}_t = b\exp(cT) \qquad \textbf{(2-13)}$$

where t is time in hours, $b=1.45\text{x}10^{-5}$, c=0.012 and T is the absolute temperature. All other symbols have the same meaning as in EQ. 2-12. One should note that EQ. 2-14, which was derived for a particular superalloy, is similar in form by not identical to the classical coarsening kinetics, though quite simplified due to the absence of a diffusion coefficient and interfacial energy, among other things. One could use Eq. 2-14 in Eq. 2-11 to determine the spacing between second phase particles.

Microstructural evolution in Ni-base superalloys can also result in rafting. Rafting is the coalescence of second phase particles (γ') into linear channels, as shown in Fig 2-29.

Figure 2-29 Micrograph of Rafting in a Single Crystal Superalloy [19]

The driving force for rafting is the existence of γ/γ' lattice misfit, defined as

$$\delta = 2\left[\frac{a_{\gamma'} - a_{\gamma}}{a_{\gamma'} + a_{\gamma}}\right] \qquad \textbf{(2-14)}$$

where δ is the lattice misfit and $a_{\gamma'}$ and a_{γ} are the γ' and γ lattice parameters, respectively. Superalloys with a negative lattice misfit result in rafts perpendicular to the applied tensile load, while superalloys with a positive lattice misfit have rafts parallel to an applied tensile load. Changing the loading direction has the effect on the raft orientation of changing the sign of the materials lattice misfit [2]. Since most commercial superalloys have a negative lattice misfit values, one concludes that tensile loading leads to perpendicular rafts and compressive loading leads to parallel rafts, for the majority of the superalloys available. Where as pure creep results in long γ' channels, creep-fatigue results in shorter γ' channels separated by matrix [4].

2.7 Damage Mechanisms in Ni-base Superalloys Experiencing TMF

The nature of thermomechanical fatigue may induce multiple damage mechanisms at different times in the TMF cycle, as well as couple the damage mechanisms present. There are four primary damage mechanisms associated with Ni-base superalloys experiencing TMF, depending upon test conditions. The primary damage mechanisms are creep, fatigue, creep-fatigue and environmental-fatigue. The component life is greatly influenced by which deformation mechanism is dominant. Creep dominated deformation results in crack initiation from internal micropores [4, 49, 75]. Whereas cracks typically initiate in fatigue dominated specimens at the surface due to intrusions and extrusions created by the egress of dislocations driven by cyclic plasticity [22, 28, 49, 76]. Crack initiation in Ni-base superalloys experiencing environmental-fatigue damage typically occurs as a result of interactions between cyclic plasticity and environmentally degraded microstructure, i.e. oxidation [8, 65, 71, 75, 77, 78] and/or γ' depletion [52, 64-66, 68].

Creep effects in a strain controlled fatigue test results in reducing the stress at which the high temperature hold is applied, leading to a decrease in mean stress in the case of tensile holds and an increase in mean stress for compressive holds [36, 67]. Creep can be introduced in in-phase TMF tests as well as out-of-phase TMF tests. In IP TMF tests creep can result as a function of the temperature-load profiles, without the introduction of a high temperature hold time. Out-of-phase TMF tests, on the other hand, typically only experience creep when high temperature hold times are present. As such, the traditional IP TMF test may be used to determine the response of fatigue loading, as

well as creep-fatigue loading for the material of interest. Out-of-phase TMF tests can be used to determine material response to fatigue, as well as creep-fatigue and environmental fatigue loading. The fatigue response of superalloys was discussed in Section 2.4 and environmental-fatigue interactions were discussed in Section 2.5.4.

There have been considerable studies conducting TMF tests on Ni-base superalloys. One study, performed on the second generation single crystal superalloy CMSX-4 found that crack nucleation always occurred preferentially in the γ channels, and that most fracture surfaces were of macroscopic {110} and {111} planes [9]. Another TMF study on polycrystalline IN100 between 600°C and 1050°C found that the hysteresis loops stabilized to a consistent value within a few cycles, regardless of the applied strain range [75]. This stress relaxation is most likely a result of creep-fatigue interactions. This same study determined that the majority of the cracks initiated at oxidized MC carbides, indicating that fatigue life was dominated by fatigue-environmental interactions. In order to induce temperature dependent damage mechanisms, thermomechanical fatigue testing requires that the specimen be heated, obviously. The ASTM standard governing TMF testing, ASTM E2368, requires that the temperature profile within the gage section be uniform within +/- 1% X maximum temperature (K) or +/- 3 (K), whichever is greater [79]. Not only is this requirement intended to ensure that test results are comparable, it is also intended to minimize temperature gradient induced strain fields, potentially leading to unintended deformation mechanisms. A resent study on the effects of temperature gradients in TMF testing has shown that a) the existence and/or severity of temperature gradients in the specimen had no effect upon cycles to failure for Nimonic 90 tested in OP TMF, and b) FEA results

indicate that the stress induced by temperature gradients in OP TMF tests was minimal [80].

A separate test waveform, the Bithermal fatigue (BiF) test, can also be used to produce particular damage mechanisms. This waveform is characterized by isothermal loading separated by non-stressed temperature changes. The OP BiF test would have a high-temperature compressive half cycle and a low temperature tensile half cycle, while the IP BiF test would have a high-temperature tensile half cycle and a low temperature compressive half cycle. Out-of-phase TMF and OP BiF waveforms are provided in Figure 2-30.

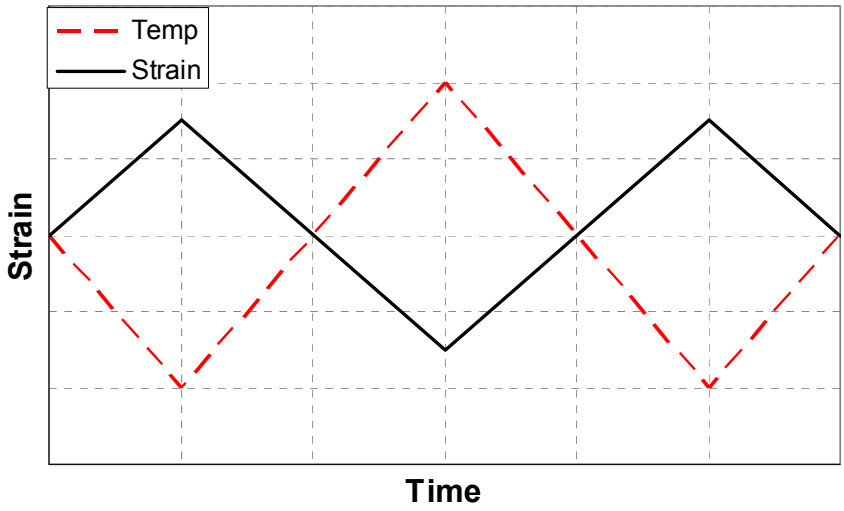

(a)

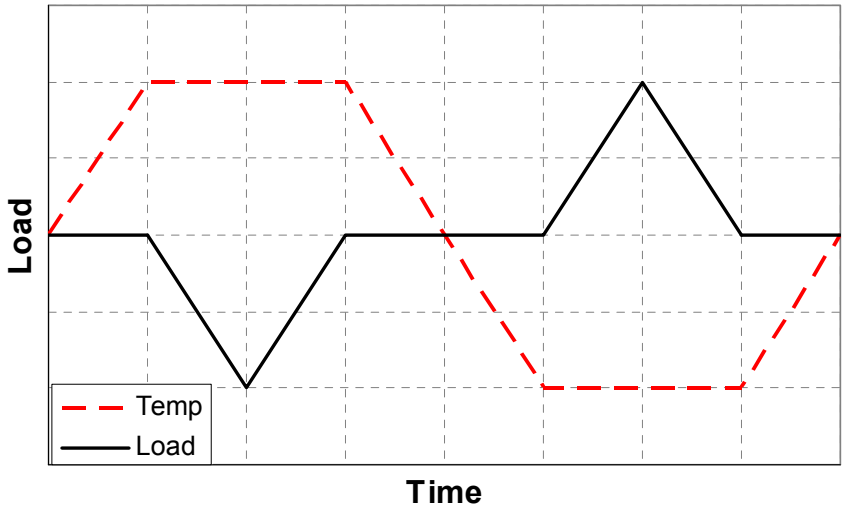

(b)

Figure 2-30 Temperature and Strain Waveforms: (a) OP TMF, (b) OP BiF

Bithermal fatigue tests have been successfully used to isolate dominant damage mechanisms in different temperature regimes [8, 49, 75, 81-84]. One fatigue study on Rene N4 found that, on an inelastic strain range basis, BiF is more damaging to the material than LCF conducted at either the BiF cycles high temperature or low

temperature [49]. This author also concluded that one can limit the number of concurrently active damage mechanisms by proper choice of temperature, strain levels and hold times. The BiF tests has been used extensively at NASA to isolate dominant damage mechanisms [8, 84]. These researchers determined that when plotting inelastic strain range versus cycles to failure, the Bithermal fatigue results followed one of two trends, depending upon test waveform and applied inelastic strain. Figure 2-31 shows the results of their work.

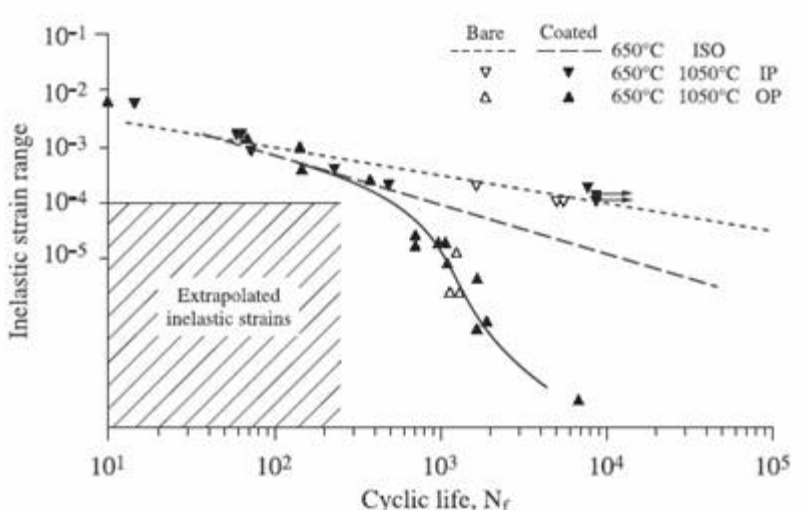

Figure 2-31 Comparison of Isothermal LCF, IP BiF and OP BiF for Bare and Coated PWA 1484 [84]

Isothermal LCF and IP BiF results follow the same trend; furthermore OP BIF results deviate from this trend only at inelastic strains lower than ~10^{-4} in/in. The study concluded that all test results were fatigue dominated except for the OP BiF which deviated from the isothermal LCF trend.

The implementation of a single waveform which captures the life limiting aspects of TMF damage would be of great benefit to researchers. In an attempt to simplify testing of turbine component materials, Remy and coworkers have performed a considerable amount of work in an attempt to determine if the results of LCF tests can be

used to predict TMF results [44, 71, 75, 77, 85]. The general consensus from these studies is that TMF data does not compare well to LCF results conducted at the high temperature, low temperature, or average temperature of the TMF tests. The BiF test, on the other hand, is believed to act as a bridge between LCF damage mechanisms and TMF damage mechanisms, as several studies have pointed out [8, 49, 81, 82, 84]. It is generally accepted, then, that a testing protocol employing multiple test-types is required to flush out dominant damage mechanism and mechanism interaction. Two researchers have recently performed parametric TMF studies which shed light upon the dominant damage mechanisms present as a function of TMF waveform, temperature and hold times. In separate studies, Gordon [86] performed creep, LCF, creep-fatigue IP TMF and OP TMF experiments while Kupkovits [67] performed creep, IP TMF and OP TMF. Through the judicious use of these different waveforms these researchers effectively isolated dominant damage mechanisms, for their respective materials, as a function of cycle type and test parameters, resulting in deformation mechanism maps of sorts.

In closing, several studies have determined that the OP TMF and OP BiF waveforms are the most damaging, and are therefore life limiting in turbine components [8, 44, 49]. This is primarily due to the environmental-fatigue interactions introduced in these cycle types.

2.8 Thermomechanical Fatigue (TMF) Life Prediction Methodologies

High temperature deformation and life modeling of superalloys run the gamut of damage mechanism interaction and computational complexity; from simple first order "go-no-go" design tools to "physics-based" models which incorporate such effects as dislocation density and second-phase particle interaction.

An example of a rather simple life estimation scheme was presented in Section 2.4.2. In this study the authors determined that a simple Schmid analysis could be used to predict lives of single crystal Ni-base superalloys of various primary orientations [5]. A micromechanics-based life model was presented for the second generation nickel-base single crystal superalloy CMSX-4 [9]. In this work the researchers sought to investigate the role of the materials microstructure on TMF failure. To this end they proposed using a micromechanics based model to account for the misfit strain between the γ and γ' phases. This method utilized the Eshelby equivalent inclusion method to determine the average stress field approximation in the γ and γ' phases, $(\sigma_{ij})\gamma$ and $(\sigma_{ij})\gamma'$ respectively. The stress fields are then used to determine the plastic work for each phase in an attempt to estimate relative amounts of damage. The plastic work (W_p) is defined on a per-cycle basis as

$$W_p = \int \sigma_{ij} d\varepsilon_{p,ij} \qquad \textbf{(2-15)}$$

where $\varepsilon_{p,ij}$ is the second order plastic strain tensor. The model performed well as a general indicator of damage accumulation, though by no means could it estimate life accurately. Nissley utilized a fracture mechanics approach to determine life prediction for TMF of superalloys [10]. Specifically an effective J-integral, which accounts for thermal exposure, was used to predict TMF lives of PWA 1480 and MAR-M509. In this model, an increment of crack extension $\left(\frac{da}{dN}\right)$ is determined by

$$\frac{da}{dN} = AJ_{eff}\upsilon^c \qquad \textbf{(2-16)}$$

where J_{eff} is the effective J-integral

$$J_{eff} = \pi(a + a_o)(\beta^2 f W_{eff}^{tot})^b - J_{th} \quad \textbf{(2-17)}$$

and

$$1/\upsilon = \int^{cycle} \exp\left[\frac{Q_o T}{T_0 - 1}\right] dt \quad \textbf{(2-18)}$$

A, a, a_0, b, c and T_0 are material constants, β accounts for strain hardening, W_{eff}^{tot} is the total effective work, J_{th} the threshold J-integral and Q_0 is an activation energy. The model works well at predicting TMF lives for these materials under the conditions tested, and requires a minimum number of tests to calibrate.

A classical example of a life model which incorporates interactions between dominant damage mechanisms was proposed for the high temperature low cycle fatigue behavior of the polycrystalline superalloy Rene 80 [87]. This model is predicated on the assumption that when this material is subjected to high temperature LCF, cracks will initiate at locations where localized plastic deformation impinges upon an oxidized grain boundary, cause by high temperature exposure.

$$N_i = C\left(\frac{\upsilon}{1 + \upsilon * t_h}\right)\exp\left(\frac{Q}{RT}\right)\Delta\varepsilon_{in}^b \quad \textbf{(2-19)}$$

C and b are fitting constants, ν is the cycle frequency, t_h the hold time (if any), Q an activation energy, R the universal gas constant, T the absolute temperature and $\Delta\varepsilon_{in}$ is the inelastic strain range. The relationship effectively couples the fatigue-environmental interactions occurring in this material when subjected to LCF at 871° C via the incorporation of the inelastic strain range and oxidation kinetics. Milligan and Antolovich [33] used a similar approach to determine a physics-inspired yield model for PWA 1480. They determined that the yielding of this material was a thermally activated

process, and should therefore be described using the following modified Arrhenius relationship

$$\sigma_y = A * \exp\left(\frac{Q'}{RT}\right) \quad \textbf{(2-20)}$$

where σ_y is the yield stress, A is a material specific constant, R the universal gas constant, T the absolute temperature and Q' is a temperature and strain rate dependent activation energy for yielding. They determined that below 760° C, Q' = 0. As such, the term 'A' would be equal to the athermal flow stress below 760° C. Though seemingly simple, the functional form is a direct result of microscopy identifying underlying deformation mechanisms. Another model which incorporates dominant damage interactions was developed to estimate the lives of MAR M509 specimens experiencing isothermal LCF at 900°C [71]. This model considers fatigue-oxidation interactions as the primary damage divers for high temperature LCF conditions. The life estimation equation is a linear damage summation accounting for crack advance due to matrix oxidation as well as carbide oxidation:

$$(da/dN)_{OX} = (da/dN)_{OX.M}(1 - f_c^*) + (da/dN)_{OX,C} f_c^* \quad \textbf{(2-21)}$$

where $(da/dN)_{OX}$ is the average crack extension per cycle due to oxidation, $(da/dN)_{OX.M}$ is the oxidation driven crack extension per cycle in the matrix, $(da/dN)_{OX.C}$ the oxidation driven crack advance per cycle in the carbides, and f_c^* is the effective fraction of carbides on the crack path. This model accounts for the underlying deformation physics through the coupling of fatigue driven-oxidation assisted crack growth. This relationship

performed well under the test conditions and predicted the majority of the LCF lives within a factor of 2X.

There have been several physics-based fatigue models proposed which are based upon slip band morphology. The quantification of slip band morphology is then used as an internal state variable accounting for damage. One such study on the coarse-grained nickel base superalloy KM4 used first principles to quantify the materials slip irreversibility [31]. The slip irreversibility (f) is defined by

$$f = \frac{N_{ed/\varepsilon}}{N_{\exp/\varepsilon}} \qquad \textbf{(2-22)}$$

where $N_{ed/\varepsilon}$ is the number of dislocations exiting a free surface per unit of plastic strain range as a result of a single cycle and $N_{\exp/\varepsilon}$ is the expected number of local dislocations based upon the average distance between slip bands. Their results indicate that there was a clear relationship between the net irreversibility determined and fatigue crack propagation thresholds, and could therefore be used as a fatigue damage parameter for materials experiencing fatigue. Another study determined that the fatigue life of specimens is intrinsically linked to the length scale of: a) the material, b) specimen and c) slip steps, as well as physical properties such as yield strength and Young's modulus [22]. This model presumes that a fraction of plastic strain contributes to surface slip steps via the egress of edge dislocations. These surface slip steps, in turn, lead directly to crack initiation. By equating a portion of the inelastic strain to measurable slip quantities and using the assumption that displacement due to Mode II sliding is roughly equal to Mode I crack opening, the following relationship is proposed [22],

$$N_i = \frac{\Delta K_{th}^2}{4\sigma_y E(f\Delta\varepsilon_{in})h_s} \quad \textbf{(2-23)}$$

where N_i are the cycles to crack initiation, ΔK_{th} is the threshold stress intensity, σ_y the yield strength, E the modulus of elasticity, $f\Delta\varepsilon_{in}$ the fraction of the inelastic strain which contributes to slip ireversability, and h_s is the spacing between slip bands. The model was further modified to incorporate grain and gage-section size effects based upon their effect of slip irreversibility. When used to predict the fully reversed cycles to initiation of polycrystalline titanium and high strength low alloy steel (HSLA) the model performed quite well. These models show promise as an indicator of accumulated fatigue damage.

Cumulative damage models can also be cast in such a way as to be physics-based. The work of Neu and Sehitoglu is a good example of this [88, 89]. In their model, which was initially calibrated for 1070 steel experiencing TMF, the three primary damage mechanisms of environmental fatigue, creep and fatigue are summed to determine the total life to crack initiation.

$$N_i = \left(\frac{1}{N_i^{fat}} + \frac{1}{N_i^{cr}} + \frac{1}{N_i^{env}} \right)^{-1} \quad \textbf{(2-24)}$$

The total cycles to crack initiation, N_i, is determined by the linear summation of the number of cycles to failure is fatigue acted independently, N_i^{fat}, the number of cycles leading to failure by creep alone, N_i^{cr}, and the number of cycles to failure due to environmental fatigue interaction, N_i^{env}. The fatigue, creep and environmental fatigue modules are defined as [89]

$$N_i^{fat} = C\left(\Delta\varepsilon_{mech}\right)^d \tag{2-25}$$

$$N_i^{cr} = \Phi^{CREEP} \int_0^t A \exp\left(\frac{-\Delta H}{RT(t)}\right)\left(\frac{\alpha_1 \overline{\sigma} + 2\alpha_2 \sigma_H}{K}\right)^m dt \tag{2-26}$$

$$\frac{1}{N_i^{env}} = \left[\frac{h_{cr}\delta_0}{B\Phi^{ENV}\left(K_{peff}^{ENV} + K_{peff}^{\gamma'}\right)}\right]^{-1/\beta} \frac{2\left(\Delta\varepsilon_{mech}\right)^{\left(2/\beta\right)+1}}{\dot{\varepsilon}^{1-\alpha/\beta}} \tag{2-27}$$

The fatigue module includes material specific fitting constants, C and d, and the mechanical strain range, $\Delta\varepsilon_{mech}$. The constants are both fit to lower-temperature low cycle fatigue (LCF) data to minimize environmental and creep effects. The creep module includes a phasing term, Φ^{creep}, activation energy ΔH, universal gas constant, R, and the cycle temperature as a function of time T(t). The terms α_1 and α_2 account for relative amounts of damage in tension and compression, $\overline{\sigma}$ is the effective stress, σ_H the hydrostatic stress, K the drag stress, while A and m are material dependent constants. The environmental-fatigue module also includes a phasing term,

$$\Phi^{ENV} = \frac{1}{t_c}\int_0^{t_c} \phi^{ENV}\, dt \tag{2-28}$$

where ϕ^{ENV} is defined as

$$\phi^{ENV} = \exp\left[-\frac{1}{2}\left(\frac{\left(\dot{\varepsilon}_{th}/\dot{\varepsilon}_{mech}\right)+1}{\xi^{OX}}\right)^2\right] \tag{2-29}$$

in which ζ^{ox} accounts for the sensitivity of the coupling of fatigue and oxidation to cyclic phasing that promotes damage. The phasing term, Φ^{ENV}, effectively accounts for temperature-strain phase differences by forcing the term to a value of one for OP TMF and zero for IP TMF. The oxidation and γ' depletion terms within the environmental-fatigue module, K^{ENV} and $K^{\gamma'}$ respectively, are defined as,

$$K_{peff}^{ENV} = \frac{1}{t_c}\int_0^{t_c} D_{OX} \exp\left(\frac{-Q_{OX}}{R \cdot T(t)}\right) dt \qquad \textbf{(2-30)}$$

and

$$K_{peff}^{\gamma'} = \frac{1}{t_c}\int_0^{t_c} D_{\gamma'} \exp\left(\frac{-Q_{\gamma'}}{R \cdot T(t)}\right) dt \qquad \textbf{(2-31)}$$

The terms D_{ox} and Q_{ox} are the oxidation diffusion coefficient and activation energies, while the $D_{\gamma'}$ and $Q_{\gamma'}$ are the γ' diffusion coefficient and activation energies, respectively. The environmental-fatigue module also includes terms which account for: 1) the material ductility within the environmentally affected zone, δ_o, 2) the critical crack length at which the environmental attack trails behind the advancing crack tip, h_{cr} 3) the strain rate sensitivity, α; and 4) terms accounting for total environmentally induced crack length, B and β. These equations effectively account for the independent damage mechanisms of fatigue, creep and environment-fatigue when used to estimate thermomechanical fatigue (TMF) component life. Furthermore the environmental-fatigue and creep modules account of the interactions between dominant damage mechanisms (creep-fatigue and environmental-fatigue). This life estimation model has been used as is, and in modified versions, by several researchers in order to accurately estimate life to TMF crack initiation in Ni-based superalloys [67, 70, 86, 90].

Finally, a physics based model for the creep of nickel-base superalloys incorporating microstructural evolution was proposed by Manonukul and coworkers [72]. This model incorporates superalloy-specific microstructural evolution, such as γ' volume fraction and coarsening, into a more traditional constitutive creep relation. The result is a model which accounts for microstructural temperature-dependent deformation mechanisms (e.g. dislocation bowing versus cutting). The elegance of this model results from the use of classical creep relations, material-specific microstructural evolution as well as material-specific deformation modes. The product is a model which predicts creep response incredibly well.

The purpose of this section was to introduce the reader to the general types of constitutive and life models currently in existence. Additional discussion on high temperature life modeling can be found in papers by Sehitoglu [91], Cai et al. [92], McDowell et al. [18], Pineau and Antolovich [1], Halford [81] as well as to the recent work of Manson and Halford [93].

2.9 Summary

This chapter has provided an overview of superalloy composition, microstructure, applications and deformation. An important conclusion to be drawn is the general lack of fundamental understanding of damage mechanism interactions and the effects that these interactions have upon life. Though research has been performed on dominant damage mechanisms experienced in TMF, the interaction of these mechanisms is yet to be quantified in a simple, physically admissible way. As an example, the work of Reuchet and coauthors provide some insight to the effect that fatigue may play in base-material environmental degradation [71], and the extensive successful implementation of the Neu-

Sehitoglu [88, 89] model to predict life has shown that incorporating damage mechanism interactions is critical to life estimation. However, there still exists the need for computationally inexpensive life estimation schemes which are relatively easy to calibrate and, most importantly, are based upon the underlying deformation physics involved in TMF cycles.

CHAPTER 3. THERMOMECHANICAL FATIGUE - EXPERIMENTAL PROCEDURE AND RESULTS

3.1 Introduction

Uniaxial thermomechanical fatigue (TMF) and bithermal thermomechanical fatigue (BiF) tests were performed on single crystal PWA 1484 specimens in different crystal orientations. Dominant damage mechanisms and mathematical relationships relating BiF and TMF tests are proposed.

3.2 Specimens

Cast cylindrical bars of PWA 1484 in the heat-treated condition were supplied by Pratt & Whitney. The dimensions were approximately 16 mm diameter by 230 mm long. Bars with three different crystal orientations, nominally <001>, <111> and <123>, were studied. The bars were machined into fatigue specimens shown in Fig 3-1 following ASTM E606-04. Machining was handled by both Cincinnati Testing Labs and MarTest.

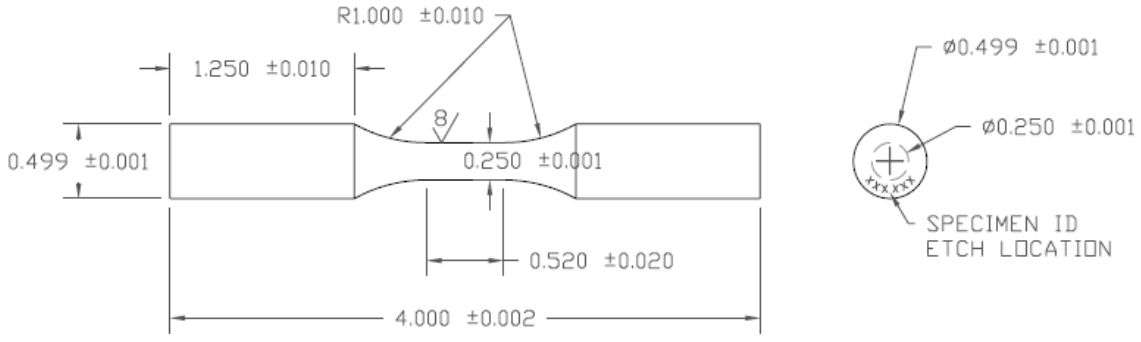

Figure 3-1: Fatigue Specimen Drawing

A material tracking protocol was established for this project so that whenever any material changed hands, i.e. receipt as raw material; shipping to machine shop; receipt of finish-machined specimens, documentation was generated for tracking purposes. Specifically material receiving, material shipping and material traveler documents were created. Representative examples of material receiving, material shipping and material traveler documents are provided in the Appendix. The Appendix also includes all specimen drawings and material-orientation details for all material for which this data was supplied

3.3 Equipment

Thermomechanical fatigue tests were performed on an MTS 44.5 kN (10 kip) axial closed-loop servo-hydraulic test frame. The load cell resolution for this system is +/- 0.44 kN. MTS 646 water cooled hydraulic collet grips, seen in Fig 3-2, were installed and alignment was maintained within 12.7 μm (0.0005") during testing.

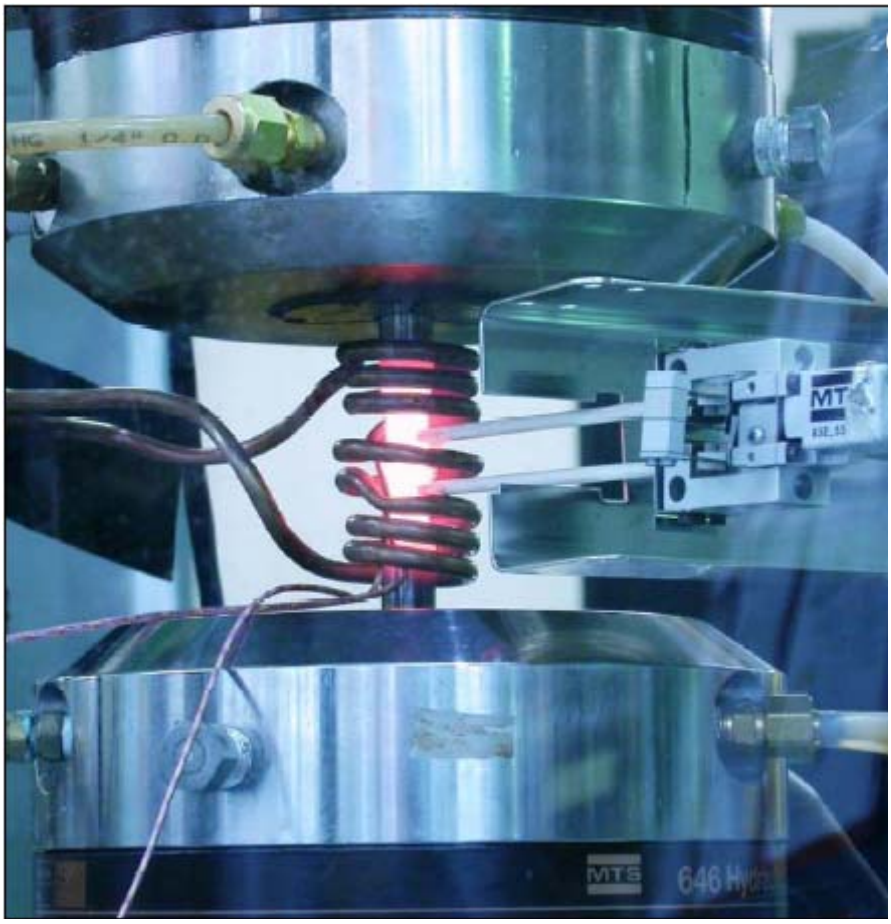

Figure 3-2: TMF Experiment

The test system was controlled by a two-channel MTS Teststar Classic controller using Testware SX software. Specimen heating has handled by an Ameritherm 2 kW induction heater. A seven-loop, 23 mm ID, copper coil, made of 4.76mm OD (3/16") tubing, was used to heat the fatigue specimens, shown in Fig 3-2. Two Type K thermocouples were welded to the specimen at the radius-gage section transition, just outside the gage section. The induction heater was controlled by a Watlow model 945A-2FK5-A000 PID controller having +/- 1 ° C resolution. The closed-loop temperature circuit consisted of the above mentioned PID controller which receives the set point signal from the Testware software. Axial strain was measured using a 12.7mm gage

MTS model 632.52E-14 high temperature extensometer with 130mm long (nominal) ceramic V-chisel rods. The extensometer which was used in TMF tests has an operating range of 20% strain and was calibrated to a range of +/- 2%. The closed axial loop consisted of the Testware software, the axial hydraulic cylinder and the feedback came from either the extensometer, LVT or the load cell, depending upon control scheme.

3.4 Verification of Adherence to TMF Test Standards

3.4.1 ASTM TMF test criteria

All TMF tests performed for this work conformed to ASTM E 2368-04, Standard Practice for Strain Controlled Thermomechanical Fatigue Testing [79]. The standard provides definitions, testing protocols/criteria and data presentation requirements. Of primary importance is the testing criteria set forth to ensure test validity. The standard lists four primary requirements to ensure test validity, they are paraphrased as follows:

1. The maximum allowable temperature gradient over the specimen gage section within a cycle shall be the greater of +/- 1% x Tmax (in Kelvin) or +/- 3 K, where Tmax is the maximum temperature for the particular test-cycle of interest.
2. The maximum stress-strain hysteresis width during zero load, load-control, thermal cycling shall be less than 5% x $\Delta\varepsilon_{th}$, where $\Delta\varepsilon_{th}$ is the thermal strain range for each test-specific thermal cycle.
3. The error between the temperature/mechanical strain phasing shall not exceed the bounds established by Error $\leq \varphi$ +/- 5°, where φ is the temperature/mechanical strain phasing in degrees.

4. During mechanical strain control testing, the mechanical strain range shall not deviate from the desired value by more than 2% x $\Delta\varepsilon_m$, where $\Delta\varepsilon_m$ is the mechanical strain range defined by $\Delta\varepsilon_m = \Delta\varepsilon_T - \Delta\varepsilon_{th}$. $\Delta\varepsilon_T$ is the total strange range as recorded by the extensometer and $\Delta\varepsilon_{th}$ is defined below.

3.4.2 Procedures employed to ensure test validity per ASTM

ASTM E 2368-04 was used as minimum criteria for test validity while setting up and conducting the TMF tests performed for this work. As such, equipment verification and test procedures were implemented to ensure that the 4 criteria listed in the previous section were satisfied for each test. The protocols and procedures implemented are listed below in the same order as presented in section 3.4.1.

1. In order to ensure that the temperature gradient in the gage section of the specimens was within allowable range, 10 temperature readings were recorded from a single specimen at 550°C, 850°C, 950°C and 1050°C. This was achieved by welding 10 thermocouples (TC) to a single specimen as shown in Figures 3-3 and 3-4.

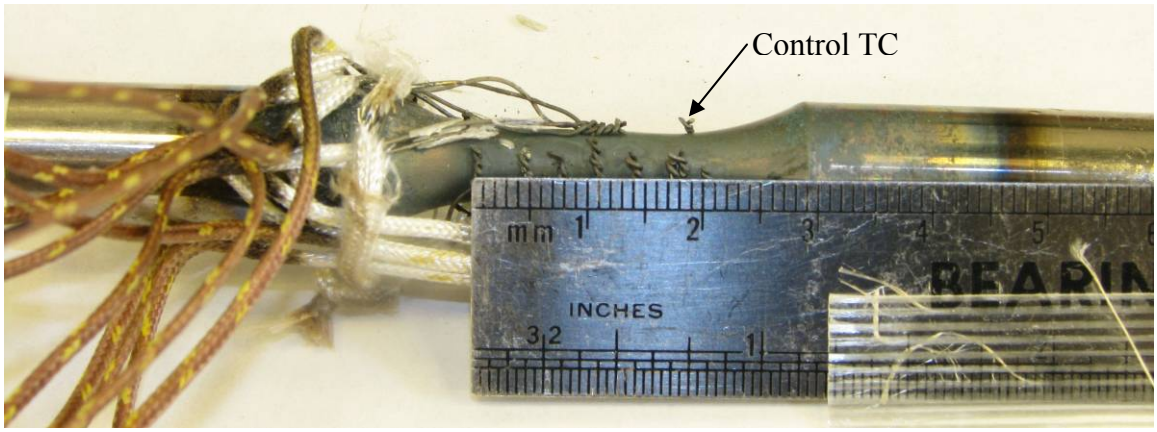

Figure 3-3 Induction Coil Verification: 6 Thermocouples Welded longitudinally along Gage Section

Figure 3-4: Induction Coil Verification: 4 Thermocouples Welded Circumferentially Around Center of Gage Section

The thermocouple location marked "control" in Fig. 3-3 was used as the feedback thermocouple. The induction heater coil was modified until a sufficiently small temperature gradient was achieved. Results from this verification tests are shown in Table 3-1.

Table 3-1 Specimen Temperature Gradient Test Results

Control	553			850			950			1050		
Th-couple	Temp (° F)	Temp (° C)	PASS	Temp (° F)	Temp (° C)	PASS	Temp (° F)	Temp (° C)	PASS	Temp (° F)	Temp (° C)	PASS
1	1029	554	1	1550	843	1	1720	938	1	1920	1049	1
2	1038	559	1	1561	849	1	1735	946	1	1930	1054	1
3	1041	561	1	1560	849	1	1740	949	1	1929	1054	1
4	1028	553	1	1549	843	1	1727	942	1	1910	1043	1
5	1039	559	1	1563	851	1	1745	952	1	1928	1053	1
7	1020	549	1	1547	842	1	1732	944	1	1917	1047	1
8	1029	554	1	1545	841	1	1724	940	1	1906	1041	1
9	1035	557	1	1553	845	1	1720	938	1	1919	1048	1
10	1016	547	1	1545	841	1	1721	938	1	1912	1044	1

The "PASS" column indicates the results of a rubric which tests for results confirming to ASTM standards; a value of "1" indicates that that results are within allowable tolerance.

2. In order to ensure that the thermal hysteresis was within the allowable limits, thermal cycling in force control was conducted prior to each test. The temperature-controller PID values were adjusted as needed until the recorded strain hysteresis was within the specified value. Once the hysteresis criterion was

satisfied, a third-order polynomial was fit to the thermal strain vs. temperature data. This polynomial estimates thermal strain as a function of current temperature. The polynomial was then input into the Testware software. The actual TMF test program then performs two verification checks to ensure that thermal hysteresis is minimized. First, cycles one through three of the TMF test program collect data for force controlled thermal cycling. Next, cycles four through seven collect data for strain controlled thermal cycling. This data is used upon completion of the test to verify that a) thermal strain hysteresis values are within range, and b) the thermally induced loads are "experimentally insignificant" as suggested by ASTM E 2368-04.

3. Temperature/mechanical strain phasing was determined prior to test initiation. This was done by running a force-controlled test having a force range of 2224 N (500 pounds), R=-1 and test-specific temperature profile. Upon completion of three full cycles a plot was made of force vs. time and temperature vs. time on the same set of axis. The correct force/temperature phase was determined and input to the Testware software. The process was repeated until phasing was correct for the testing conditions. The final phase angle was then set in the Testware software, and the software maintained that phase value for the duration of the test.
4. Criterion four listed above is verified upon completion of the TMF test. Plots of maximum and minimum mechanical strain versus time are created to ensure that the strains experienced during the course of the test were within acceptable limits.

3.5 Testing/Control/Programs

Fatigue testing for this work consisted of mechanical-strain controlled TMF tests. The mechanical strain is defined as $\varepsilon_m = \varepsilon_T - \varepsilon_{th}$. The total strain, ε_T, is the strain as measured by the extensometer. The thermal strain, ε_{th}, is calculated from a third order polynomial function of temperature, as outlined earlier. The Testware software calculates the control strain, ε_m, real-time during the test. Out-of-phase (OP) TMF tests have a mechanical strain wave form that is phased $\varphi = 180°$ with respect to the temperature waveform, while in-phase (IP) tests have a phase angle of $\varphi = 0°$. Figure 3-5 and 3-6 provides simple IP and OP control wave forms. All TMF tests performed had a cycle time of 180 seconds.

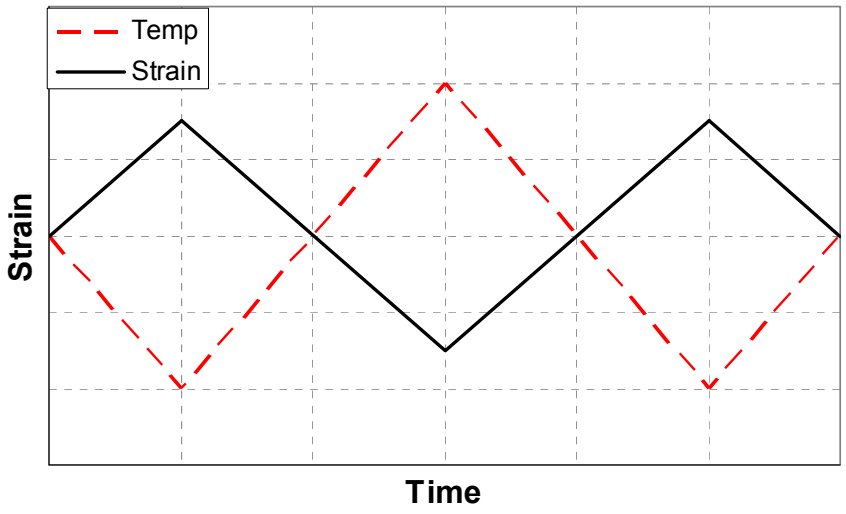

Figure 3-5 OP TMF Temperature-Time and Mechanical Strain-Time waveforms

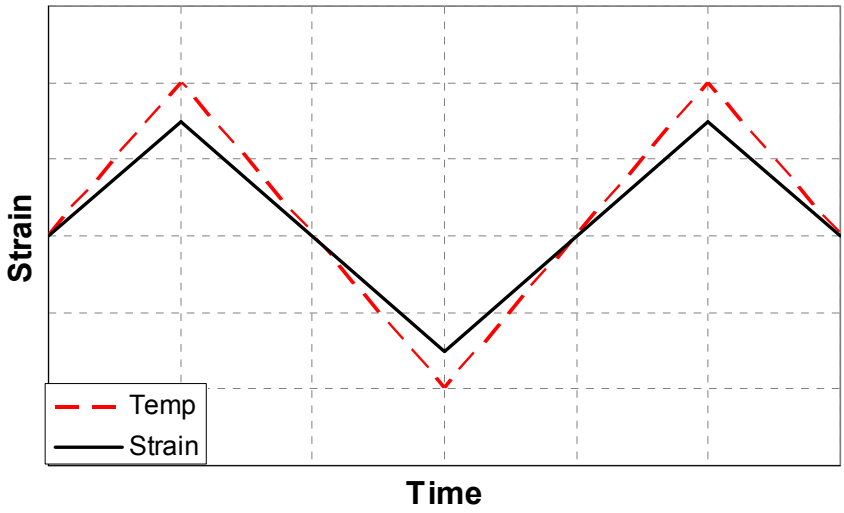

Figure 3-6: IP TMF Temperature-Time and Mechanical Strain-Time waveforms

Out-of-phase Bithermal fatigue (BiF) test cycle consists of a high-temperature compressive half cycle, followed by a load-free transition to low temperature, a low temperature tensile half cycle and finally a load-free transition to high temperature, illustrated in Fig 3-7. Bithermal fatigue cycle segment lengths were established to match those for the TMF tests. Specifically, both the high temperature and low temperature half cycles were 90 seconds in length, as are both of the load-free temperature transitions. This was done to ensure that loading and temperature rates between the two test types (TMF and BiF) were identical for comparison purposes. The BiF tests were also conducted in mechanical strain control.

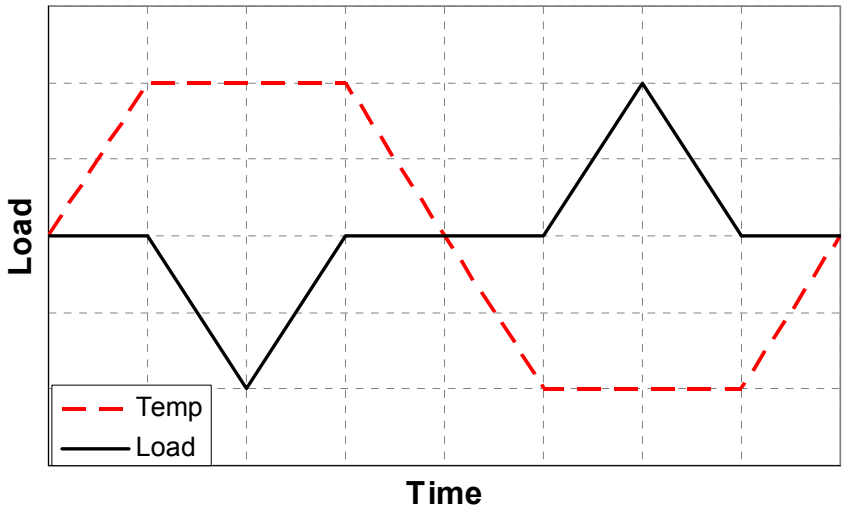

Figure 3-7: OP BiF Temperature-Time and Load-Time Waveforms

The TMF and BiF Testware programs created for this work all followed a similar protocol:

- Increase temperature to test mean temperature. The temperature was then allowed to stabilize for 180 seconds.
- Perform three force-controlled thermal cycles at zero force.
- Perform three strain-controlled thermal cycles at zero strain.
- Stabilize specimen temperature at test mean temperature value for 180 seconds.
- Begin compressive half cycle

All TMF and BiF tests were conducted in the ambient atmosphere of the Mechanical Properties Research Laboratory (MPRL) in the high bay of the Manufacturing Related Complex building at Georgia Institute of Technology. The step-by-step start-up procedure as well as sample TMF and BiF control algorithms are provided in the Appendix.

3.6 TMF Test Matrices

The goal of this project is to formulate a physics-inspired model which accurately predicts single crystal superalloy TMF life. In doing so, it is first necessary to characterize the dominant damage mechanisms active for different loading conditions, as well as the interaction of these damage mechanisms whenever appropriate. Chapter 2 of this work provided insight to the difficulty of determining a deformation model for this class of material. Specifically, single crystal deformation response as a function of temperature, orientation and inelastic strain must be fully characterized. In order to create a deformation model for PWA 1484, the experimental plan must answer the following questions:

- What are the dominant factors controlling life in components experiencing OP TMF?
    - What slip systems are active and what is the driving force behind their activation?
    - What inelastic deformation mechanisms are active? Specifically, does dislocation glide dominate or has a climb mechanism been activated.
    - What creep mechanisms are active, if any? Does creep dominate or does a fatigue-creep interaction?
    - What are the environmental effects? Specifically one needs to be aware of oxidation, γ'-depletion as well as material second-phase particle coarsening.

A Schmid analysis has been shown to sufficiently correlate the relative amounts of inelastic deformation in single crystal superalloy to the material orientation [3-6, 38, 39, 94]. Any well designed test matrix whose aim is to determine material response for a single crystal should activate the octahedral and cube slip systems separately [95]. Verification tests should also be performed in "other" orientations. To address these issues, specimens of nominal <001>, <111> and <123> were requested for testing. Figure 3-8 locates the three requested material orientations on a standard stereographic triangle, while Figure 2-9 of provides Schmid analysis results for the four orientations shown in Fig 3-8.

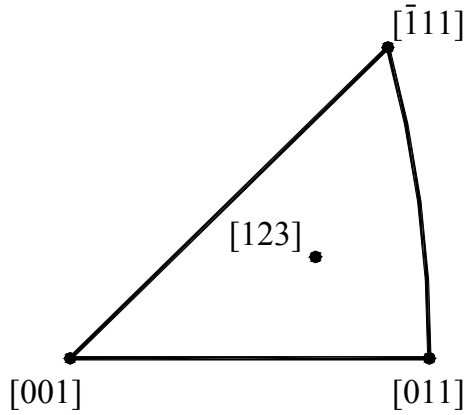

Figure 3-8: Requested Material Orientation on Stereographic Triangle

In order to activate a range of inelastic deformation mechanisms, TMF tests of different strain ranges are proposed. Additionally, temperature dependent deformation mechanisms were studied by varying the test maximum and effective temperature. Bithermal fatigue tests were proposed to decouple the effects of simultaneously varying temperature and strain. As pointed out in Chapter 2, these tests provide insight to the effect of single damage mechanisms, and when compared to TMF tests provide a basis

for understanding of the deformation mechanism interaction. The detailed test matrix is provided in the Appendix.

3.7 Crack Initiation Criteria

Crack initiation life includes the cycles to nucleate the crack and also grow to a detectible size. Because there are different methods for detecting a crack, a well defined initiation criterion must be consistently used to compare lives. Halford et al. [83] define crack initiation as 0.8mm, Remy and colleagues [44, 71, 75, 77, 85] define crack initiation as 50 μm. Moreover, the same researcher may have multiple definitions for crack initiation size. As an example, Remy often uses two crack sizes as initiation criteria, 0.3 mm and 50 μm [44, 71, 75, 77, 85], the former for life determination and the latter for microstructurally sensitive initiation. Certainly the crack initiation criterion chosen depends upon the capabilities of the laboratory to accurately measure a crack.

It is desirable to couple the crack initiation criteria to a materials microstructure, given that a physics-inspired life estimation scheme would be inherently linked to the microstructure. Malpertu et al. [85] proposed a crack initiation criterion for the polycrystalline superalloy IN100 based upon a critical crack size scaled to the "depth of interdendritic areas", as research indicates that cracks predominantly initiate in this region during high temperature low cycle fatigue. Crack initiation for this research has been defined in a similar manner. Specifically, crack initiation occurs when a thumbnail shaped edge-crack exists which has a radius equal to three times the materials average dendrite spacing, as depicted in Figure 3-9. The existence of such a crack reduces the load carrying capabilities of the specimen by an amount equal to A'/A_0, where A' is the

specimen cross-sectional area when a thumbnail crack exists, and A_0 is the initial cross-sectional area. PWA 1484 average dendrite spacing was found to be 0.178 mm (0.007"), as indicated in Figure 3-10. With a specimen diameter of 12.7 mm, the quotient A'/A_0 would have a value of $A'/A_0 = 0.996$.

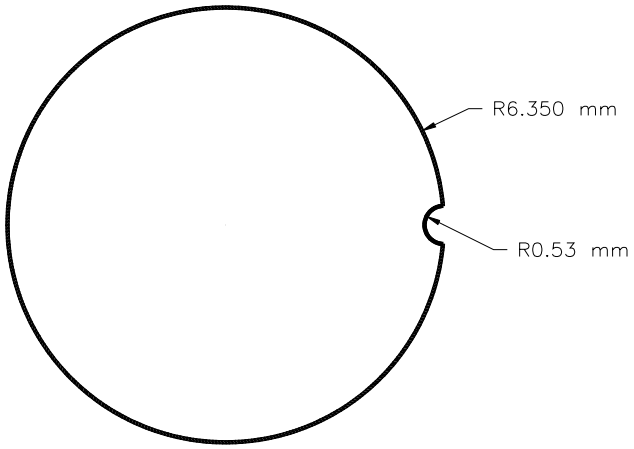

Figure 3-9: Schematic of Crack Initiation Criteria

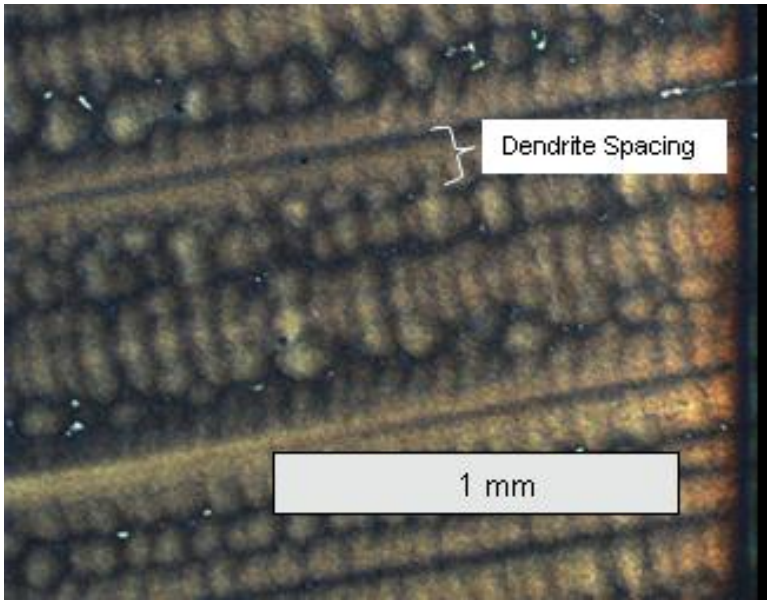

Figure 3-10: PWA 1484 Dendrite Spacing

It is then imperative that a concise and repeatable method for post-test crack initiation determination be proposed and adhered to for the duration of testing. The following crack initiation criterion was used for this study:

- A thumbnail crack, having radius equal to 0.53 mm (0.021”), exists in a test specimen when the tensile load-carrying capabilities of the specimen drop by an amount equal to $(1 - A'/A_0)$, or 1%, for two consecutive fatigue cycles.

3.8 Fatigue Test Results

A complete list of results for fatigue tests conducted for this study is provided in Table 3-2. The results are divided into three groups: baseline tests, supporting fatigue tests and off-axis tests. The baseline tests were primarily used to isolate dominant damage mechanisms and model calibration, whereas the supporting tests were used for model verification.

Table 3-2 Fatigue Test Results (Tests marked with an * will be used as Baseline tests in Chapter 6)

Baseline Fatigue Tests

Waveform	Orientation	R	Hold time (s)	Δε(mech) (-)	ε_a(mech) (-)	Δε(in) @ Ni/2 (-)	Ni/2 (cycle)	Ni (cycle)	Nf (cycle)	Tmin (deg C)	Tmax (deg C)	Teff (deg C)
OP-TMF*	001	-0.9	0	0.013	0.0065	0.003517	54	107	116	550	1050	953
OP-TMF*	001	-0.9	0	0.009	0.0045	0.000869	236	471	560	550	1050	953
OP-TMF*	001	-1.0	0	0.005	0.0025	0.000065	905	1810	2409	550	1050	953
OP-BiF*	001	-0.8	0	0.013	0.0065	0.002944	38	76	119	550	1050	1002
OP-BiF*	001	-0.9	0	0.009	0.0045	0.000179	185	370	408	550	1050	1002
OP-BiF*	001	-1.0	0	0.007	0.0035	0.000096	211	421	956	550	1050	1002

Supporting Fatigue Tests

Waveform	Orientation	R	Hold time (s)	Δε(mech) (-)	ε_a(mech) (-)	Δε(in) @ Ni/2 (-)	Ni/2 (cycle)	Ni (cycle)	Nf (cycle)	Tmin (deg C)	Tmax (deg C)	Teff (deg C)
OP-TMF	001	-0.4	0	0.013	0.0065	0.003076	45	89	110	550	1050	953
OP-TMF	001	0.0	0	0.009	0.0045	0.000567	280	560	781	550	1050	953
OP-TMF	001	-1.0	0	0.013	0.0065	0.002411	231	461	584	550	1050	953
OP-TMF	001	-1.0	0	0.009	0.0045	0.000725	305	610	1012	550	1050	953
OP-TMF	001	-0.6	300-HT	0.013	0.0065	0.000577	32	64	71	550	1050	1027
OP-BiF	001	-0.9	0	0.01216	0.00608	0.001247	42	84	118	550	1050	1002
OP-BiF	001	-0.8	0	0.0106	0.0053	0.001162	59	117	-	550	1050	1002
OP-BiF*	001	-1.0	300-HT	0.007	0.0035	0.000100	-	230	-	550	1050	1032
OP-BiF*	001	-1.0	300-HT	0.009	0.0045	0.002680	42	83	101	550	1050	1032
OP-BiF*	001	-1.0	300-HT	0.013	0.0065	0.004417	36	71	77	550	1050	1032
OP-BiF	001	-1.0	0	0.009	0.0045	0.000099	1874	3748	7423	550	900	865

Off-Axis Fatigue Tests

Waveform	Orientation	R	Hold time (s)	Δε(mech) (-)	ε_a(mech) (-)	Δε(in) @ Ni/2 (-)	Ni/2 (cycle)	Ni (cycle)	Nf (cycle)	Tmin (deg C)	Tmax (deg C)	Teff (deg C)
OP-TMF	111	-1.0	0	0.005	0.0025	0.000702	124	247	309	550	1050	953
OP-TMF	111	-1.0	0	0.009	0.0045	0.003246	16	31	52	550	1050	953
OP-TMF	111	-1.0	0	0.013	0.0065	0.006656	11	22	27	550	1050	953
OP-TMF	~123	-0.9	0	0.005	0.0025	0.000628	283	565	619	550	1050	953
OP-TMF	~123	-1.0	0	0.007	0.0035	0.001741	111	223	379	550	1050	953
OP-TMF	~123	-1.0	0	0.009	0.0045	0.003710	24	48	107	550	1050	953

Table 3-2 lists the waveform, specimen nominal orientation, strain ratio (R), high-temperature hold time, mechanical strain range (Δε(mech)), mechanical strain amplitude (ε_a(mech)), inelastic strain range at half life ((Δε(in) @ Ni/2), cycles to half life (Ni/2), cycles to initiation (Ni), cycles to failure (Nf), as well as minimum, maximum and effective cycle temperature. The cycles to crack initiation, Ni, is based on a 1% load drop. The inelastic strain range for each test was determined by measuring the width of the stress-mechanical strain hysteresis loop (at zero stress) for the half life cycle; and the cycles to failure was determined by specimen separation.

The effective temperature equation used for this work was first proposed in a different form by McDowell et al. [18]

$$\exp\left(\frac{-Q}{RT_{eff}}\right) = \frac{1}{\Delta T}\int_{T\min}^{T\max} \exp\left(\frac{-Q}{RT}\right)dT \qquad \textbf{(3-1)}$$

where Q is an effective activation energy for high temperature deformation mechanisms, R is the universal gas constant, and ΔT the temperature range of the cycle ($\Delta T = T_{max} - T_{min}$). The equation determines an effective temperature by integrating over the maximum and minimum temperatures in the cycle. However, an effective temperature calculated in this way does not take into account the amount of time spent at these temperatures. The sole purpose for the determination and subsequent use of an effective temperature is to account for temperature activated deformation mechanisms which follow an Arrhenius relationship. This relationship provides the rate at which a reaction occurs, and therefore is time dependant. Additionally, there exists a temperature below which the thermally activated processes do not occur. As such the determination of an effective temperature should include the time at a particular temperature given that the temperature in question is above the minimum temperature for the reaction to occur. To this end the following effective temperature equation is proposed

$$\exp\left(\frac{-Q}{RT_{eff}}\right) = \frac{1}{\Delta t}\int_{t1}^{t2} \exp\left(\frac{-Q}{RT(t)}\right)dt \qquad \textbf{(3-2)}$$

where T(t) is the cycle temperature as a function of time for the portion of the cycle with temperatures above the activation temperature. The minimum activation temperature was chosen as 800˚C based upon the literature review, and the integration occurs over the cycle period ($\Delta t = t_1 - t_2$).

3.9 Plots

When plotting inelastic strain range versus cycles to failure, the BiF and TMF results diverge similar to what was observed by Gayda and coauthors [8, 84].

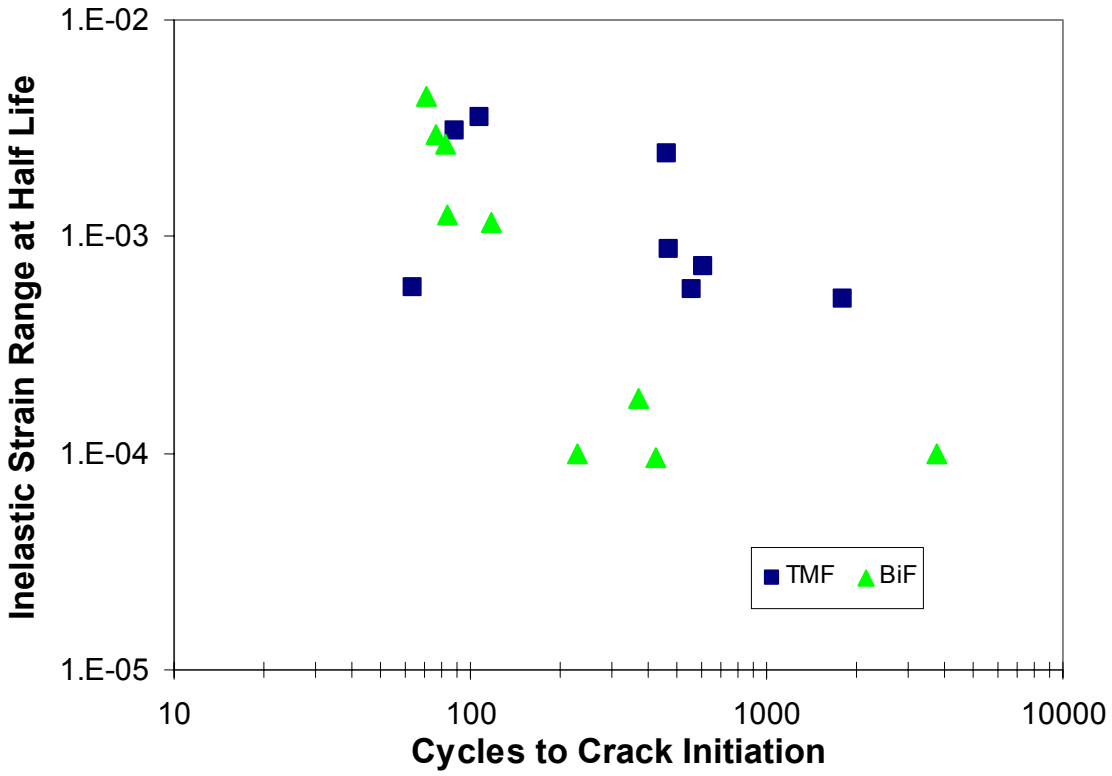

Figure 3-11 Fatigue Test Results (OP TMF and BiF): Inelastic Strain Range versus Cycles to Crack Initiation, <001> Specimens

Figure 3-11 indicates that the PWA 1484 BiF test results diverge from the TMF test results when plotting inelastic strain range versus cycles to failure. When delineating cycle effective temperature a trend emerges, as shown in Fig 3-12.

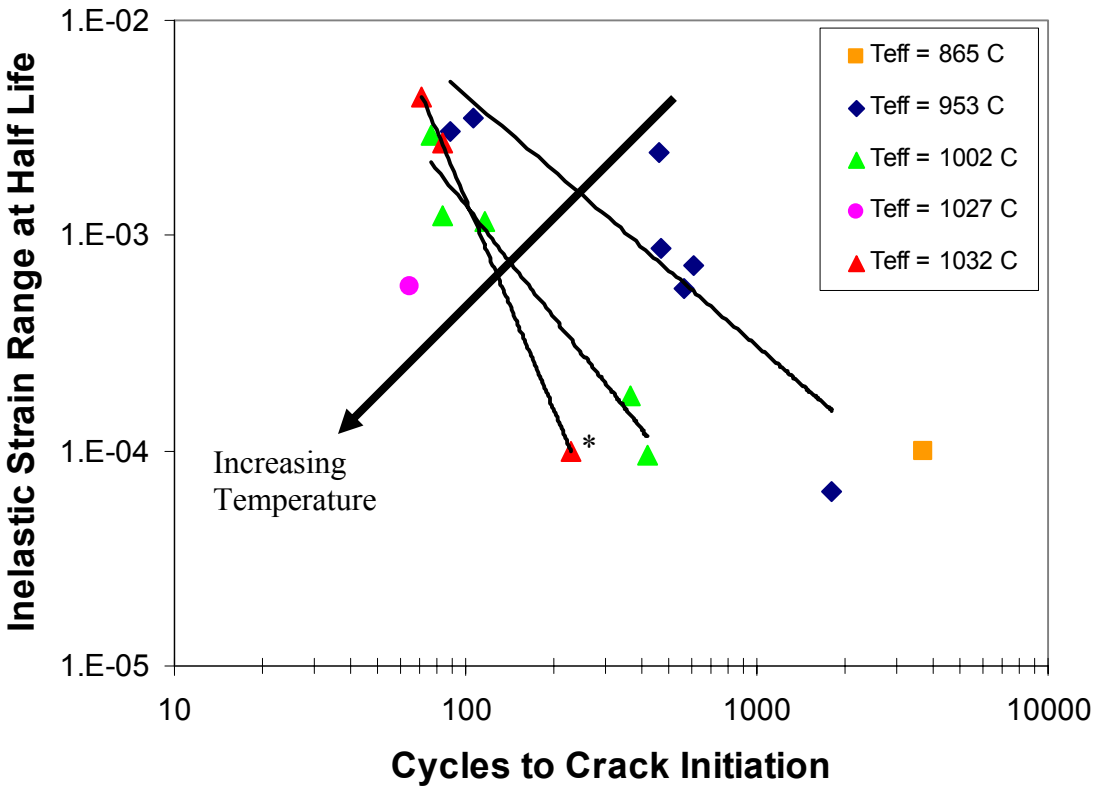

Figure 3-12 Fatigue Test Results (OP TMF and BiF) Delineated By Effective Temperature, <001> Specimens

The data point marked with an asterisk was terminated due to thermocouple failure. Though the specimen life was an order of magnitude longer than that shown, the life indicated on Figure 3-12 is representative of the number of cycles experienced by the specimen at the desired temperature range (prior to thermocouple failure). In general, there is an inverse relationship between effective temperature and cycles to failure. The point of Fig 3-12 is not to infer that an effective temperature correlates life for OP BiF and TMF tests, rather it shows that increasing the effective temperature of the test reduces life, as one might expect. This is due to the effective cycle temperature playing a primary role in determining dominant damage mechanisms for each of the cycle types.

For clarification, the effective temperatures shown in Fig. 3-12 have the following test parameters:

- T_{eff}=865°C: OP BiF with T_{min}=550°C and T_{max}=900°C
- T_{eff}=953°C: OP TMF with T_{min}=550°C and T_{max}=1050°C
- T_{eff}=1002°C: OP BiF with T_{min}=550°C and T_{max}=1050°C
- T_{eff}=1027°C: OP TMF with T_{min}=550°C and T_{max}=1050°C with 5 minute high temperature holds
- T_{eff}=1032°C: OP BiF with T_{min}=550°C and T_{max}=1050°C with 5 minute high temperature holds

Based upon specimen microscopy one can postulate as to the primary damage mechanisms operating for each of the tested specimens. Figure 3-13 repeats Figure 3-12 with dominant damage mechanisms for each test indicated on the figure.

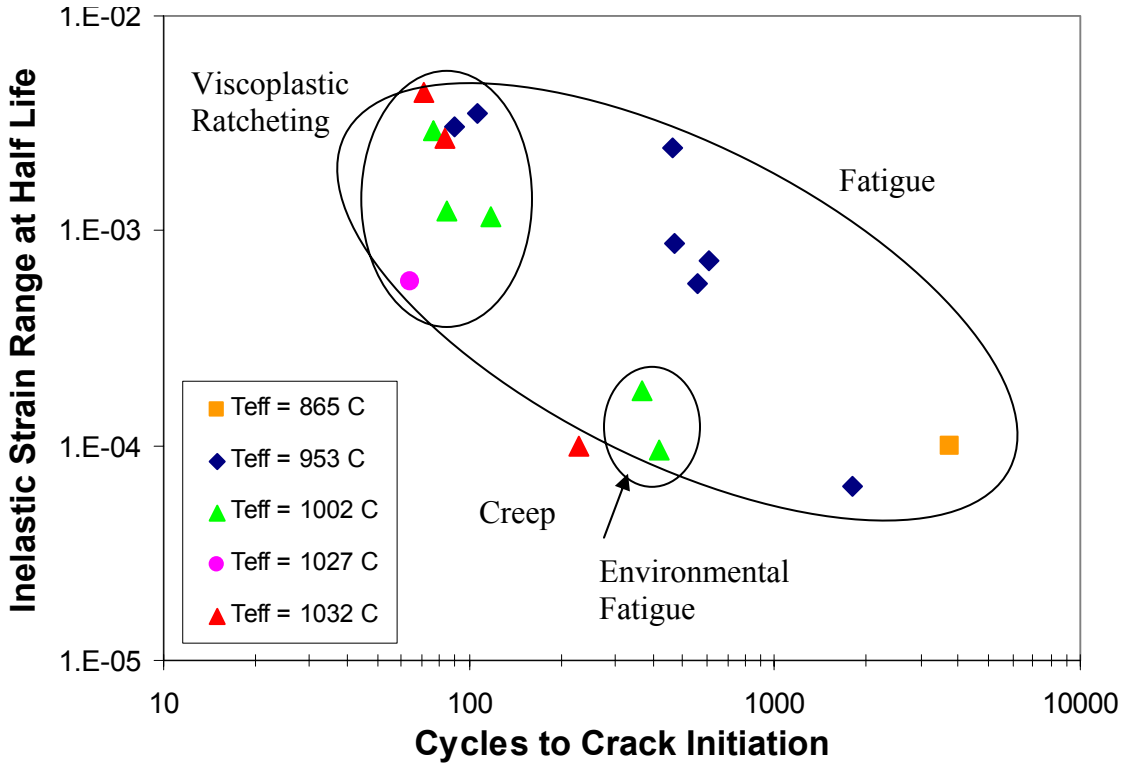

Figure 3-13 Fatigue Test Results (OP TMF and BiF)- Dominant Damage Mechanisms, <001> Specimens

Figure 3-14 shows <001> TMF and BiF test results in such a way as to graphically delineate dominant damage mechanisms as a function of test variables.

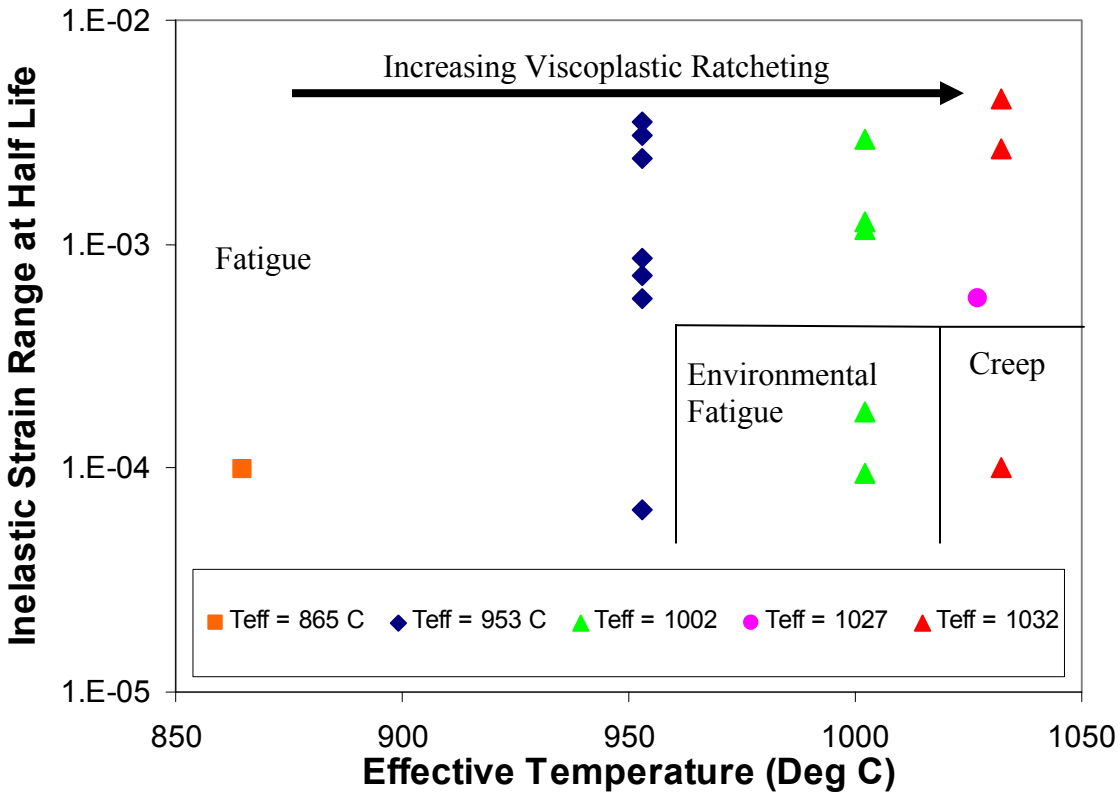

Figure 3-14 Deformation Mechanism Map for OP BiF and TMF

The basis for the dominant damage characterization is provided below.

3.10 Dominant Damage Mechanism Characterization

A select number of TMF and BiF tests were chosen as baseline tests for later comparison. The inelastic strain range versus cycles to crack initiation for the baseline tests is shown in Figure 3-15.

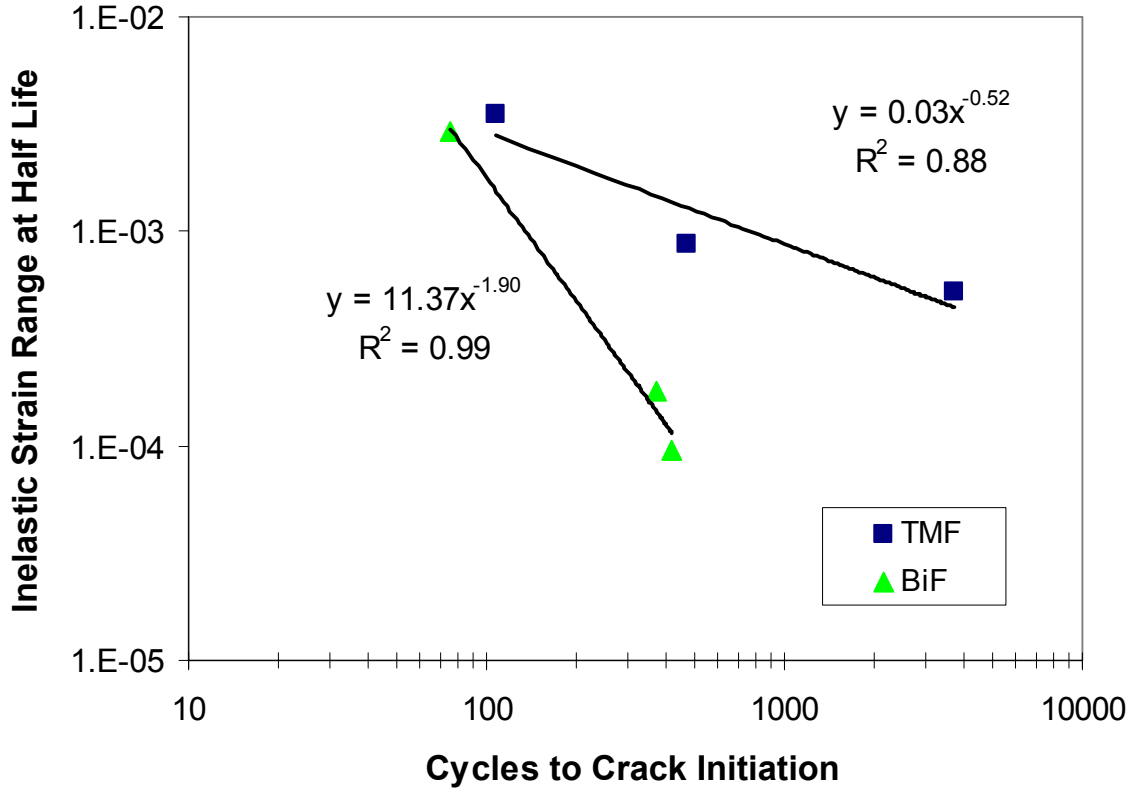

Figure 3-15 Baseline OP TMF and BiF Tests, <001> specimens

3.10.1 Baseline TMF Tests

Plots of select hysteresis loops (cycle 1, and cycle Ni/2) for each of the baseline TMF tests are provided in Figures 3-16 through 3-20 (even). Additionally, a plot depicting the maximum and minimum stress as a function of cycle were created for each fatigue test and are shown in Figures 3-17 through 3-21 (odd).

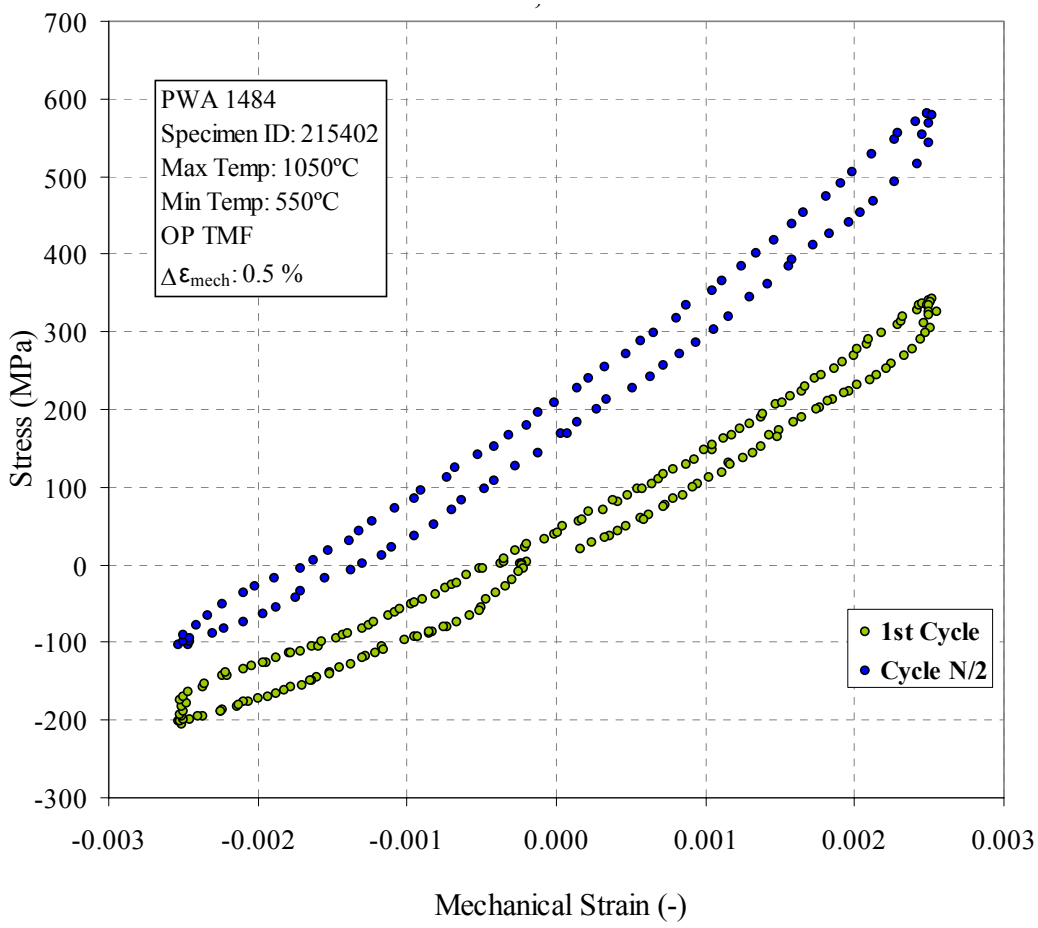

Figure 3-16 $\Delta\varepsilon_{mech}$ = 0.5%, OP TMF Baseline Test Hysteresis Loops- Ni=1810 Cycles

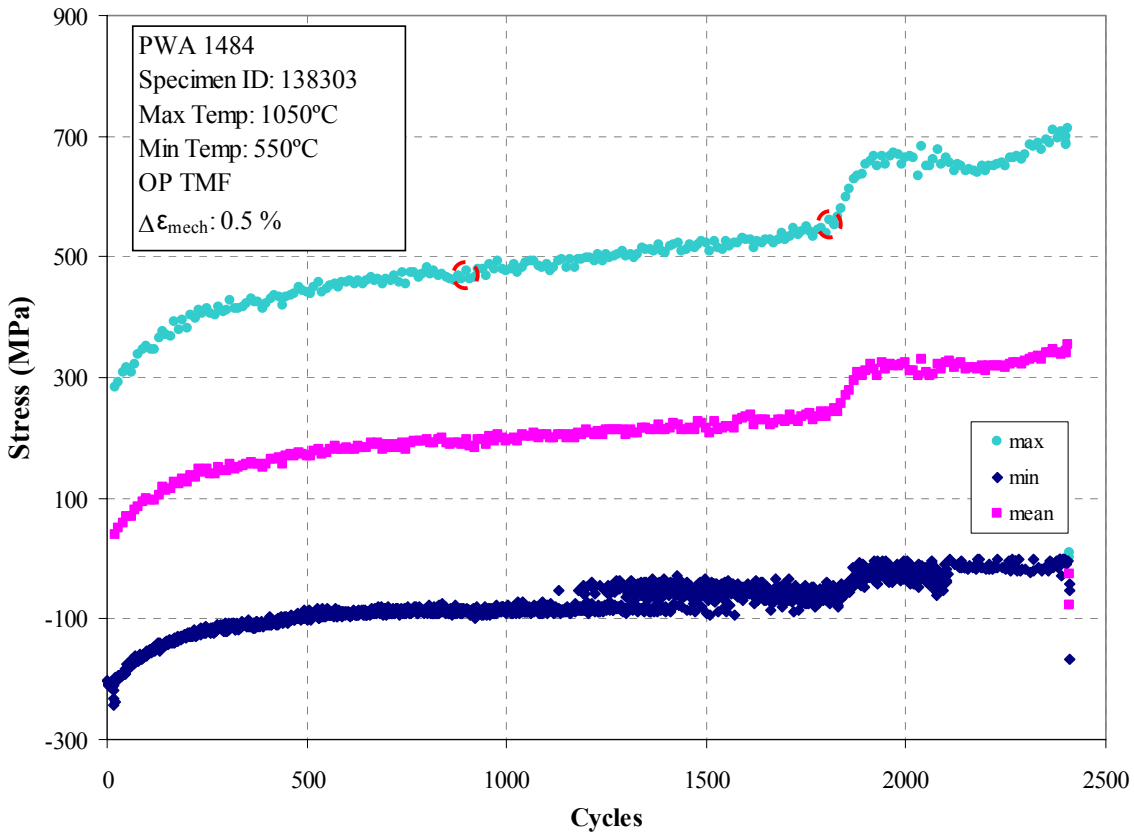

Figure 3-17 Δεmech = 0.5%, OP TMF Baseline Test Stress Evolution- Ni=1810 Cycles

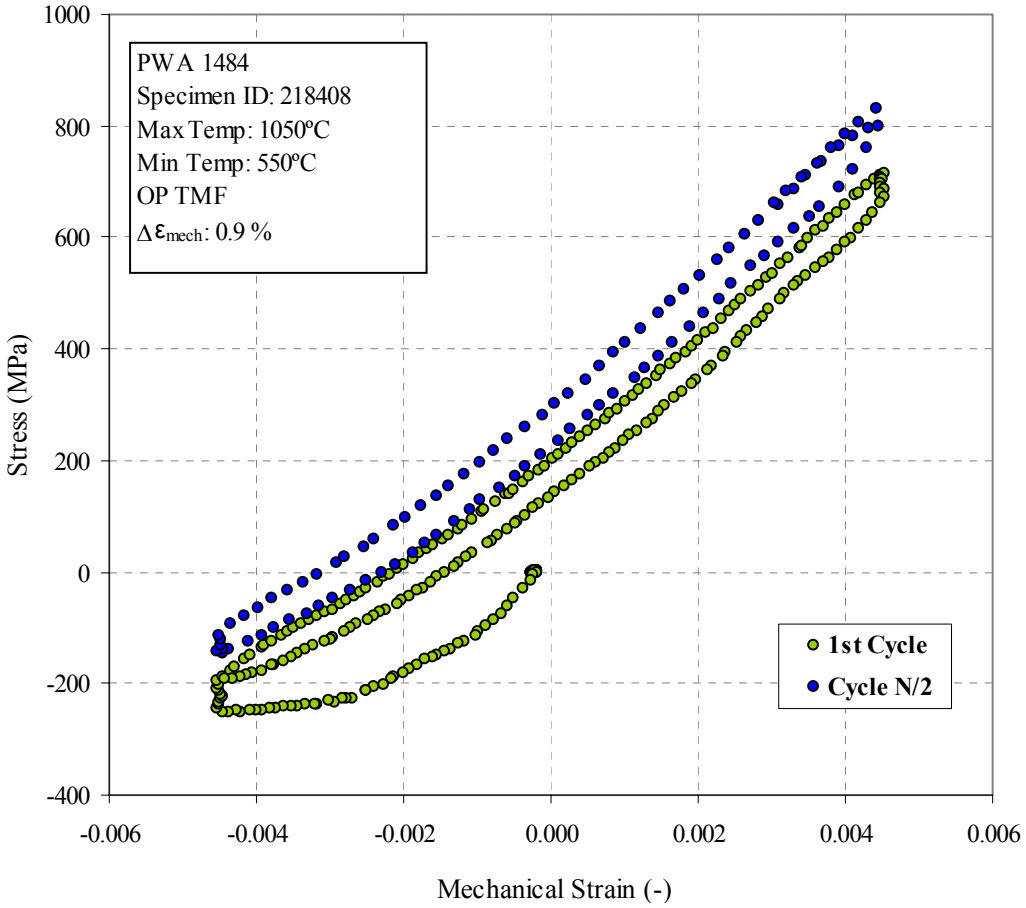

Figure 3-18 Δεmech = 0.9%, OP TMF Baseline Test Hysteresis Loops- Ni=471 Cycles

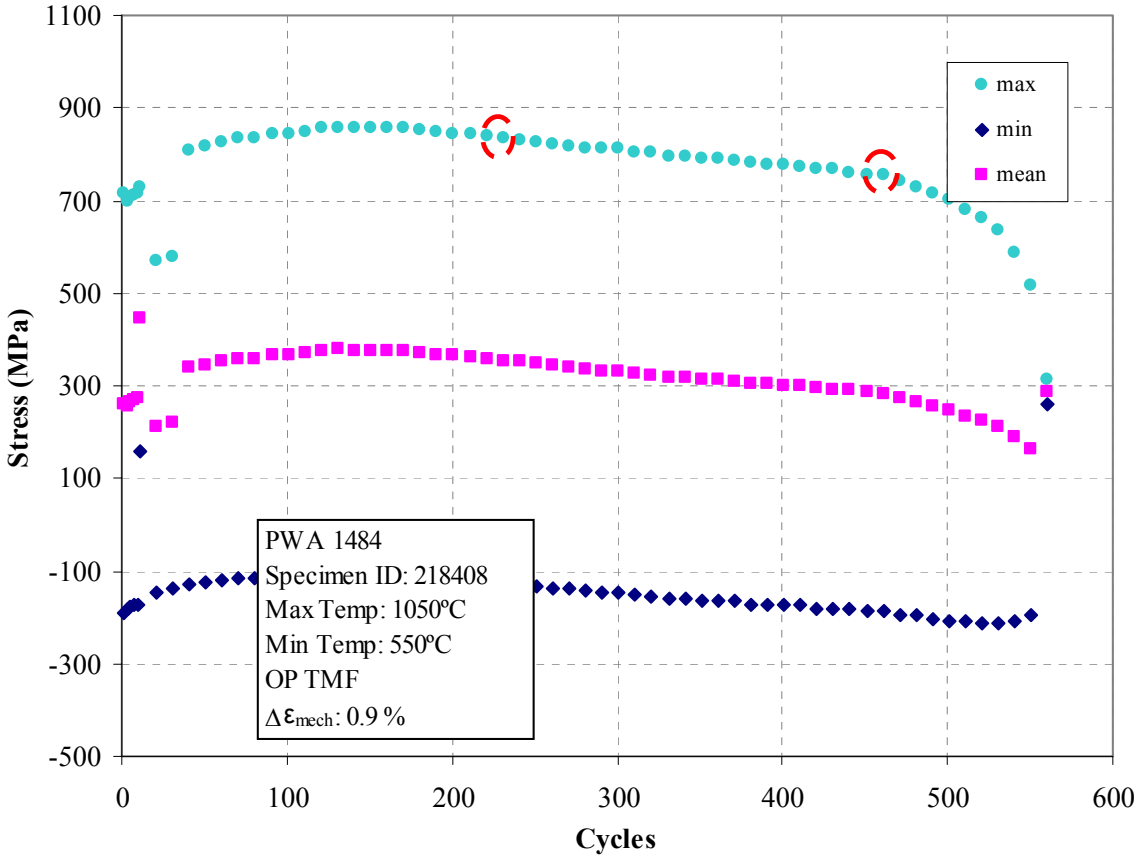

Figure 3-19 Δεmech = 0.9%, OP TMF Baseline Test Stress Evolution- Ni=471 Cycles

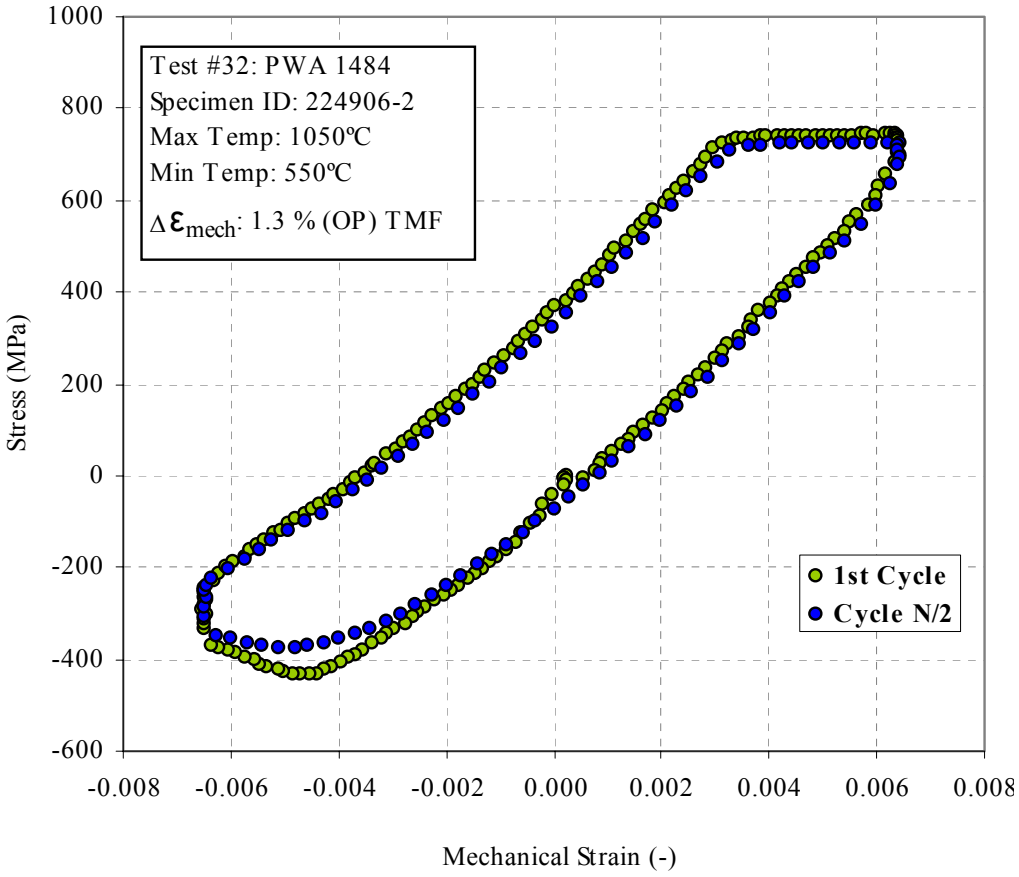

Figure 3-20 Δεmech = 1.3%, OP TMF Baseline Test Hysteresis Loops- Ni=80 Cycles

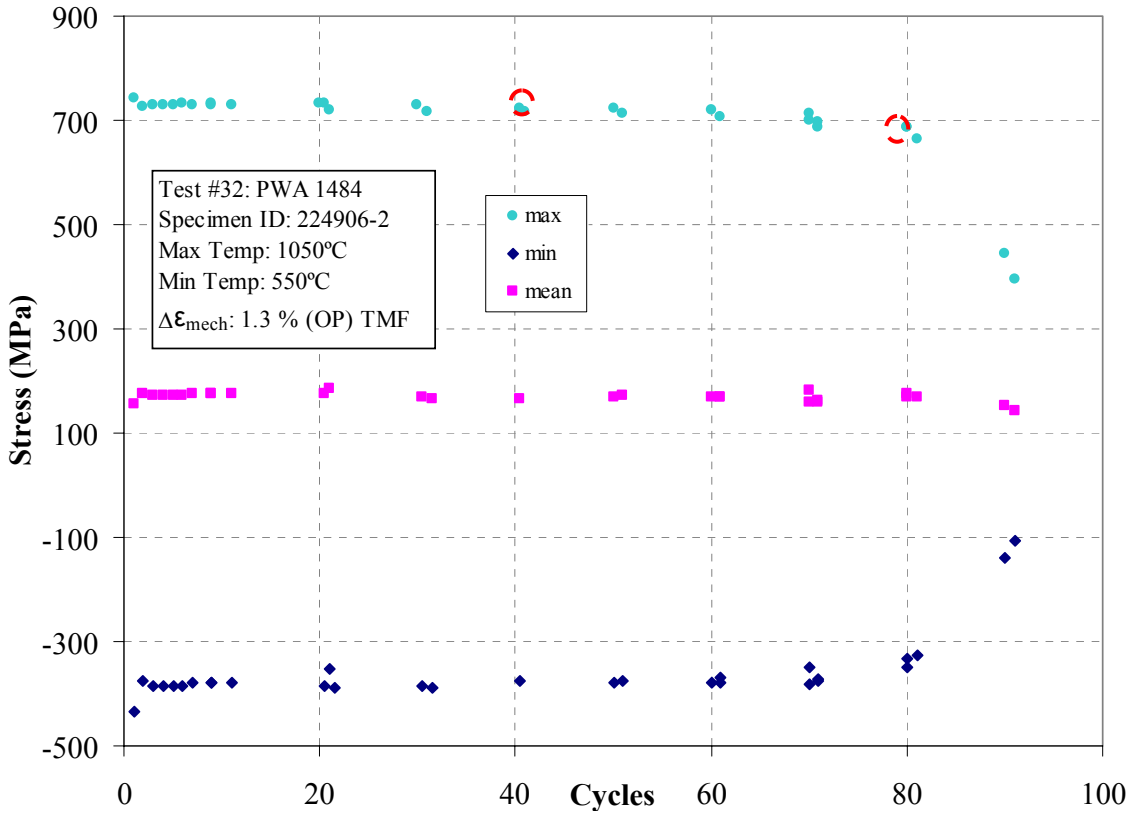

Figure 3-21 Δεmech = 1.3%, OP TMF Baseline Test Stress Evolution- Ni = 80 Cycles

3.10.2 Baseline BiF Tests

Figures 3-22 through 3-26 (even) provide the hysteresis loops, while Figures 3-23 through 3-27 (odd) depict the stress evolution as a function of cycle for the baseline BiF tests.

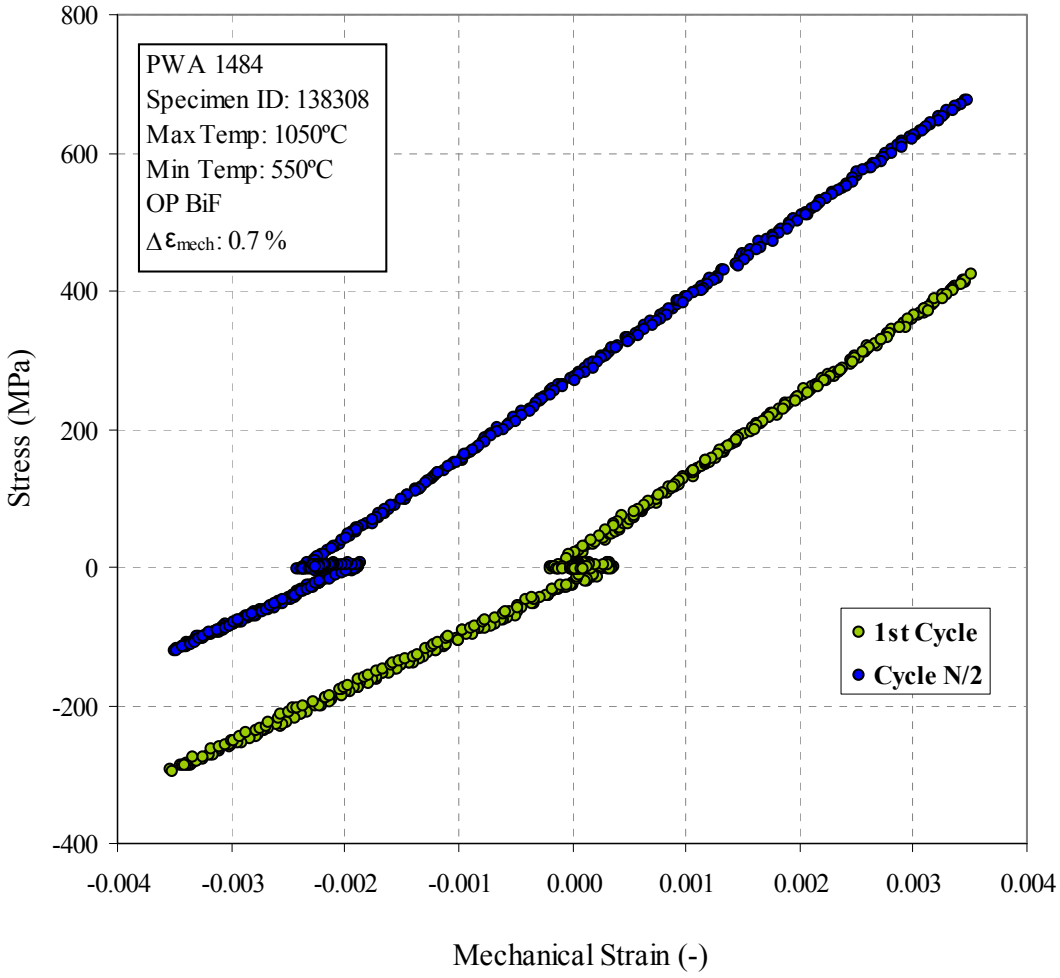

Figure 3-22 Δεmech = 0.7%, OP BiF Baseline Test Hysteresis Loops- Ni=421 Cycles

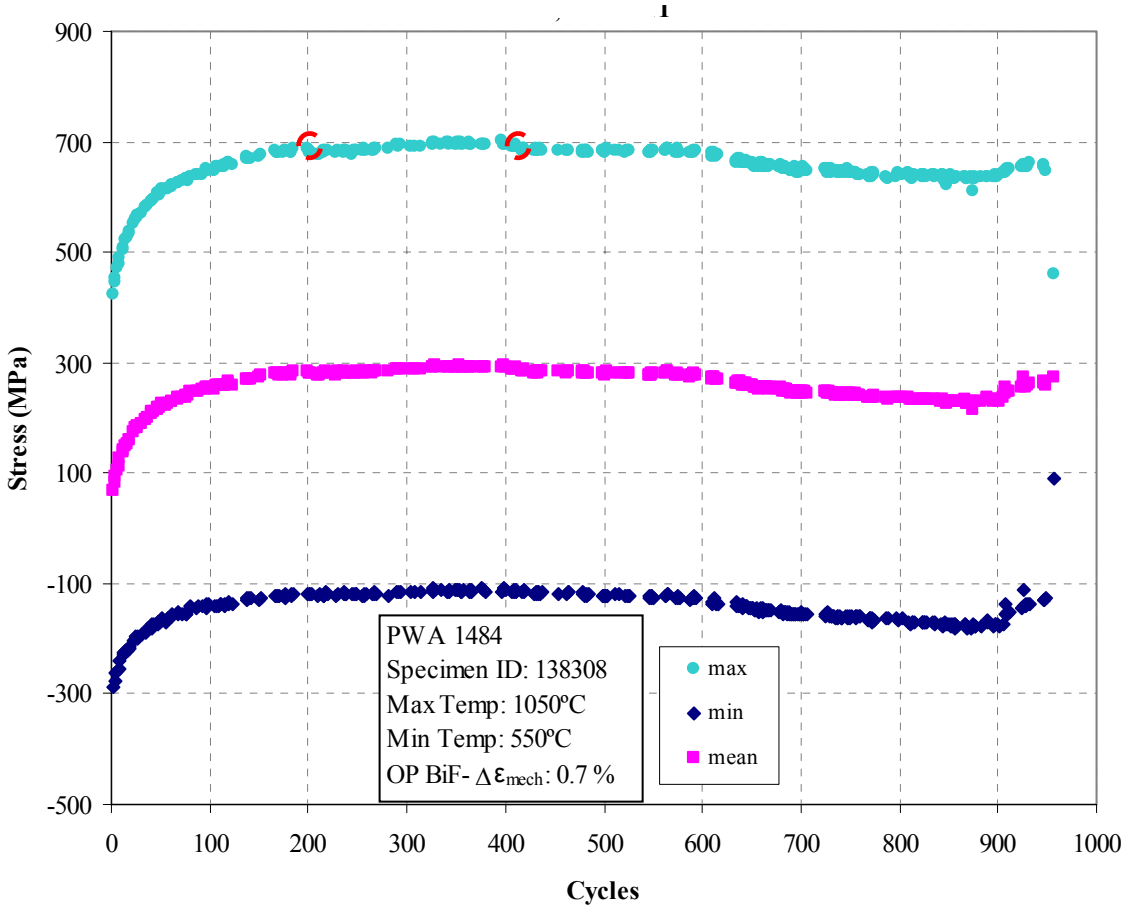

Figure 3-23 Δεmech = 0.7%, OP BiF Baseline Test Stress Evolution- Ni=421 Cycles

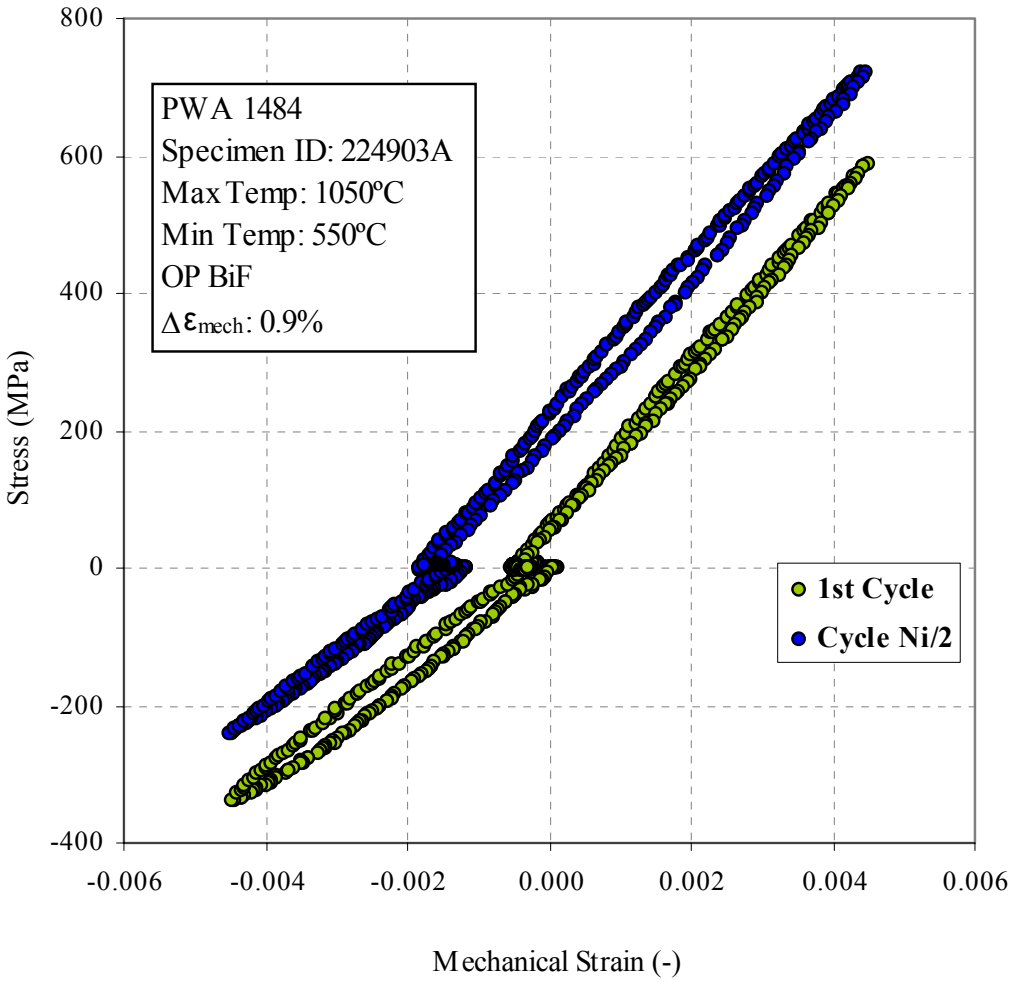

Figure 3-24 Δεmech = 0.9%, OP BiF Baseline Test Hysteresis Loops- Ni=370 Cycles

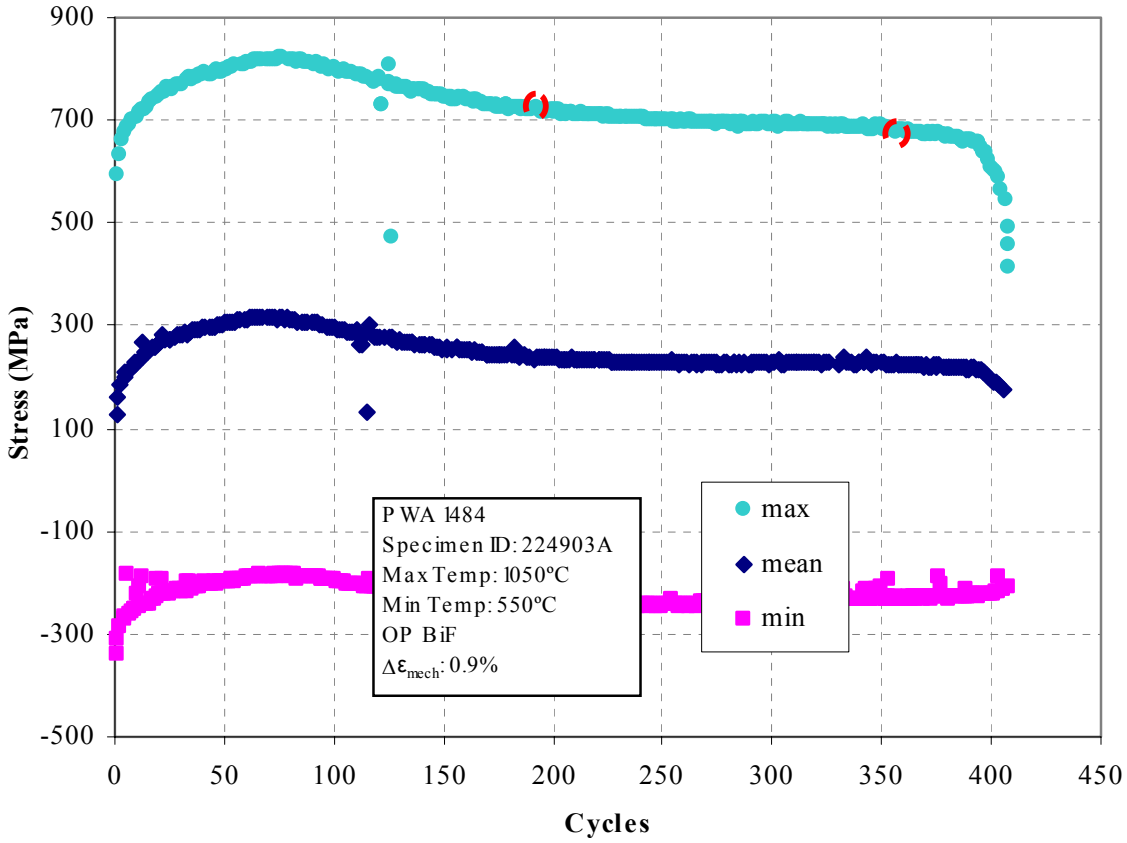

Figure 3-25 Δεmech = 0.9%, OP BiF Baseline Test Stress Evolution- Ni=370 Cycles

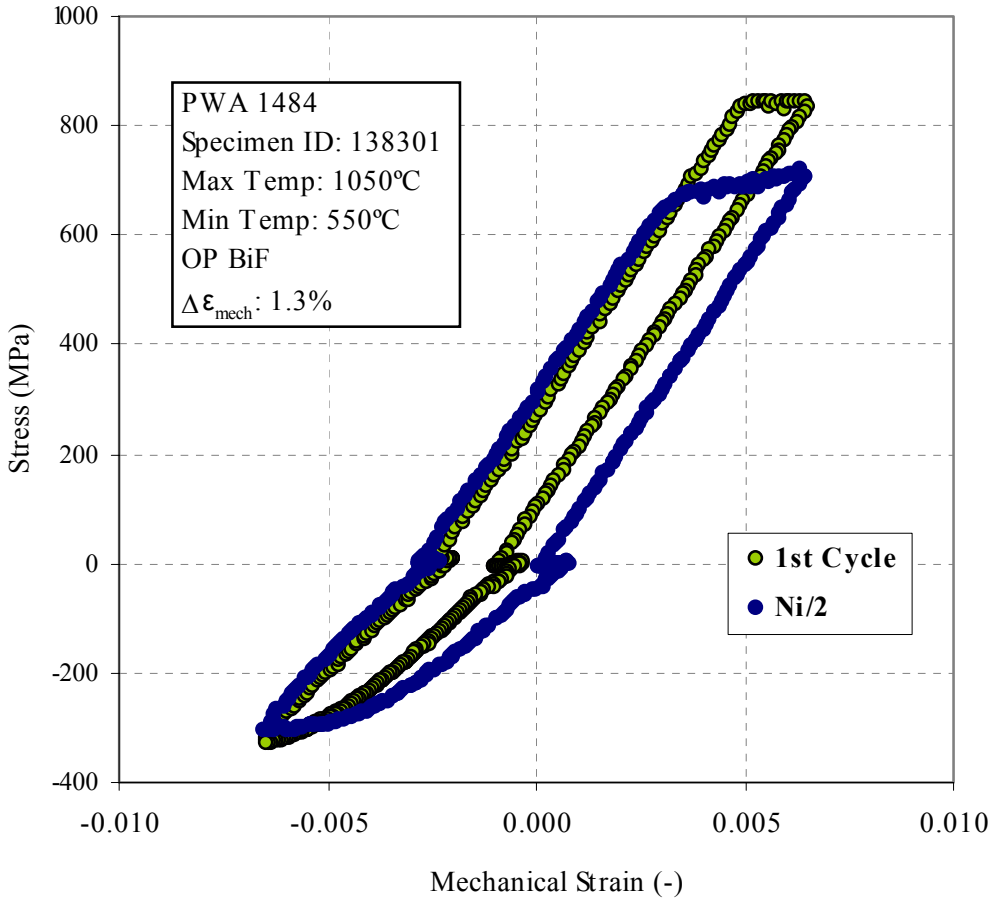

Figure 3-26 Δεmech = 1.3%, OP BiF Baseline Test Hysteresis Loops- Ni=76 Cycles

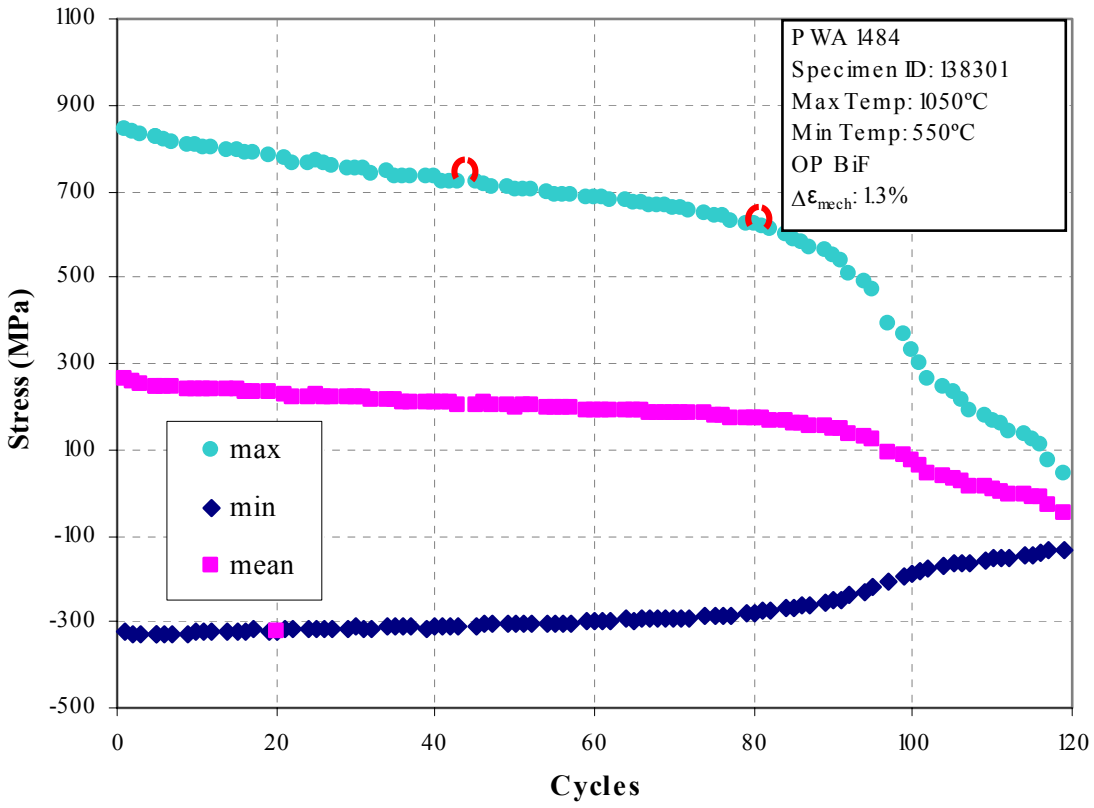

Figure 3-27 Δεmech = 1.3%, OP BiF Baseline Test Stress Evolution- Ni=76 Cycles

3.10.3 TMF versus BiF

Figure 3-11 through 3-15 in Section 3.9 indicate that there may have been some deformation mechanism segregation between the BiF and TMF tests, similar to the results of Gayda et al. [84]. Specifically, it is hypothesized that the BiF specimens experienced more environmentally induced degradation than the TMF specimens, when tested at similar mechanical strain ranges. In order to isolate these dominant damage mechanisms a series of microscopy analysis were conducted, the details of which follow. Furthermore, a relationship is proposed which maps BiF results onto TMF results, and visa versa.

3.10.3.1 Specimen Surface Characterization

Surface images of each of the baseline specimens were recorded using an International Scientific Instruments DS130 scanning electron microscope.

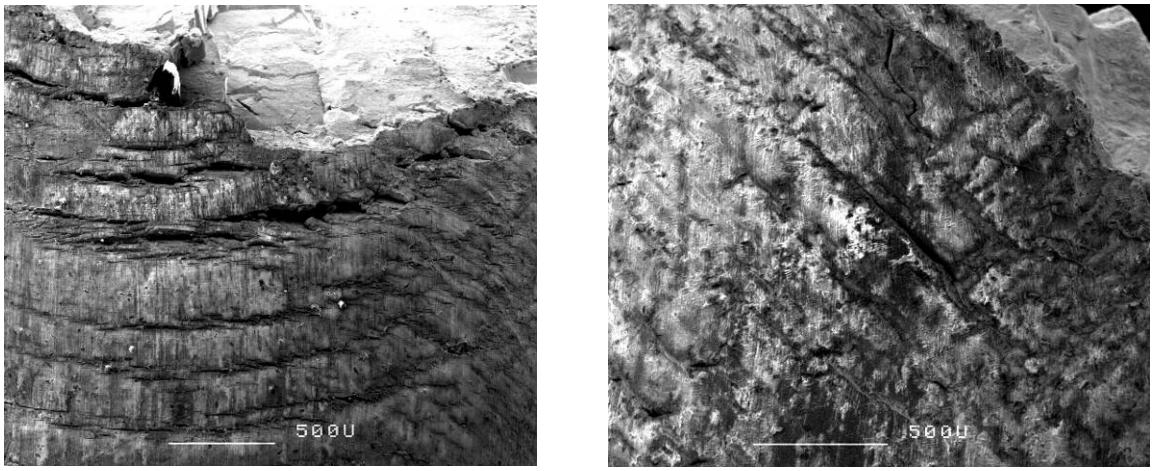

Figure 3-28 Surface Images of specimens tested at Δεmech = 1.3%- OP TMF (left), OP BiF (right)

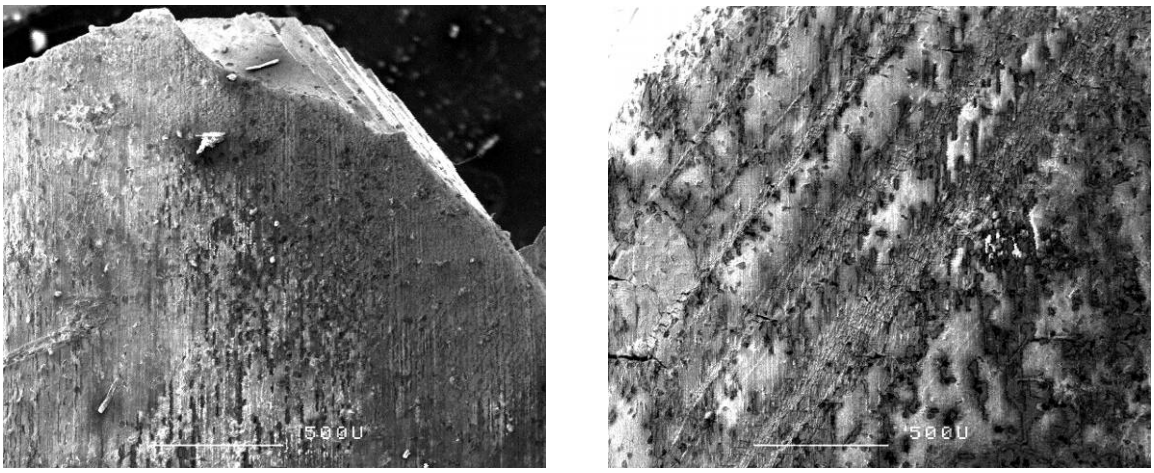

Figure 3-29 Surface Images of specimens tested at Δεmech = 0.9%- OP TMF (left), OP BiF (right)

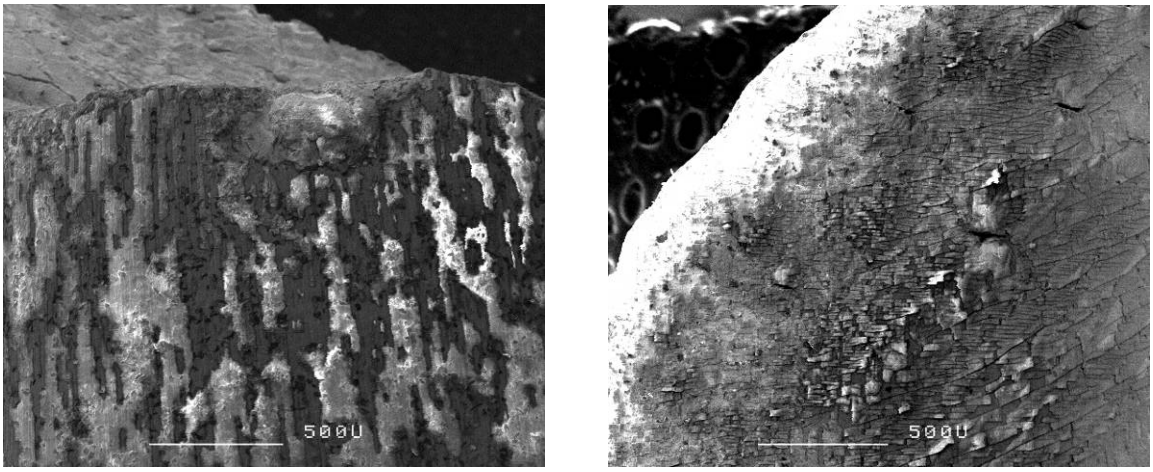

Figure 3-30 Surface Images of specimens tested at Δεmech = 0.5% OP TMF (left), Δεmech = 0.9% OP BiF (right)

The surface SEM images clearly show that the specimens tested in bithermal fatigue experience more environmental degradation than the specimens tested in thermomechanical fatigue, for similar mechanical strains below $\Delta\varepsilon_{mech}$ = 1.3%. Figure 3-28 indicates that the specimens tested at a mechanical strain range of 1.3% experienced similar amounts of environmental damage. All of the baseline TMF and BiF specimens experienced crack initiation at the material surface. However, the 0.7% and 0.9% OP BiF specimens appear to have considerable environmentally assisted crack initiation mechanisms, relative to the other test specimens as shown in Fig 3-29 and 3-30.

Comparing the side images of each baseline test specimens provide a starting point for dominant damage characterization.

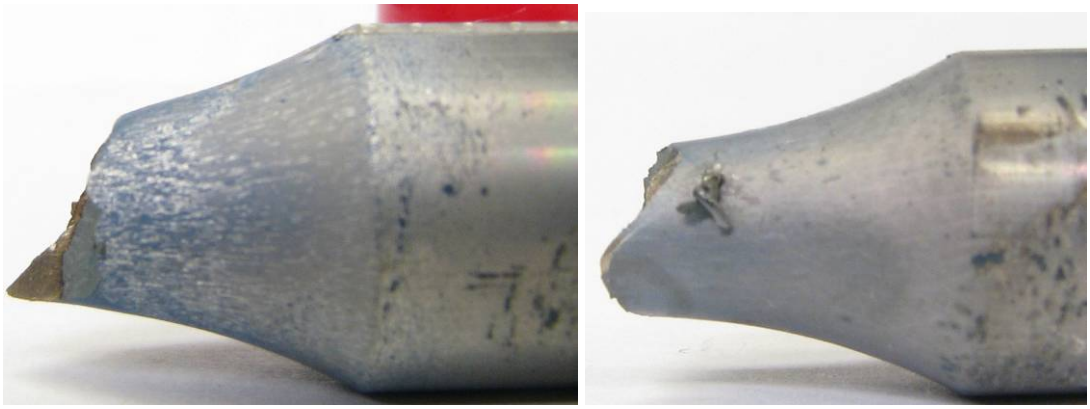

Figure 3-31 0.5% OP TMF (left), 0.9% OP TMF (right)

Figure 3-32 1.3% OP TMF (left), 1.3% OP BiF (right)

Figure 3-33 0.7% OP BiF (left), 0.9% OP BiF (right)

When comparing the tested specimens one immediately notices that the 0.5% and 0.9% OP TMF specimens exhibit similar surface deformation, as shown in Fig 3-30. Specifically both specimens exhibit no necking and minimal specimen surface plasticity. Conversely the 1.3% OP BiF and TMF specimens experienced considerable combined necking and bulging. Furthermore these specimens exhibit similar amounts surface plasticity, as characterized by the slip steps apparent in Fig 3-32. Whereas the 0.5% and 0.9% OP TMF specimens exhibit minimal environmental damage (Fig 3-30), the 0.7% and 0.9% OP BiF specimens exhibit considerable amounts of surface plasticity, oxidation and minimal bulging/necking, if any (Fig 3-33).

Microscopy of the baseline BiF and TMF specimens sectioned collinear to the loading axis are provided in Fig's 3-34 through 3-36.

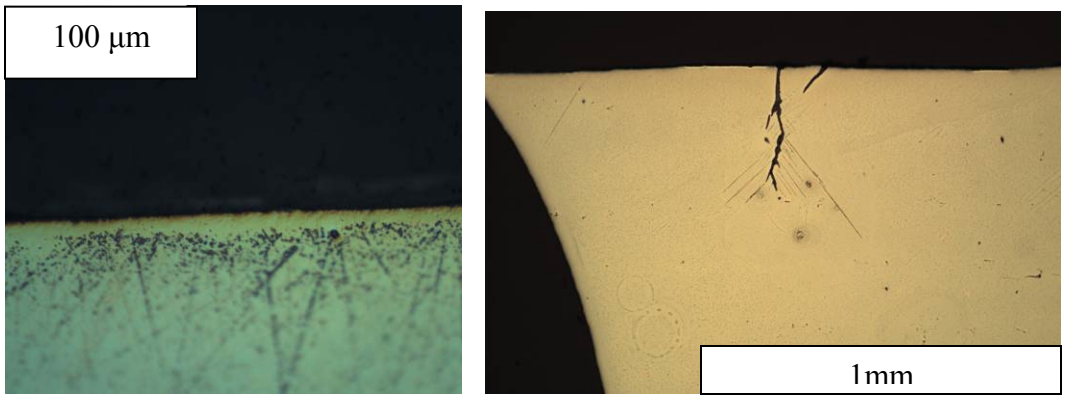

(a) **(b)**

Figure 3-34 Specimen Cross-Sections Near Free Surface: 0.5% OP TMF (a), 0.9% OP TMF (b)- loading direction horizontal

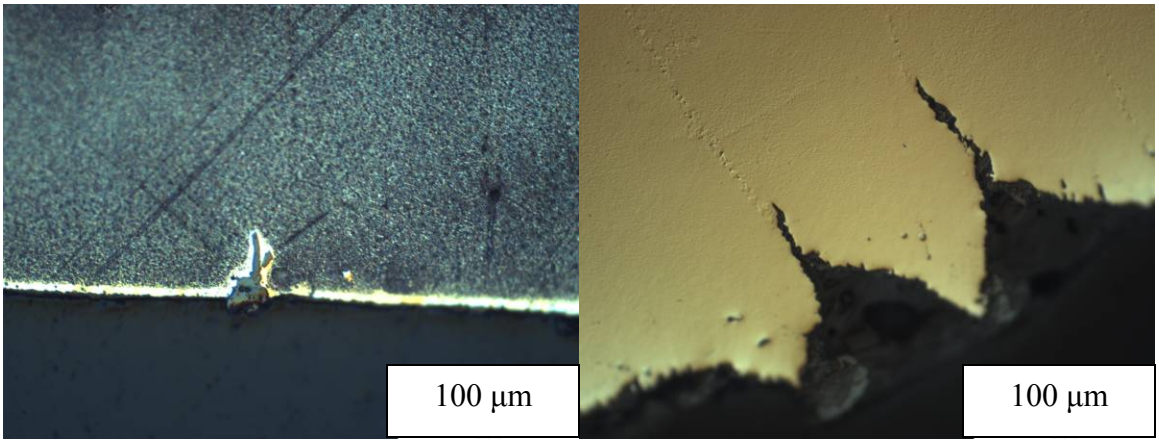

(a) **(b)**

Figure 3-35 Specimen Cross-Sections Near Free Surface: 1.3% OP TMF (a), 1.3% OP BiF (b)- loading direction horizontal

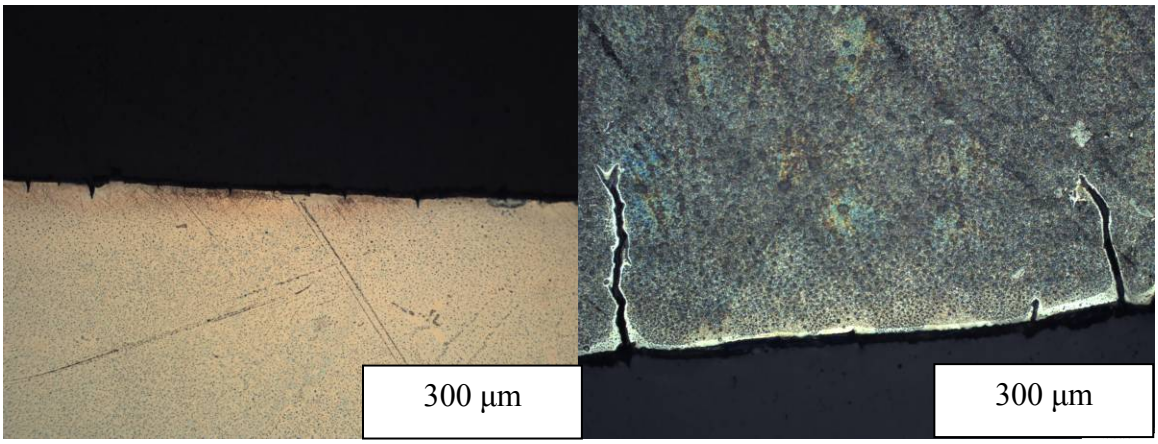

(a) **(b)**

Figure 3-36 Specimen Cross-Sections Near Free Surface: 0.7% OP BiF (a), 0.9% OP BiF (b)- loading direction horizontal

The 0.5% and 0.7% mechanical strain range OP TMF specimens (Figure 3-34 (a) and (b) respectively) exhibit minimal non-terminal cracking and very little oxide growth. The 1.3% OP TMF (Figure 3-35 (a)) and the 1.3% OP BiF (Figure 3-35 (a)) specimens both experienced considerable oxidation. The figures indicate that the oxide spikes occur where secondary dendrite arms intersect the free surface. Furthermore the TMF

specimen exhibited minimal surface cracking while the BiF specimen had considerable cracking in the deformed gage section. The 0.7% and 0.9% mechanical strain range specimens (Figure 3-36 (a) and (b) respectively) exhibit considerable non-terminal surface cracking. All non-terminal cracks in these specimens are oxidized and accompanied by a γ' depleted zone around the crack.

The general conclusions drawn from the transverse section pictures include:

- OP TMF specimens (0.5%, 0.7% and 1.3% mechanical strain range) exhibit minimal non-terminal surface cracks in and around the gage section, implying that the fatigue damage mechanism dominated life of these specimens.
- OP BiF specimens (0.7%, 0.9% and 1.3% mechanical strain range) all exhibit a considerable number of non-terminal surface cracks. All surface cracks are oxidized and have a sub-surface γ' depleted region surrounding the crack.

Beyond relative amounts of environmental damage, the transverse sections of the baseline test specimens also revealed that:

- Short circuit diffusion of oxygen occurs along slip planes as shown in Figure 3-37.
- Fracture surfaces are comprised of crystallographic facets, as seen in Figures 3-37 and 3-38
- Slip bands impinging upon an oxide spike create a crack, as shown in Figures 3-39 and 3-40.

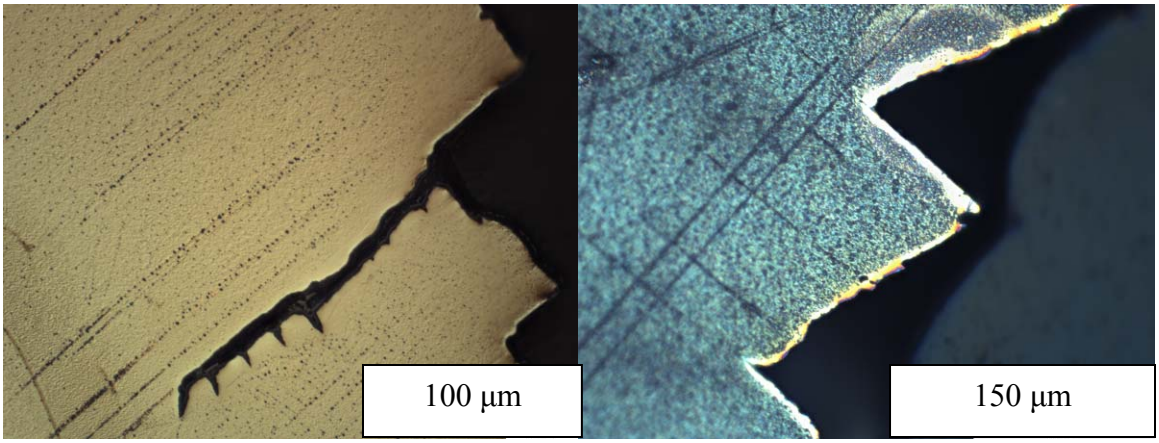

(a) **(b)**

Figure 3-37 Specimen Cross-Sections at Fracture Surfaces: 0.9% OP TMF (a), 1.3% OP TMF (b)- loading direction horizontal

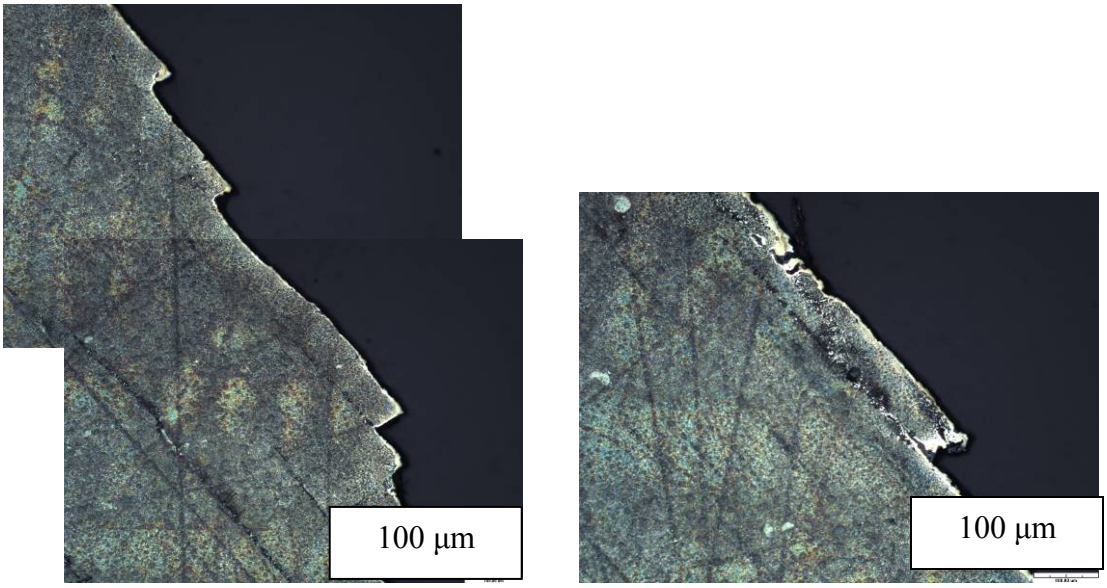

Figure 3-38 Specimen Cross-Sections at Fracture Surfaces: 0.9% OP BiF- loading direction horizontal

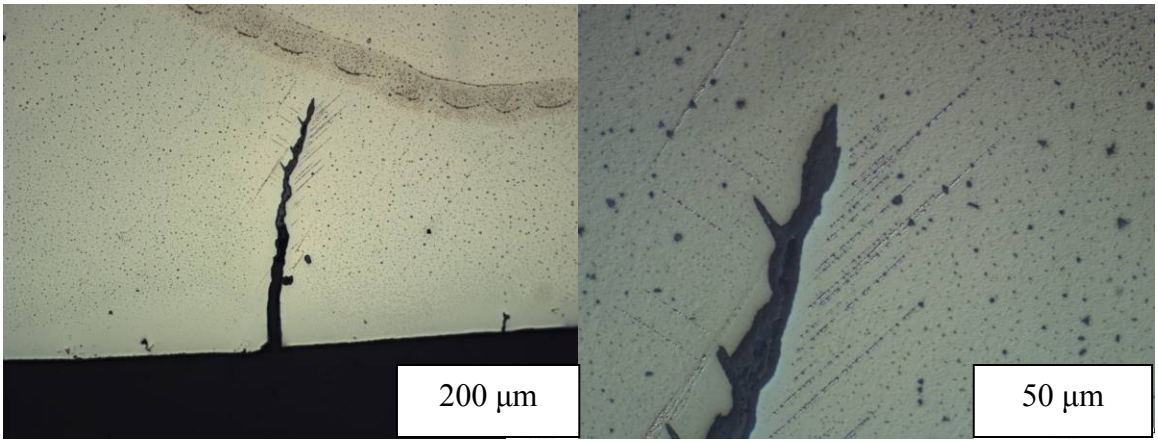

Figure 3-39 Specimen Cross-Sections Near Surface: 0.9% OP TMF- loading direction horizontal

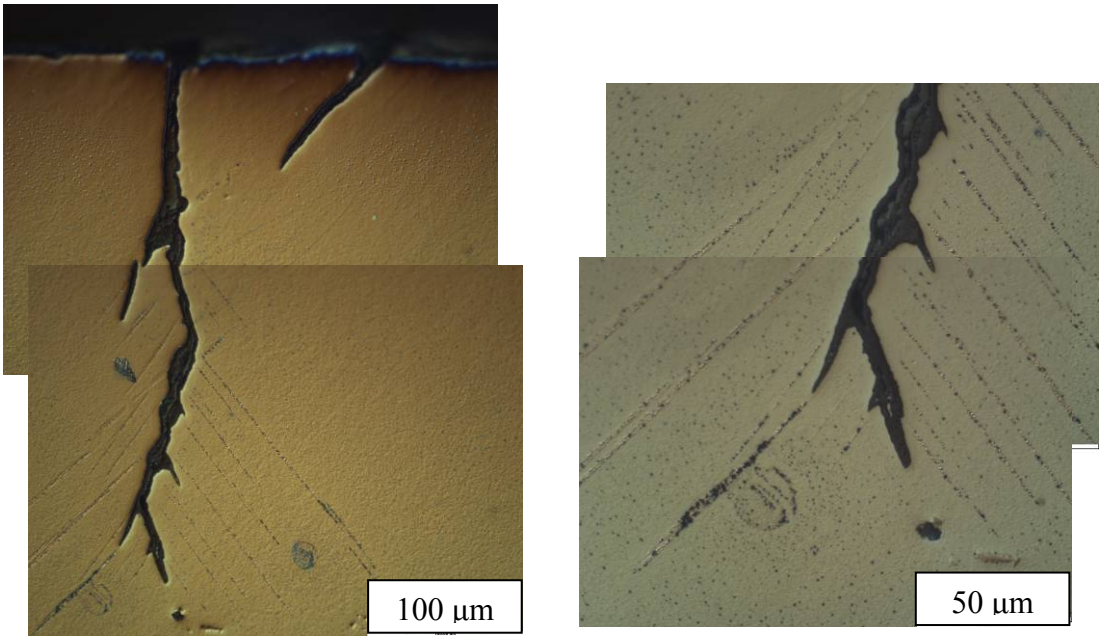

Figure 3-40 Specimen Cross-sections Near Free Surface: 0.9% OP TMF- loading direction horizontal

Furthermore, the viscoplastic ratcheting mechanisms effect upon the dendritic microstructure was captured by stitching all of the cross-section pictures of the 1.3% mechanical strain range OP BiF test having 5 min high temperature holds, shown in Fig 3-41.

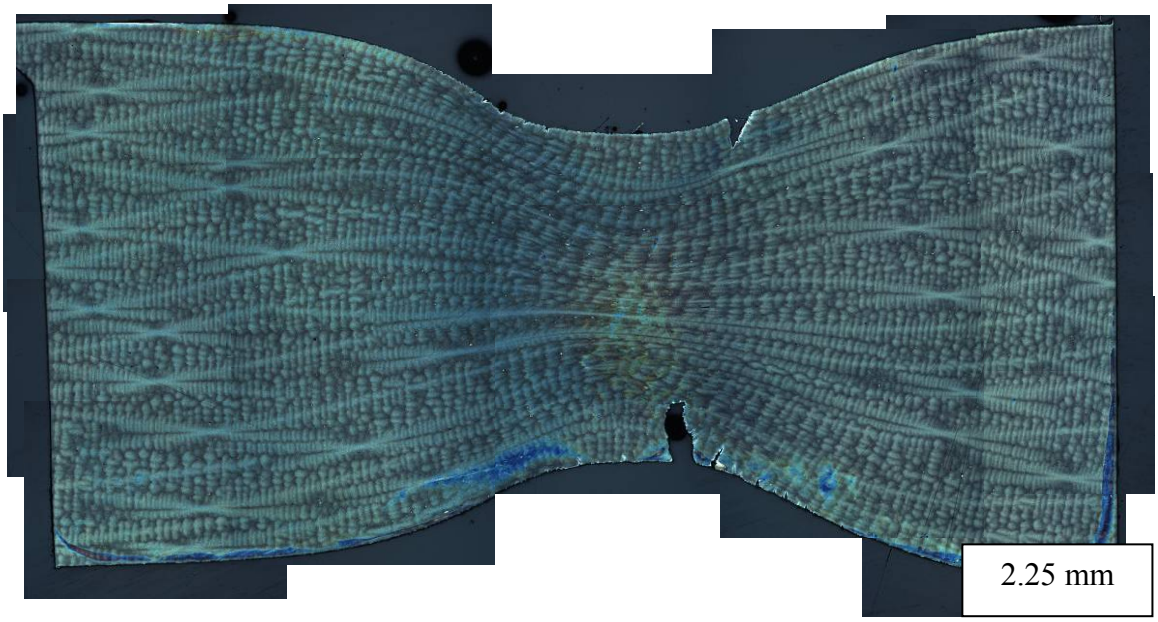

Figure 3-41 Specimen Cross-Section: <001> Orientation, 1.3% OP TMF 5 min High Temperature Hold- loading direction horizontal

The considerable necking experienced by the strain-controlled test specimen shown in Figure 3-41 has resulted in effectively creating a "notched" specimen with a reduced gage section of approximately 0.3" (7.62 mm) yielding an approximate 60% reduction in area. Additionally, the considerable amount of surface cracking experienced by this specimen indicates crack branching on crystallographic planes, as shown in Figure 3-42.

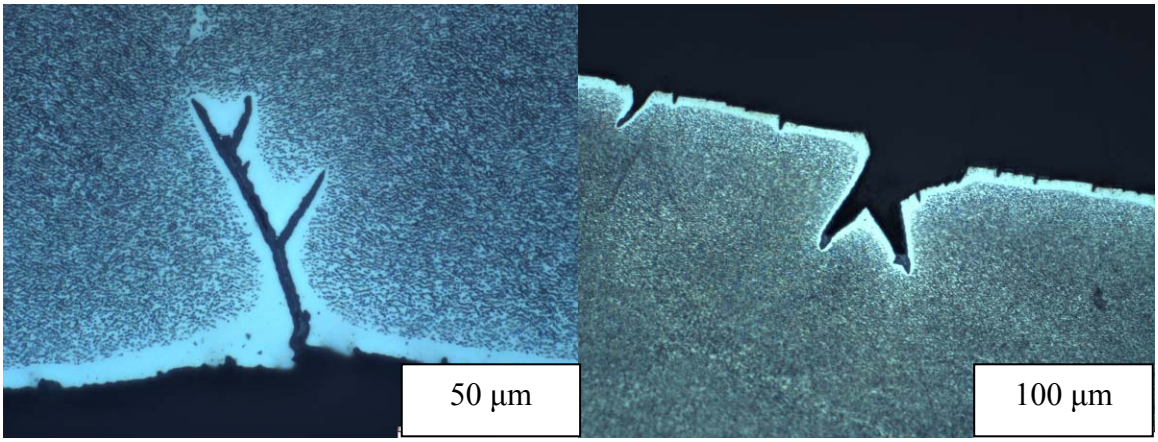

Figure 3-42 Specimen Cross-Sections Near Free Surface: <001> Orientation, 1.3% OP TMF 5 min High Temperature Hold- loading direction horizontal

3.10.3.2 γ' depletion characterization

Microscopy was performed on the three Bithermal and three thermomechanical fatigue baseline test specimens in order to determine the relative amount of thermally assisted base-material degradation via γ'-depletion. Specifically, baseline specimens were first sectioned, then mounted and polished as detailed in Chapter 4. Then images of the γ' depleted region were recorded using an Olympus BX40 optical microscope fitted with an Olympus digital camera at 500X and 1000X zoom, at four locations per specimen. Representative images are shown in Figures 3-43 and 3-44.

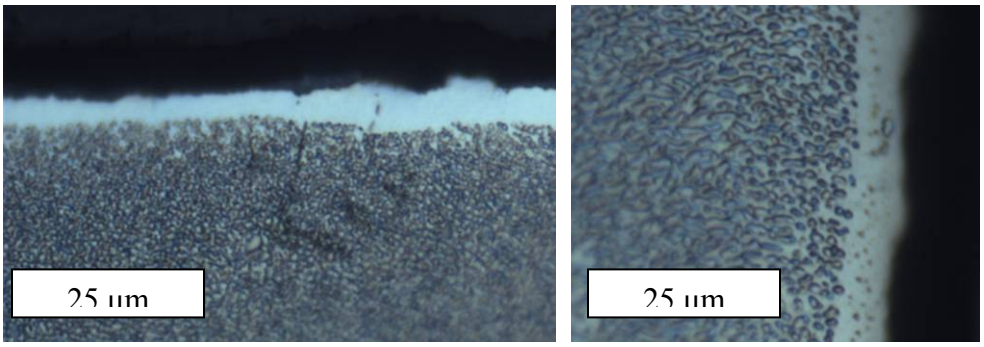

(a) **(b)**

Figure 3-43 Fatigue Specimen γ' Depletion (a) Specimen 138301, (b) Specimen 138303

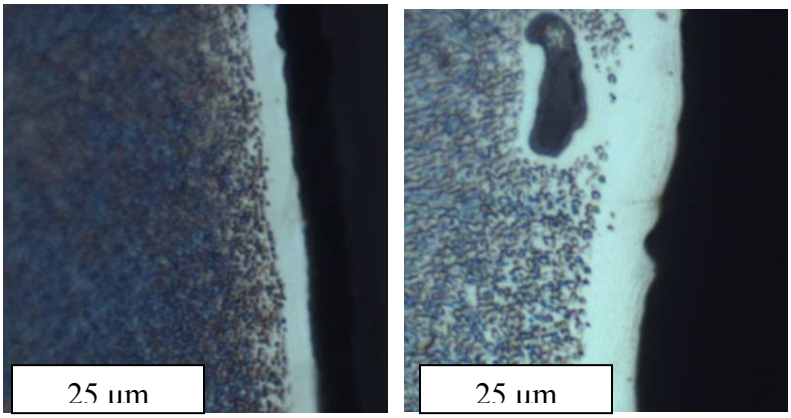

(a) **(b)**

Figure 3-44 Fatigue Specimen γ' Depletion (a) Specimen 138312, (b) Specimen 224903A

Finally, a minimum of nine measurements were averaged per specimen to determine γ' depletion depth, as shown versus cycles to failure in Fig 3-45.

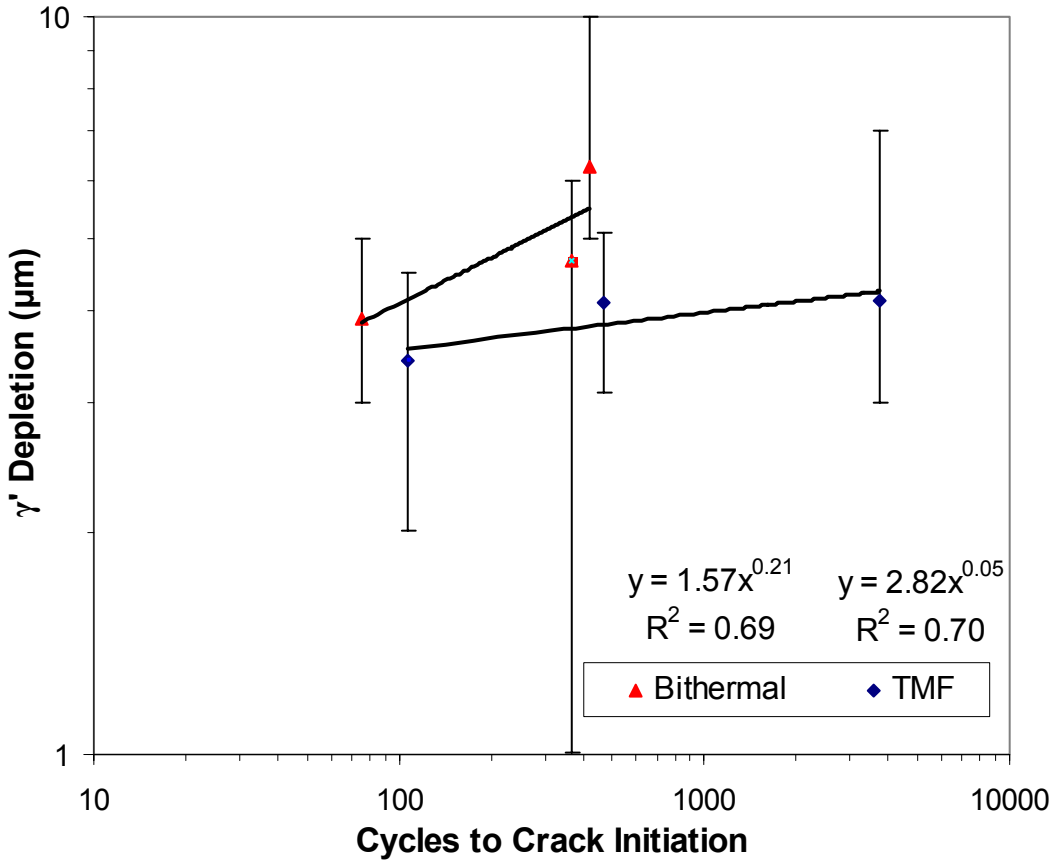

Figure 3-45 γ' Depletion versus cycles to crack initiation

Specimens tested in BiF conditions experienced more γ' depletion than those tested in TMF. This should not be all that surprising given that the effective temperature of the BiF waveform is 49° C higher than that of the TMF waveform.

3.10.3.3 Dominant damage mechanisms- conclusion

Microscopy of the six baseline TMF and BiF specimens indicate the following:

1. The 1.3% OP TMF and BiF specimens experienced a similar dominant damage mechanism characterized by fatigue accompanied by viscoplastic ratcheting.

2. The 0.5% and 0.7% OP TMF specimens both exhibited fatigue as the dominant damage mechanism. These specimens exhibit slightly more environmental damage than do the 1.3% tested specimens
3. The 0.7% and 0.9% OP BiF specimens experienced considerable environmentally assisted fatigue. As such the dominant damage mechanism for these tests was fatigue-environment interaction.

3.10.3.4 TMF vs. BiF- mathematical relationships

It is desired to determine an equation which relates the inelastic strain range of a TMF test to the inelastic strain range of a BiF test. When looking at the short test results (high strain range) of both the TMF and BiF cycles types shown in Figure 14, coupled with the 1.3% baseline TMF and BiF microscopy results, one concludes that the waveforms produce similar dominant damage mechanisms. However, at lower strain ranges the different test waveforms yield different dominant damage mechanisms, with the BiF waveform being more affected by environmental-fatigue interactions. A mathematical relationship collapsing the data must take these environmental interactions into account, presumably through an Arrhenius term. To that end the log of the inelastic strain range trend equation for the BiF tests (Fig 3-15) was plotted versus the inelastic strain range trend equation for TMF tests (Fig 3-15), and is shown in Fig. 3-46. The log trend line fit to this data provides the relationship between these two test parameters, Equation 3-3.

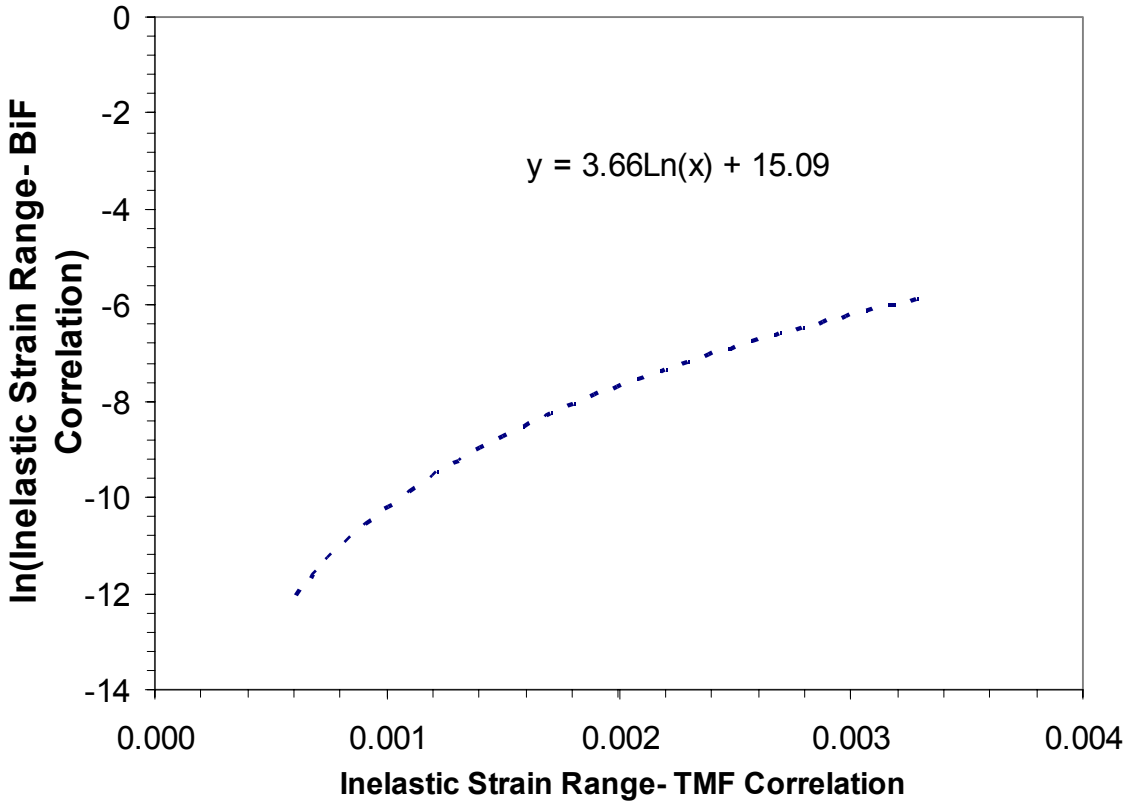

Figure 3-46 Calculated BiF Inelastic Strain Range versus Caluclated TMF Inelastic Strain Range

$$\Delta\varepsilon_{in}^{BiF} = \left(\Delta\varepsilon_{in}^{TMF}\right)^{3.664}\exp(15.090) \qquad \text{for } \Delta\varepsilon_{in}<\sim 0.0029 \qquad \textbf{(3-3)}$$

$$\Delta\varepsilon_{in}^{BiF} = \Delta\varepsilon_{in}^{TMF} \qquad \text{for } \Delta\varepsilon_{in}>\sim 0.0029$$

Assuming a thermally activated process which follows an Arrhenius relationship, the following would hold.

$$15.090 = \frac{Q}{RT} \qquad \textbf{(3-4)}$$

EQ 3-4 is the assumed Arrhenius exponential for the bithermal tests. The nature of BiF tests exposes the material to high temperature (1050˚ C) for 90 seconds, or a quarter of the overall cycle time. Using an effective temperature of 1001.7˚ C, the activation energy (Q) for this phenomena would be Q = 159.95 kJ/mol. Kupkovits [67] and Sehitoglu [70] found that the activation energies for oxidation (Qox) and gamma-prime depletion (Qγ')

in other Ni-base superalloys were very close. Kupkovits calculated values of 89.7 kJ/mol and 86.0 kJ/mol for Qox and Qγ' respectively for CM247LC DS; while Sehitoglu and Boismier found 175.9 kJ/mol and 163.3 kJ/mol for Qox and Qγ' respectively for MAR M247. Antolovich et. al [96] found a Qox value of 40.2 kJ/mol for Rene 80, another Ni-base superalloy. These studies indicating that the value of the effective activation energy calculated here is reasonable.

In order to validate the hypothesis that the primary difference between the Bithermal fatigue tests and thermomechanical fatigue tests is the existence of a thermally activated process in the BiF test that isn't as dominant in the TMF test, one need only to compare the differences in lives at a given inelastic strain range (Fig. 3-15) and the difference in lives at a given amount of base material degradation (Fig. 3-45), for each of the two test types. The hypothesis would be supported if the two completely different damage drivers provide similar life relationships.

Figure 3-47 shows the relationship between the trend in BiF lives versus the trend in TMF lives for a given inelastic strain range (trends shown in Fig 16), determined by

$$Ni^{BiF} = Ni^{TMF\,(0.3073)} \exp(2.88) \quad \textbf{(3-5)}$$

and the relationship between the trend in BiF lives versus the trend TMF lives for a given amount of γ' depletion (trends shown in Fig 37) described by

$$Ni^{BiF} = Ni^{TMF\,(0.2375)} \exp(3.17) \quad \textbf{(3-6)}$$

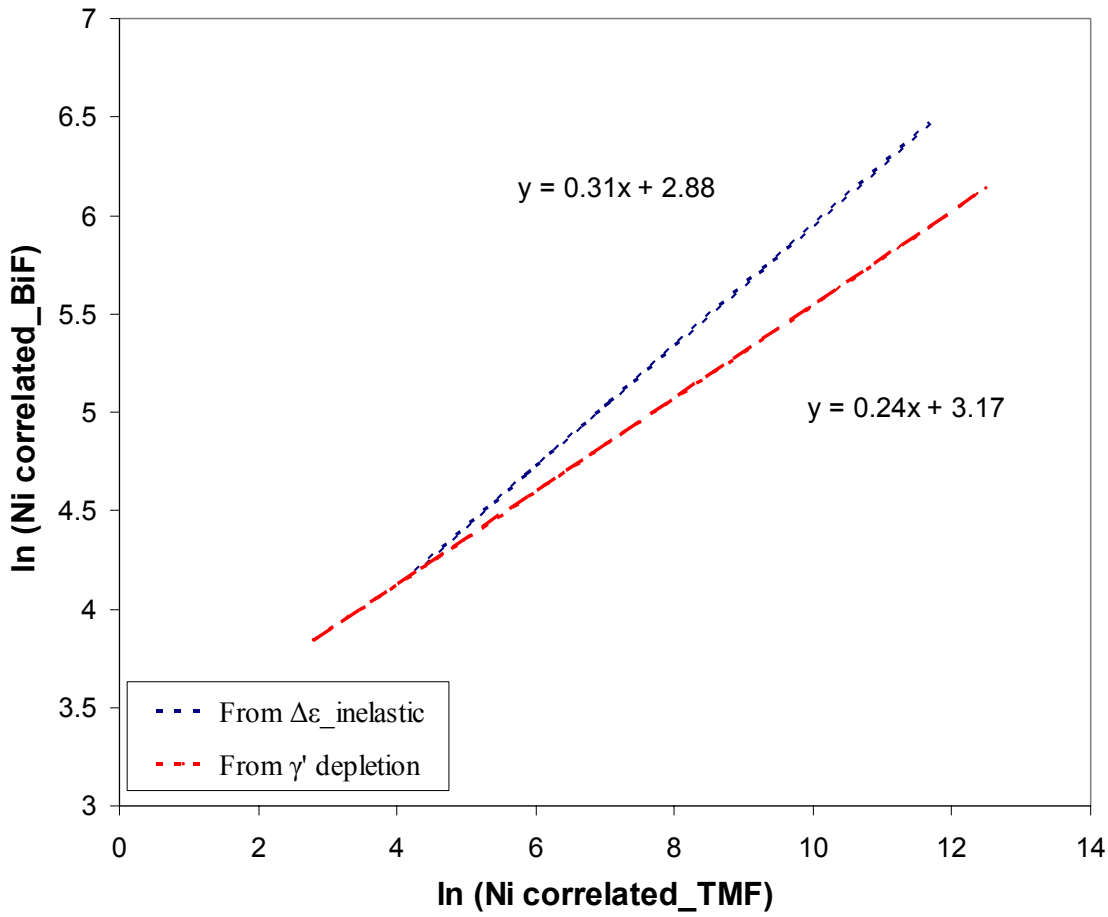

Figure 3-47 Life Prediction Relationships for a Given Inelastic Strain Range

Equations 3-5 and 3-6 are sufficiently similar to conclude that there exists a dominant environmentally assisted damage mechanism in the Bithermal fatigue tests that is not as pronounced in the TMF test. The relationships shown in Equation 3-5 and 3-6, coupled with the relationship in Equation 3-3, along with the associated value of activation energy, leads one to conclude that the differences between the results for the two test types can be attributed primarily to this environmental damage mechanism.

The determination of Equation 3-3 allows one determine an "effective" inelastic strain range, $\Delta\varepsilon^{in}$(eff-BiF), for the BiF tests that would correspond to the inelastic strain range of the TMF tests having similar lives. As such one could then either use the

effective inelastic strain range for a Bithermal test, $\Delta\varepsilon^{in}$(eff-BiF), or the inelastic strain range from the TMF test, $\Delta\varepsilon^{in}$(TMF), to determine life. Furthermore, BiF tests could then be performed in place of TMF tests, and visa versa.

3.11 Orientation Effects

Single crystal PWA 1484 specimens having three different primary crystallographic loading directions were tested. Specifically specimens having nominal <001>, <111> and <123> orientations were tested in OP TMF with a minimum temperature of 550° C and a maximum temperature of 1050° C. The influence of orientation is summarized in Figures 3-48 through 3-50.

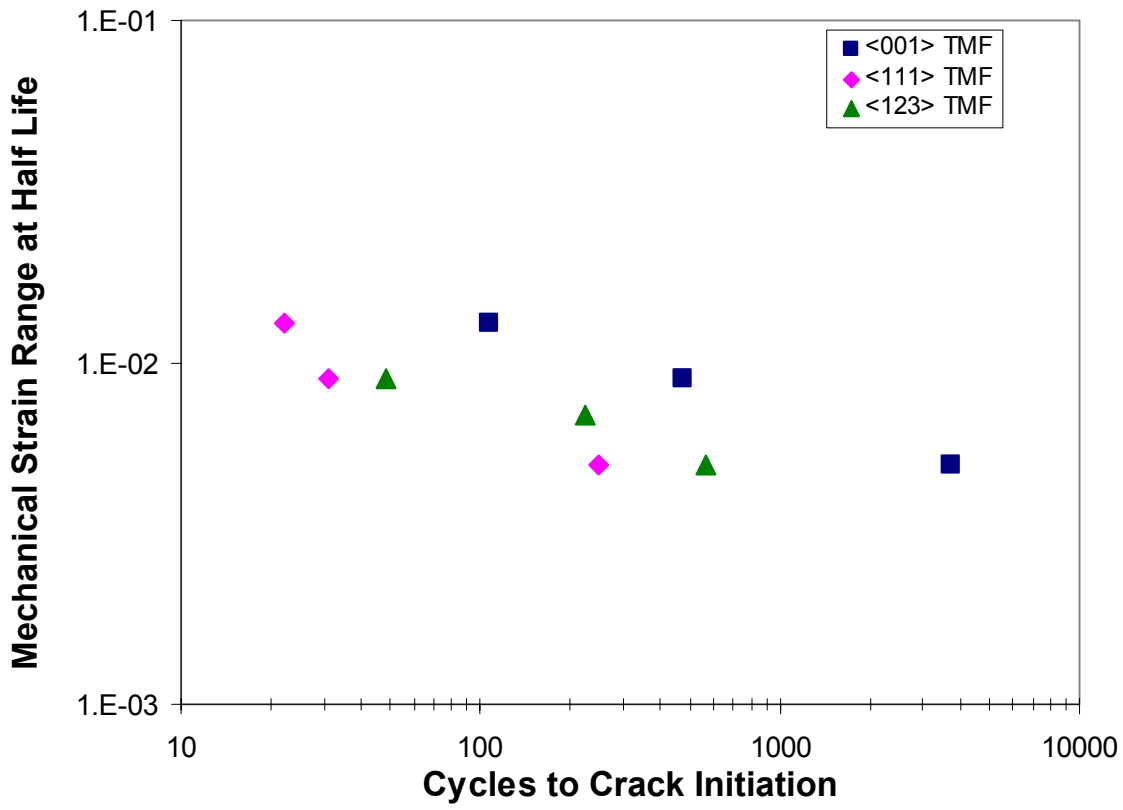

Figure 3-48 Fatigue Test Results (TMF) as a Function of Primary Crystallographic Orientation-Mechanical Strain Range

On a mechanical strain range basis, the <001> orientation has the longest OP TMF lives while the <111> orientation has the shortest lives. Furthermore the <001> orientation has TMF lives nearly an order of magnitude longer <111> oriented specimens.

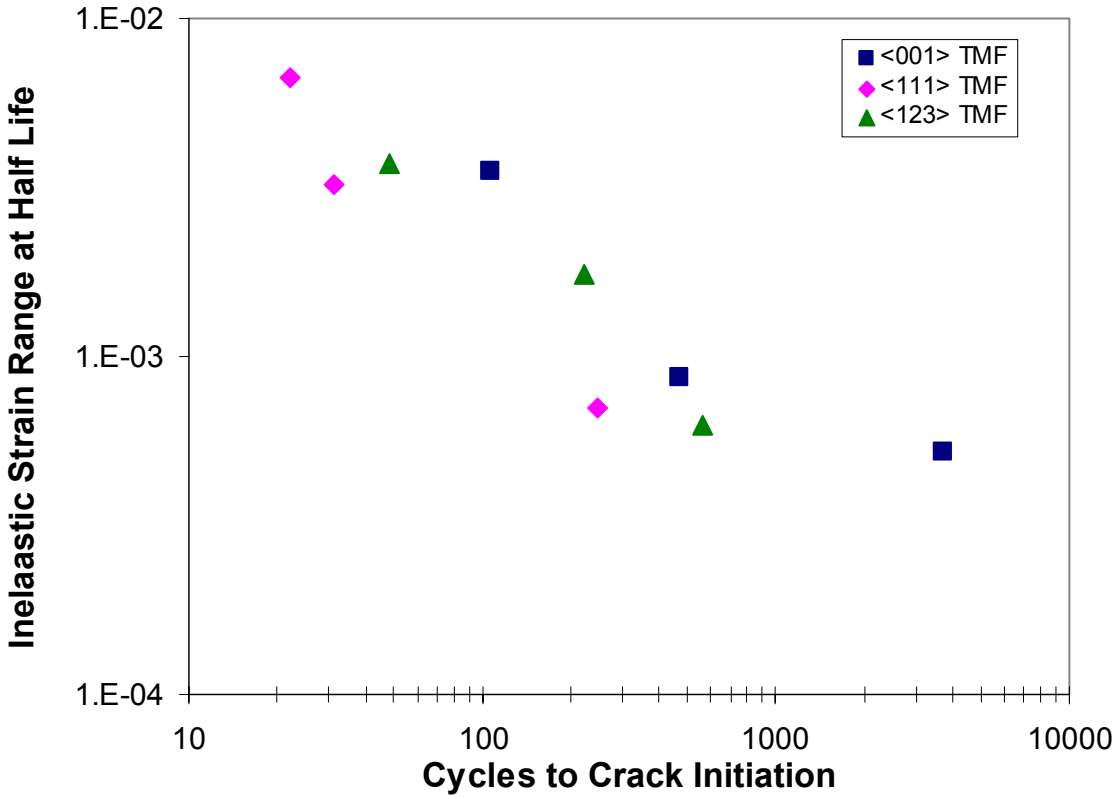

Figure 3-49 Fatigue Test Results (TMF) as a Function of Primary Crystallographic Orientation-Inelastic Strain Range

The general life trends on an inelastic strain range basis match those found for mechanical strain range versus cycles to crack initiation. However the data is collapsed considerably with the largest life difference between <111> and <001> orientations for a similar inelastic strain range being a factor of 3X.

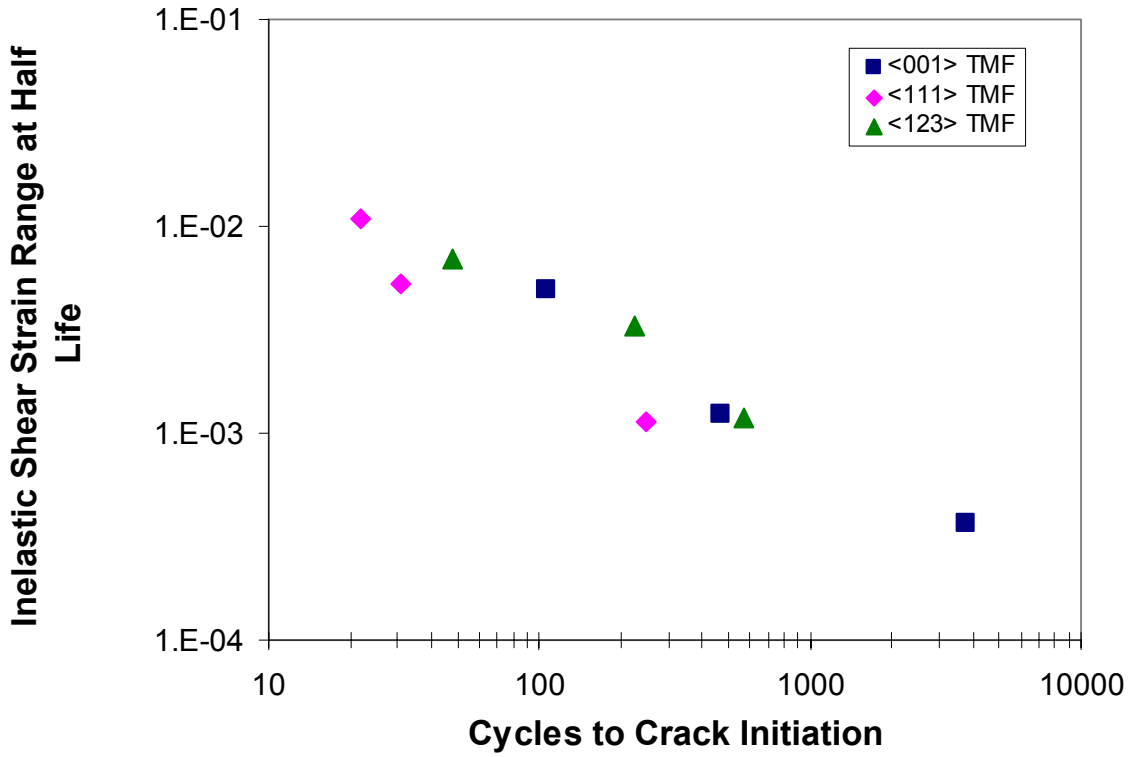

Figure 3-50 Fatigue Test Results (TMF) as a Function of Primary Crystallographic Orientation-Inelastic Strain Range on Slip System Having Highest Schmid Factor

When comparing the inelastic shear strain range on the slip system having the highest Schmid factor versus cycles to crack initiation, the general life trends found for the other strain-life plots hold. However, when plotting in this way the <001> and <123> orientation results collapse to a single trend, while the <111> orientation has lives averaging an order of magnitude lower.

PWA 1484 loaded in the <001> orientation has the longest lives and <111> has the shorted lives, for a given amount of applied strain. It is difficult to determine from the above figures which parameter collapses the strain-life curves best as a function of crystallographic orientation (e.g. mechanical strain range, inelastic strain range, or

inelastic shear strain range on a particular slip system). Therefore, all of the strain measures where graphed versus life on the same axis, as shown in Figure 3-51.

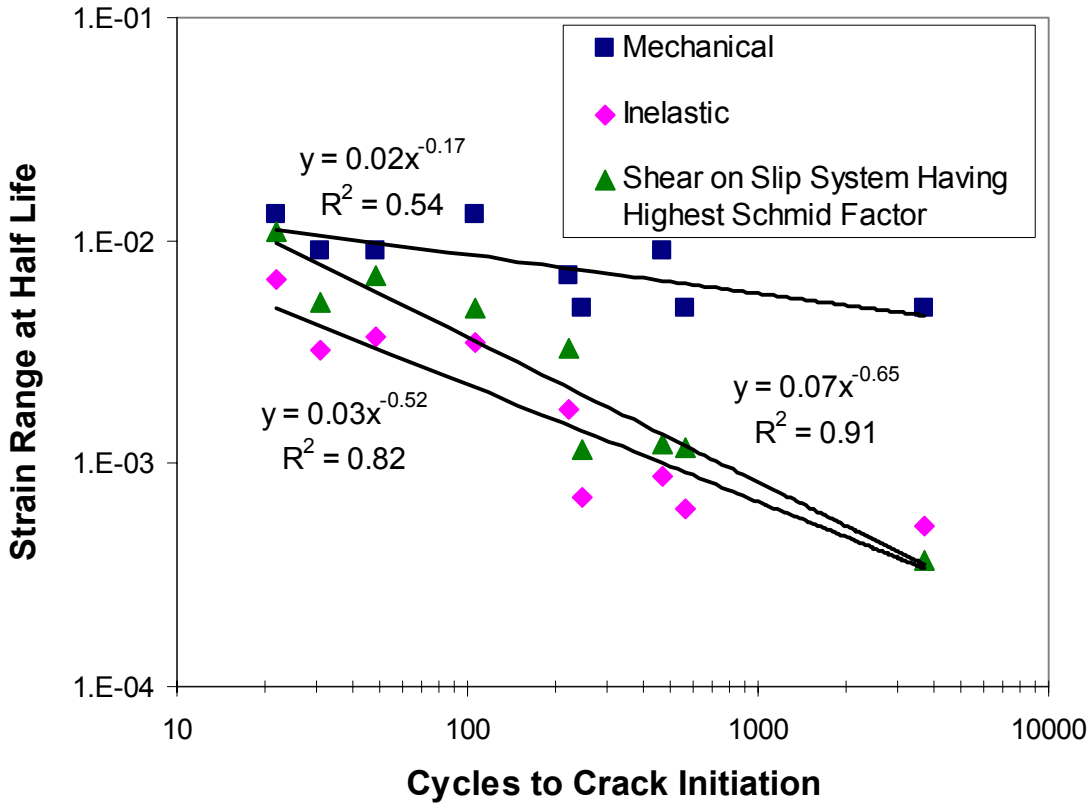

Figure 3-51 Fatigue Test Results (TMF) as a Function of Primary Crystallographic Orientation-Comparison of Strain-Life Plot Styles

Inelastic shear strain range (on the slip system of highest Schmid factor) at half life collapses the three orientations strain-life curves best, while mechanical strain range does the worst job. This is not surprising given the findings of researchers performing critical plane modeling in single crystal superalloys [6, 38, 39, 94].

3.12 Discussion

Bithermal fatigue and TMF tests were performed on single crystal superalloy PWA 1484 having <001>, <111> and <123> orientations. An effective temperature

equation was proposed and used to compare tests having different waveforms. The test matrix for this work successfully activated multiple dominant damage mechanisms. The microscopy of the tested specimens in conjunction with mathematical modeling has lead to conclusions about which damage mechanisms were active in each test. The following conclusions were made:

1. BiF tests having T_{min} of 550° C, T_{max} of 1050° C, mechanical strain lower than $\Delta\varepsilon < 1.0\%$ and no hold times experienced environmental fatigue as the dominant damage mechanism.
2. TMF and BiF tests having T_{min} of 550° C, T_{max} of 1050° C, mechanical strain greater than $\Delta\varepsilon > 1.0\%$ and no hold times experienced combined fatigue-viscoplastic ratcheting damage mechanisms.
3. Increasing the effective temperature of the test waveform, whether TMF or BiF increases dominance of creep mechanisms.

Furthermore, microscopy results indicate that crack initiation occurred as a result of fatigue-environmental interactions manifesting as either: a) slip band impingement upon environmentally degraded material (oxide-spike, oxidized slip band, etc.), or b) crack initiation in the brittle surface oxide which them propagates into the base material. These interactions are shown in Figures 3-37 through 3-40 and Figure 3-42, respectively. Deformation mechanism maps for PWA 1484 experiencing OP TMF are provided. Furthermore, results from off-axis specimen tests (<111> and <123>) indicate that a strain–life curve using the inelastic shear strain range (on the slip system of highest Schmid factor) at half life collapses the life trends best for all orientations studied. Finally, a mathematical relationship was proposed which relates the inelastic strain range

of BiF test results to those of the TMF results. The relationship introduces an effective activation energy which accounts for the difference in environmentally-assisted damage mechanisms between the two test types.

It should be apparent that the determination of dominant damage mechanisms performed here was greatly aided by the use of multiple fatigue waveforms. Specifically, the use of both TMF and BiF waveforms and the selective application of various effective temperatures resulted in the characterization of three primary deformation regimes. If nothing else this chapter should provide reasoning for future use of the BiF waveform in OP TMF characterization studies.

CHAPTER 4. ENVIRONMENTAL EFFECTS

4.1 Introduction

High temperature γ' depletion studies were conducted on the single crystal Ni-base superalloy PWA 1484 to determine the influence of exposure temperature, time and surface roughness. The goal of this section is to characterize the material response to isothermal non-stressed high temperature environments, and then to develop a modified relationship for γ' depletion occurring in TMF and BiF tests that include the effect of an applied stress on the high temperature material degradation kinetics. These relationships will be utilized in the life estimation relationships presented in Chapter 6 of this work

The material studied in this work has a two phase microstructure consisting of a γ matrix and γ' precipitates. The primary difference in composition between the two phases is the amount of aluminum in the γ' precipitates where as the matrix has minimal aluminum content in substitutional positions. When exposed to high temperatures the aluminum diffuses from the γ' phase toward the material surface, forming an oxide or oxides, according to the thermodynamic stability of the oxides in question. Once the aluminum diffuses from the precipitates, the denuded material is effectively 100% matrix (γ). As the precipitates provide the primary strengthening mechanism for the alloy at high temperatures (as depicted in Fig 4-1), this γ' depleted zone resulting from high temperature exposure creates a subsurface region which is then susceptible to further damage at high temperatures.

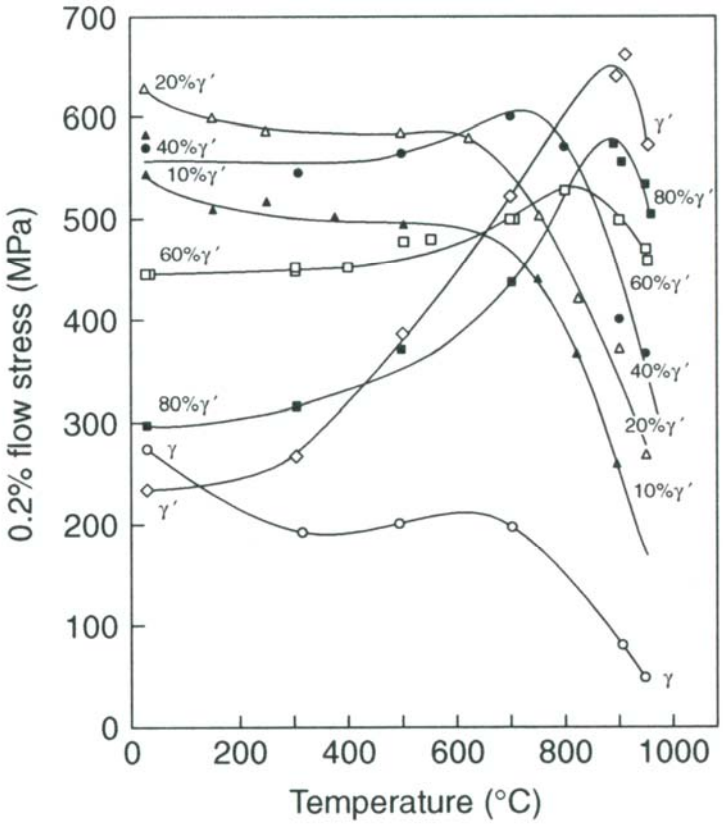

Figure 4-1 Yield Stress as a Function of Temperature and γ' Volume Fraction (%) in Ni-Cr-Al Ternary Alloys [2]

Given that the oxide is largely comprised of chromium and aluminum from the γ' phase, one would expect that the oxidation kinetics are intrinsically linked to the γ' depletion kinetics. Hence one can infer oxidation kinetics from the γ' depletion kinetics (or at least develop correlations from), which are far easier to determine for materials which do not produce a consistently adherent oxide scale. The original intent of this work was to characterize both the oxidation and γ' depletion kinetics of this alloy. However, an adherent oxide does not form on PWA 1484 at all temperatures and exposure times studied. As such considerable oxide spallation occurred making it extremely difficult to quantify oxidation kinetics. The γ' depletion of each sample, on the other hand, can be

clearly seen and readily measured after chemically etching the specimen. As a result this work focuses on the γ' depletion kinetics for PWA 1484.

This work establishes a single γ' depletion kinetics equation for PWA 1484 between 850° and 1050° C from non-stressed isothermal exposures. Additionally, arguments are presented and literature evidence is cited to support the notion that the kinetics of γ' depletion closely matches that of oxidation. In other words, the rate controlling processes are identical. Furthermore a relationship is provided for γ' depletion as a function of surface finish. Finally a relationship is provided which links the isothermal non-stressed depletion kinetics and that experienced in TMF and BiF cycles.

4.2 Material

Oxidation and γ' depletion studies were performed on the second generation single crystal superalloy PWA 1484. The materials microstructure is comprised of small, typically coherent, $Ni_3(Al/X)$ $L1_2$ (FCC-like) precipitates (γ'), embedded in a nickel FCC matrix (γ) [18]. The nominal chemical composition of PWA 1484, along with the first generation precursor to the alloy, PWA 1480 is compared in Table 4-1.

Table 4-1 Nominal composition of PWA 1480 and PWA 1484 (wt %) [7]

	Ni	Cr	Ti	Mo	W	Re	Ta	Al	Co	Hf
PWA 1480	58.5	10	1.5	-	4	4	12	5	5	-
PWA 1484	59.6	5	-	2	6	3	8.7	5.6	10	0.1

The service-condition alloy has a primary γ' particle size between 0.25 and 0.35μm, a γ' volume fraction of approximately 63%, a density of 8.94 x 10^{-3} kg/cm^3, an incipient melting temperature of 1338° C and a γ' solvus temperature of 1299° C [7].

4.3 Experimental Procedures and Results

4.3.1 Sensitivity of Surface Roughness

The vast majority of the high temperature degradation studies conducted on superalloys were done on specimens which were prepared using P600 grit (European grade) SiC paper [50, 57-59]. ASTM E606 test specimens as well as turbine components, however, have a different surface roughness than that provided by P600 SiC paper. In order to determine the sensitivity of surface roughness on the γ' depletion kinetics of PWA 1484, a series of high temperature tests was conducted at 1050° C on nominally <001> oriented specimens having varying surface roughness values. The surface roughnesses were produced using different (European FEPA) grades of SiC paper. The test schedule for the surface roughness characterization in provided in Table 4-2.

Table 4-2 Surface Preparation Oxidation Test Schedule, All Tests Performed at 1050° C

SiC Grit	Oxidation Time (hr)
P280	30, 150, 300
P360	30, 150, 300
P1200	30, 150, 300
P4000	30, 150, 300

The arithmetic average (R_a) surface roughness values for the PWA 1484 specimens prepared with various SiC papers (P360, P1200 and P4000) was determined

using a Veeco, Model NT2000 Wyco non-contact, profilometer coupled with Veeco Vision Software. In addition to the SiC prepared specimens, the surface roughness of a fatigue test specimen machined per ASTM E606 was measured. All roughness values presented are an average of a minimum of five measurements. The results are provided in Table 4-3.

Table 4-3 Surface Roughness Values for Various Levels of Specimen Preparation

SiC Grit (FEPA)	SiC Grit (USA)	Ra (nm)	Deviation (nm)	
P280*	240	~200	-	-
P360	400	128	4	-2
P1200	600	49	7	-5
P4000	1200	8	4	-2
Fatigue Specimen		197	66	-54

The surface roughness value for the P280* grit paper was determined by interpolating the trend produced from SiC paper particle size (used to prepare the surface) versus the measured surface roughness. This was done to ensure that a series of γ' depletion specimens had similar surface roughness to that of a fatigue test specimen.

The surface roughness γ' depletion tests were performed in laboratory air in a Lindberg 3-zone Model 59744-A tube furnace. Specimens having nominal <001> orientated oxidation surfaces and an average diameter and thickness of 13mm and 6mm, respectively, were prepared to the desired surface roughness with SiC paper on a Struers RotoPol-15 polishing system equipped with a Struers RotoForce-1 attachment. Once polished, the specimens were cleaned in an ultrasonic bath of dish soap and water for 5 minutes, followed by a rinse of acetone and ethanol. The specimens were then placed in the tube furnace on a Kaowool® ceramic fiber insulating wafer. The vertical orientation

of the specimens ensures that oxidation forms, un-hindered, on both sides of the specimen, thereby providing more surface area to measure oxide or γ' depletion thickness. Figure 4-2 shows a representative oxidation sample on the insulating wafer with primary crystallographic orientation marked.

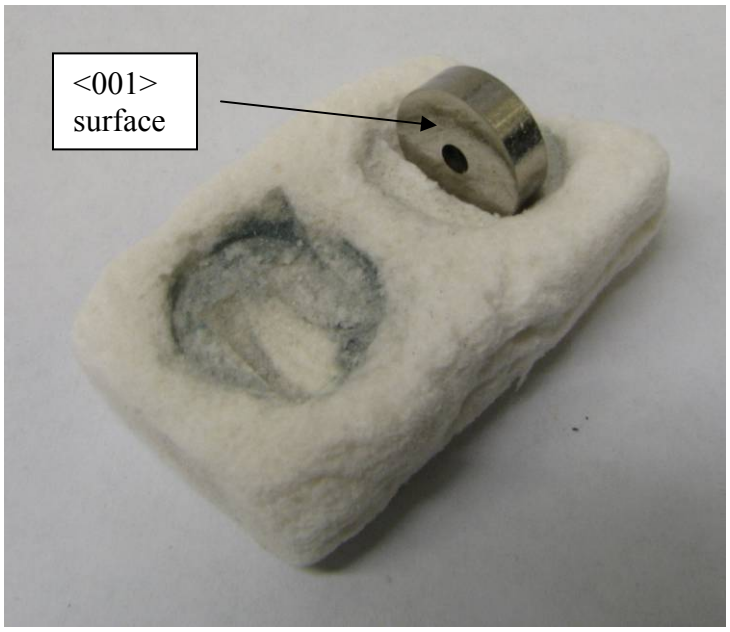

Figure 4-2 Oxidation Specimen on Insulating Wafer Prior to High Temperature Exposure

After the prescribed exposure time the furnace was turned off and allowed to cool to room temperature with the specimens inside. This slow cooling rate was found to reduce oxide spallation by reducing thermal shock. Furthermore this procedure should minimize continued oxidation given the rate equations' exponential dependence upon temperature. Each test specimen (full disc) was then mounted upright using a spring clip in two-part Struers Epofix epoxy. The mounted specimens were then ground (until a large portion of the specimen cross section was exposed) and polished using the schedule detailed in Table 4-4.

Table 4-4 Final Polish Schedule (Struers Products)

Step	Preparation Disc (Material)	Force (N)	Speed (RPM)	Suspension	Lubricant	Time (min)
Coarse Grind	P360 AD (SiC)	30	150	None	Water	3+
Fine Grind I	P1200 AD (SiC)	25	150	None	Water	5
Fine Grind II	P4000 AD (SiC)	25	150	None	Water	5
Coarse Polish	MD Mol (Woven wool)	20	150	DiaPro Mol	None	8
Fine Polish	MD Chem-OP-S (Porous synthetic)	15	150	OP-S Suspension	None	2

Figure 4-3 shows a representative mounted and polished specimen.

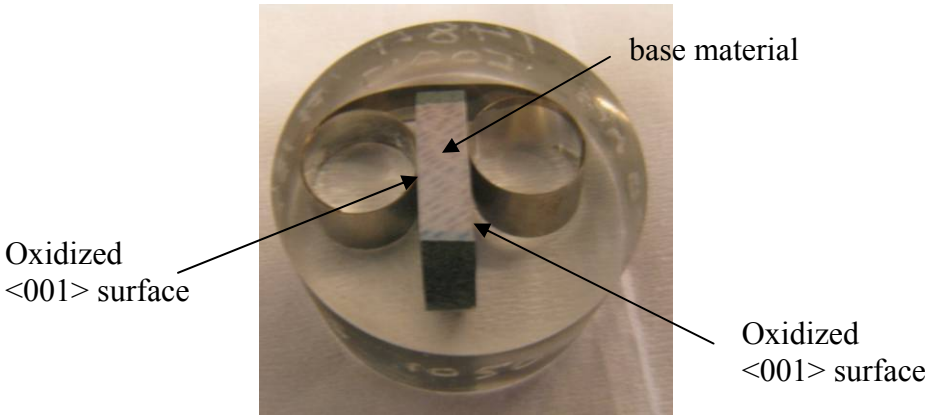

Figure 4-3 Representative Oxidation Specimen Mounted and Etched

The polished specimens were etched using a waterless Kalling's solution consisting of 2 grams of 98% $CuCl_2$, 40 mL of 95% ethanol and 40 mL of 36.5-38.0% HCl. Each specimen was submerged and minimally agitated in the etch solution for 40 seconds. The waterless Kalling's etch effectively highlights the dendritic features and the

γ'-depleted zones, making it possible to measure this region of high temperature material degradation, as shown in Figure 4-4.

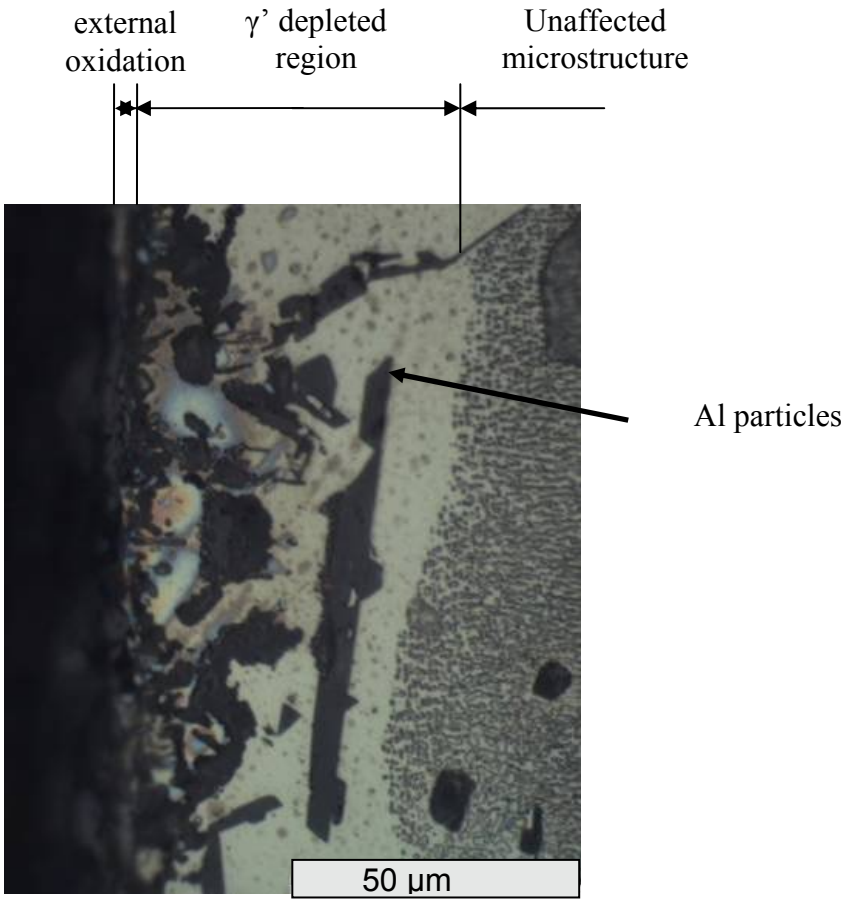

Figure 4-4 Optical Image of Mounted, Polished and Etched Oxidation Specimen, 1050° C for 300 Hours, 1000X Zoom

Figure 4-4 depicts a typical test specimen, with the oxidized free surface on the left, a region of internal Al particles within the γ' depleted region, followed by the virgin microstructure on the right. A considerable number of oxidation studies performed on Ni-based superalloys resulted in similar material degradation to that shown in Fig 4-4 [50, 51, 53, 58, 59, 63]. Images of the tested specimens (12 separate locations per specimen) were recorded using an Olympus BX40 optical microscope fitted with an

Olympus digital camera at 500X and 1000X zoom. Three γ' depletion depths were measured and recorded at twelve specimen locations, yielding 36 measurements total for each specimen. Average results from the γ' depletion tests explaining the sensitivity of surface roughness are shown in Table 4-5 and Figure 4-5.

Table 4-5 Results Evaluating Sensitivity of Surface Roughness

Time (hr)	SiC Grit	Ra (nm)	Deviation (nm)		γ' depletion (μm)	Deviation (um)	
30	P280	197	65.6	-54.4	(-)	(-)	(-)
	P360	128	3.6	-1.7	3.0	1.5	-0.5
	P1200	49	7.3	-4.7	2.7	0.8	-0.7
	P4000	8	3.6	-2.4	2.5	1.0	-0.5
150	P280	197	65.6	-54.4	7.8	2.8	-4.3
	P360	128	3.6	-1.7	(-)	(-)	(-)
	P1200	49	7.3	-4.7	6.7	2.8	-3.7
	P4000	8			5.5	1.5	-3.0
300	P280	197	65.6	-54.4	(-)	(-)	(-)
	P360	128	3.6	-1.7	5.6	0.1	-3.1
	P1200	49	7.3	-4.7	3.7	1.8	-1.2
	P4000	8	3.6	-2.4	2.4	0.6	-0.4

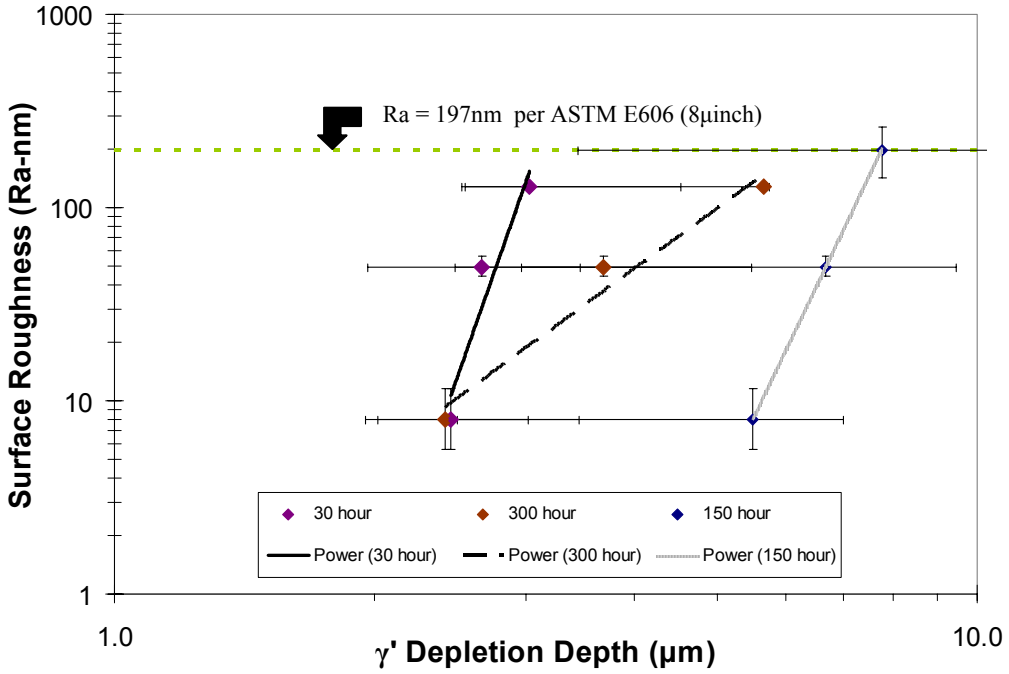

Figure 4-5 γ' Depletion Study at 1050° C- Sensitivity of Surface Roughness

The 150 hour oxidation results do not converge with the 30 and 300 hour results at the finest surface roughness value (R_a = 7.8 nm). This may be explained by the specimens that were used in the study. The 30 and 300 hour oxidation specimens were in the as-supplied condition where as the 150 hour specimens were taken from the end of a single, previously tested, TMF specimen. As such only the slope of the 150 hr trend line will be used in further analysis.

4.3.2 Kinetics of γ' Depletion

In order to determine the γ' depletion kinetics of PWA 1484, a series of isothermal, still laboratory air, high temperature tests was performed using the finest SiC preparation step in Table 4-4. The testing matrix for this work is provided in Table 4-6.

Table 4-6 Furnace Oxidation Test Matrix

Temp (deg. C)	Time (hours)	# of Specimens	Orientation	Surface Preparation
850	5	2	<001>	P4000
	24.75	1	<001>	P4000
	31	1	<001>	P4000
	150	2	<001>	P4000
	270	2	<001>	P4000
950	5	1	<001>	P4000
	30	1	<001>	P4000
	150	2	<001>	P4000
	300	2	<001>	P4000
1050	5	2	<001>	P4000
	30	3	<001>	P4000
	150	4	<001>	P4000
	300	4	<001>	P4000

The high temperature tests detailed in Table 4-6 were performed in a 3-zone Lindberg Model 59744-A tube furnace. The ~13mm diameter x ~6mm thick specimen discs were prepared to a Ra = 7.86 nm surface finish by following the polishing steps outlined in Table 4-4. The prepared specimens were placed in the tube furnace following the procedure outlined in Section 4.3.1. Upon completion of each test the specimens were mounted, polished and etched following the procedures outlined in Section 4.3.1.

4.3.2.1 Observations

Results of the γ' depletion kinetics tests performed on PWA 1484 indicate that the material does not always form a protective oxide layer. Results also indicate that, generally, an adherent oxide forms below 950˚ C, while considerable spallation occurs at 1050˚ C, as shown in Figure 4-6.

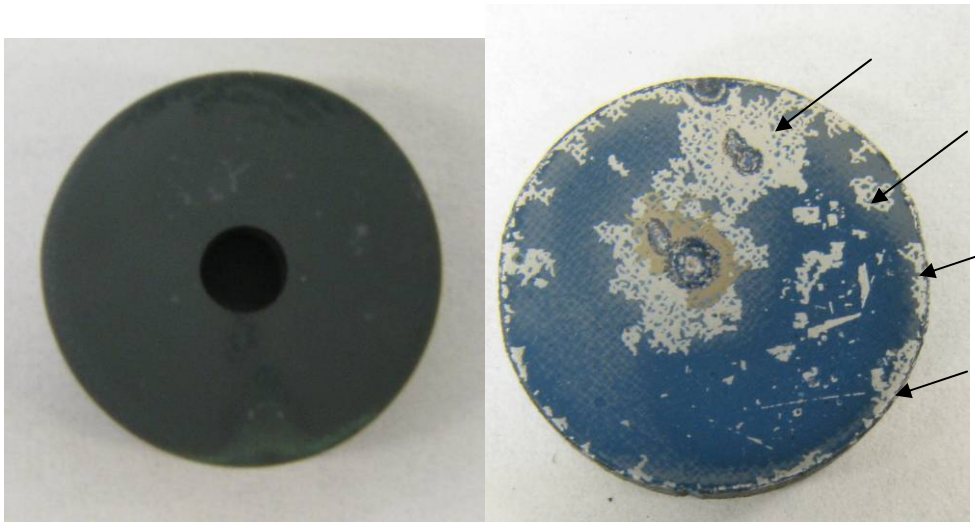

Figure 4-6 Relative Amounts of Oxide Spallation: 850 C Left, 1050C Right, both for 300 hrs. Representative Spalled Regions indicated by arrows.

Furthermore, the amount of spallation was found to be dependent upon high temperature exposure time. Figure 4-7 shows images of specimens oxidized at 1050˚C for 5, 30, 150 and 300 hours with spalled regions indicated by arrows.

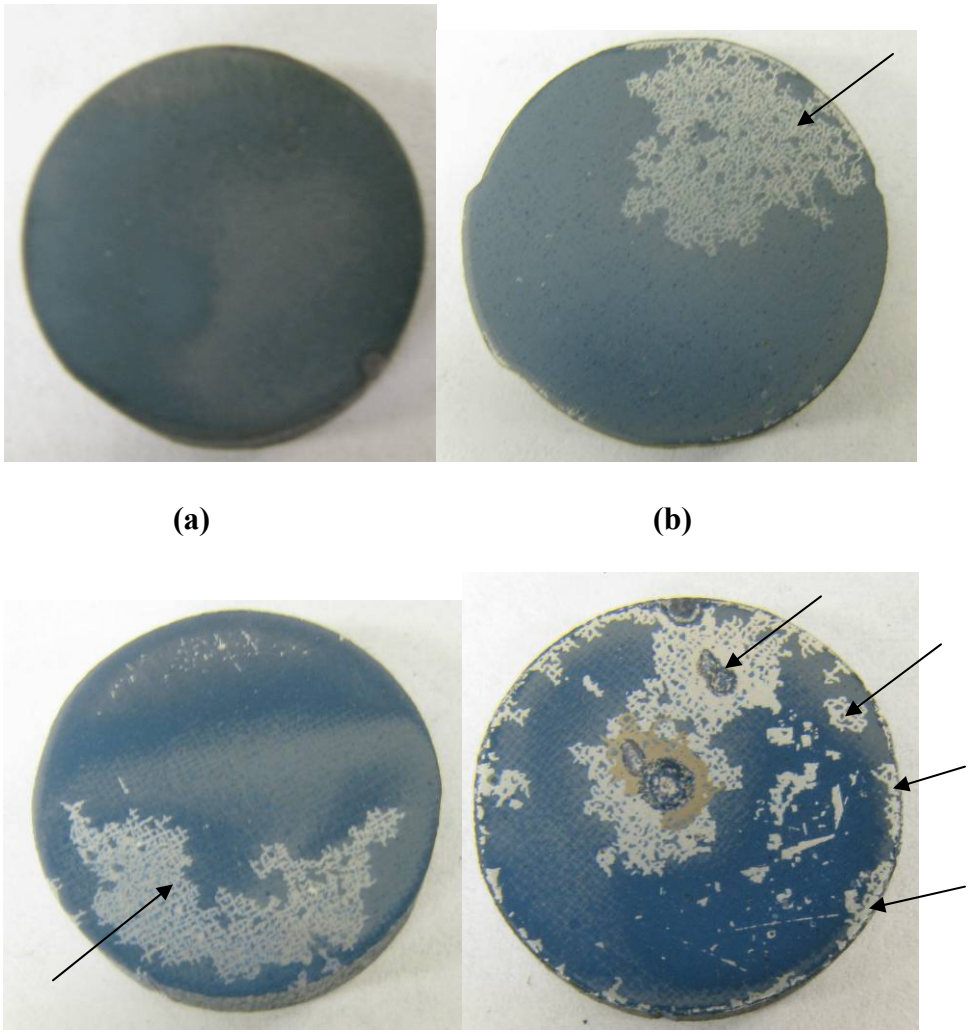

Figure 4-7 Surface Oxide Spallation as a Function of Time: (a) 1050C for 5 hr, (b) 1050C for 30 hr, (c) 1050C for 150 hr, (d) 1050C for 300 hr. Spalled Regions indicated by arrows.

One can clearly see that the amount of oxide spallation increases with increasing exposure time at 1050˚ C. These results are similar to the results of Nychka et al. [57] who performed oxide spallation studies on PWA 1484. They found that the oxide formed on this alloy consists of an α-alumina (Al_2O_3) inner layer, and an outer spinel ($(Ni)Cr,Al,Co)_2O_4$) layer which is interspersed with tantalum rich oxide particles. Moreover, they concluded that oxide spallation increased with sulfur content (ppm

quantities) and surface roughness. They also noted that considerable spallation occurred when PWA 1484 was exposed to 1200° C in still laboratory air. Furthermore, Bouhanek et al. [56] found that oxide scales formed at 1100° C on six different superalloys were not adherent, and spalled extensively. It should be noted that the oxide spallation encountered in this work was observed after the specimen reached room temperature. As such one must question whether the spallation occurred as a result of high temperature exposure or rather occurred during cooling, due to the mismatch between the base material and oxide coefficient of thermal expansion. Given that the alumina oxide spalled extensively, and that alumina typically produces an adherent oxide, it is hypothesized that the oxide spallation occurred as a result of specimen cooling rather than during high temperature exposure. The change in temperature experienced by these test specimens is indicative to that seen by turbine blades during service; as such the oxide spallation is of concern.

When looking at the oxidized surfaces produced in this work, one also notices the different oxide morphologies between the base material dendritic and interdendritic regions, an example is shown in Figure 4-8.

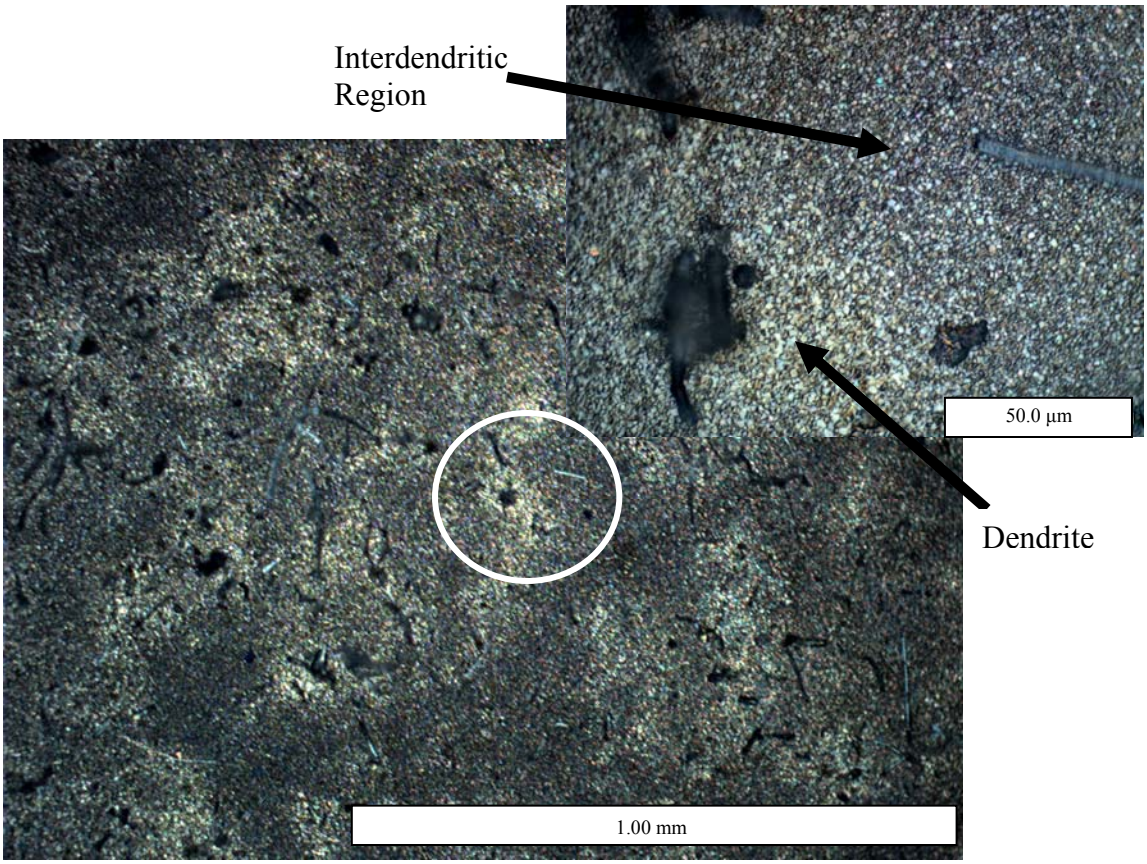

Figure 4-8 Optical Image Showing Variation in Oxidation with heterogeneity , 1050˚ C for 150 hr

Figure 4-8 shows the oxidized <001> surface of a PWA 1484 specimen tested at 1050˚ C for 150 hours. The dendrites can be clearly seen. Krupp and Christ [63] also observed that similar oxide segregation between dendritic and interdendritic regions on a single crystal superalloy. Li et al. [58, 59] and Krupp and Christ [63] determined that a (Ni,Co)O oxide primarily exists in the dendritic regions whereas an α-Al_2O_3 primarily exist in the interdendritic areas, due to base material elemental segregation of Al, Ti and Ta into the interdendritic regions and W, Mo, and Cr into the dendritic regions [58, 59].

Oxide morphology can also vary on different portions of the same specimen, as shown in Figure 4-9.

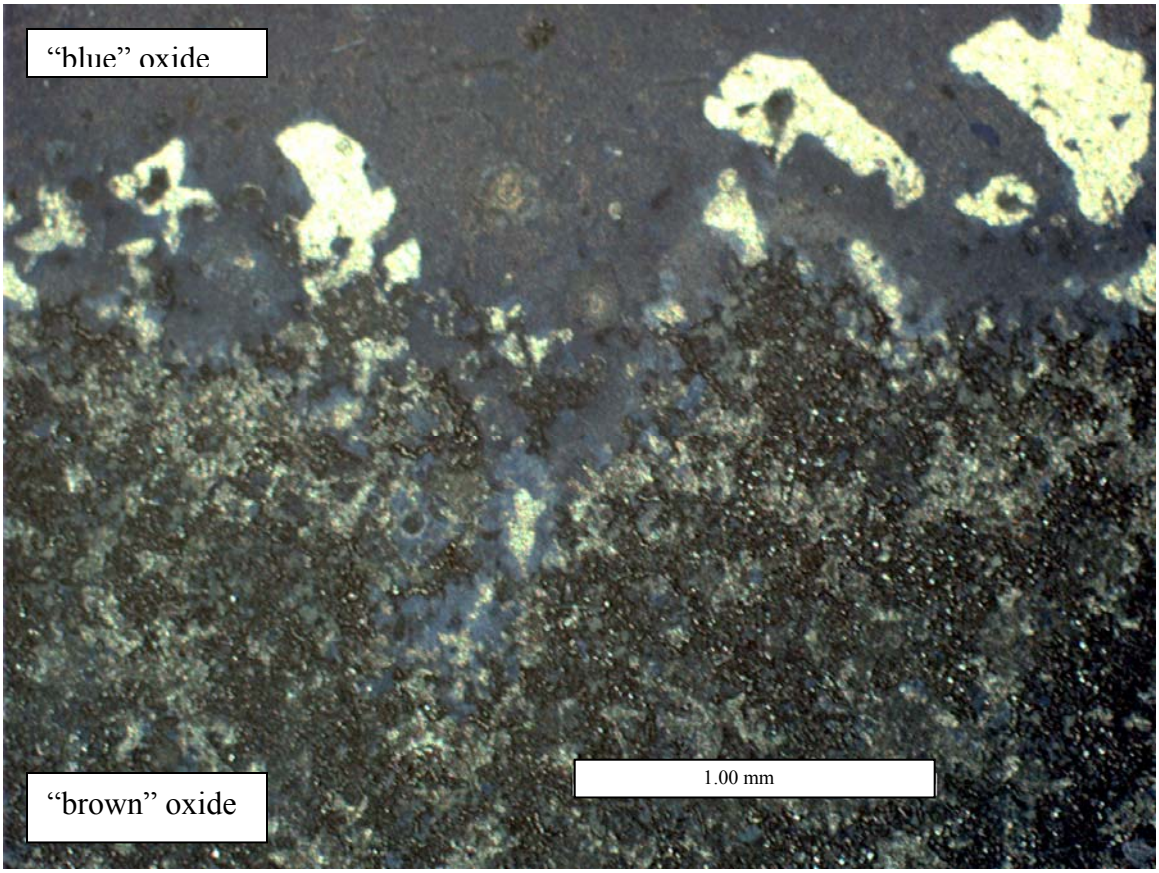

Figure 4-9 Specimen Surface Exposed to 1050 C for 300 hrs

Note in Fig 4-9 that the scale at the lower portion of the picture is dark brown while the oxide in the top portion of the picture has a blue tinge. Furthermore, the bluish oxide exhibits considerable spallation where as the brown oxide does not. The oxidation of Ni-base superalloys typically falls within three "Groups" as determined by the oxidation behavior of Ni-Al-Cr ternary alloys [50]. When sectioning through the specimen shown in Figure 4-9, one finds that the base material degrades differently depending upon which oxide is dominant, as shown in Figure 4-10.

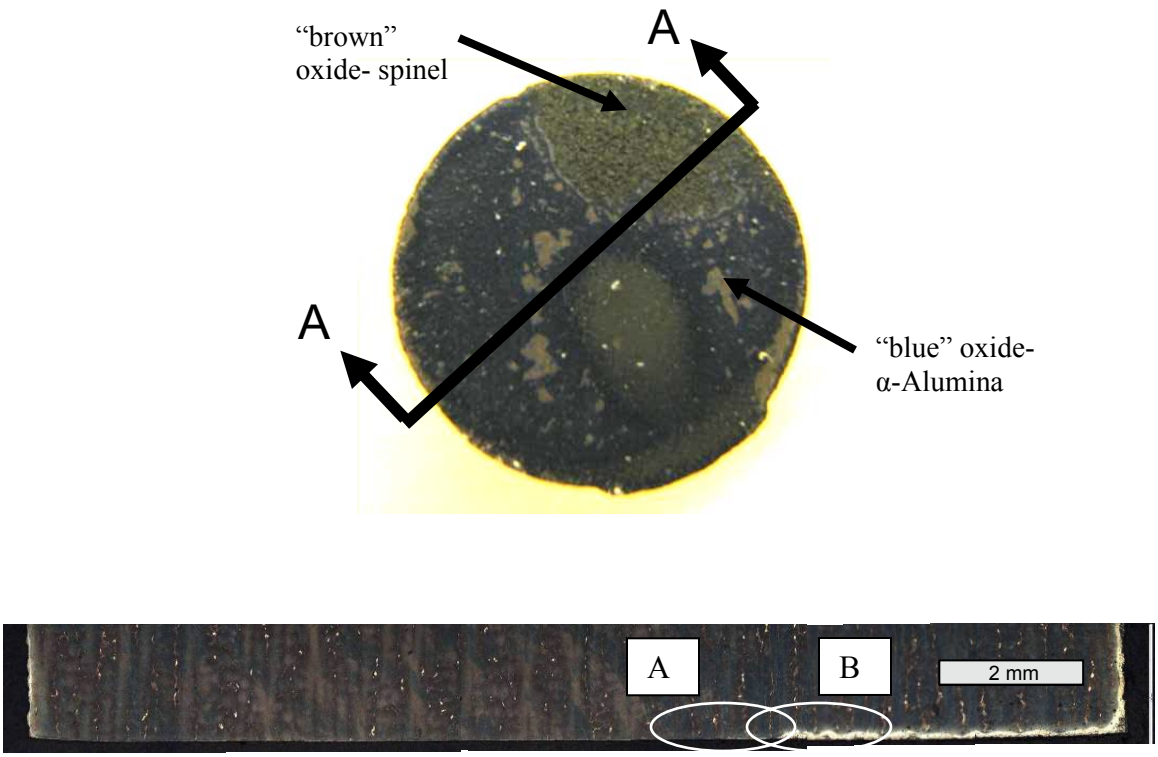

Figure 4-10 Top: Specimen Tested at 1050˚C for 300 hours. Bottom: Cross Section A-A

(a) Region A

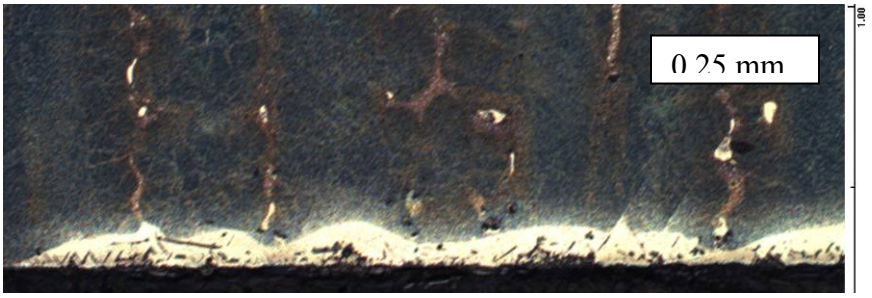

(b) Region B

Figure 4-11 Blown up Regions of Different Oxides. Region A (a), Region B (b)

The dark brown oxide is accompanied by a considerable subsurface γ' depleted zone, shown in Figure 4-11, while the base material below the bluish oxide has little, if any, γ' depletion.

4.3.3 Oxide Characterization

Oxides were analyzed using energy-dispersive X-ray spectroscopy (EDS) at the Materials Analysis Center of the Georgia Tech Research Institute. Specifically, a Hitachi S-4100 field emission scanning electron microscope utilizing Vantage V1.3 software determined both the chemical composition and likely oxide composition of the oxides produced at 850°, 950° and 1050°C.

4.3.3.1 Competing Oxides Determined from Cross-Section EDS

The specimen shown in Figures 4-10 (1050°C for 300 hours) was analyzed for chemical and oxide composition with EDS. The "blue" oxide shown in Figures 4-10 is a combination of 32% Al_20_3 and 28% NiO. Presumably the alumina which formed in this area of the sample is responsible for reducing the ingress of oxygen sufficiently as to produce a considerably smaller γ' depleted region relative to the "brown" oxide. The "brown" oxide was determined to consist of two phases, specifically Al_2O_3 and NiO interspersed with spinel particles, as shown in Figure 4-12.

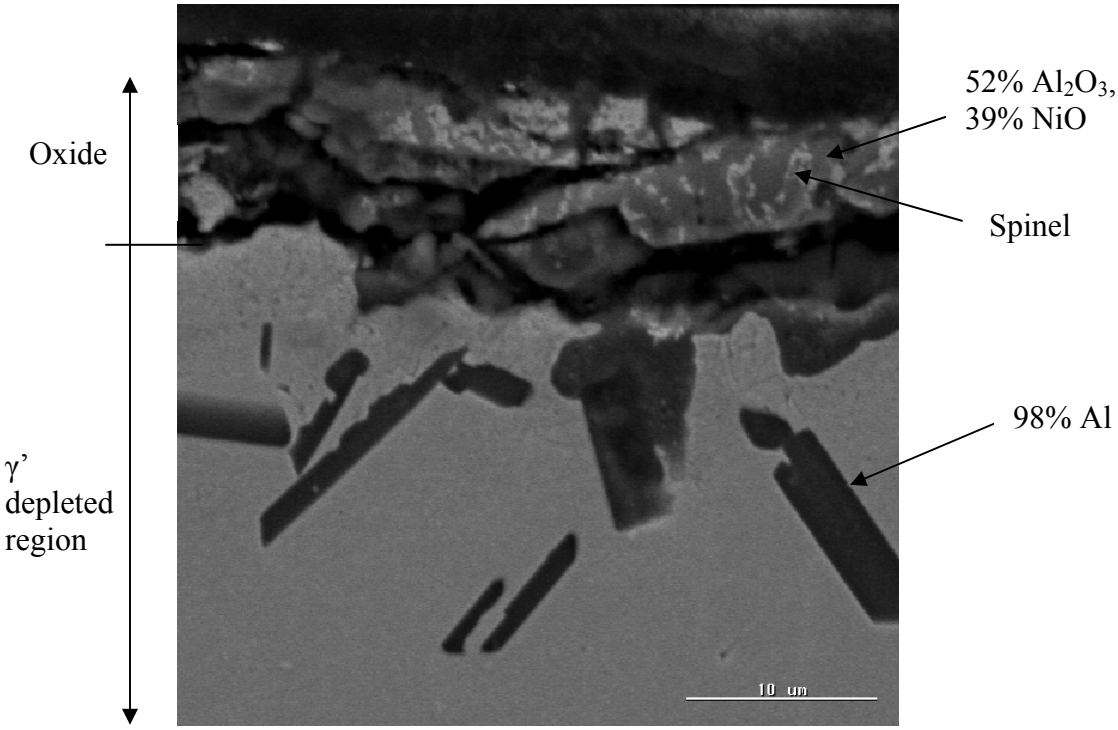

Figure 4-12 Competing Oxides- "brown" Oxide

The oxide which produced the considerable γ' depleted region (shown in Figure 4-10, 4-11 (b) and 4-12) exhibits considerable oxide wedging. Wedging can be thought of as an interaction between oxide plates, in which one plate "wedges" below another similar to tectonic plate interactions on the earths crust. The wedging can be seen in

Figure 4-12. Nychka et al. [57] also encountered this spallation mechanism when they studied the oxidation of PWA 1484. This phenomenon may be understood by calculating the Pilling-Bedworth ratio (R_{PB}) for the oxides found [97]. The ratio is determined from

$$R_{PB} = \frac{M_{oxide}\rho_{metal}}{nM_{metal}\rho_{oxide}} \quad \textbf{(4-1)}$$

where M_{oxide} and M_{metal} are the molecular mass of the oxide and metal, respectively, ρ_{oxide} and ρ_{metal} are the densities of the oxide and metal, respectively, and n is the number of metal atoms per one molecule of oxide. A value of $R_{PB} < 1$ usually indicates a "broken" non-protective oxide coating, $1 < R_{PB} < 2$ indicates a protective oxide and $R_{PB} > 2$ indicates that the oxide would likely spall, based upon empirical observations. For reference, pure Al_2O_3 oxide on PWA 1484 would have an $R_{PB} = 1.43$ and pure NiO would have $R_{PB} = 1.26$, indicating that the oxides would be protective. The oxide labeled as "52% Al_2O_3-39% NiO" has a R_{PB}=0.277 and the oxide labeled as "spinel" has a R_{PB}=0.337. The Pilling-Bedworth ratio correctly predicts that this oxide will be non-protective. A similar analysis was performed on the more protective "blue" oxide resulting in R_{PB}=0.261. Though the "blue" oxide had a very low R_{PB}, it none-the-less resulted in a negligible γ' depleted region, relative to the "brown" oxide. This may be the result of the spinel doping which occurred in the "brown" oxide. The addition of a more friable oxide in small quantities (doping) would result in a less-stable coating.

4.3.3.2 Dominant Oxides Determined from Surface EDS

EDS (point measurement) results indicate that the oxide produced from 850°C exposure for 300 hours was 22% Cr_2O_3, 12% CoO, and 58% NiO.

Exposure at 950°C for 150 hours resulted in two different oxides forming on PWA 1484. The dendritic regions produced an oxide composed of 10% CoO and 89% NiO, while the interdendritic region yielded 83% NiO, 10% CoO, 3% Cr_2O_3 and 4% Al_2O_3. The differences in oxide formation according to base-material region (dendritic vs. interdendritic) is no doubt due to the elemental segregation that occurs within these regions during casting [58, 59]. SEM images of the oxides formed in these areas are shown in Figures 4-13 and 4-14.

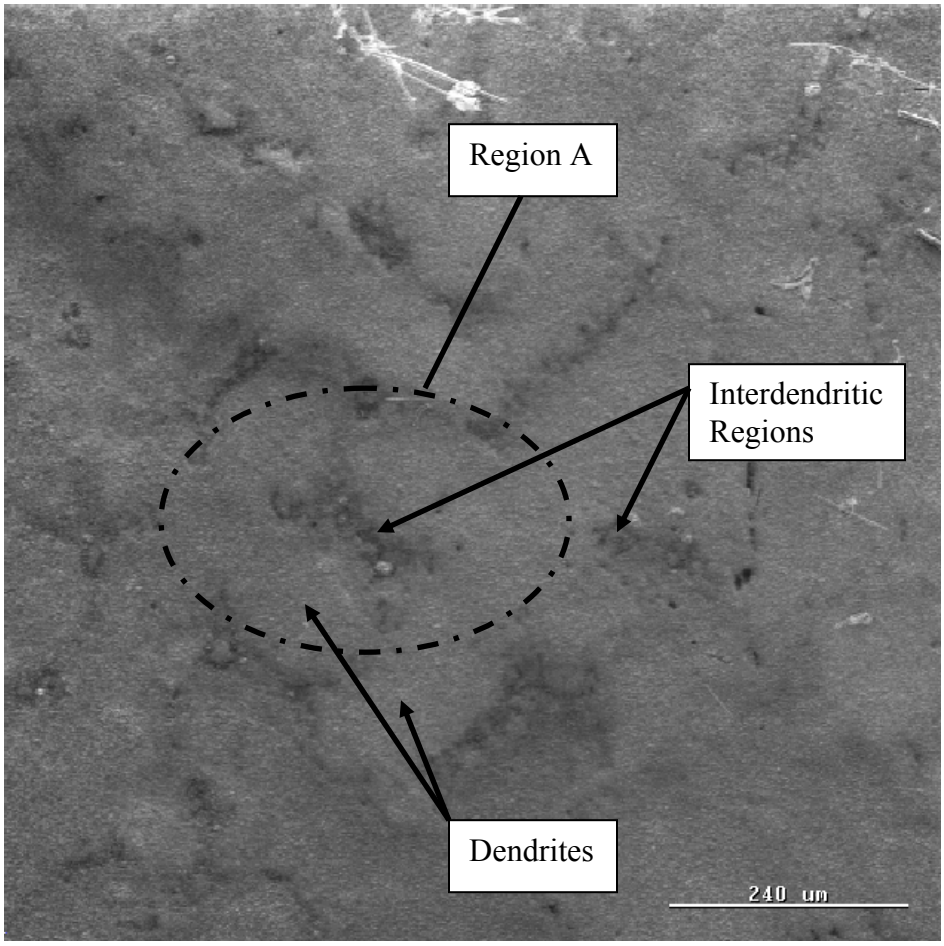

Figure 4-13 SEM Image of Oxides Formed On PWA 1484 at 950°C for 150 Hours- Dendrites Denoted by Red Outlines

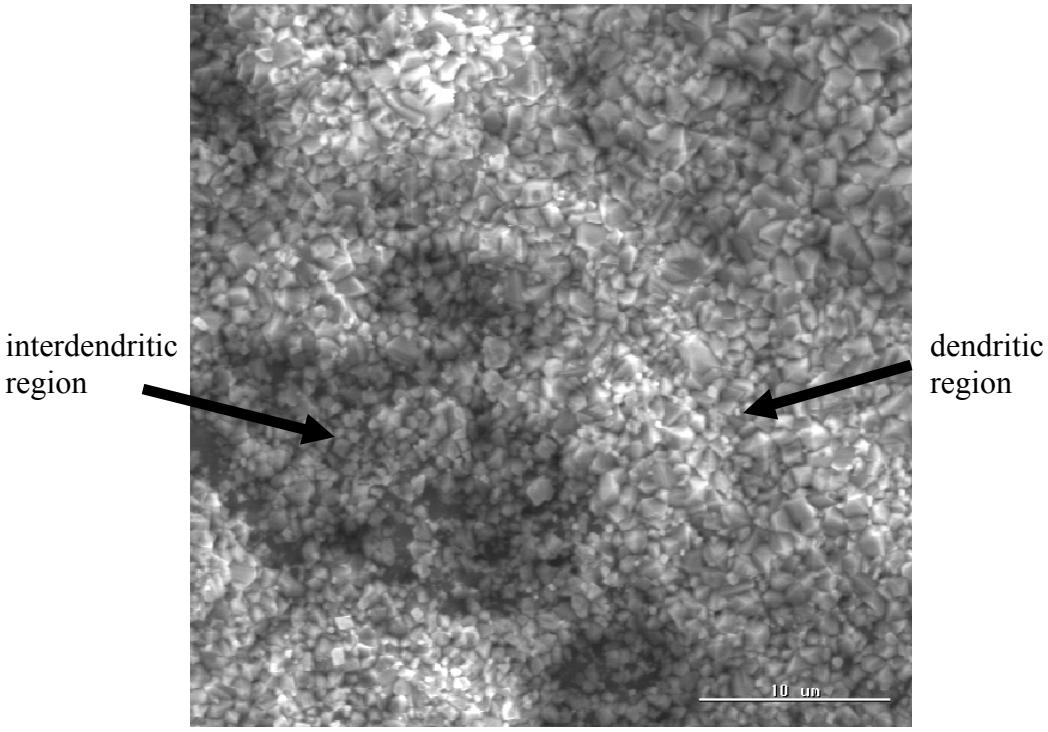

Figure 4-14 SEM Image of Oxides Formed On PWA 1484 at 950°C for 150 Hours- Region A

The surface of a PWA 1484 sample exposed to 1050°C for 150 hours was also analyzed. The results indicate that the dominant oxide formed under these conditions consists primarily of 14% Al_2O_3, 11% Cr_2O_3 and 51% NiO, similar to the results of the "brown" oxide analyzed as part of Section 4.3.3.1.

Several of the EDS analyses indicate the presence of a silicon oxide (SiO). As silicon is not a constituent of PWA 1484, it is believed that Si was introduced during specimen preparation. This could have occurred during one of two steps: 1) as part of the initial surface prep using SiC paper, or 2) during the final polishing step (of cross-sections) due to the colloidal silica polishing suspension (OP-S). Whereas contamination by the latter process can not be avoided, a final polish using Struers MD Mol prior to high temperature exposure may mitigate contamination due to the former.

Results of EDS of the oxides formed on PWA 1484 as a function of time and temperature are consistent with that found in the literature for other Ni-base superalloys [53, 56, 58, 59].

The complete results of oxide EDS are provided in the Appendix.

4.3.4 Measurements of γ' Depletion

Twelve images of each specimen were recorded at magnifications of 500X and 1000X. Images of samples exposed for (nominally) 30 hours, 150 hours and 300 hours at 850°C, 950°C and 1050°C are shown in Fig 4-15 through 4-17.

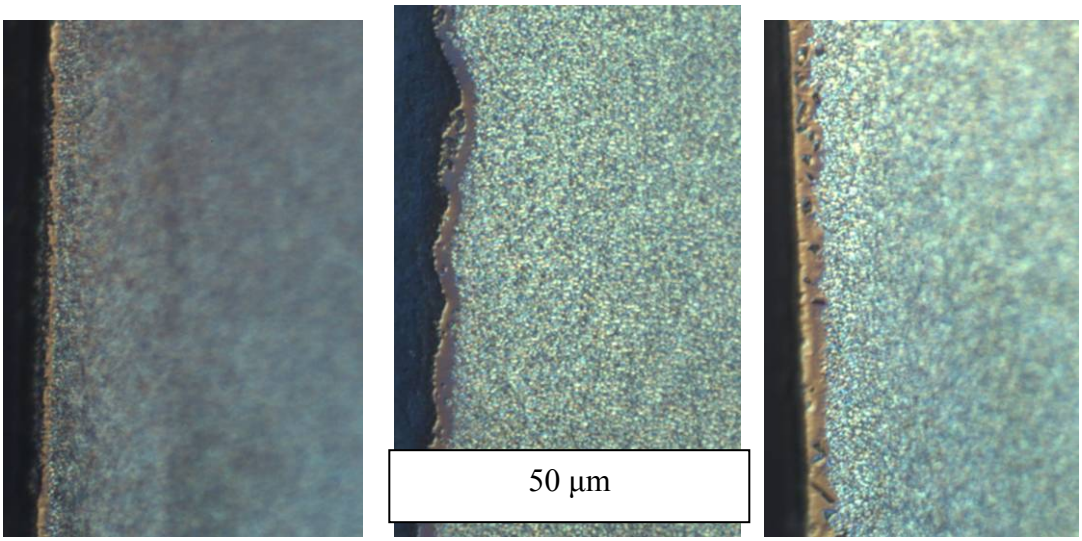

Figure 4-15 γ' Depletion at 850°C for (a) 31 hours, (b) 150 hours and (c) 270 hours. All at Same Scale

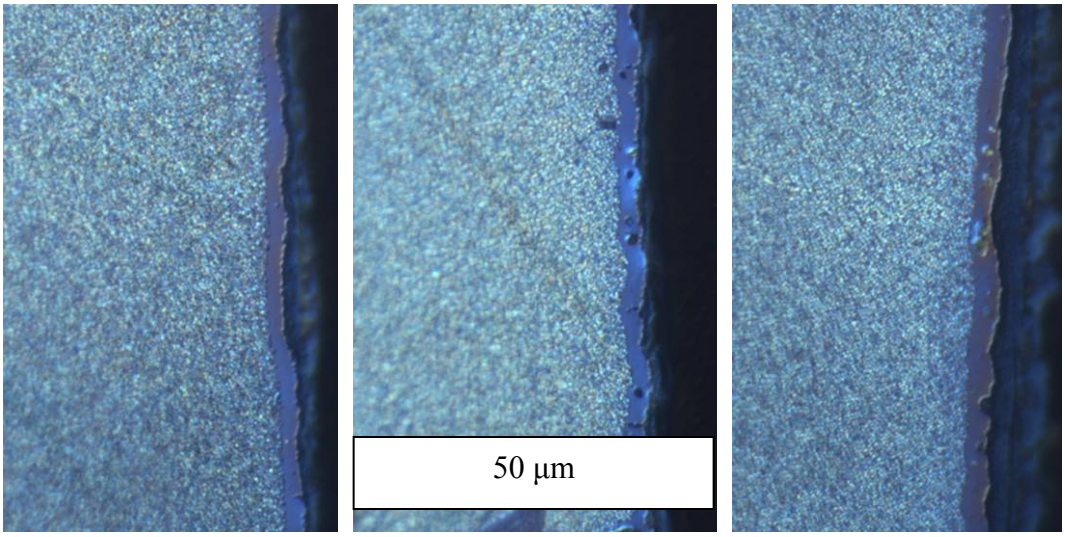

Figure 4-16 Depletion at 950°C for (a) 30 hours, (b) 150 hours and (c) 300 hours. All at Same Scale

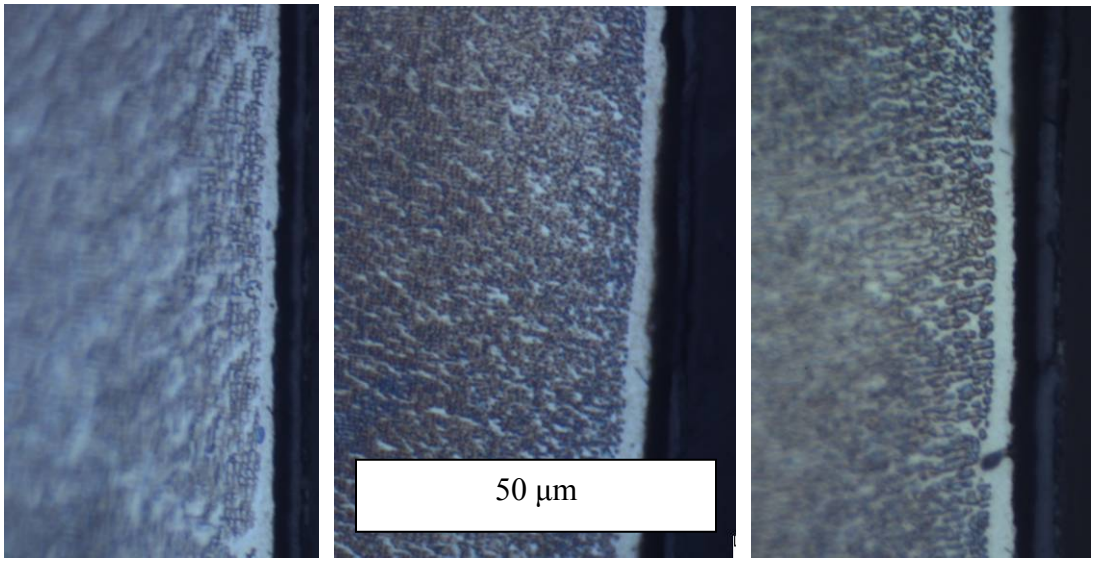

Figure 4-17 Depletion at 1050°C for (a) 30 hours, (b) 150 hours and (c) 300 hours. All at Same Scale

The average γ' depletion thickness at each temperature and time are shown in Table 4-8. These values are plotted in Figures 4-18 through 4-20. The average values for all temperatures are shown in Figure 4-21.

Table 4-7 Average γ' Depletion Values

850° C		950° C		1050° C	
time (hr)	γ'-depletion (μm)	time (hr)	γ'-depletion (μm)	time (hr)	γ'-depletion (μm)
5	0.223	5	1.375	5	1.500
24.75	0.708	30	2.420	30	1.938
31	1.063	150	2.406	150	2.750
150	2.588	300	2.948	300	2.948
270	2.227				

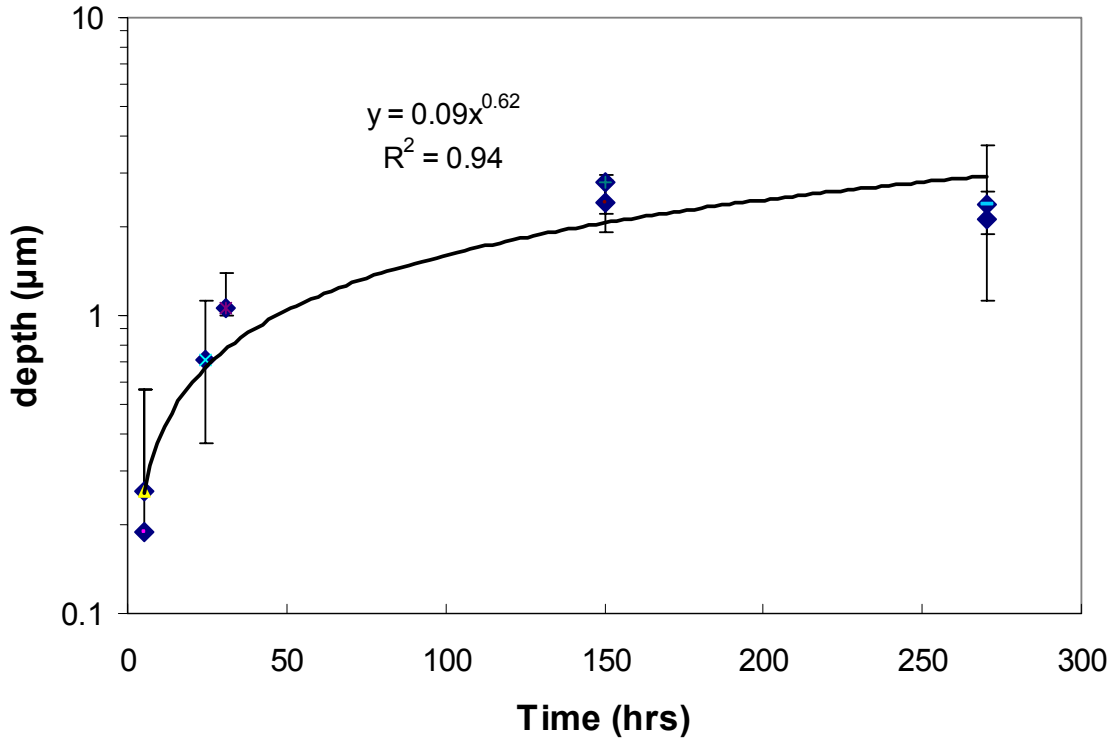

Figure 4-18 γ' Depletion Kinetics at 850° C

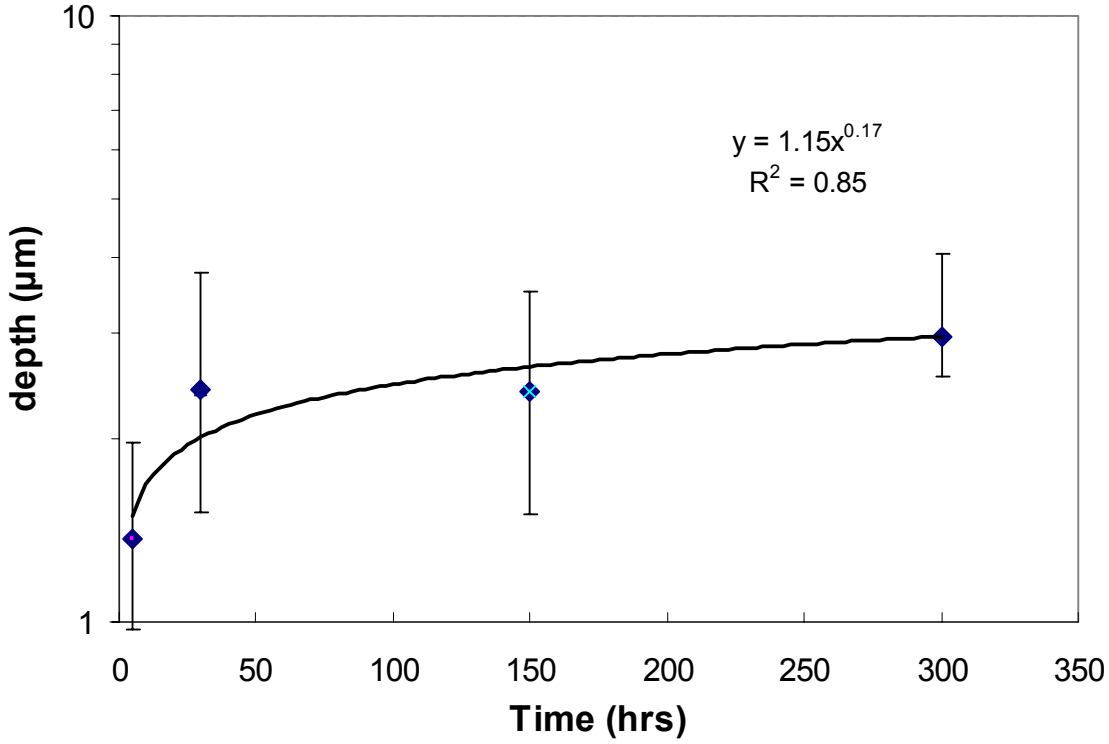

Figure 4-19 γ' Depletion Kinetics at 950° C

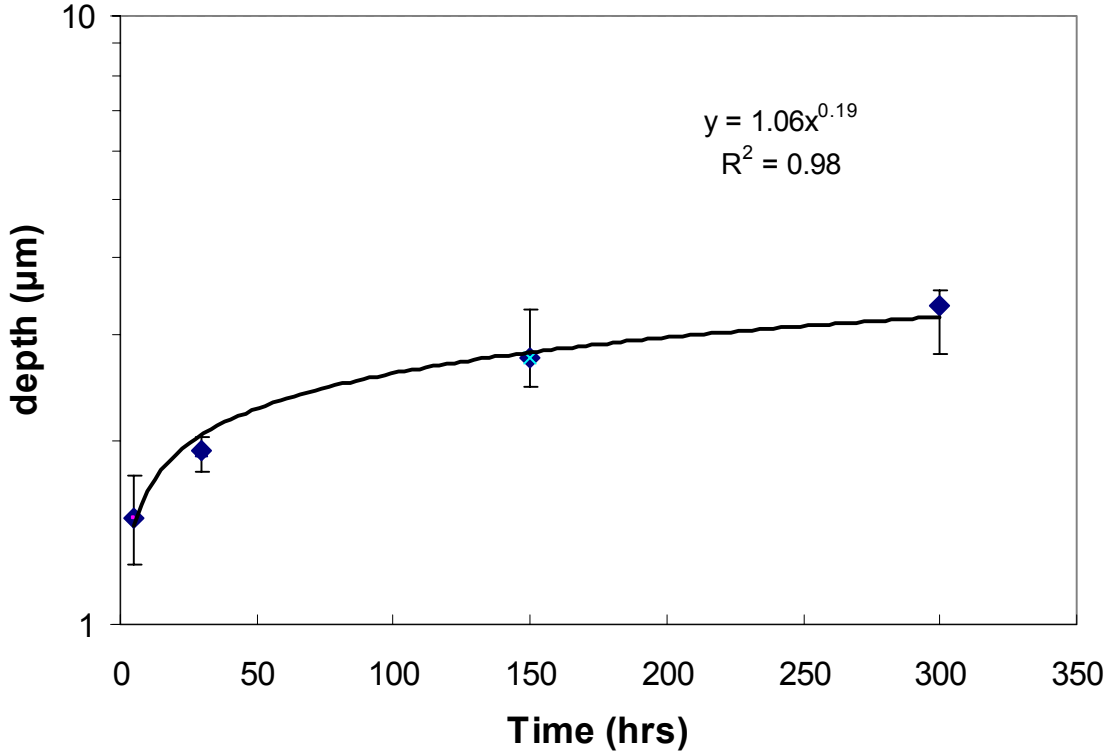

Figure 4-20 γ' Depletion Kinetics at 1050° C

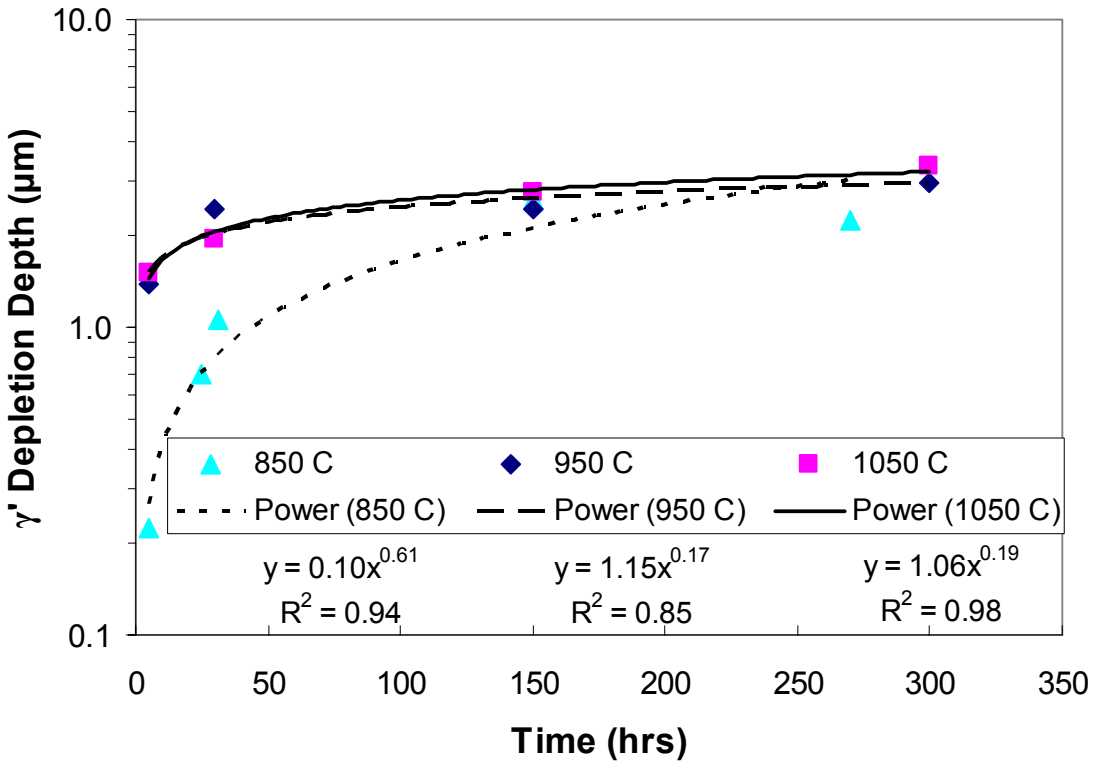

Figure 4-21 γ' Depletion Kinetics for PWA 1484 at 850˚C, 950˚C and 1050˚C

The difference in the time exponent for γ' depletion at the temperatures studied supports the conclusion that different oxides form on PWA 1484 at different temperatures. Energy-dispersive X-ray spectroscopy confirms that at 850°C a combination of Cr_2O_3, CoO and NiO are produced, while at temperatures above 850°C NiO, Al_2O_3 and a spinel dominate. Rezai-Aria et al. [98] Determined that the oxidation kinetics of Mar-M509 followed a different rate law above 900°C than below this temperature, supporting the conclusions here. Furthermore these results indicate that the oxide that forms at 850° C remains transient for considerably longer times than those formed at 950° and 1050° C.

4.4 Analysis

4.4.1 Sensitivity of Surface Roughness

The relationship between surface roughness and γ' depletion kinetics, characterized by the average γ' depletion values, is shown in Figure 4-22.

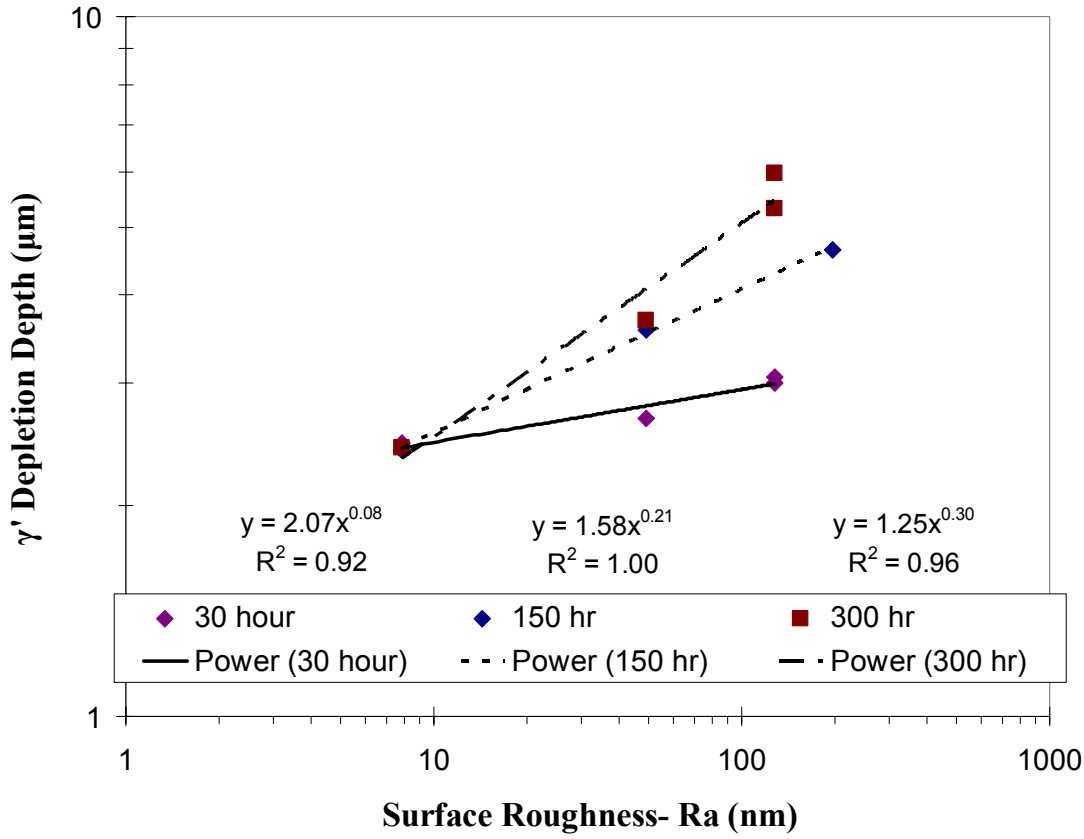

Figure 4-22 Sensitivity of Initial Surface Roughness on γ' Depletion Depth- 1050C

The 150 hour results in Fig 4-22 are shifted compared to the results shown in Fig 4-5. As explained earlier, the exponent on surface roughness for each independent trend line is of importance to this work, therefore shifting of the data does not affect the analysis, as this has no bearing on the exponent value.

A single relationship between γ' depletion kinetics, surface roughness and time of exposure is sought in order to be implemented for materials having different surface roughnesses. The following relationship is proposed for PWA 1484 at 1050˚ C:

$$X_{\gamma'} = A * R_a^{\ b} * t^c \qquad \textbf{(4-2)}$$

where "$X_{\gamma'}$" is the γ' depletion thickness; A, b and c are constants; R_a the arithmetic average surface roughness in nanometers and t is the time of exposure in hours. Values for the constants A, b and c were determined as 0.72, 0.20 and 0.17 respectively. In order to validate Eq 4-2, the correlated γ' depletion thicknesses are compared to the actual values as shown in Figures 4-23 and 4-24

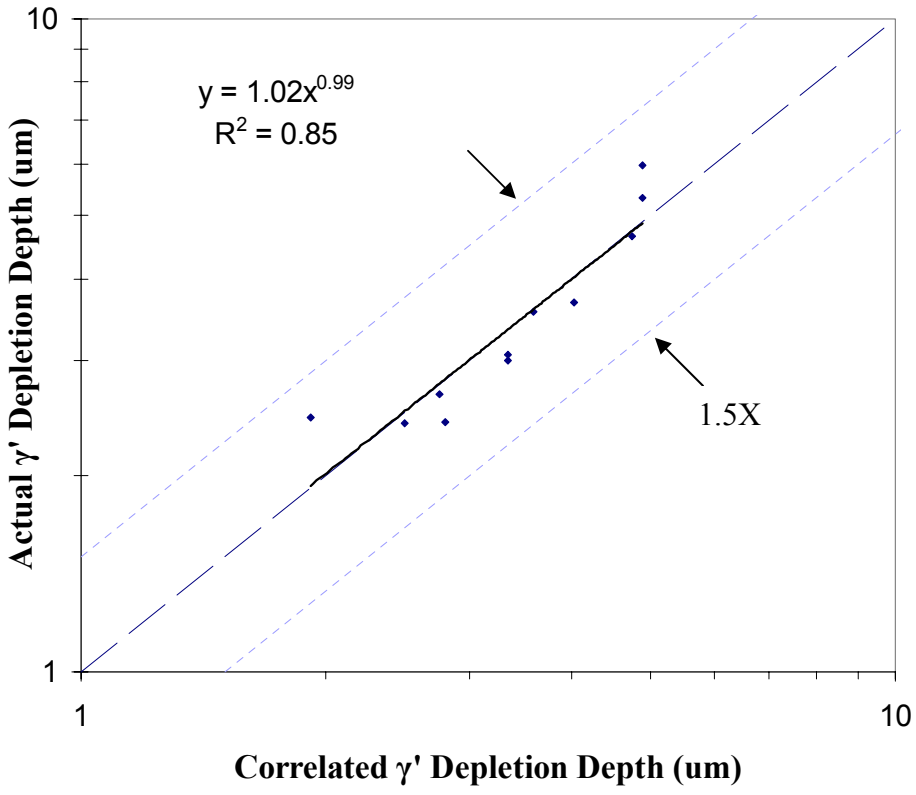

Figure 4-23 Oxidation Surface Roughness Model Validation

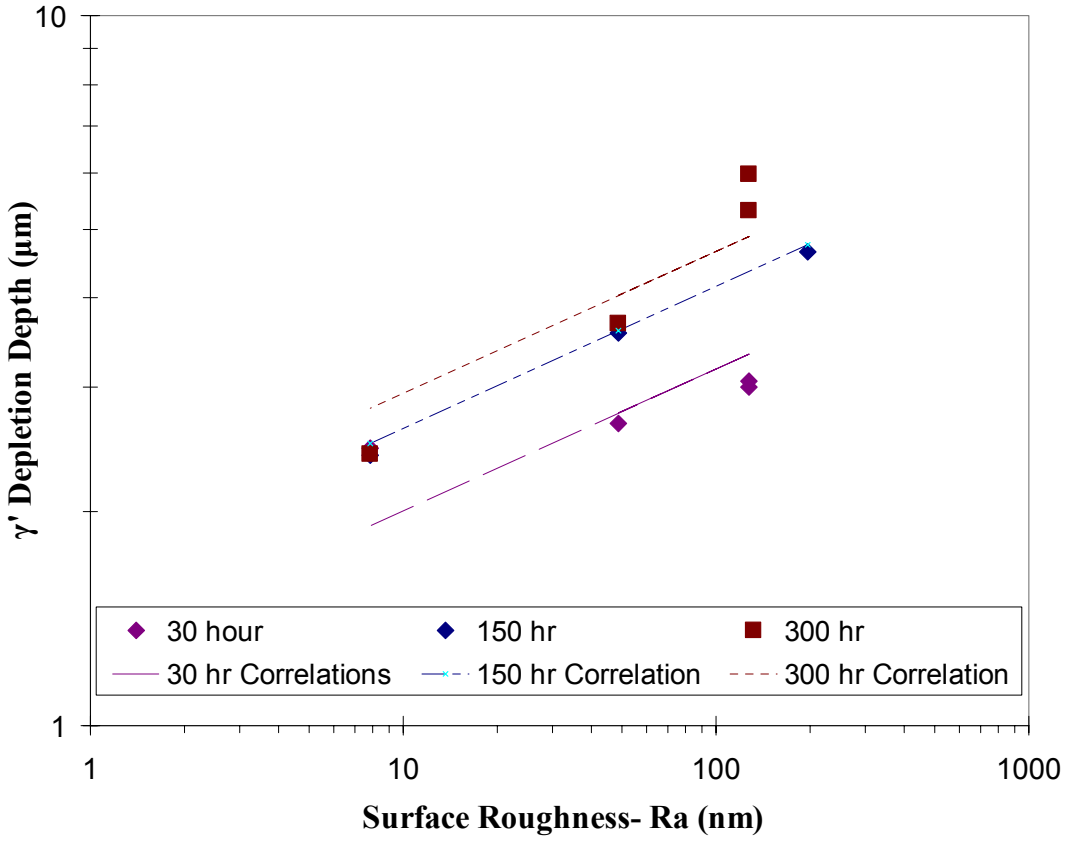

Figure 4-24 Sensitivity of Initial Surface Roughness on γ' Depletion Depth- 1050C. Experimental data and Correlations

The model correlates the effects of surface roughness on γ' depletion, well within a factor of 1.5X from the actual values.

4.4.2 Non-Stressed Oxidation

The primary goal of this section is to derive a single equation for γ' depletion kinetics as a function of temperature and time of exposure. Based upon classical oxidation kinetics [99, 100],

$$X = \left(AD_0 t\right)^n \qquad \textbf{(4-3)}$$

where X is the oxide depth, A is a material dependent constant, D_0 is a temperature dependent diffusion coefficient of Arrhenius form and t is time, an equation of the form [100]

$$X_{\gamma'} = A * \exp\left(\frac{-nQ}{RT}\right) * t^n \qquad \textbf{(4-4)}$$

is expected; where "$X_{\gamma'}$" is the oxidation thickness, A is a material and temperature dependent constant, n is a material dependent constant, Q is an activation energy, R the universal gas constant and T is the absolute temperature. Utilizing the γ' depletion kinetics trends provided in Fig 4-21, an average time exponent of n = 0.31 was established. Comparing the time exponent determined for the γ' depletion kinetics of PWA 1484 to literature data for other alloys, Table 4-9, one finds that the exponent determined here is reasonable and that the majority of the γ' depletion kinetics studies found sub-parabolic trends, i.e. a time exponent n < 1/2.

Table 4-8 γ' Depletion Time Exponent Values: Determined for PWA 1484 and Taken from Literature, GTD 111 [62], Rene N4 [65], CM247LC DS [67]

Superalloy	Temperature (deg C)	Exponent
PWA 1484	850-1050	0.31
GTD 111	871-1093	0.20
Rene N4	1093	0.32
CM247 LC DS	850-1050	0.45

Using this value of n, the activation energy term, n*Q, and the prefactor "A" in Equation 4-3 was determined as shown in Fig 4-25

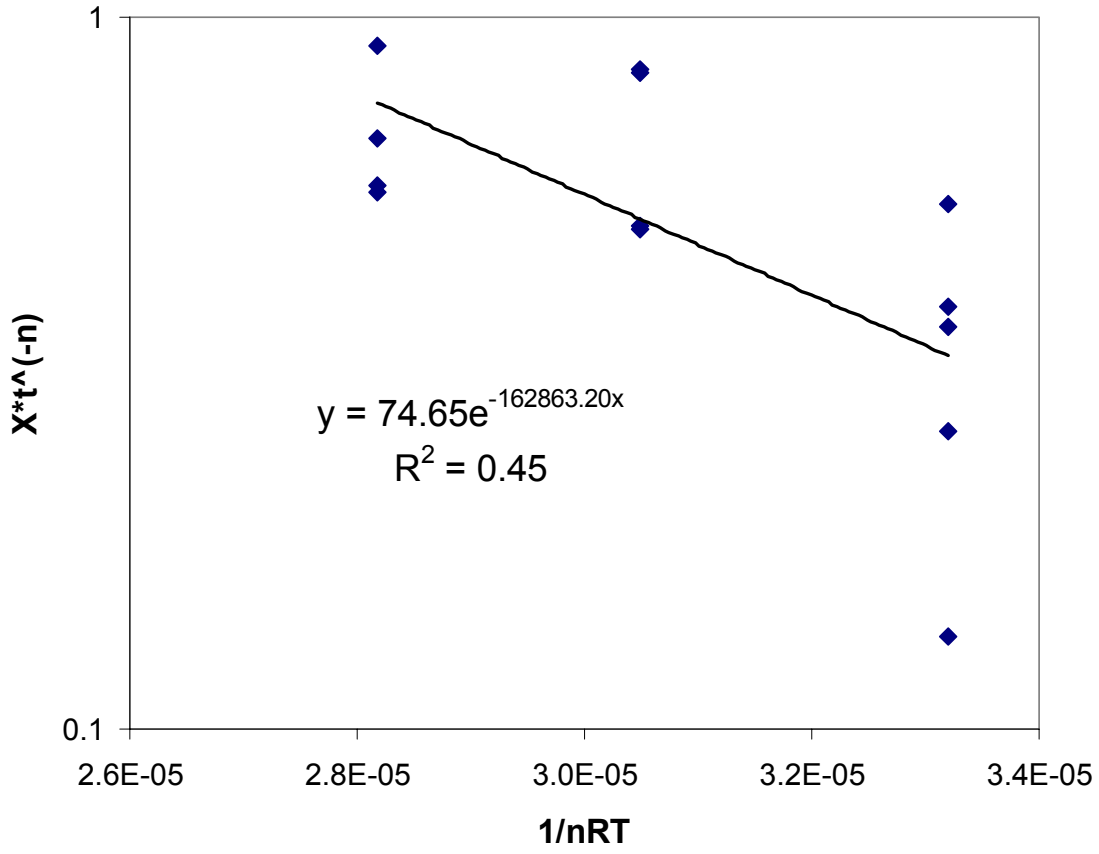

Figure 4-25 Determination of Activation Energy for γ' Depletion,

The values determined for A and Q were 74.65 and 162.9 kJ/mol, respectively. The activation energy for γ' depletion is consistent with ones published in the literature, Table 4-10, but the value determined for A is considerably smaller. Given that γ' depletion data was only collected at three temperatures, and that the kinetics for the 850°C tests result in a wider range of depletion depths, (resulting a wider data band in Figure 4-25) combine to yield the relatively low correlation coefficient (R^2=0.4529).

Table 4-9 γ' Depletion Kinetics Prefactor and Activation Energy: Determined for PWA 1484 and Taken from Literature, GTD 111 [62], MAR-M247 [70], CM247LC DS [67]

Superalloy	Temperature (deg C)	n (-)	A ($\mu m/t^n$)	Q kJ/mol
PWA 1484 SC	850-1050	0.31	74.7	162.9
GTD 111 DS	871-1093	0.2	1153.0	258.5
MAR-M247 PC	500-1000	0.5	8570.0	163.3
CM247LC DS	850-1050	0.45	2766.6	191.1

A large(r) value for "A" would lead to increased oxidation kinetics, relative to a smaller value. The difference in values for the kinetics prefactor in these materials can be explained by comparing the chemical composition of the alloys listed in Table 4-11.

Table 4-10 Chemical Compostion of Superalloys for which γ' Depletion Kinetics are Known

Material	Composition (Weight %)													
	Al	B	C	Co	Cr	Hf	Mo	Re	Ta	Ti	W	Zr	Hf	Ni
PWA 1484	5.6	-	-	10	5	-	2	3	8.7		6	-	0.1	Bal.
PWA 1480	5	-	-	5	10	-	-	-	12	1.5	4	-	-	Bal.
GTD 111	3	0.01	0.1	9.4	14	0.15	1.5	-	3	5	3.7	0.01	-	Bal.
MAR-M247	5.5	0.015	0.15	10	8	1.5	0.6	-	3	1	10	0.03	-	Bal.
CM247LC DS	5.6	0.015	0.07	9.2	8.1	1.4	0.5	-	3.2	0.7	9.5	0.015	-	Bal.

PWA 1484's improvement in oxidation resistance over the first generation alloy PWA 1480 can be attributed to the second generation alloys increase in Al content, a "relatively high Ta content" and the lack of Ti [7]. With this in mind, PWA 1484 is compared to GTD 111, MAR-M247 and CM247LC DS in Table 4-11. The compositional differences that created an oxidation resistance improvement over PWA 1480 also apply to the other alloys compared. The comparison in Table 4-10 is somewhat deceptive, in that a comparison is being made between a single crystal superalloy (PWA 1484) and directionally solidified alloys. One cannot make a direct

comparison as the grain boundaries in the directionally solidified alloys diffuse oxygen at a faster rate than does the matrix [22]. The difference in composition as well as grain boundary diffusion most likely explains the differences in the prefactor "A" between the materials. One will note that the values of the activation energies for GTD 111 and CM247LC DS provided in Table 4-10 are modified from the original literature values. After studying the literature, one determines that these authors likely didn't account for the time exponent acting upon the activation energy, as described by Equation 4-3. The published activation energy values were modified using

$$Q = nQ_{pub} \tag{4-5}$$

where Q is the activation energy provided in Table 4-10, n is the time exponent from the original literature, provided in Table 4-10, and Q_{pub} is the activation energy published by the original authors.

The application of the Equation 4-3 used to predict γ' depletion for all test results is shown in Figure 4-26.

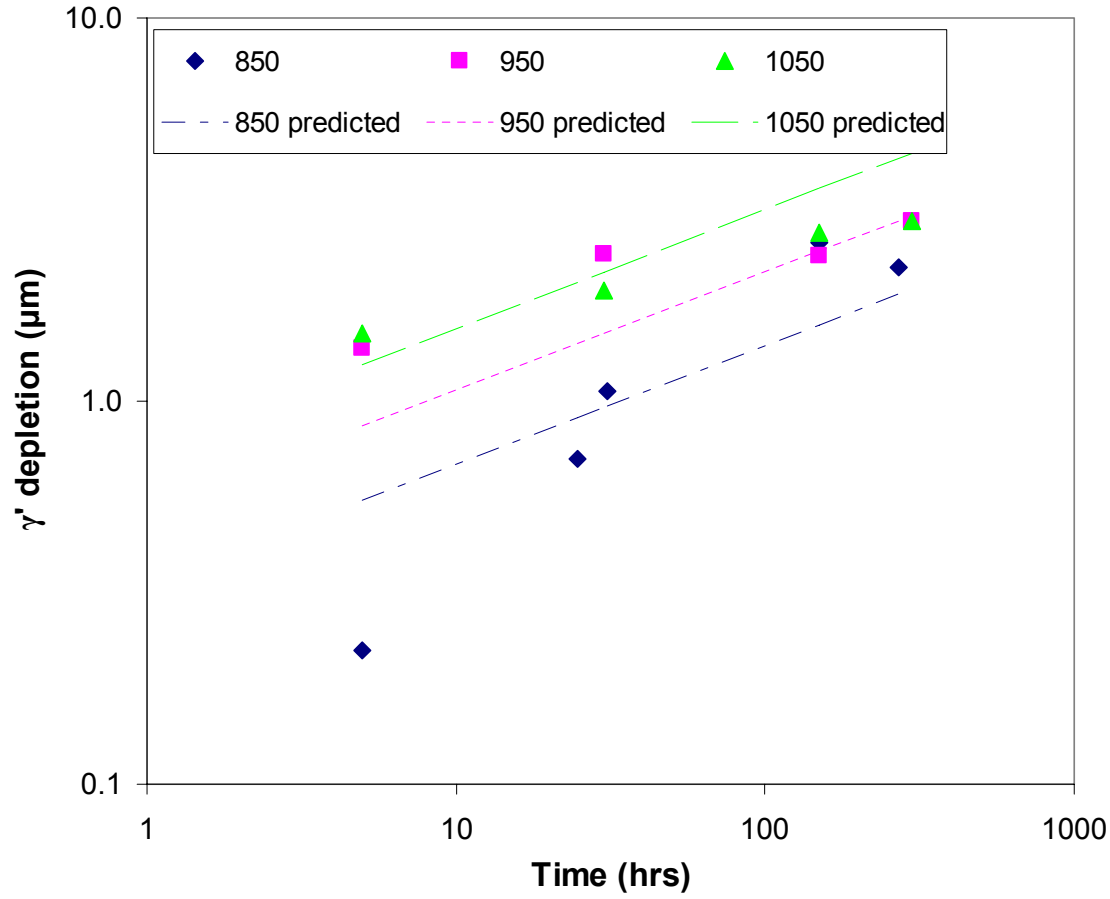

Figure 4-26 γ' Depletion, Actual and Predicted

The 850° C test results indicate that the oxide forming at this temperatures remains transient far longer than do the oxides forming at 950° C and 1050° C. This is depicted by the divergence of actual and predicted values in the 850° C data shown in Fig 4-26.

In order to test the efficacy of the single γ' depletion kinetics equation over the temperature range of 850° C and 1050° C, the model predictions were plotted against the actual experimental values, as shown in Figure 4-27.

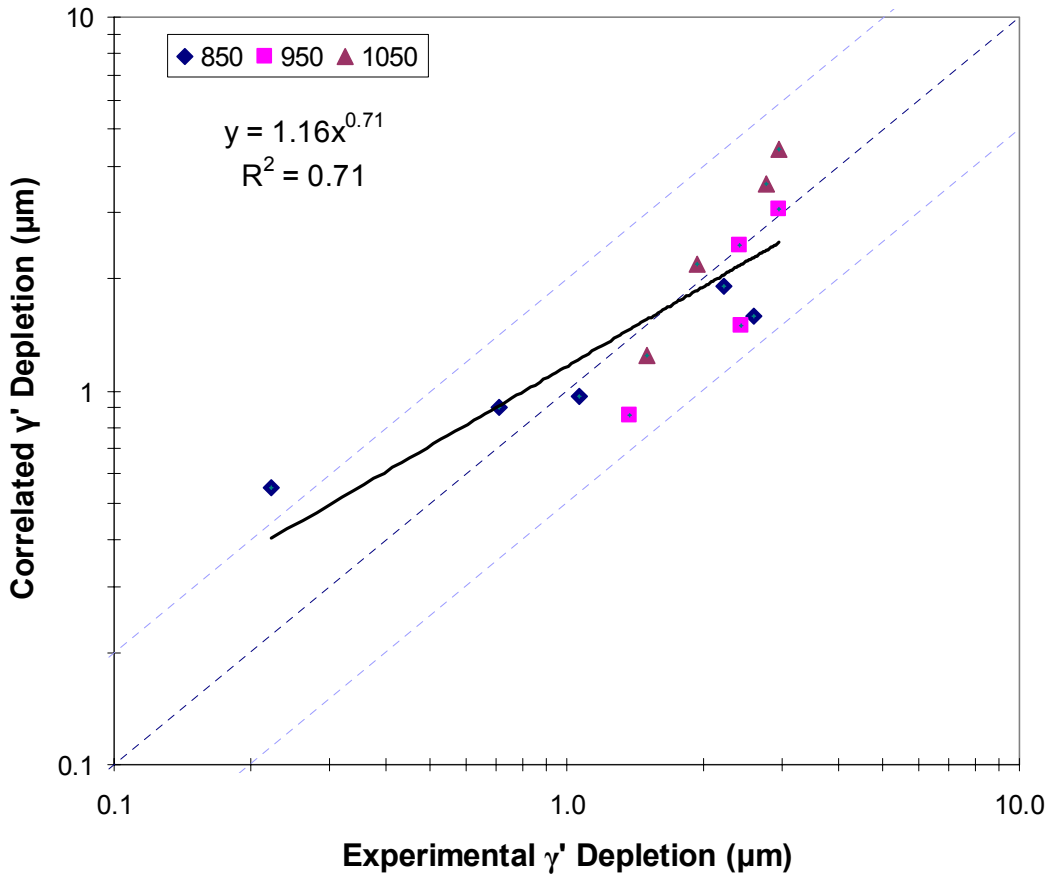

Figure 4-27 Results of γ' Depletion Kinetics Relationship

Figure 4-27 indicates that the relationship determined for γ' depletion does a fair job of predicting this phenomenon, with all predictions but one lying within a factor of two from the actual test data.

4.5 Coupled Fatigue-Oxidation

Tested thermomechanical fatigue and Bithermal fatigue specimens were sectioned transverse to the loading axis in order to characterize the amount of stress-enhanced γ' depletion resulting from the tests. The fatigue tests for which γ' depletion data was recorded is shown in Table 4-12.

Table 4-11 PWA 1484 TMF and BiF Test Data

Baseline Fatigue Tests

Waveform	Orientation	R	Hold time (s)	Δε(mech) (-)	ε_a(mech) (-)	Δε(in) @ Ni/2 (-)	Ni/2 (cycle)	Ni (cycle)	Nf (cycle)	Tmin (deg C)	Tmax (deg C)	Teff (deg C)
OP-TMF*	001	-0.9	0	0.013	0.0065	0.003517	54	107	116	550	1050	953
OP-TMF*	001	-0.9	0	0.009	0.0045	0.000869	236	471	560	550	1050	953
OP-TMF*	001	-1.0	0	0.005	0.0025	0.000065	905	1810	2409	550	1050	953
OP-BiF*	001	-0.8	0	0.013	0.0065	0.002944	38	76	119	550	1050	1002
OP-BiF*	001	-0.9	0	0.009	0.0045	0.000179	185	370	408	550	1050	1002
OP-BiF*	001	-1.0	0	0.007	0.0035	0.000096	211	421	956	550	1050	1002

This data is used to determine the amount of time each specimen experienced temperatures above that for which significant oxidation and γ' depletion occurs, determined to be approximately 800° C [52, 56, 58, 101, 102]. Specifically, the time of exposure was determined using the following equation

$$t = N_f * t_{cycle}^{800} \quad \textbf{(4-6)}$$

where t is the overall exposure time in hours, N_f is the number of cycles to failure and t_{cycle}^{800} is the cycle time at temperatures above 800° C. A plot of γ' depletion versus time of exposure, as determined by EQ 4-5, is shown in Figure 4-28.

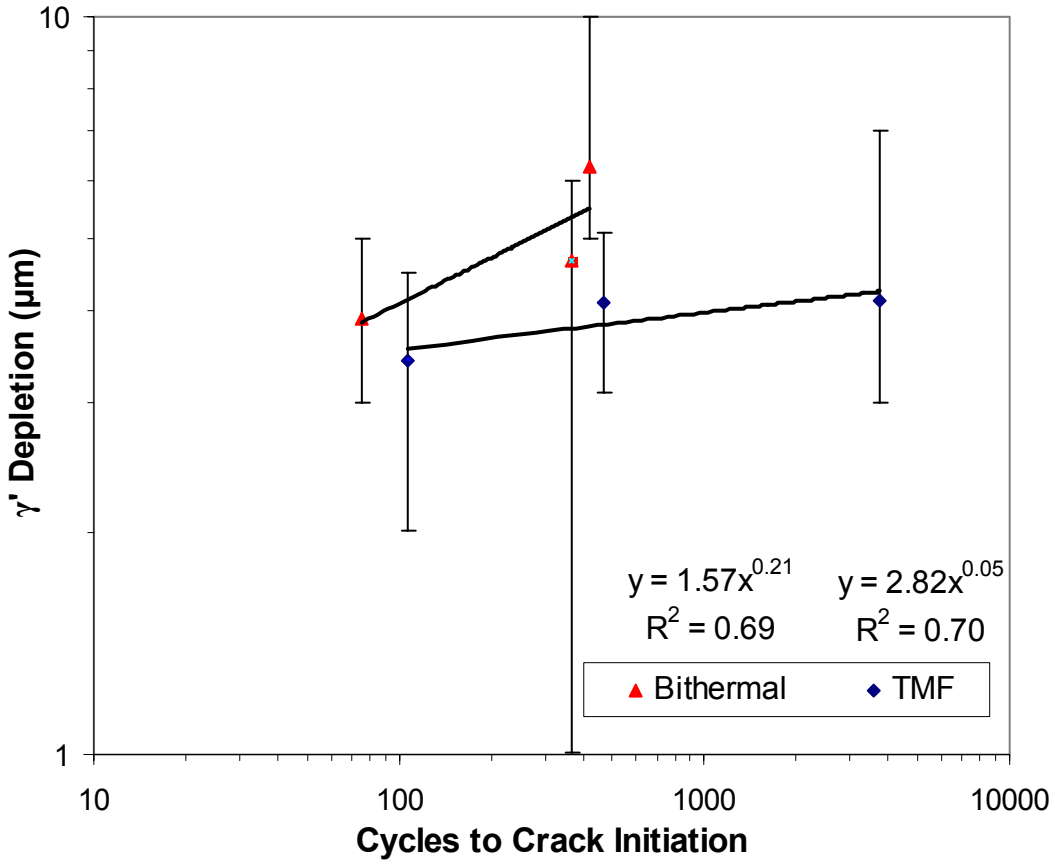

Figure 4-28 γ' Depletion versus Time at Temperatures Above 800° C for PWA 1484 Fatigue Tested Specimens

The stressed and non-stressed γ' depletion results are compared using the effective temperature of the fatigue tests, determined by

$$\exp\left(\frac{-Q}{RT_{eff}}\right) = \frac{1}{\Delta t}\int_{t1}^{t2}\exp\left(\frac{-Q}{RT(t)}\right)dt \qquad \textbf{(4-7)}$$

where Q is an activation energy, R the universal gas constant, t_1 an initial time, t_2 a final time, $\Delta t = t_2 - t_1$, T(t) the fatigue cycle temperature waveform as a function of time, and T_{eff} the effective temperature for the cycle. Solving for the cycle effective temperature,

one can then plot these results along with the stress-free isothermal γ' depletion results, as shown in Figure 4-29.

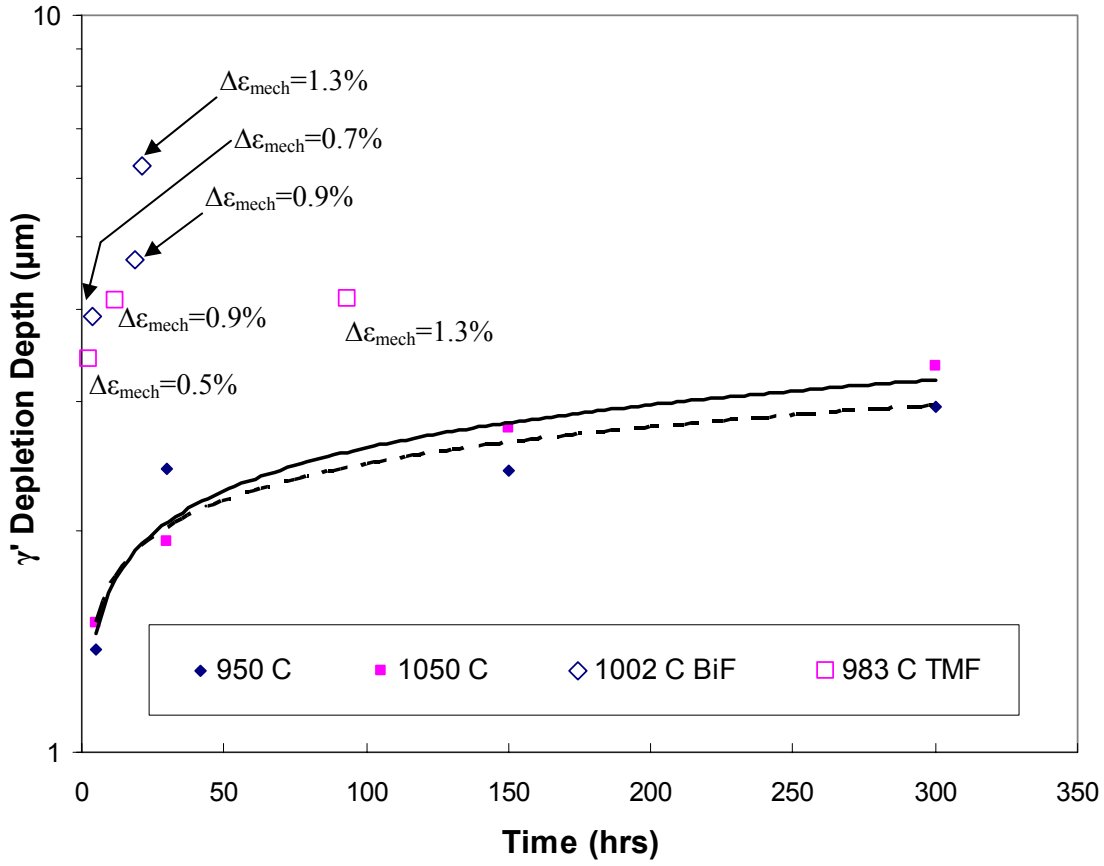

Figure 4-29 γ' Depletion Kinetics for Stressed and Non-stressed specimens

The stress enhanced γ' depletion kinetics are increased over the non-stressed kinetics, as shown in Fig 4-29. An increase in the oxidation and γ' depletion kinetics of superalloys due to the application of stress is well documented [64, 65, 71]. As the application of stress results in increased oxygen and elemental diffusion rates, the results presented in Fig 4-29 follow a reasonable trend.

On a cycle-by –cycle basis, the stress enhanced γ' depletion is related to the non-stressed kinetics by

$$X_{\gamma'}^{stressed} = X_{\gamma'}^{0} B \exp\left(\frac{\overline{V}|\tau_{\min}|}{RT_{eff}}\right) \quad \textbf{(4-8)}$$

where $X_{\gamma'}^{0}$ are the non-stressed kinetics defined by Eq 4-3, B is a constant, $|\tau_{\min}|$ is the absolute value of the minimum shear stress at half life (occurring at 1050°C), $\overline{V}$ is a volume over which the shear stress acts, and R and T_{eff} have their usual meanings.

The inclusion of a stress in the Arrhenius term of a kinetics relationship follows the form from that of other high temperature diffusion based mechanisms (e.g. creep). Furthermore, Reuchet et al. [71] determined a similar relationship for the stressed, short-circuit based, oxidation kinetics of Mar- M509

$$\frac{da}{dN_{ss}} = f_c^* \alpha_c^0 \exp(b\sigma) t^{1/4} \quad \textbf{(4-9)}$$

where $\frac{da}{dN_{ss}}$ is the rate of crack advance due to short circuit oxidation, f_c^* and b are material specific constants, α_c^0 is the non stressed oxidation kinetics which follow an Arrhenius relationship, σ the maximum tensile stress and t the cycle time. One will note that the exponent on time is ¼, rather than the traditional parabolic relationship determined by Wagner for parabolic oxidation [100]. This is due to the short circuit diffusion process being modeled. It has been shown that oxidation along grain boundaries [103] as well as interdendritic oxidation [71] follows a $t^{1/4}$ relationship. This may explain the time exponents determined for non-stressed oxidation at both 950°C and 1050°C. Whereas Eq. 4-8 uses the maximum tensile stress, the minimum shear stress at half life collapsed the stressed kinetics in this study. The minimum shear stress in OP TMF cycles occurs at the maximum temperature. As such the use of the minimum shear

stress in this case accounts for the interaction between the high temperature diffusion and the stresses aiding said diffusion. Furthermore, the use of the shear stress rather than the hydrostatic stress can be understood by the damage processes occurring in this cycle. The shear stress acts as the driving force for dislocations. The dislocation velocity is increased as the temperature is increased. As the dislocations exit the material surface, driven by shear stresses at high temperatures, the oxide scale is broken, thereby exposing the base material to the damaging environment and effectively increasing oxidation kinetics. The dependence of high temperature damage mechanisms on the absolute value of shear stress was utilized by Tinga et al. [104], following the work of Yeh and Krempl [105], in their high temperature damage rule accounting for dislocation climb.

The experimental γ' depletion versus that correlated by Equation 4-7 is shown in Fig 4-30.

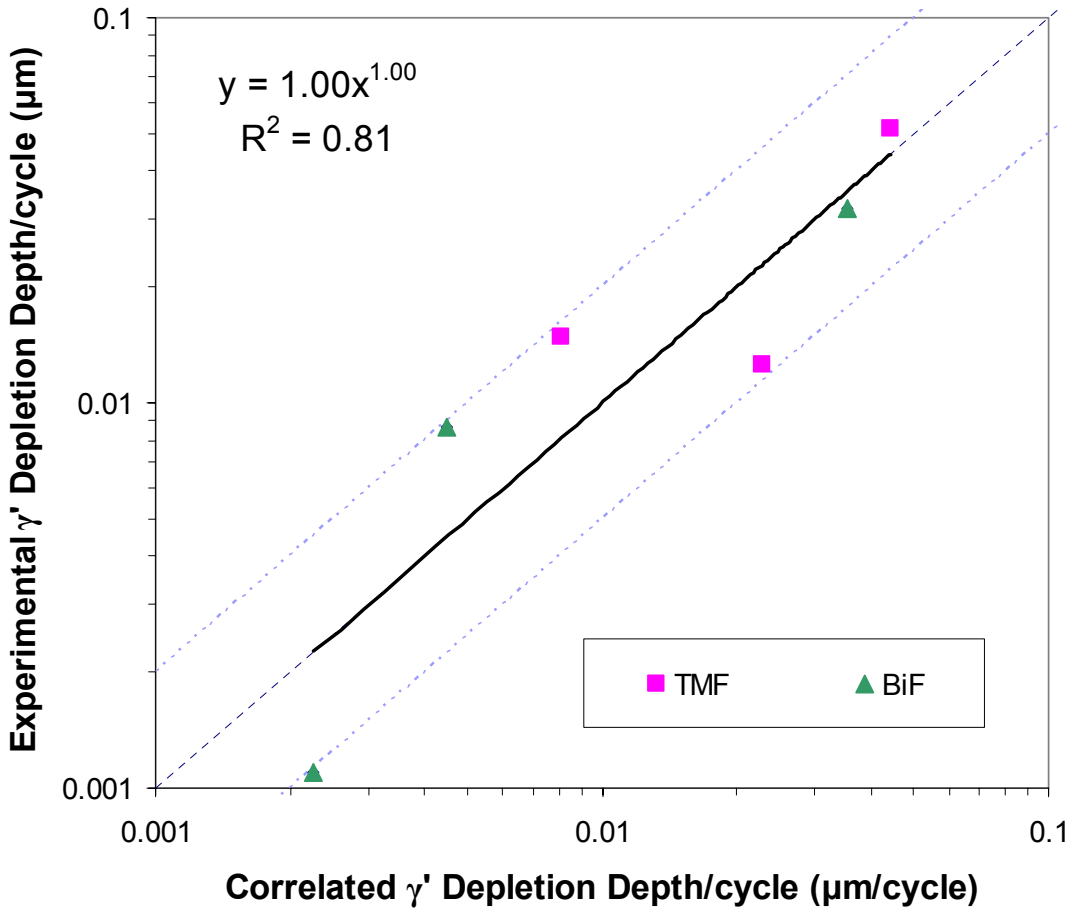

Figure 4-30 Correlated Stress-assisted γ' Depletion Kinetics

The value of B was determined as B = 305 and the volume was determined as $\overline{V}$ =161 m^3/mol.

4.6 Discussion

Based upon the results of this work, and an extensive literature review, it is concluded that PWA 1484 oxidizes in a manner similar to what Giggins and Pettit [50] term a "Transition Alloy". This oxidation behavior is characterized by several stable oxides competing concurrently on the alloy surface and a γ' depleted layer, depending upon temperature and subsurface chemical composition, among other things. The two

most common oxide morphologies consists of either a friable outer spineal ($Ni(Cr,Al,Co)_2O4$) with subsurface α-Al_2O_3 particles, or an outer oxide scale of $(Ni,Co)Al_2O_4$ and $NiCr_2O_4$ spinels with Al_2O_3, and an inner oxide of adherent α-Al_2O_3.

An equation relating γ' depletion kinetics to material surface roughness was proposed and fit to experimental data. The equation

$$X_{\gamma'} = A * R_a^{\ b} * t^c$$

incorporates the surface roughness (Ra) and time of exposure (t) to the γ' depletion depth $X_{\gamma'}$. The relationship does a good job of predicting the effects of surface roughness upon oxidation kinetics for specimens tested at 1050° C. It is understood that this is the first high-temperature study which explains the sensitivity of surface roughness on γ' depletion kinetics. Additionally, a single relationship based upon classical diffusion kinetics was proposed which predicts the non-stressed γ' depletion kinetics, $X_{\gamma'}^0$, for PWA 1484 between 850° C and 1050° C.

$$X_{\gamma'}^0 = A * \exp\left(\frac{-nQ}{RT}\right) * t^n$$

One should note that the oxidation kinetics, and resulting surface oxides, at 850° C are different than those at 950° C and 1050° C. As such the activation energy determined here should be thought of as an "effective" activation energy for the γ' depletion processes occurring between these temperatures. None-the-less, the predictive capabilities of the γ' depletion kinetics relationship is sufficient for engineering purposes.

Finally, a relationship is proposed which links the non-stressed γ' depletion kinetics to the kinetics found after TMF and BiF testing by

$$X_{\gamma'}^{stressed} = X_{\gamma'}^{0} B \exp\left(\frac{\overline{V}|\tau_{\min}|}{RT_{eff}}\right)$$

where $X_{\gamma'}^{0}$ are the non-stressed kinetics defined by Eq 4-3, B is a constant, $|\tau_{\min}|$ is the absolute value of the minimum shear stress at half life (occurring at 1050°C), $\overline{V}$ is a volume over which the shear stress acts, and R and T_{eff} have their usual meanings. This relationship accounts for the stress-enhanced oxidation occurring by short-circuit diffusion along shear driven dislocation networks. The stress-enhanced γ' depletion kinetics relationship will be used in Chapter 6 as part of the formulation of the OP TMF life predictive model.

CHAPTER 5. SLIP BAND SPACING

5.1 Introduction

The purpose of this study is to determine a relationship for the slip band spacing as a function of inelastic strain and temperature. Cracks tend to initiate at a location where slip steps, in the case of monotonic loading, and persistent slip bands, in the case of cyclic loading, impinge upon the materials free surface [106]. Furthermore, OP TMF lives are typically limited by the interaction of low(er) temperature plastic strains and environmentally degraded material. The slip band spacing defines the probability of forming a crack at an environmentally degraded boundary. Isolating and quantifying the kinetics of these mechanisms will enable the future implementation of this relationship into a coupled fatigue-environmental physics-inspired model. Hence the careful measurement of the slip band spacing is critical to understanding the evolution of inelastic deformation as a function of temperature and applied strain as well as interaction with environmentally effected regions of the material. Furthermore this analysis is critical for the complete understanding of fatigue interactions occurring in thermomechanical fatigue. The relationship resulting from this study, specifically determined for the single crystal superalloy PWA 1484, would shed light upon the crack formation processes occurring as a result of the OP TMF tests performed for this research.

5.2 Slip Band Spacing Hypothesis

Slip steps produced on the material surface as a result of the application of monotonic plastic strain are more defined than the PSB's and their associated intrusions

and extrusions produced from cyclic straining [106]. Furthermore strain in Ni-base superalloys, e.g. Nimonic 90, tends to localize in a few deformation bands from the very first cycle [107]. The notion that all slip planes activated for a given amount of inelastic strain occurs during the initial cycle is supported by multiple studies [26, 28, 31, 108]. In fact, one such study determined that the deformation structure of the single crystal superalloy SC16 was unaffected by load reversals [45]. Shyam and Milligan [26], when considering cycle type for a similar analysis concluded that "While the deformation is monotonic instead of cyclic, substantial insight into the deformation behavior can still be gained from these types of studies". Therefore, one might assume that a single cycle may be indicative of the deformation resulting from a particular value of applied inelastic strain. Results provided here, however, do not support this notion.

Given that slip band formation at temperatures below $0.4*T_m$ (where T_m is the material melting temperature) is dependent upon dislocation glide, and to a lesser extent cross slip and climb, and that dislocation movement through the material matrix is dependent upon the amount of energy imparted to the system, one might assume that the relationships in Equations 2-5 and 2-6, determined for a single temperature, can be expanded to include a temperature range using an Arrhenius form. Specifically, one might use a functional form similar to the rate equation for lower-temperature discrete-obstacle controlled plasticity, which has the form [25]

$$\dot{\gamma} = A\tau_s^{\,n} \exp\left[\frac{-\Delta F}{kT}\left(1-\frac{\tau_s}{\hat{\tau}}\right)\right] \qquad \textbf{(5-1)}$$

where $\dot{\gamma}$ is the strain rate; A is a lumped parameter which includes the Burgers vector, shear modulus, dislocation velocity and the shear stress; ΔF is the total free energy

(activation energy) required to overcome an obstacle without the aid of an external stress; k the Boltzmann constant; T the absolute temperature; τ_s the shear stress; $\hat{\tau}$ the flow strength at 0 K. Due to the essentially two-phase microstructure of PWA 1484, one can readily assume that the rate of dislocation movement, and hence slip band formation, is primarily controlled by the γ' phase.

The monotonic data provided in [31] and shown in Table 5-1 provide a basis for the functional form of a slip band spacing relation as a function of temperature. The slip band spacing, C, can be related to the applied inelastic strain, $3\% < \varepsilon^{in} < 25\%$, as a function of temperature, T, for the polycrystalline superalloy KMA by

$$C = B\left(\varepsilon^{in}\right)^{n} \exp\left(\frac{Q}{RT}\right) \qquad \textbf{(5-2)}$$

where B and n are material specific fitting parameters, Q an activation energy in kJ/mol, R the universal gas constant (8.314 J/mol-K) and T the absolute temperature. Upon calibrating Eq 5-2, the following parameter values were determined: B=2.16, n=-0.53 and Q=3.00 kJ/mol. The correlated slip band spacing compared to the actual values provided in Table 5-1 are shown in Figure 5-1.

Table 5-1 Slip Band Spacing as a Function of Inelastic Strain and Temperature [31]

The average values of slip line spacing (L_{av}) and slip offset values (δ_{av}) from all conditions studied in this investigation

	20 °C		550 °C			650 °C
	$\varepsilon_p \sim 3\%$	$\varepsilon_p \sim 25\%$	$\varepsilon_p \sim 3\%$	$\varepsilon_p \sim 9\%$	$\varepsilon_p \sim 25\%$	$\varepsilon_p \sim 3\%$
L_{av} (μm)	4.80	1.14	2.15	1.06	0.70	1.35
δ_{av} (nm)	63.8	86.9	43.4	44.6	62.3	31.0

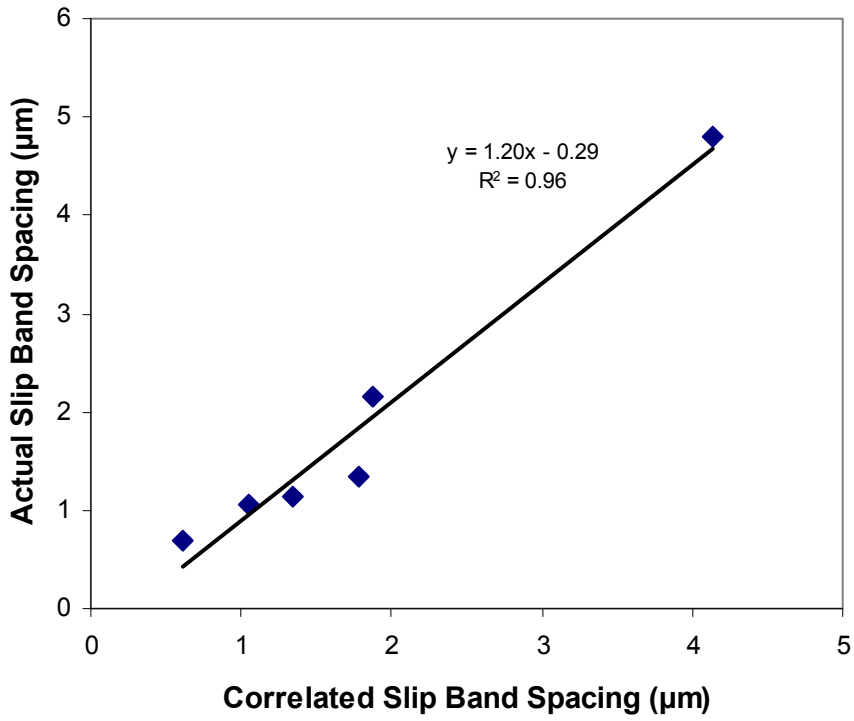

Figure 5-1: Actual Slip Band Spacing Versus Estimates Provided By Equation 3. Data From [31]

Expanding upon the above analysis of the results provided by [26, 31], it is hypothesized that the slip band spacing, C, in the single crystal superalloy PWA 1484 is also related to the inelastic strain and temperature by Eq. 5-2 Furthermore, based upon the arguments of [26, 28, 31, 45, 107, 108], one presumes that the inelastic strain in a monotonic test will sufficiently describes the deformation produced from a cyclic test having a maximum strain equal to that in the monotonic test, so long as subsequent yielding does not occur in the opposite loading direction. This hypothesis will be tested through cyclic slip band spacing tests.

5.3 Experimental Procedure

5.3.1 Test Matrix

The objective is to develop a relationship for the slip band spacing of PWA 1484 as a function of inelastic strain and temperature. Uniaxial tensile tests were performed to determine the effects of temperature and inelastic strain upon slip band spacing for this alloy. A single specimen was tested at each temperature. A specimen was loaded to an initial strain in strain control and then unloaded to zero force in force control. The inelastic strain for each test was determined as the mechanical strain at zero force after unloading. After each strain increment the specimen was removed and pictures were taken at 50X and 100X zoom using an Olympus BX40 optical microscope fitted with an Olympus digital camera. The pictures were then stitched together manually in an Excel document so that the entire gage section was visible in a single picture. The slip band spacing was measured, and that same specimen was strained an additional amount, and so on until the final strain value was reached for that temperature.

Tests were performed on smooth specimens of "dog bone" style conforming to ASTM E606 [109]. Figure 5-2 shows the geometry and surface finish of the specimens as supplied. Additionally, the specimens were polished to a nominal 7.8 nm surface finish (mirror finish) using P1200 and P4000 grit SiC paper. Argon was used in the higher temperature tests to help minimize oxidation formation so that slip bands could be easily identified on the specimen surface.

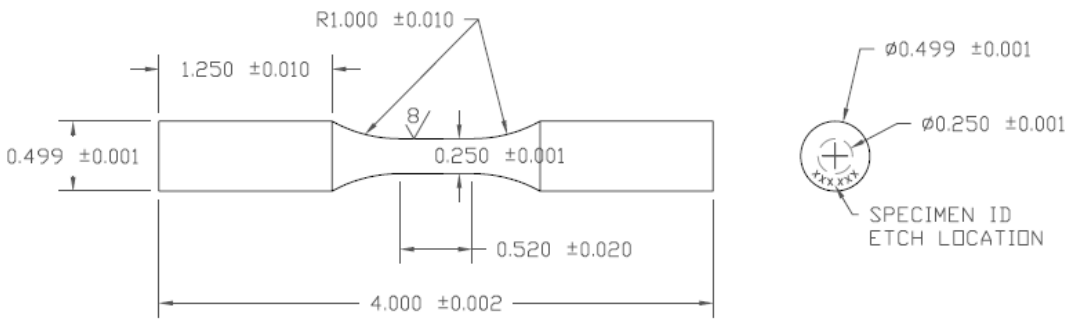

Figure 5-2: Slip Band Spacing Specimen Geometry (all dimensions in inches)

The test matrix for monotonic slip as a function of temperature is provided in Table 5-2.

Table 5-2: Test matrix for Determination of Slip Band Spacing Morphology

Test #	Temp (deg C)	ε_{mech} (%)	ε' (1/s)
1	21	0.9	0.0003
		1.3	0.0003
		2.0	0.0003
2	450	1.1	0.0003
		1.3	0.0003
		1.5	0.0003
3	550	1.1	0.0003
		1.6	0.0003
		2.2	0.0003
4	650	1.1	0.0003
		1.5	0.0003
		2.1	0.0003

The test temperatures were chosen to ensure that dislocation climb and elemental diffusion were not activated during the tests and that γ' shearing was the primary deformation mechanism. The minimum inelastic strain values were chosen based upon the known yield behavior of the material at each temperature value, with the subsequent strain values simply being incrementally larger. The strain rate used for these tests was

chosen in an attempt to minimize strain burst effects during testing, as this phenomenon has been reported by other researchers on similar materials [33].

In order to test the hypothesis that slip system activation, for a given amount of inelastic strain, is localized in the material within the first cycle, room temperature fatigue tests were performed in strain control for loading and force control for unloading. The test was stopped after 1 cycle, 5 cycles, 20 cycles and 50 cycles, the specimen was removed and the slip spacing determined. The specimen was then placed in the test machine and cycled further. In the first test, the specimen was loaded to a mechanical strain of $\varepsilon_{mech} = 0.9\%$, then unloaded to zero stress. The subsequent tests were performed at a $\Delta\varepsilon_{mech} = 0.765\%$, $\varepsilon_{max} = 0.9\%$ corresponding to a strain ratio $R_\varepsilon = 0.15$.

5.3.2 Test Equipment

Uniaxial tests were performed on an MTS 44.5 kN (10 kip) axial closed-loop servo hydraulic test frame. The load cell resolution for this system is +/- 0.22 kN. Specimens were gripped using MTS 646 water cooled hydraulic collet grips. The test system was controlled by a two-channel MTS Teststar Classic controller using Testware SX software. Induction heating using the coil shown in Fig 5-3 (consisting of a seven-loop 23 mm ID copper coil, made of 4.76mm OD (3/16") tubing) was used to heat the specimens. Two Type K thermocouples were welded to the specimen at the radius-gage section transition, just outside the gage section. Axial strain was measured using a 12.7mm (0.500") gage MTS model 632.52E-14 high temperature extensometer with 130mm long (nominal) ceramic rods with V-chisel ends. The extensometer has an

operating range of 20% strain and was calibrated to +/- 2% amplitude to ensure sufficient strain resolution. A picture of the test system is provided in Figure 5-3.

Tests performed at higher temperatures employed an "environmental chamber", shown in Fig 5-3. Industrial purity argon (99.5%) was supplied to this chamber at two locations, 180° apart. The oxygen content in the chamber was reduced from that typical of air (22.2% O_2) to below 1.0% O_2, as measured by Oxigraf Model 02L oxygen analyzer.

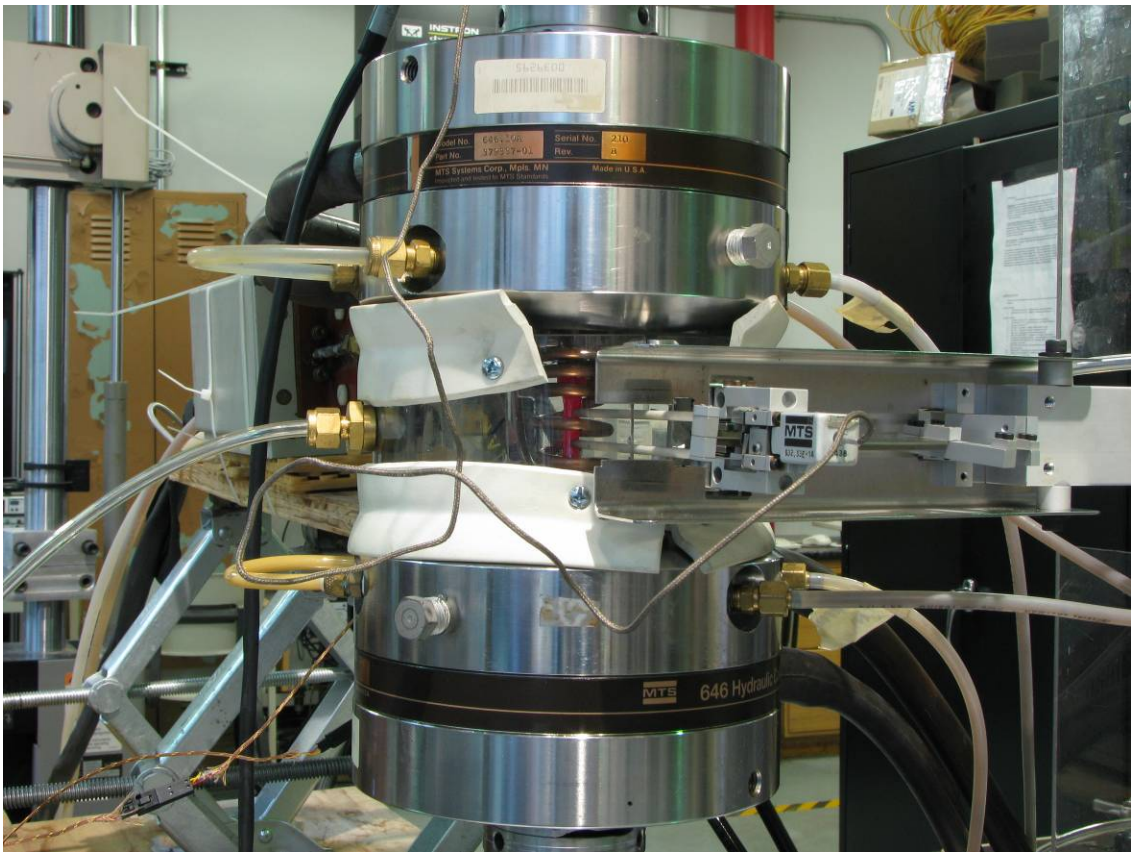

Figure 5-3: Slip Band Characterization Experimental Set Up With Environment Chamber

5.4 Experimental Results

5.4.1 Measurement of Slip Band Spacing

Specimens were observed to have either sparse slip, shown in Fig 5-4, or homogeneous slip, shown in Fig 5-5. The slip band spacing observed on specimens with sparse slip was measured differently from specimens having homogeneous slip. The average apparent spacing for sparse slip specimens (d_{app}) was determined by dividing the specimen reduced section length (13.21mm) by the total number of slip bands. The average apparent slip spacing (d_{app}) for homogeneous slip was determined by counting the number of slip bands that intersected a line drawn collinear to the axial centerline of the specimen (nominally [001] crystallographic orientation) and dividing the line length by the total number of slip bands. The minimum length used for homogeneous slip spacing determination was 2.0 mm. Dividing the line length by the number of slip bands intersecting the line provides the average apparent spacing for the specimen.

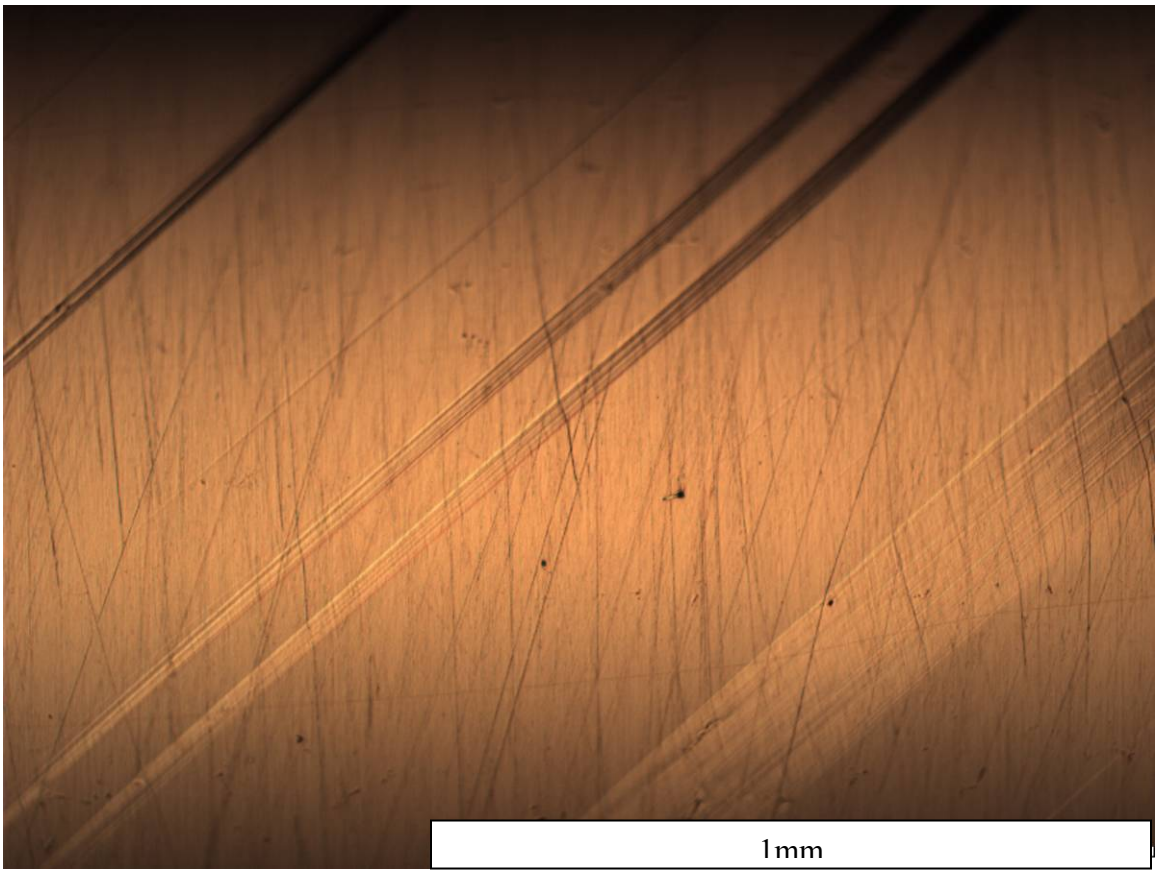

Figure 5-4 Gage Section of PWA 1484 After Monotonic Tensile Testing at 25° C, ε_{in} = 0.672%- Example of Sparse Slip

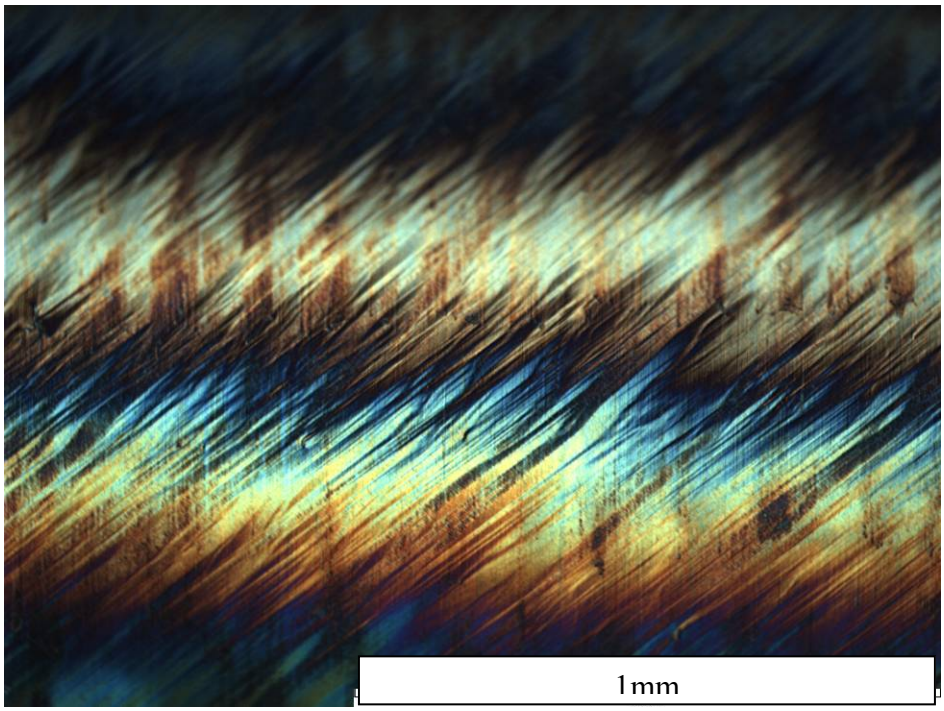

Figure 5-5 Gage Section of PWA 1484 After Monotonic Tensile Testing at 650° C, ε_{in} = 0.757%- Example of Homogeneous Slip

Slip occurs on the {111} planes on FCC crystals. As the specimens used in this study were of nominal <001> orientation, the slip bands traced an ellipse as they intercepted the surface. For perfect [001] specimen orientation, the normal to the slip band would be oriented at an angle of θ=54.74° from the loading axis, as determined by

$$\theta = \cos^{-1}\left(\frac{(001)\bullet(111)}{\|(001)\| * \|(111)\|}\right) \qquad \textbf{(5-3)}$$

However, the longitudinal axis of the specimens used in this work deviated from <001>. The minimum <001> deviation was 2.8° and the maximum deviation was 6.9°. In order to determine the true slip band spacing, pictures were taken at two quadrants of the cylindrical specimen, 90° apart, such that two quadrants of the surface-intercepting ellipse were recorded (see Fig 5-6). In this way the primary angle between the slip band

and the specimen centerline (ϕ) could be determined using the following procedure: (1) The normal to the slip plane was determined using $\vec{n} = \vec{a} \times \vec{b}$, where $\vec{a}$ and $\vec{b}$ are defined similar to that shown in Figure 5-7; (2) the angle between the slip plane normal and the loading direction (001) was determined using $\phi = \cos^{-1}\left(\frac{(001) \bullet \vec{n}}{\|(001)\| * \|\vec{n}\|}\right)$.

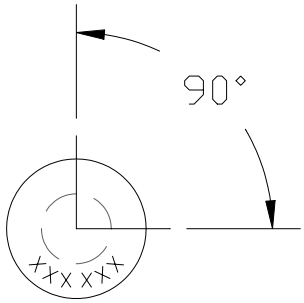

Figure 5-6 Schematic Indicating Axial Locations of Pictures Used in Slip Plane Normal Determination

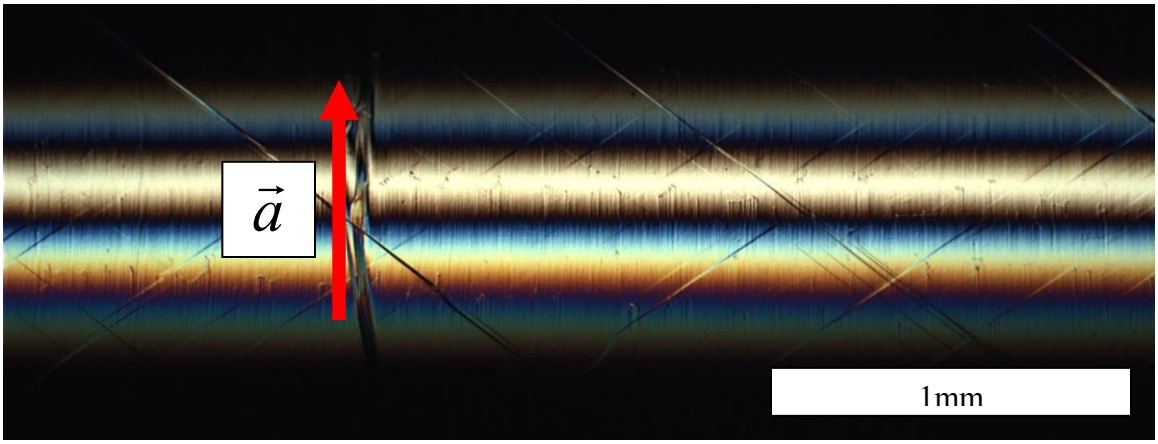

(a)

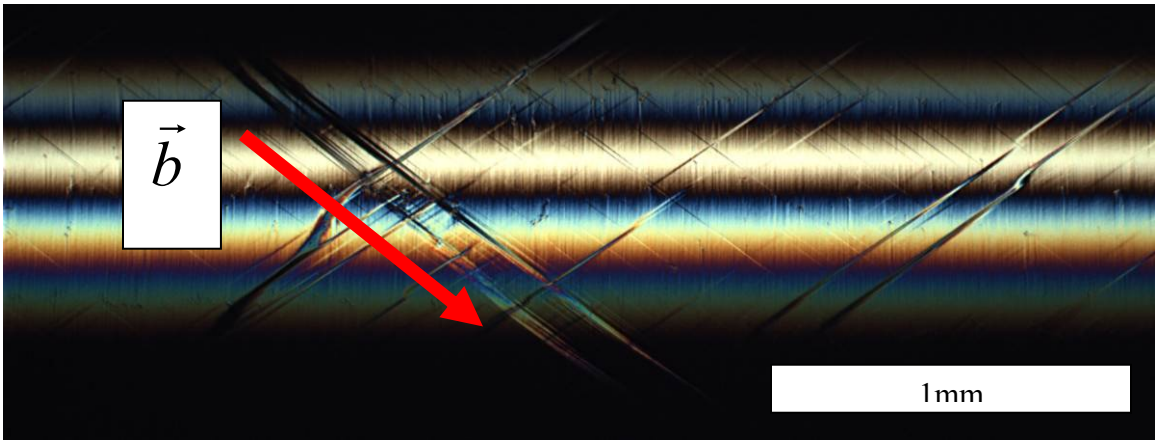

(b)

Figure 5-7 Figures Indicating Method for Determining Orthogonal Vectors Defining Slip Plane: (a) Apex of Minor Axis, (b) Apex of Major Axis

A rigorously correct estimate of slip band spacing was then determined using

$$d_{corr} = d_{app} \bullet \cos(\phi) \qquad \textbf{(5-4)}$$

where d_{corr} is the corrected slip band spacing, d_{app} is the apparent spacing defined above and ϕ is the angle made between the slip band normal and the specimen centerline. For loading precisely applied in the (001) orientation a Schmid analysis indicates that 8 slip

systems would be activated simultaneously, four of which may be visible on a specimen. Often multiple slip systems were activated during slip band testing, as shown in Fig 7. However, only slip band spacing from a single slip system are compared with subsequent strain tests.

5.4.2 Cyclic Slip Results

A stress-strain plot for all cyclic slip band tests is shown in Figure 5-8 and the results are summarized in Table 5-3.

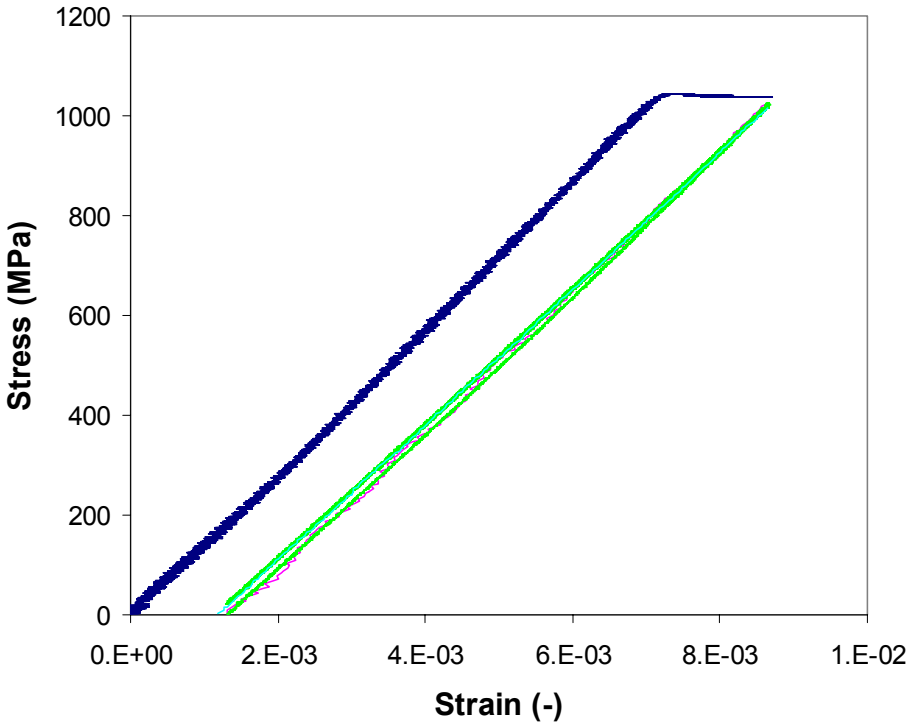

Figure 5-8 Stress-Strain Curves for Room Temperature Cyclic Slip Tests

Table 5-3 Room Temperature Cyclic Slip Band Spacing Results

	# of Cycles	# of Slip Bands	Apparent Spacing (mm)	Angle (deg)	Corrected Spacing (mm)
Side 1	1	103	0.1282	34.4	0.0724
	6	101	0.1308	34	0.0731
	26	117	0.1129	34.3	0.0636
	76	136	0.0971	34.1	0.0544
Side 2	1	83	0.1591	34	0.0890
	6	91	0.1451	34.5	0.0822
	26	90	0.1468	34.3	0.0827
	76	101	0.1308	34.1	0.0733
Side 3	1	99	0.1334	37.9	0.0820
	6	110	0.1201	38.6	0.0749
	26	125	0.1057	37.8	0.0648
	76	138	0.0957	38.1	0.0591

Slip spacing decreases with increasing strain cycling. Slip band spacing as a function of cycles is shown in Figure 5-9.

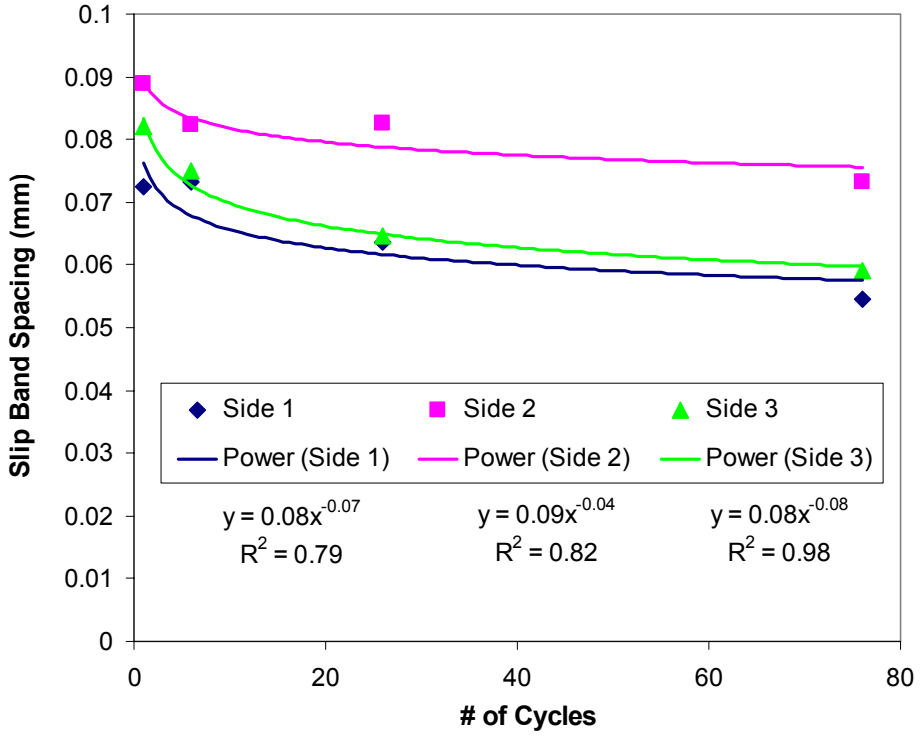

(a)

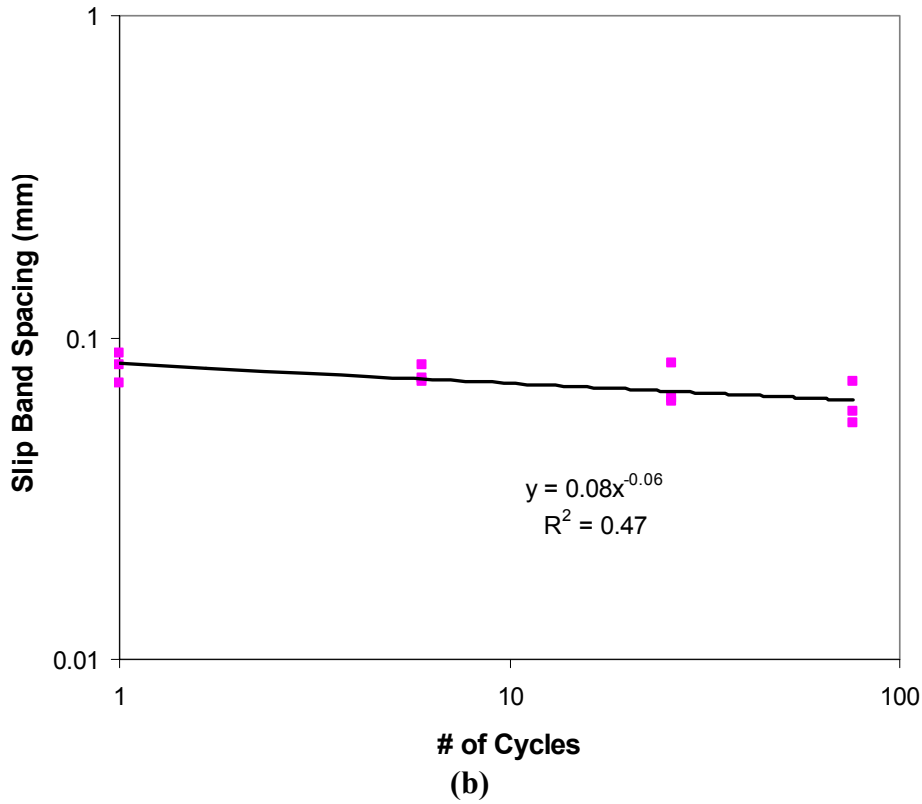

(b)

Figure 5-9 Slip Band Spacing as a Function of Cycles: (a) 3 Locations Corresponding to Different Slip Systems, (b) All Data

The power law relationship between slip band spacing and number of cycles does indeed indicate that as the number of cycles increase, more slip bands are activated, thereby decreasing slip band spacing. The results do not support the hypotheses of [26, 28, 31, 108]. The exponent on cycles, -0.06, however, is quite small.

5.4.3 Monotonic Slip Results

The stress-strain responses for monotonic slip tests performed at each temperature are shown in Figures 5-10 through 5-13.

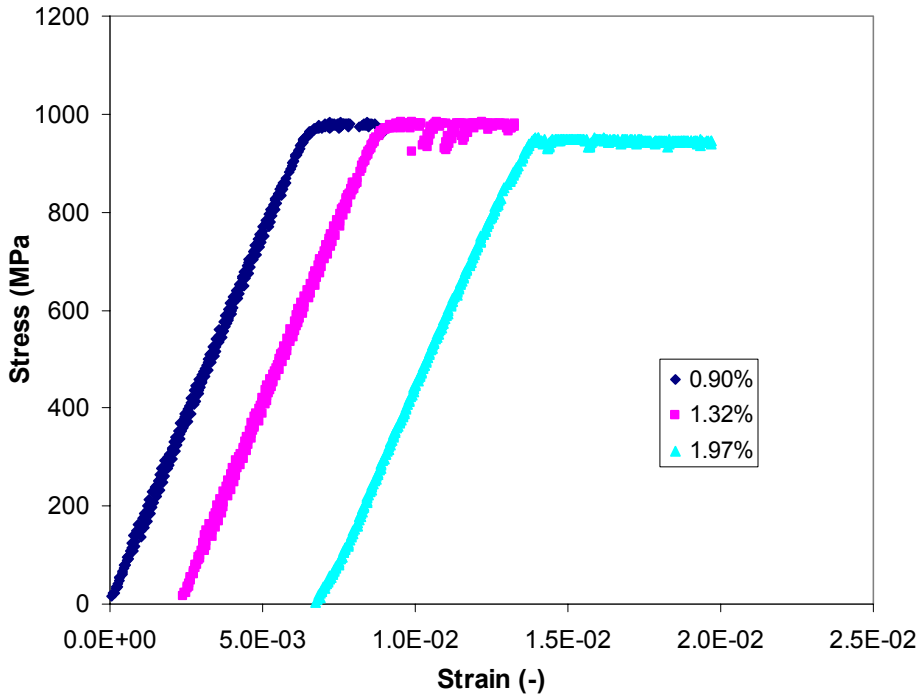

Figure 5-10 Stress Strain Response at 21° C

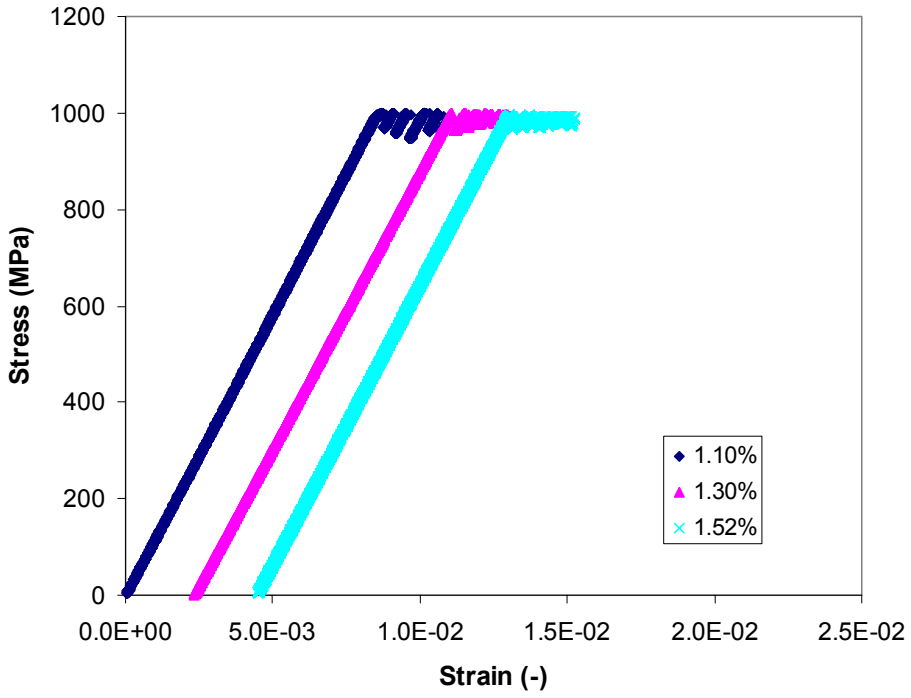

Figure 5-11 Stress Strain Response at 445° C

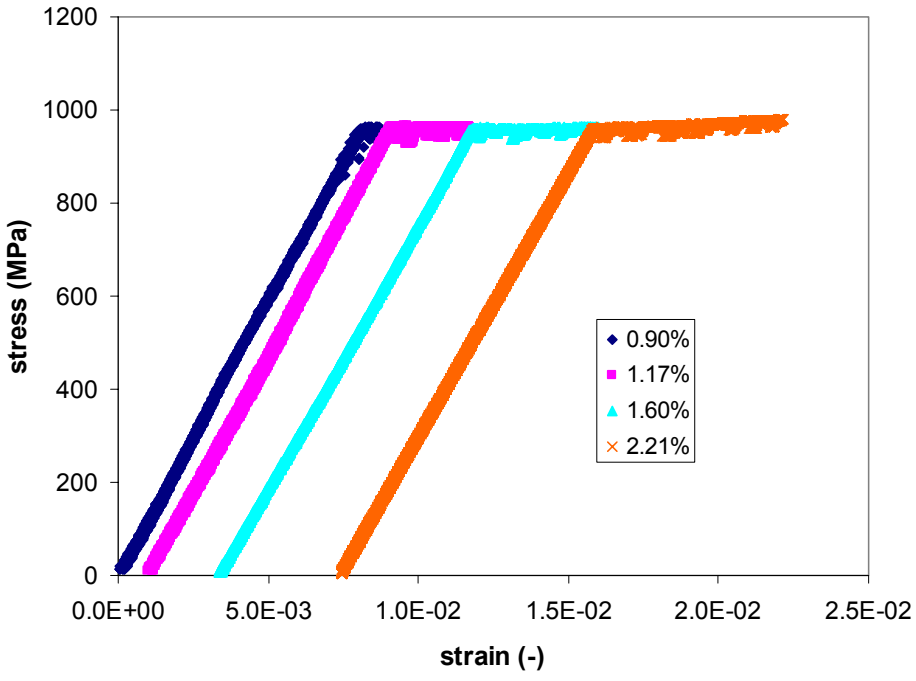

Figure 5-12 Stress-Strain Response at 545° C

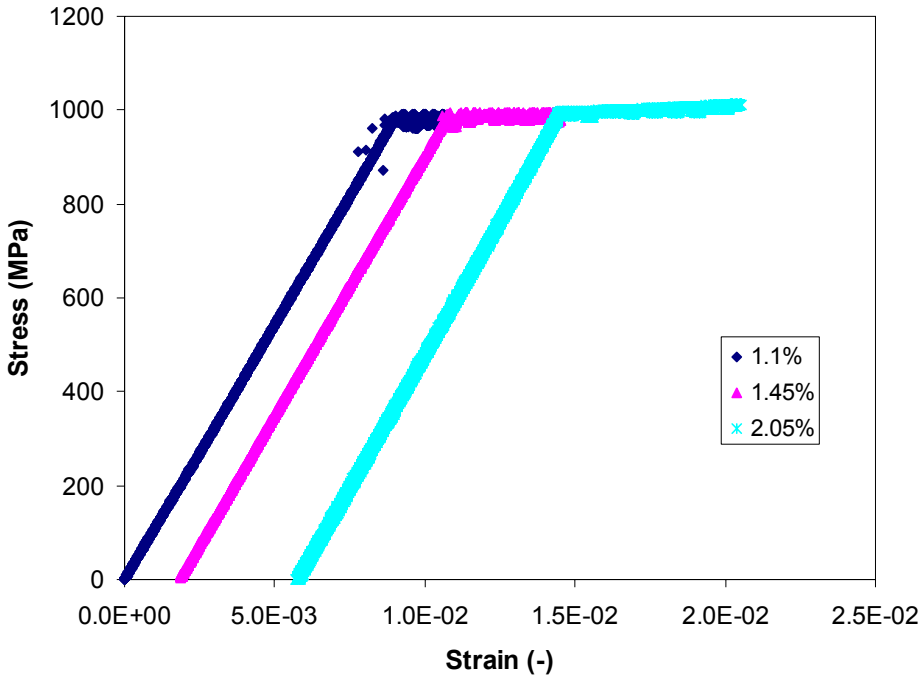

Figure 5-13 Stress-Strain Response at 650° C

Monotonic tests of PWA 1484 produced considerable strain bursts in the inelastic regime. The strain-burst behavior was most pronounced at the lower test temperature and occurred with decreasing magnitude as the temperature was increased.

Results from slip band spacing experiments are summarized in Table 5-4.

Table 5-4 Slip Band Spacing as a Function of Inelastic Strain and Temperature

Temperature (deg C)	ε_{mech} (%)	ε_{in} (%)	# of Slip Bands	Corrected Spacing (mm)
21	0.900	0.234	19	0.428
	1.320	0.673	37	0.220
	1.970	1.303	84	0.097
450	1.100	0.237	44	0.284
	1.300	0.447	82	0.153
	1.520	0.668	176	0.073
550	1.170	0.336	75	0.118
	1.600	0.739	30	0.036
	1.600	0.739	39	0.047
	2.210	1.350	195	0.028
	2.210	1.350	80	0.027
650	1.100	0.182	88	0.088
	1.450	0.579	297	0.026
	2.050	1.160	546	0.014

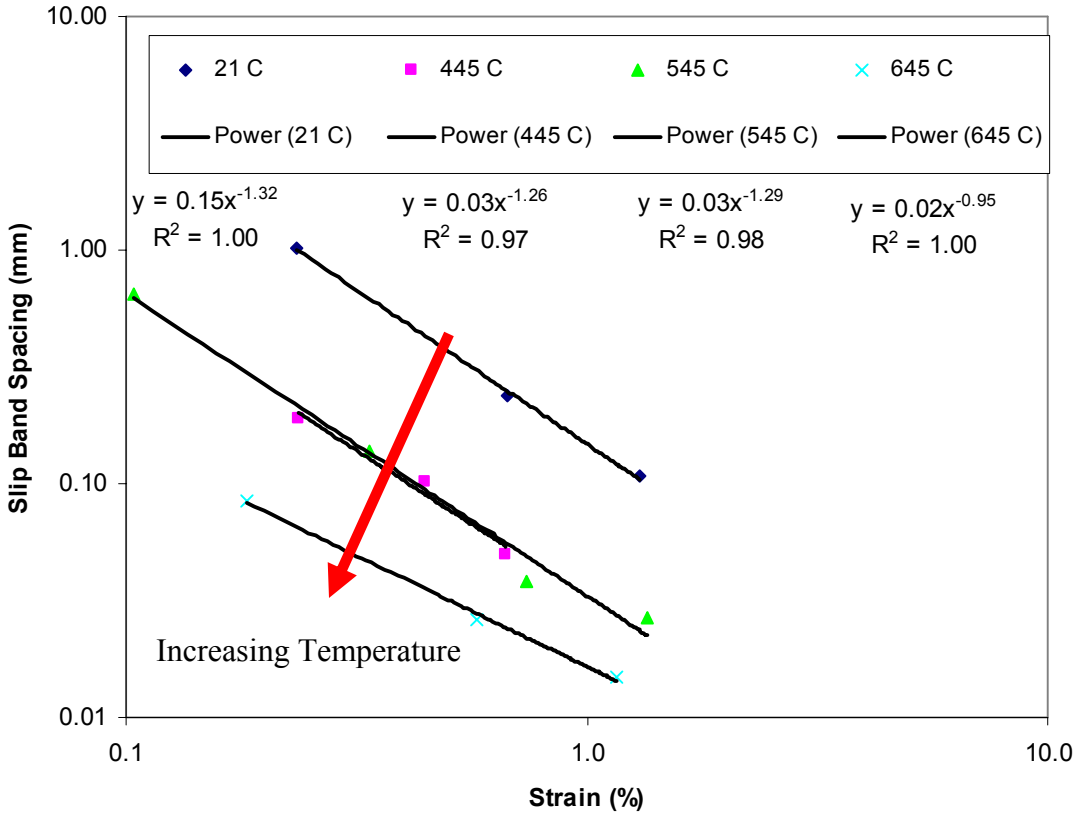

Figure 5-14 Slip Band Spacing as a Function of Inelastic Strain at Various Temperatures

Slip band spacing decreases with increasing inelastic strain, as shown in Figure 5-14. Below 650° C, this material exhibits three distinctive regions of slip band spacing morphology as a function of temperature: (1) low temperature slip at 21° C resulting in very diffuse slip spacing, (2) a transitional slip spacing response occurring at 450° and 550° C and (3) a homogeneous slip response occurring at 650° C. Based upon the strain exponents the dominant mechanisms appear to be similar between 21° C and 550° C, while the slip mechanism appears to change between 550° C and 650° C. At temperatures between ~400° C and ~750° C, all superalloys transition from a primarily glide dominated dislocation movement to a glide and climb mechanism (see Table 2-5). Furthermore, Gayda and coworkers [8] determined that 650° C was the upper limit of "low temperature" behavior for PWA 1480, a similar single crystal superalloy to that studied here. One can assume then, that dislocation climb becomes more dominant in PWA 1484 at temperatures between 550° C and 650° C. Therefore, "intermediate" deformation mechanisms are presumed to set in at temperatures above approximately 600°C in PWA 1484.

5.5 Mathematical Relationships

The relationship between slip band spacing, C, temperature and inelastic strain for the single crystal superalloy PWA 1484 between 21°C and 550°C is described well by Eq 5-2. Slip spacing results from the 650° C tests were excluded because the activation energy is different than at lower temperatures.

The overarching goal of this study is to determine a physics-inspired life estimation scheme for PWA 1484 experiencing out-of-phase (OP) thermomechanical

fatigue (TMF). Out-of-phase TMF is dominated by the interaction of high-temperature compressive damage mechanisms and low(er)-temperature tensile damage mechanisms. As such, this research includes development of a relationship for slip band spacing which accounts for low(er) temperature deformation mechanisms, i.e. dislocation glide and strain level.

Using the relationships between slip spacing and inelastic strain shown in Figure 5-14, an average strain exponent value of n = -1.29 was used in the model. The activation energy, Q, was determined by fitting the model data, shown in Fig 5-15.

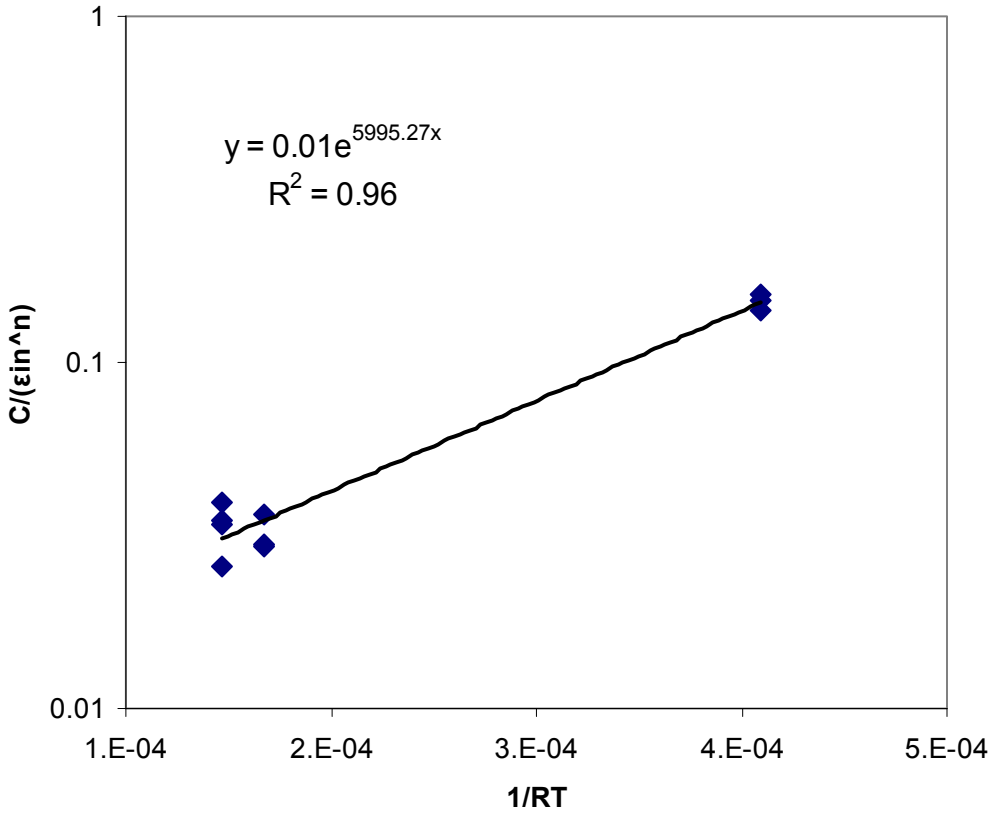

Figure 5-15 Method for Determining Pre-factor and Activation Energy

The average activation energy for the processes involved in slip, at the temperatures tested, was Q = 6.056 kJ/mol-K and the pre-factor in EQ 5-2 is B=1.260 x 10^{-2}. To test

the validity of the relationship in Equation 5-2, the estimated slip band spacing as a function of temperature was plotted against the test results, shown in Figure 5-16.

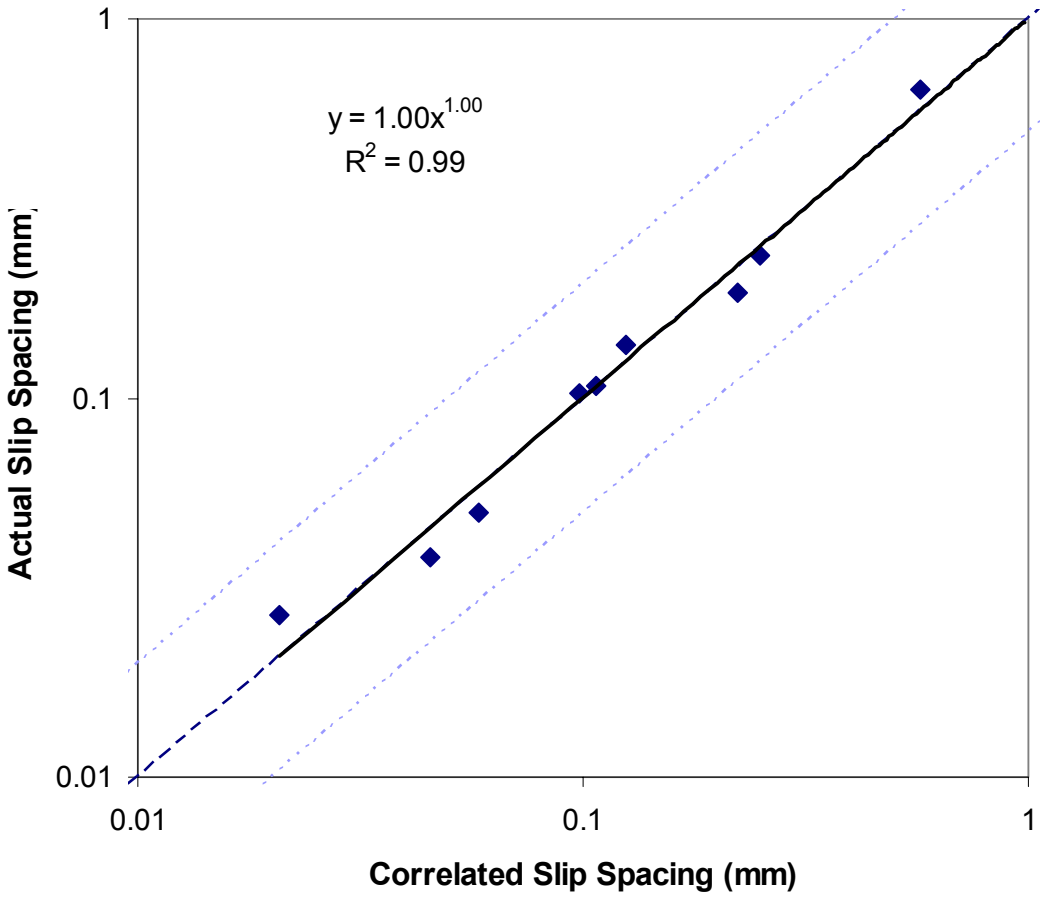

Figure 5-16 Slip Band Spacing Model Verification

Equation 5-2 does an excellent job at correlating slip band spacing for temperatures between 21° C and 550° C, as shown in Fig 5-16, with all correlated values falling within a factor of 1.5X of the actual test results.

The test results were then used to determine the relationship between slip band spacing and inelastic shear strain on the slip system having the highest Schmid factor as a function of temperature.

$$C = B * \gamma_{in}^{\ n} * \exp\left(\frac{Q}{RT}\right) \qquad \textbf{(5-5)}$$

Model calibration yielded B = 3.975E-3, n = -1.29 and an activation energy of Q = 6.056 kJ/mol.

Note that the strain exponent determined here is different from those reported in the literature for polycrystalline materials [22, 26-28, 30, 110]. The vast majority of the slip spacing relationships found in the literature for polycrystalline materials had a strain exponent on the order or n = -0.5. The difference between the results found here and the literature can be explained by looking at two of the studies [28, 29] discussed in Chapter 2. First, Venkataraman et al. [28] determined that the strain exponent value should be n = -0.5 when the system is in a minimum energy state, for polycrystalline materials. Their model is based upon grain boundary pinning of edge dislocations. As the material studied here is single crystal, the minimum energy argument presented by Venkataraman and coworkers is strictly inapplicable to the current study. As such the strain exponent value of n = -0.5 should not be expected from this material based upon their argument. The study conducted by Thompson et al. [29] on polycrystalline copper and brass sheds light on the relationship between grain size and slip band spacing. They performed slip spacing studies on copper having grain sizes of 3.4 μm, 15 μm and 150 μm and brass having grain sizes of 10 μm, 20 μm and 115 μm. They did not report a relationship between slip distance and strain. However, their data, plotted in Figure 5-17, clearly shows that the strain exponent depends upon grain size.

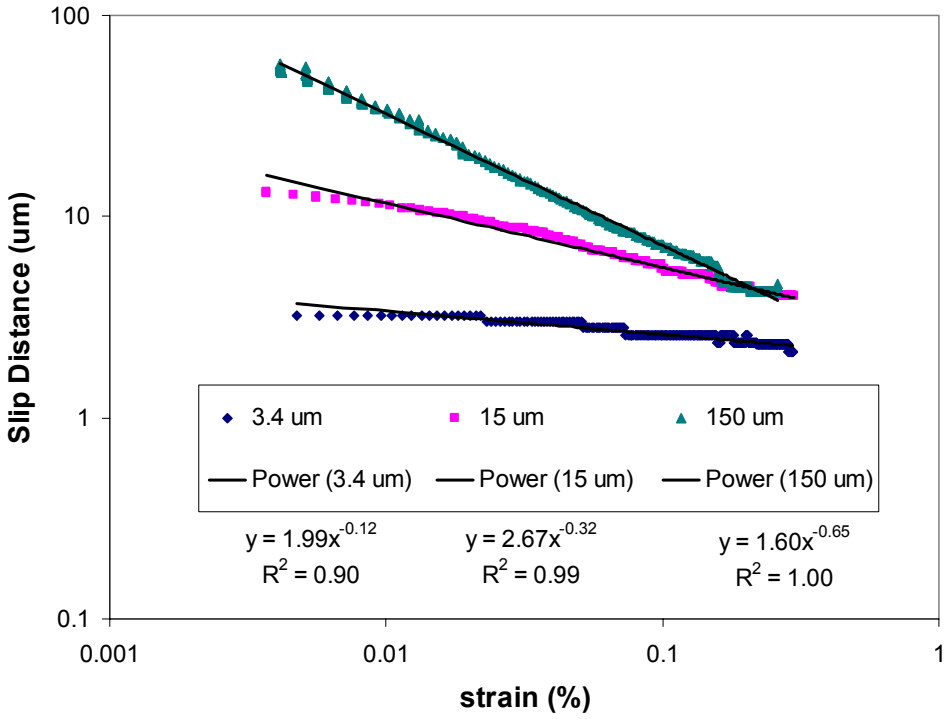

(a)

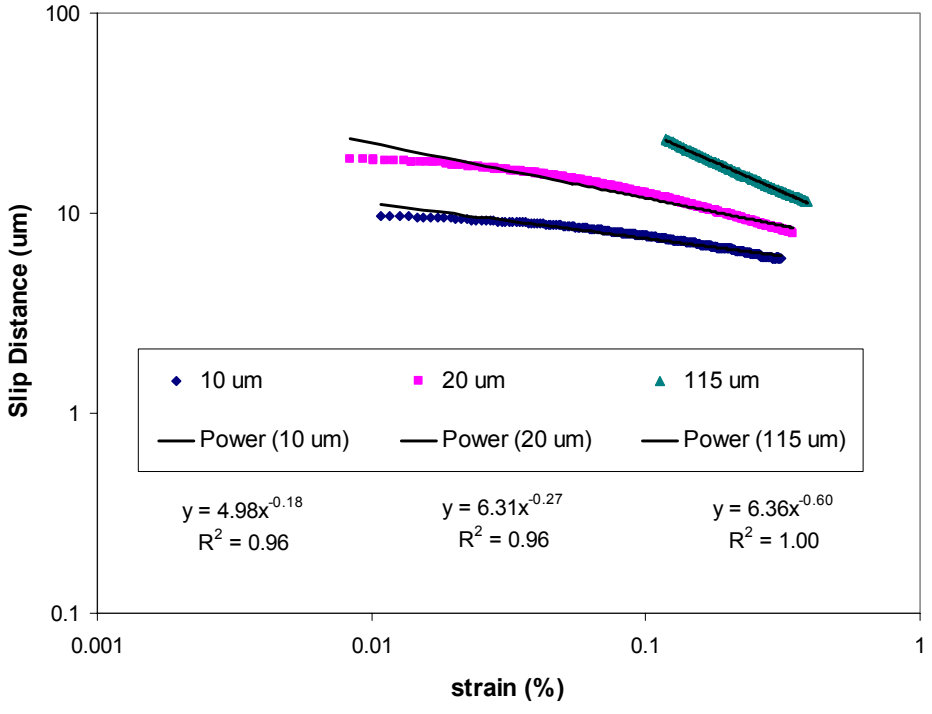

(b)

Figure 5-17 Slip Band Spacing as a Function of Grain Size for (a) Copper and (b) Brass. Data from [29]

The results indicate that as the grain size increases, the strain exponent becomes increasingly negative. Plotting all of Thompson et al.'s results as the absolute value of the strain exponent versus the inverse grain size provides a relationship to estimate "effective grain size" from the strain exponent determined for this work.

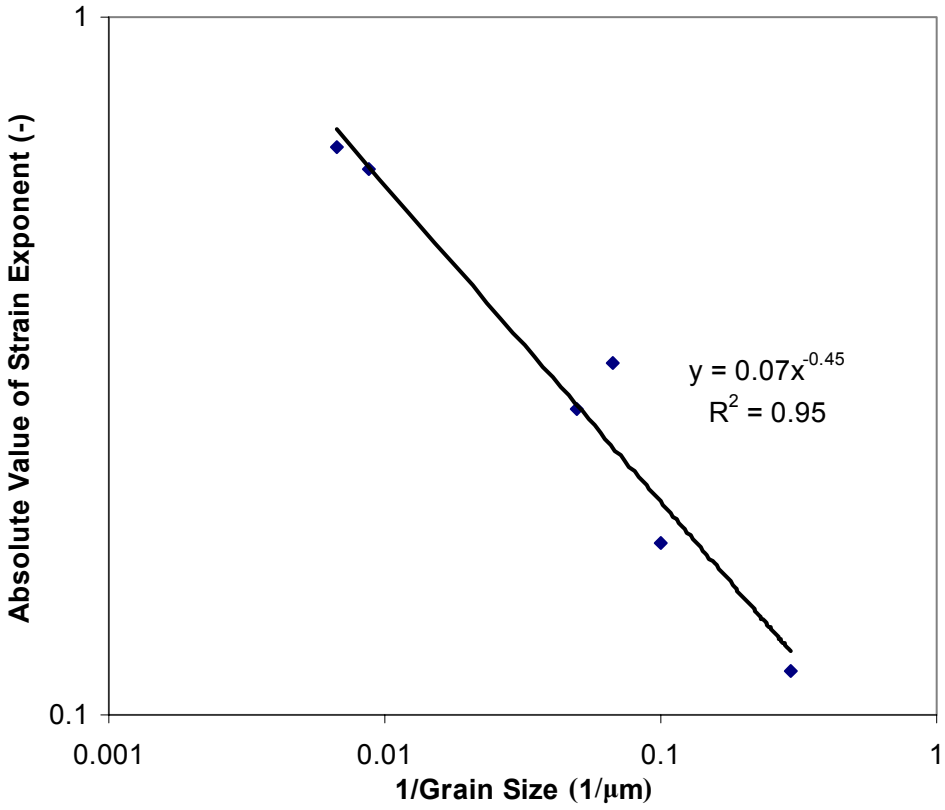

Figure 5-18 Relationship between Strain Exponent and Grain Size. Data From [29]

Using the regression fit in Figure 5-18 and a strain exponent of n=-1.29, the "effective grain size" is 0.595 mm, which is roughly an order of magnitude smaller than the gage section of the specimens tested for this study (6.35 mm). Interestingly the "effective grain size" calculated is roughly three times the average dendrite spacing determined for PWA 1484 (0.178 mm), which is the criteria for crack initiation used in this work. Though it appears as though there is not a direct correlation between

Thompson et al.'s grain-dependent data and the work performed here, the trends from the polycrystalline study are in line with the results of this study. One must be cautioned against putting too much stock in the discrepancy between the polycrystalline results and those of this work, as the polycrystalline work comprises a small data set. Furthermore, the grain size and distributions in the Thompson et al. study were created by "recrystallization after cold work". This process would likely affect the materials dislocation source density as well as dislocation density. As such their results may not be comparable to results for "virgin" material.

As such the strain exponent of n = -1.29 found for single crystal PWA 1484 appears to be a reasonable value, as a more negative strain exponent is in line with the grain size study results. Furthermore, the activation energy for slip in single crystal PWA 1484 at temperatures below 550° C (Q = 6.056 kJ/mol) is in line with the results determined here from the test results of Syam and Milligan [31] for the polycrystalline superalloy KM4 (Q = 3.000 kJ/mol).

Incorporating the cyclic slip results given in Table 5-3 with the monotonic slip results yields the following relationship relating slip band spacing, C, inelastic strain ε^{in} and number of cycles N

$$C = B\varepsilon_{in}^{n} \exp\left(\frac{Q}{RT}\right) N^{a} \qquad \textbf{(5-6)}$$

where B = 3.975E-3, n = -1.29, Q = 7.00 kJ/mol and a = -0.0653.

5.6 Summary

This study has determined a single relationship between slip band spacing, applied inelastic strain and number of cycles between the temperature range of 21° C and 550° C. The relationship

$$C = B\varepsilon_{in}^{n} \exp\left(\frac{Q}{RT}\right) N^{a}$$

where C is the slip band spacing, ε_{in} the applied inelastic strain, B, n and a are material specific constants, Q the apparent activation energy for the dominant process controlling slip, R the universal gas constant, T is the absolute temperature and N the number of cycles. Additionally, the transition between intermediate and high temperature deformation responses for PWA 1484 was determined to be between 550° and 650° C based upon slip band characterization. There appears to be a fundamental relationship between grain size and the strain exponent of equations similar to Eq. 2-5; however as of yet there is not enough information to determine this relationship. One can conclude, however, that the absolute value of the strain exponent is proportional to the grain size; or perhaps another microstructure-specific length which may play a dominant role dislocation pinning, e.g. dendrite spacing.

CHAPTER 6. CRACK INITIATION LIFE MODELING

6.1 Introduction

The OP TMF and BiF life modeling exercises performed for this work are presented. First, the Neu-Sehitoglu model is implemented in a somewhat simplified "engineering life prediction" form. Second, the results from the γ' depletion and slip band studies are employed in the derivation of an improved physics-inspired life model which predicts the number of cycles to crack initiation for PWA 1484 components experiencing OP TMF and BiF waveforms, as a function of primary crystallographic orientation and fundamental damage mechanisms and their interactions.

6.2 Neu-Sehitoglu Model

The cumulative damage life model of Neu and Sehitoglu (N-S) [88, 89] was used to predict OP TMF crack initiation lives of single crystal PWA 1484. This model has been successfully used to predict TMF lives for the superalloys Mar-M247 and GTD-111 [70, 86]. The N-S cumulative damage model has the general form,

$$N_i = \left(\frac{1}{N_i^{fat}} + \frac{1}{N_i^{cr}} + \frac{1}{N_i^{env}} \right)^{-1} \quad \textbf{(6-1)}$$

where the fatigue, creep and environmental modules, modified for directionally solidified materials [67], are defined respectively as

$$N_i^{fat} = C_{in} f_{in}(\omega)(\Delta\varepsilon_{mech})^{d_{in}} \quad \textbf{(6-2)}$$

$$N_i^{cr} = \Theta_{CR}^{TMF} \exp\left(\frac{-B' f_{CR}\left(\sigma_{tens}\right)^{-k}}{RT}\right)\Phi^{CREEP} \tag{6-3}$$

$$\frac{1}{N_i^{env}} = \left[\frac{h_{cr}\delta_0}{B\Phi^{ENV}\left(K_{peff}^{ENV} + K_{peff}^{\gamma'}\right)}\right]^{-1/\beta} \frac{2\left(\Delta\varepsilon_{mech}\right)^{\left(2/\beta\right)+1}}{\dot{\varepsilon}^{1-\alpha/\beta}} \tag{6-4}$$

The fatigue damage module is based on a classic strain-life relationship; as such the mechanical strain range is used to correlate life. The fatigue module includes a orientation dependent term, ($f_{in}(\omega)$), a pre-factor and exponential. The orientation term was implemented to account for the direction of grain boundaries (in directionally solidified alloys) relative to the loading axis, however, it is conceivable that this term could be calibrated to account for differing slip system activation occurring in single crystals as a function of loading orientation. The pre-factor and exponential terms are both fit to lower-temperature low cycle fatigue (LCF) data where environmental and creep effects are negligible.

The creep module includes a phasing term, Φ^{CREEP}, which effectively weights the creep term according to cycle type, since creep damage accumulates more readily under tensile loads. The phasing term

$$\Phi^{CREEP} = \frac{1}{t_c}\int_0^{t_c} \phi^{CREEP} dt \tag{6-5}$$

is integrated over cycle time where ϕ^{CREEP} is defined as

$$\phi^{CREEP} = \exp\left(-\frac{1}{2}\left(\frac{\left(\dot{\varepsilon}_{th}/\dot{\varepsilon}_{mech}\right)-1}{\xi^{CREEP}}\right)^2\right) \tag{6-6}$$

The phasing is accounted for by the ratio of thermal to mechanical strain rates, $\dot{\varepsilon}_{th} / \dot{\varepsilon}_{mech}$, and ξ^{CREEP} defines the sensitivity of the phasing to creep damage. In application the creep phasing term is set to zero for OP TMF (temperature-strain phasing = 180°) since the tensile half cycle occurs at a temperature below which creep damage would accumulate; and one for IP TMF (temperature-strain phasing = 0°) as the tensile cycle occurs at high temperature. The creep module also includes a creep diffusion term which when integrated over cycle time effectively accounts for the temperature waveform in TMF tests,

$$\Theta_{CR}^{TMF} = \frac{1}{t_c}\int_0^{t_c} D_0 \exp\left(\frac{-Q}{RT(t)}\right)dt \qquad \textbf{(6-7)}$$

where D_0 is the diffusion coefficient, Q the activation energy, R the universal gas constant and T(t) is the temperature waveform as a function of time. The remainder of the creep module

$$\exp\left(\frac{-B' f_{CR}\left(\sigma_{tens}\right)^{-k}}{RT}\right) \qquad \textbf{(6-8)}$$

Results from fitting the Larson-Miller creep parameter to creep experiments. B' and k are fitting constants, f_{CR} is a material orientation function, σ_{tens} the peak tensile stress from the stabilized hysteresis loop, R the universal gas constant the T the absolute temperature.

The environmental-fatigue module also includes a phasing term,

$$\Phi^{ENV} = \frac{1}{t_c}\int_0^{t_c} \phi^{ENV} dt \qquad \textbf{(6-9)}$$

where ϕ^{ENV} is defined as

$$\phi^{ENV} = \exp\left[-\frac{1}{2}\left(\frac{\left(\dot{\varepsilon}_{th}/\dot{\varepsilon}_{mech}\right)+1}{\xi^{OX}}\right)^2\right] \quad \textbf{(6-10)}$$

in which ζ^{ox} accounts for the sensitivity of oxidation damage to cyclic phasing. The phasing term, Φ^{ENV}, effectively accounts for temperature-strain phase differences by forcing the term to a value of one for an OP TMF cycle where oxides formed in compression are damaged or spalled by the low temperature tensile half cycle. The environmental-fatigue interaction occurring in an OP TMF cycle is far more damaging than those of the IP cycle which has a Φ^{ENV} set equal to zero. The oxidation and γ' depletion terms within the environmental-fatigue module, K^{ENV} and $K^{\gamma'}$ respectively, are defined as,

$$K_{peff}^{ENV} = \frac{1}{t_c}\int_0^{t_c} D_{OX}\exp\left(\frac{-Q_{OX}}{R\cdot T(t)}\right)dt \quad \textbf{(6-11)}$$

and

$$K_{peff}^{\gamma'} = \frac{1}{t_c}\int_0^{t_c} D_{\gamma'}\exp\left(\frac{-Q_{\gamma'}}{R\cdot T(t)}\right)dt \quad \textbf{(6-12)}$$

The terms D_{ox} and Q_{ox} are the oxidation diffusion coefficient and activation energies, while the $D_{\gamma'}$ and $Q_{\gamma'}$ are the γ' diffusion coefficient and activation energies, respectively. The environmental-fatigue module also includes terms that account for the material ductility within the environmentally affected zone, δ_0, the critical crack length at which the environmental attack trails behind the advancing crack tip, h_{cr}, the strain rate sensitivity, α; and terms accounting for total environmentally induced crack length, B and β. These equations effectively account for the independent damage mechanisms of

fatigue, creep and environment-fatigue when used to estimate thermo-mechanical fatigue (TMF) component life.

The N-S model is used to predict OP TMF lives for the single crystal PWA 1484 test data provided in Table 3-3. The purpose of this life modeling exercise is to utilize the physics-inspired life model implemented as a simplified "engineering" life estimation scheme for specimens and components experiencing OP TMF requiring a minimum number of up-front calibration tests. As such only the <001> oriented TMF tests presented in Table 3-3 will be used in this section.

6.2.1 Neu-Sehitoglu Model Implementation

Since sufficient LCF data on PWA 1484 didn't exist the constants in the fatigue module were fit using PWA 1480 LCF lives [3]. The environmental-fatigue module constants used are those previously fit to the superalloy MAR-M247 [70]. The creep module was not used in this analysis as lives for OP TMF tests were being estimated. The Fatigue and environmental-fatigue constants used in initial model verification are shown in Table 6-1.

Table 6-1 Fatigue and Environmental Fatigue Module Constants

Term	Value	Units	Term	Value	Units	Term	Value	Units
α	0.75	-	δ	1.12E-10	$\mu m*s^{(-0.75)}$	$D_{\gamma'}$	8570.00	μm^2*s
β	1.5	-	D_{ox}	15400.00	μm^2*s	$Q_{\gamma'}$	163.30	kJ/mol
B	0.00693	$s^{(-.5)}$	Q_{ox}	175.90	kJ/mol	C_{in}	1.63E-07	-
ζ	0.44	-	h_{cr}	461.40	μm	d_{in}	-5.4306	-

6.2.2 Parametric Sensitivity Analysis

In order to determine the sensitivity of the Neu-Sehitoglu life estimation results to the various input parameters, a study was performed in which each parameter was varied by a specified amount while holding all other inputs at nominal values. Each input was varied by a minimum of +/- 20% in 0.5% increments. The input parameters which were studied as well as their nominal values are shown in Table 6-1. After an initial assessment of the sensitivities of all parameters utilized in the environmental-fatigue module, four parameters which had the highest impact on life estimation were identified: the activation energies (Q_{ox} and $Q_{\gamma'}$) used in the oxidation and γ' depletion terms (K^{ENV} and $K^{\gamma'}$), and the exponents α and β. The percent change of each of these parameters versus percent change in total estimated life is shown in Figures 6-1 through 6-4.

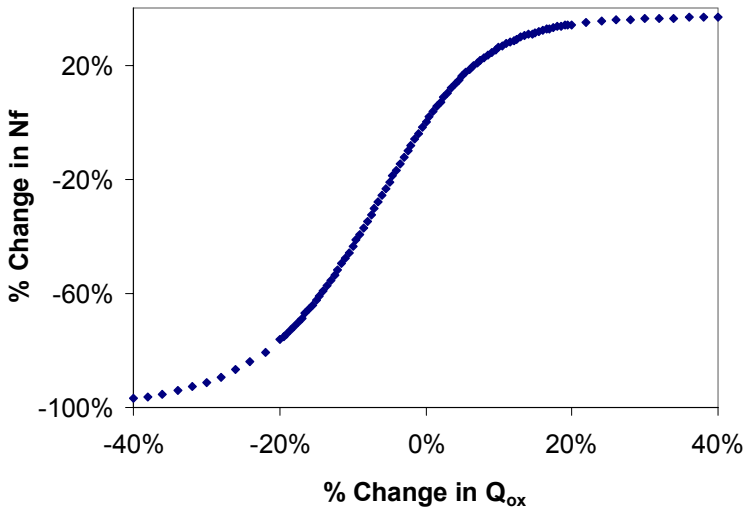

Figure 6-1 %-Change of N_f vs. %-Change of Q_{ox}

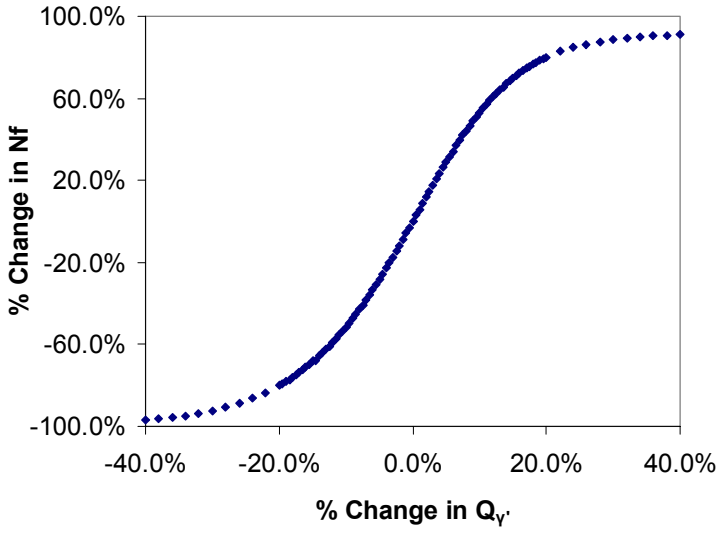

Figure 6-2 %-Change of N_f vs. %-Change of $Q_{\gamma'}$

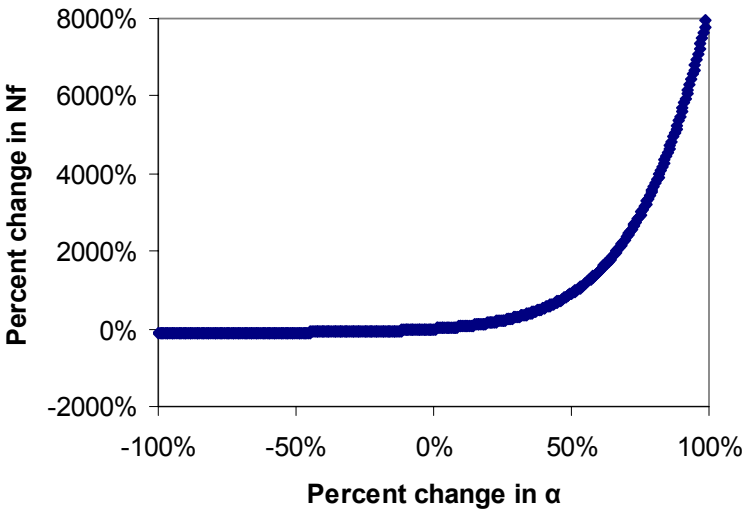

(a)

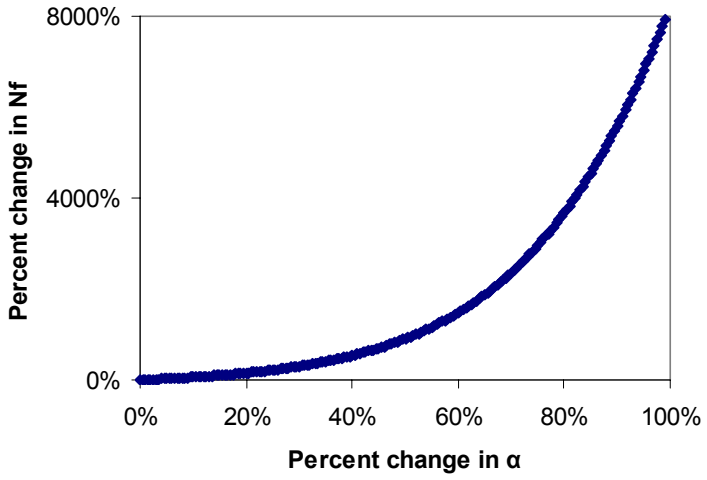

(b)

Figure 6-3 %-Change of N_f vs. %-Change of α: (a) Symmetric About Baseline Value, (b) Focus on Primary Deviation

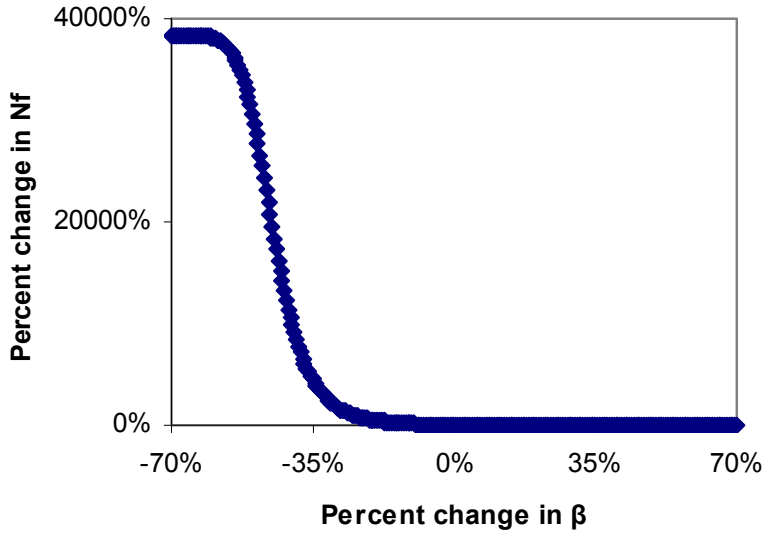

(a)

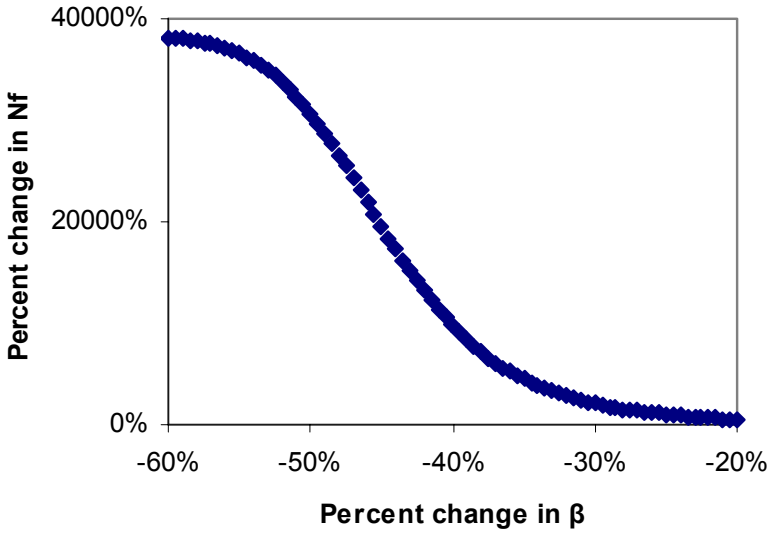

(b)

Figure 6-4 %-Change of N_f vs. %-Change of β: (a) Symmetric About Baseline Value, (b) Focus on Primary Deviation

Figure 6.2, for example, indicates that there is a 4:1 relationship between the overall life prediction results and the $Q_{\gamma'}$ value, when starting from the baseline values. Overall, variation in the strain exponent, β, has the most influence on life prediction, followed by the exponent α, γ' activation energy, $Q_{\gamma'}$, and the oxidation activation energy,

Q_{ox}. Since these four parameters have the greatest effect upon life estimation sensitivity it is clear that they must be determined for each material of interest in order to optimize model efficacy. Rather than perform lengthy tests to determine the material-specific values for these four parameters, a variation of parameters analysis was performed in order to develop the best engineering fit. If successful, a minimal number of tests would be required to calibrate and implement the N-S cumulative damage model. The variation of parameters was implemented using an error minimization algorithm in MATLAB. The algorithm first estimates the OP TMF lives for the tests presented in Table 3-3 using the N-S model, it then compares the life estimation to the actual life, and finally the algorithm varies the input parameters before repeating the process. The algorithm searches for those values that minimize the differences in the predicted and measured lives. The minimization algorithm was used to determine the values of all four of the most influential parameters while calibrating the model to the three baseline OP TMF results provided at the top of Table 3-2. The resulting parameter values are shown in Table 6-2. Calibration results from the variation of parameters study varying $Q_{\gamma'}$, Q_{ox}, α and β are shown in Fig 6-5. Life estimation results for all of the OP TMF data, using calibrated constants in Table 6-2, is shown in Fig 6-6.

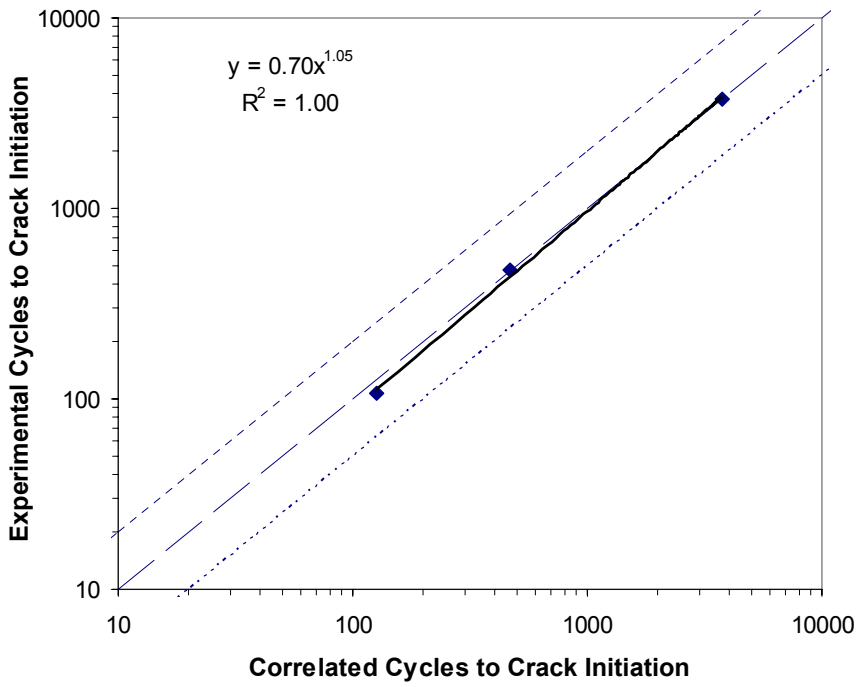

Figure 6-5 Calibration of N-S Model Using Baseline TMF Tests (Table 3-2), Variation of 4 Parameters: Qγ', Qox, α and β

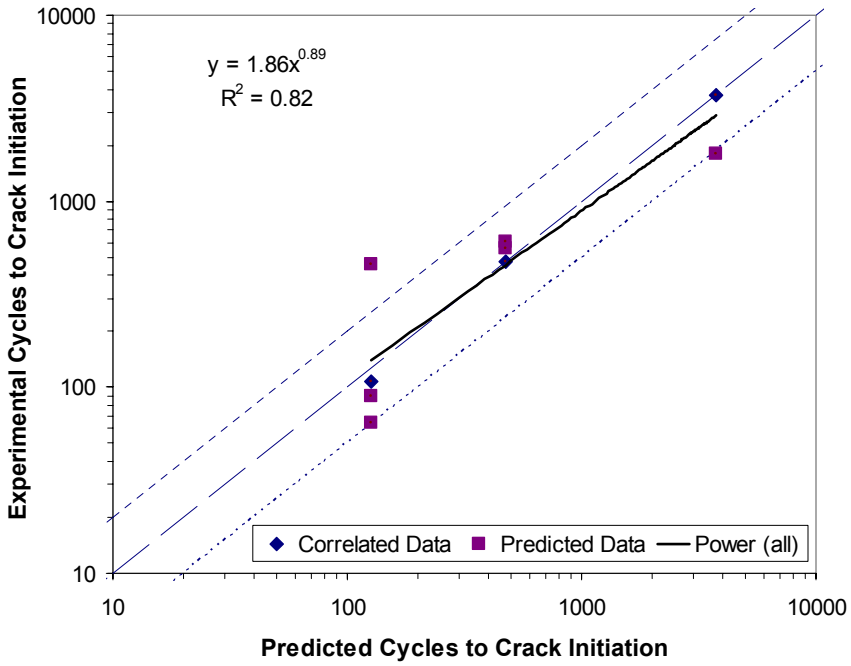

Figure 6-6 Life Estimation of TMF Tests, Variation of 4 Parameters: $Q_{\gamma'}$, and Q_{ox}, α and β

Table 6-2 Results of Variation of Parameters Study- Calibration Using Baseline PWA 1484 OP TMF Data

Parameter	Value
$Q_{\gamma'}$	88.4 kJ/mol
Q_{ox}	99.8 kJ/mol
α	1.50
β	1.00

Figure 6-7 depicts the mechanical strain range versus experimental cycles to failure, as well as the N-S environmental-fatigue module life trend (calibrated to PWA 1484) and the N-S fatigue module life trend (calibrated to PWA 1480).

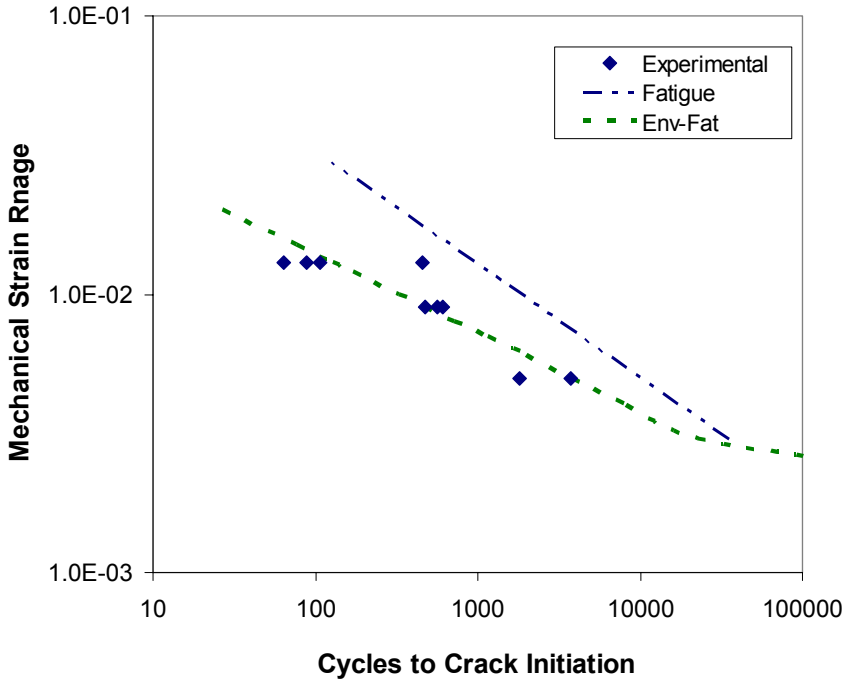

Figure 6-7 Strain Life Plot for PWA 1484 <001> OP TMF Results

Clearly the calibrated model relies upon the environmental fatigue term to set the life prediction trend while the fatigue module weights the predictions minimally.

The final life estimation algorithm calibrated to PWA 1484 performs exceptionally well, with 75% of the estimated lives falling well within a factor of 2X

from the experimental lives. Comparing the results of the variation of parameters shown in Table 6-1 to the original parameters in Table 6-2 one notices that the MAR-M247 activation energies for oxidation and γ' depletion are far greater than those determined from PWA 1484 TMF tests. This difference would result in increased oxidation and γ' depletion kinetics for the MAR-M247 alloy, relative to PWA 1484. These results aren't surprising given that the MAR-M247 alloy used in the original study [90] is polycrystalline, thereby resulting in increased grain boundary diffusion relative to the matrix. The variation of parameters also resulted in an increase of the strain and strain rate exponents β and α, indicating that the fatigue portion of the coupled environmental-fatigue interaction was likely overestimated using the MAR-M247-determined parameters, as indicated by the independent life-module estimations shown in Fig 6-7.

The results of the sensitivity of parameters study indicate that the environmental-fatigue module dominates life estimation when using the Neu-Sehitoglu cumulative damage model to predict OP TMF lives. Furthermore, it has been shown using a variation of parameters study, that a minimum number of up-front tests are required to calibrate the N-S model for use as a first-order-magnitude engineering life estimation scheme (three baseline tests were used in this study). However, it should be noted that three tests were utilized to calibrate four unknowns, likely setting up an ill-defined equation set. It is likely that in this case the initial guesses enabled an efficient convergence of parameter values, whereas more tests would likely be required to if initial parameter value guesses are not optimal.

6.3 Life Model Development

The OP TMF and BiF test results in Chapter 3, the results from γ' depletion studies presented in Chapter 4 as well as the results of Section 6.2 will be used as a backdrop for the derivation of a new/refined life estimation model for PWA 1484.

It was shown in Chapter 3 that the primary difference between the BiF and TMF test results is the dominance of an environmental damage component. Specifically, Equation 3-3 (presented again as Eq. 6-13) relates the inelastic strain range from OP TMF tests, $\Delta\varepsilon_{in}^{TMF}$, to the inelastic strain range from OP BiF tests having identical lives, $\Delta\varepsilon_{in}^{BiF}$, using the Arrhenius relation

$$\Delta\varepsilon_{in}^{BiF} = \left(\Delta\varepsilon_{in}^{TMF}\right)^{g} \exp\left(\frac{Q}{RT_{eff}^{BiF}}\right) \qquad \textbf{(6-13)}$$

where Q is an apparent activation energy for high temperature material degradation, R the universal gas constant (8.314 J/K-mol) and T_{eff}^{BiF} is the effective temperature in the BiF tests (1002° C). The exponent and activation energy in EQ 6-13 were determined as g=3.664 and Q = 160.0 kJ/mol, respectively in Chapter 3. Though it is understood that high-temperature material degradation occurs in the TMF tests, EQ 6-13 implies that the BiF tests experience enhanced degradation. The activation energy for γ' depletion of PWA 1484 under stress-free isothermal high temperature exposure (Chapter 4) is $Q_{\gamma'}$ = 162.9 kJ/mol. Based upon these results and the results of Section 6.2, one concludes that γ' depletion plays a pivotal role in the deformation mechanisms operating in specimens experiencing out-of-phase TMF and BiF.

Development of an enhanced life model utilizes the following rationale: Suppose that there exists a region of compromised base material near the edge of a single crystal

experiencing uniaxial fatigue. The compromised material may result from an oxide spike, a γ' depleted zone, or a preferentially damaged interdendritic region. If slip bands, caused by fatigue, impinge on this region, a crack of critical size (X_{crit}) will initiate. Prior to the crack reaching critical length, the kinetics of the "pre-crack" is determined by that of the damage process (i.e. γ' depletion, oxidation, etc.) and depicted as "X". This situation is shown schematically in Figure 6-8(a) and was found experimentally, as shown in Figure 6-8(b).

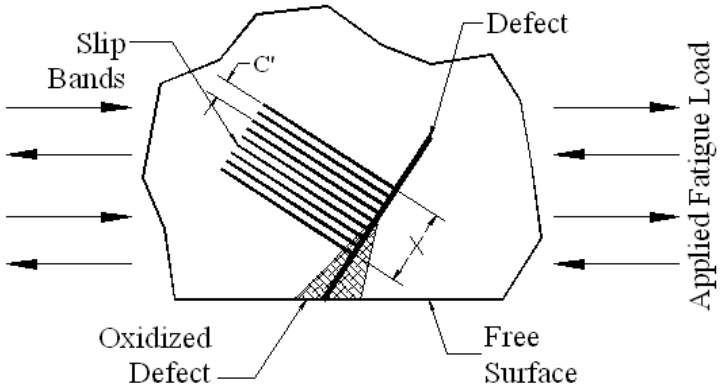

(a)

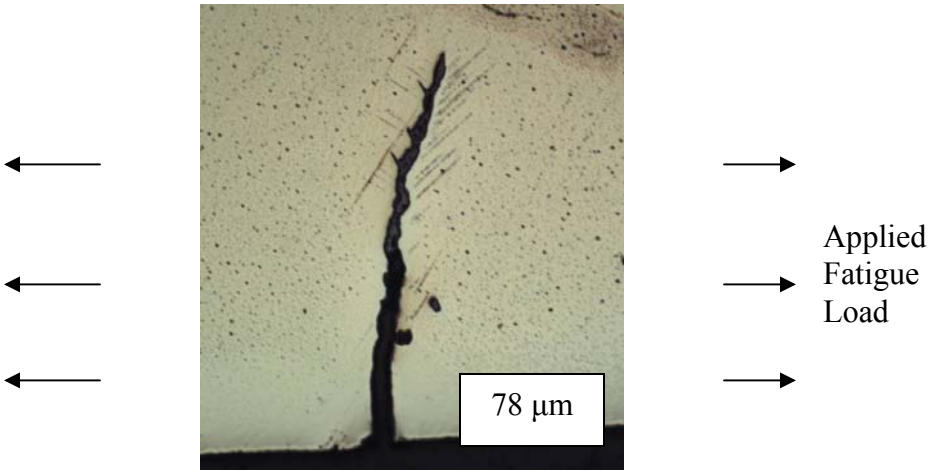

(b)

Figure 6-8 (a) Schematic of Slip Bands Impinging Upon an Oxide Spike, and (b) Optical Image of Experimentally Observed Slip Bands Impinging on Oxide Spike- Specimen Surface of $\Delta\varepsilon_{mech}$ = 0.9% OP TMF

Based upon the above arguments, a life estimation equation is proposed for PWA 1484 experiencing OP TMF and BiF. This equation was initially proposed in a slightly different form by Antolovich et al. [96] for fatigue-environmental interactions in polycrystalline René 80. The life estimation relationship

$$N_i = A\Delta\varepsilon_{in}^{-m} \exp\left(\frac{Q}{RT_{eff}}\right) t^{-n} \qquad \textbf{(6-14)}$$

incorporates the interactions between inelastic strain range, $\Delta\varepsilon_{in}$, and environmentally assisted material degradation kinetics to determine the number of cycles to crack initiation, N_i. The equation also incorporates a strain exponent (m), a prefactor (A), an activation energy (Q), the universal gas constant (R), an effective temperature (T_{eff}), the time for which the material is exposed to high temperature (t), and the oxidation rate exponent (n) set to n=1/2 for parabolic oxidation kinetics.

The physical basis for the proposed model (Eq 6-14) is as follows. One can quantify the effects that the slip bands' interaction has upon the degraded base material via the hypothesis that a critical crack length X_{crit}, exists when a minimum number of slip bands intersect the defect to nucleate a crack which can propagate under the imposed conditions. The critical crack length is then governed by

$$X_{crit} = N_s C \qquad \textbf{(6-15)}$$

where N_s is the number of slip bands intersecting the degraded base material and C is the average slip band spacing. Slip band spacing (C) is related to inelastic strain range ($\Delta\varepsilon_{in}$) by [27]

$$C = A\Delta\varepsilon_{in}^{-S} \tag{6-16}$$

where A and s are material parameters. The oxide kinetics, related to the critical crack length, are governed by the classical parabolic growth law [100]

$$X = \left[D_o \exp\left(\frac{-Q'}{R \cdot T_{eff}} \right) t \right]^n \tag{6-17}$$

where X is the depth of high temperature material degradation per cycle, D_0 is the oxidation diffusion coefficient, Q' is the effective activation energy, T_{eff} the effective temperature (Eq 3-2) and n is the oxidation rate exponent. The high temperature half cycle of a TMF test is related to the cycle frequency, ν, and hold time, t_h, (if any) by

$$t = \frac{\nu \cdot t_h + 1/2}{\nu} \tag{6-18}$$

Combining Equations 6-16, 6-17 and 6-18 Equation 6-15 yields:

$$N_i = \frac{N_s A}{D_0^n} \left(\frac{1}{\Delta\varepsilon_{in}} \right)^s \left[\exp\left(\frac{Q'}{R \cdot T_{eff}} \right) \frac{\nu}{\nu \cdot t_h + 1/2} \right]^n \tag{6-19}$$

Equation 6-19, first presented in a somewhat modified form by McDowell et al. in 1991 [18], provides a life estimation scheme that accounts for fatigue and environmental interactions. To include material orientation effects, the $\Delta\varepsilon_{in}$ is then replaced by $\Delta\gamma_{in}^{sl}$, which is the resolved shear strain on the slip system having the highest Schmid factor, as determined by

$$\frac{\gamma}{2} = \varepsilon(\bar{s} \bullet \bar{l}) \tag{6-20}$$

for 1-D loading, where $\bar{s}$ is the unit normal in the direction of slip on the slip plane of interest and $\bar{l}$ is the unit normal in the loading direction. Evolution of γ' particles is accounted for by including classical microstructural coarsening kinetics described by [73, 74]

$$\Delta r = r_t - r_0 = k(T)t^{1/3} \tag{6-21}$$

where r_t is the particle diameter at time t, r_0 the initial particle diameter, k(T) is the temperature dependant coarsening rate coefficient and t is time. Second phase particle coarsening is proportional to the spacing between particles (Eq. 2-10). Since the γ' phase acts to pin dislocations, a larger distance between obstructions enables egress of dislocations from the material without necessitating a climb or cross slip mechanism to bypass the obstacles. Therefore one presumes that as the microstructure coarsens the effective slip band spacing effectively increases. Solving Eq. 6-21 for r_t, normalizing by r_0 and multiplying by the slip band spacing yields, the following relationship for slip band spacing,

$$C = A\left(\Delta\gamma_{in}^{sl}\right)^{-S}\left(\frac{r_0 + k(T)\cdot t^{1/3}}{r_0}\right) \tag{6-22}$$

Replacing the slip band relation in Eq. 6-19 by that provided in Eq. 6-22 yields

$$N_i = \frac{N_S A}{D_0^n}\left(\frac{1}{\Delta\gamma_{in}^{sl}}\right)^s \left\{\exp\left(\frac{Q'}{R\cdot T_{eff}}\right)\frac{\nu}{\nu\cdot t_h + 1/2}\right\}^n \left[\frac{r_0 + k\cdot t^{1/3}}{r_0}\right] \tag{6-23}$$

This form of the physics-inspired model was used in [111] with some success. Results provided in Chapter 4, indicate that the stress-enhanced oxidation kinetics of specimens experiencing OP TMF are correlated by a stress-dependent rate law (Eq. 4-7).

When incorporating frequency and hold time (Eq. 6-18) as well as surface roughness (Eq. 4-2) the γ' depletion kinetics becomes

$$X_{\gamma'} = A\exp\left(\frac{-Q_{ox} + B|\tau_{\min}|}{RT_{eff}}\right)\left(\frac{\nu}{\nu \cdot t_h + 1/2}\right)^{-n}\left(\frac{R_a}{8}\right)^{-h} \quad \textbf{(6-24)}$$

where A is a material and temperature dependent diffusion coefficient, Q_{ox} is the effective activation energy and n is the time exponent determined from the non-stressed γ' depletion experiments, B is a constant which has units m^3/mol, τ_{min} is the minimum shear stress of the stabilized cycle, R the universal gas constant, T_{eff} the cycle effective temperature, ν is the cycle frequency in hours, t_h is a high temperature hold time (if any) in hours, d and h are exponents determined from γ' depletion surface roughness experiments, and R_a is the specimen surface roughness arithmetic average) in nanometers.

Furthermore, the slip band studies presented in Chapter 5 yield the following relationship for slip band spacing, C:

$$C = b\left(\Delta\gamma_{in}^{sl}\right)^{-m}\exp\left(\frac{Q_{sl}}{RT_{eff}}\right)N^{-k} \quad \textbf{(6-25)}$$

where C is the slip band spacing per (whole) cycle, b and m are fit to experimental results, $\Delta\gamma_{in}^{sl}$ is the inelastic shear strain on the slip system having the highest Schmid factor, Q_{sl} is the effective activation energy for slip occurring below ~600°C, R and T_{eff} have their usual meanings, N is the number of cycles and k is a fitting exponent accounting for the decrease in slip spacing as a function of cycles. When incorporating Equations 6-24 and 6-25 into Eq. 6-15, the life model becomes

$$N_i = \left(K\left(\Delta\gamma_{in}^{sl}\right)^{-m} \exp\left(\frac{Q_{sl} + Q_{ox} - B\left|\tau_{\min}\right|}{RT_{eff}} \right) \left(\frac{\nu}{\nu \cdot t_h + 1/2} \right)^{-n} \left(\frac{R_a}{8} \right)^{-h} \right)^{p} \qquad \textbf{(6-26)}$$

where K and p are lumped parameters. Equation 6-26 was correlated to all of the <001> orientation results from Table 3-3 using known values for all parameters except K and p, which were allowed to vary to provide the best fit. The model parameter values are shown in Table 6-3 and the correlated equation results are shown in Figure 6-9.

Table 6-3 Parameter Values From Correlation of Eq 6-26 to all <001> PWA 1484 OP TMF and BiF Results

K	6.36E-04	(-)
m	1.29	(-)
Q_{sl}	6056	J/mol
Q_{ox}	162863	J/mol
B	161	m^3/mol
n	f(temp)	(-)
d	0.17	(-)
Ra	197	nm
h	0.2	(-)
p	0.31	(-)

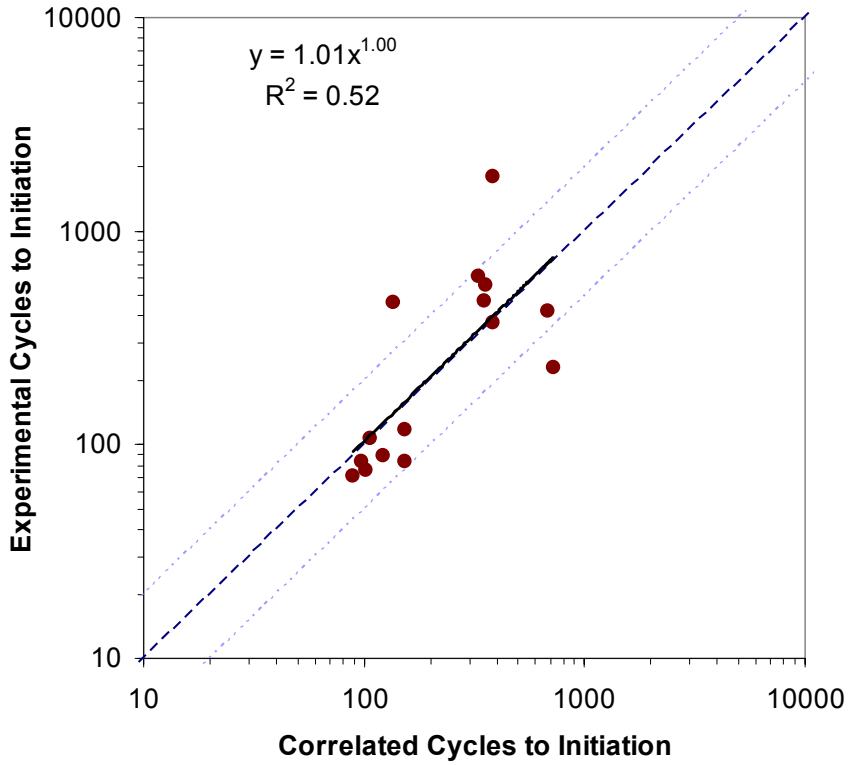

Figure 6-9 Correlation of Eq 6.26 to all <001> PWA 1484 OP TMF and BiF Results

The model does a fair job of correlating the test data, with 80% of the correlations within a factor of two. However the low correlation coefficient is concerning. The correlated results are delineated by effective cycle type in Figure 6-10.

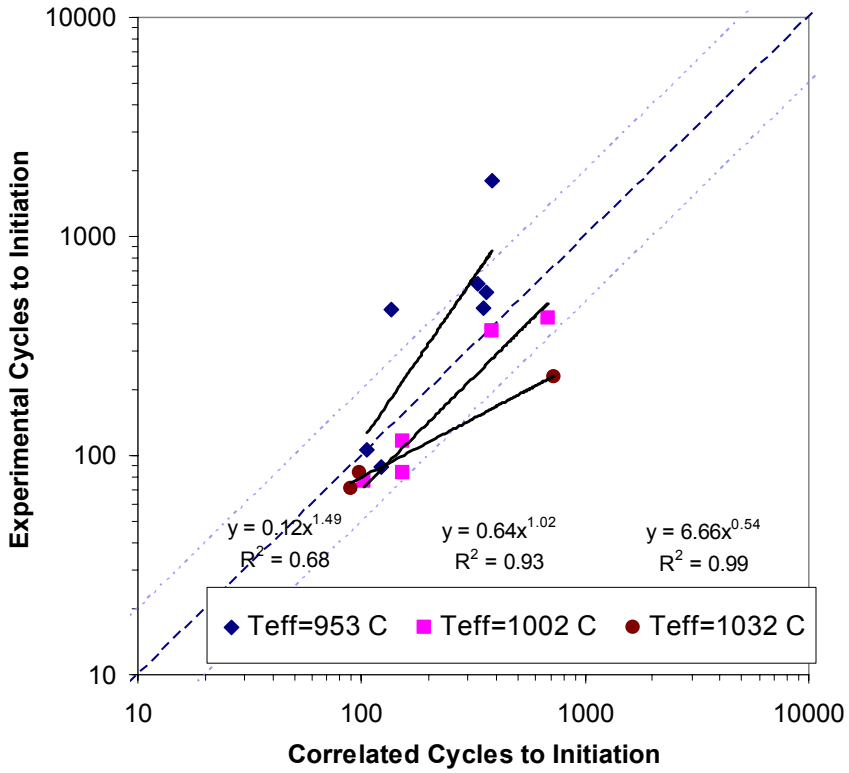

Figure 6-10 Correlation of Eq 6.26 to all <001> PWA 1484 OP TMF and BiF Results- Delineated by Cycle Effective Temperature

Given that the model incorporates multiple independent parameters ($\Delta\gamma_{in}^{sl}$ and $\tau_{\min}$) a simple strain-life plot would not accurately depict the efficacy of this models correlation, as plotting the results in this way would not produce a single trend. However, Figure 6-11 depicts the inelastic shear strain range versus experimental cycles to failure, as well as the environmental-fatigue life prediction trend from Eq 6-26 calibrated using the values in Table 6-3.

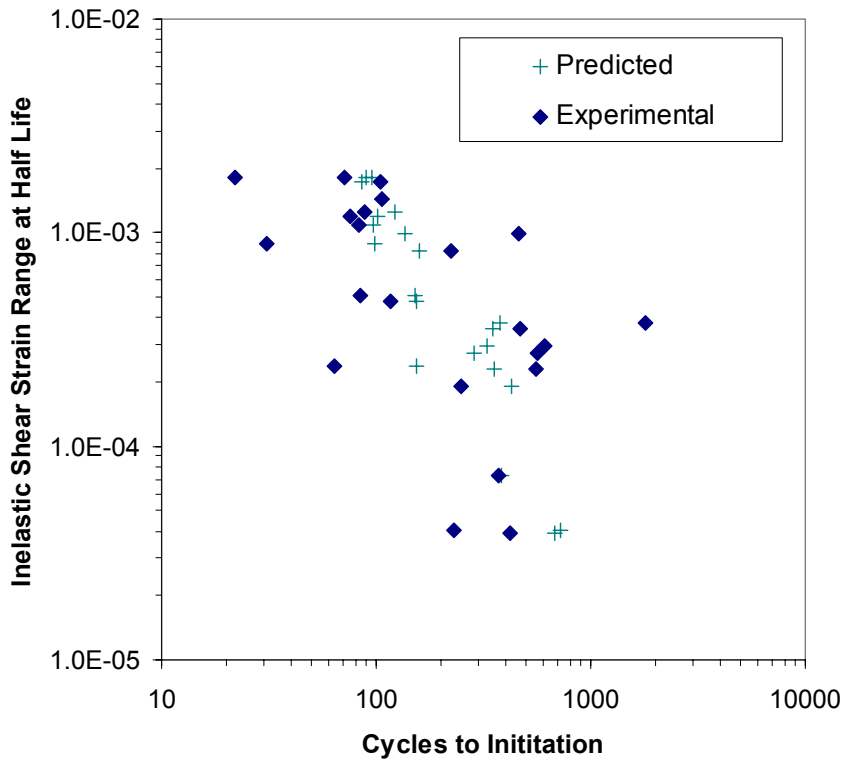

Figure 6-11 $\Delta\gamma_{in}^{sl}$ versus Cycles to Crack Initiation- Predicted Values From Eq 6-26

Figure 6-10 clearly indicates that the model does not perform well at collapsing the data on an effective temperature basis. A model intended to capture the effects of different temperature-strain cycle types should collapse this data to a single trend. In order to determine which model parameter is causing the delineation in T_{eff} correlation trends, the experimental cycles to initiation was plotted versus the slip band spacing component of Equation 6-26

$$C = \left(\Delta\gamma_{in}^{sl}\right)^{-m} \exp\left(\frac{Q_{sl}}{RT_{eff}}\right) \qquad \textbf{(6-27)}$$

and shown in Figure 6-12.

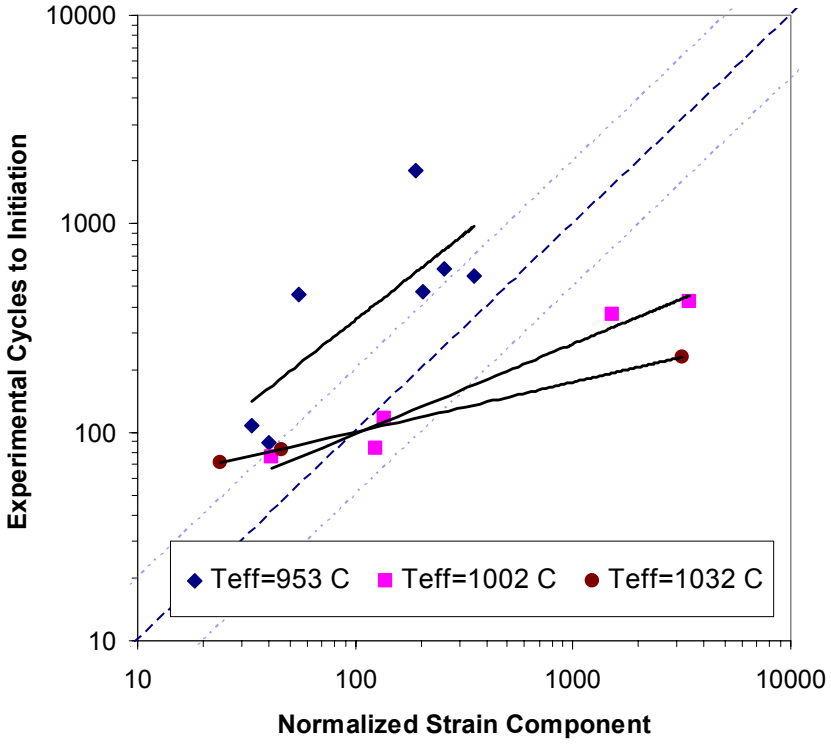

Figure 6-12 Experimental Lives versus Normalized Strain Component Life (Eq. 6-27)

Figure 6-12 clearly indicates that the slip band spacing portion of the life estimation model is not accounting for each cycles coupled strain-temperature effects. Utilizing the three baseline TMF tests (T_{eff}=1226°C), three baseline BiF tests (T_{eff}=1275°C) and the three BiF tests having 5 minute hold times (T_{eff}=1305°C) from Table 3-3, the following relationship for slip band spacing correlated the experimental data (by expanding upon Eq. 6-27)

$$C = K\left(\Delta\gamma_{in}^{sl}\right)^{-m} \exp\left(\frac{Q_{sl} + Q_{ox} - B\sigma_{\max}}{RT_{eff}}\right) N^{-k} \qquad \textbf{(6-28)}$$

where Q_{ox} is the activation energy determined for non-stressed γ' depletion studies, σ_{max} is the maximum tensile stress in the stabilized cycle (occurring at 550°C) and B is the volume over which the stress acts (identical to that found for the stressed oxidation

kinetics). Furthermore, incorporating the γ' particle coarsening as a damage parameter, as suggested in [112], the following equation would replace the prefactor "K"

$$K = 1 - D_{\gamma'} \qquad \text{where } D_{\gamma'} = 1 - \frac{r_0}{r_t} \tag{6-29}$$

where $D_{\gamma'}$ is the damage parameter, r_0 the initial γ' radius and r_t the γ' radius as a function of time. Utilizing the functional form of the experimentally determined coarsening equation for Nimonic alloys discussed in Chapter 2 (Eq. 2-13) [72], Equation 6-29 becomes

$$K = \frac{r_0}{r_0 + A\exp(uT_{eff})t^{1/3}} \tag{6-30}$$

The magnitude of r_0 is negligible with respect to the exponential term, therefore r_0 in the denominator of Eq. 6-30 may be disregarded. In which case Eq 6-30 becomes

$$K = \frac{r_0}{A\exp(uT_{eff})t^{1/3}} \tag{6-31}$$

Correlation of the expanded strain component (Eq. 6-28) and prefactor (Eq. 6-31) of the life equation (Eq. 6-26),

$$\frac{r_0\left(\Delta\gamma_{in}^{sl}\right)^{-m}}{A\exp(uT_{eff})t^{1/3}}\exp\left(\frac{Q_{sl} + Q_{ox} - B\sigma_{\max}}{RT_{eff}}\right) \tag{6-32}$$

against crack initiation life for the nine baseline tests, while allowing the terms A and u to vary, yields the relationship shown in Figure 6-13.

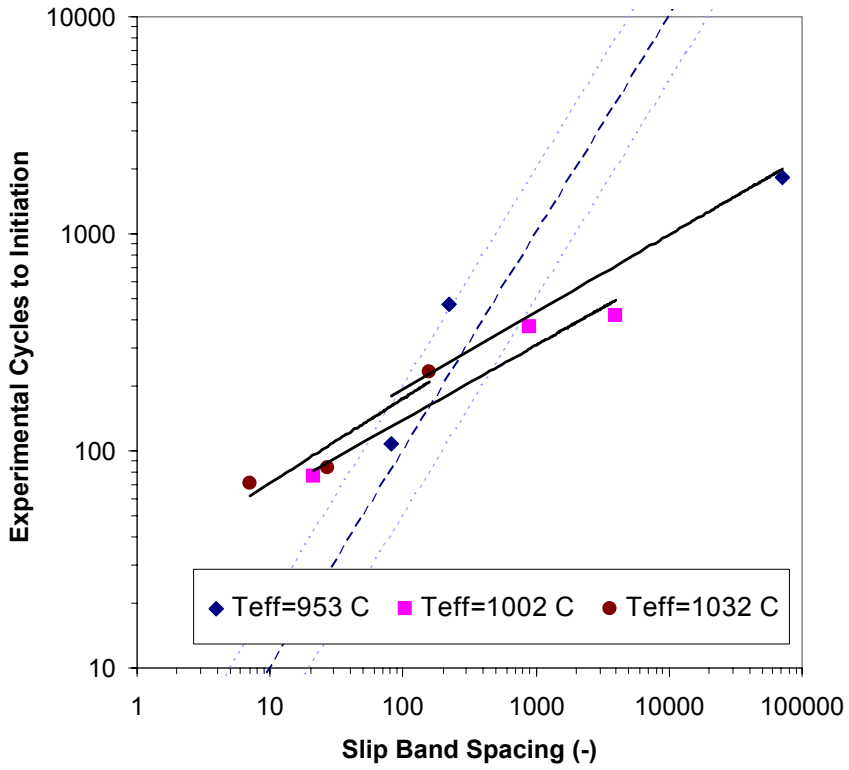

Figure 6-13 Experimental Lives versus Normalized Strain Component Life (Eq. 6-32)

Clearly the correlated strain component of the life equation (Eq 6-32) does a far better job of collapsing the data on a T_{eff} basis than does Eq 6-27. The form of Equation 6-32 is very similar to that of classical plasticity rate equations, Eq 5-1. The fact that the slip band spacing equation matches that of classical plasticity rate equations is not surprising given that they account for the same physical processes, namely dislocation movement. The inclusion of γ' coarsening as a damage parameter effectively accounts for the effect that microstructural evolution has upon TMF life.

The resulting life estimation equation is then

$$N_i = \left(\frac{Ar_o \left(\Delta\gamma_{in}^{sl}\right)^{-m}}{\exp(uT_{eff})t^{1/3}} \exp\left(\frac{Q_{sl} + 2Q_{ox} - B\left(\sigma_{\max} + |\tau_{\min}|\right)}{RT_{eff}} \right) \left(\frac{\nu}{\nu \cdot t_h + 1/2} \right)^{-(n+d)} \left(\frac{R_a}{8} \right)^{-h} \right)^{p}$$

(6-33)

where the unkown values are A, u and P. Correlating Equation 6-33 to the nine baseline test results yields the parameter values in Table 6-4 and the results for the baseline tests are shown in Figure 6-14.

Table 6-4 Parameter Values From Correlation of Eq 6.33 to all <001> PWA 1484 OP TMF and BiF Results. Value of r_0 from [7]

A	1.00E+15	(-)
r_0	300	nm
u	0.04	1/K
m	1.29	(-)
Q_{sl}	6056	J/mol
Q_{ox}	162863	J/mol
B	161	m^3/mol
n	f(temp)	(-)
d	0.17	(-)
Ra	197	nm
h	0.2	(-)
p	0.27	(-)

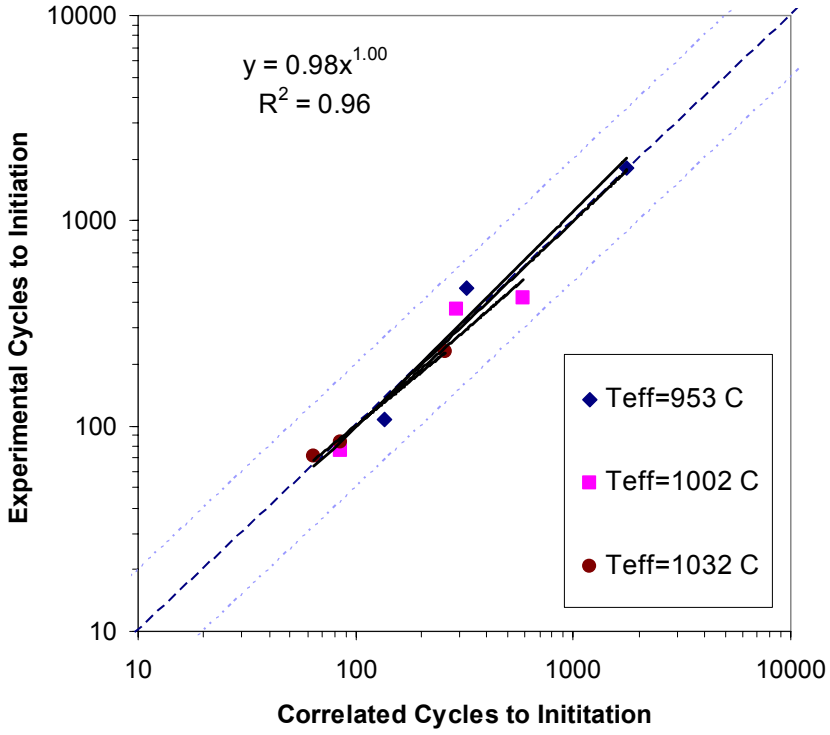

Figure 6-14 Correlation of Equation 6-33 to all <001> PWA 1484 OP TMF and BiF Baseline Results- Delineated by Cycle Effective Temperature

The newly correlated model was used estimate the remaining effective temperatures tested (865°C and 1027°C) and is shown in Figure 6-15.

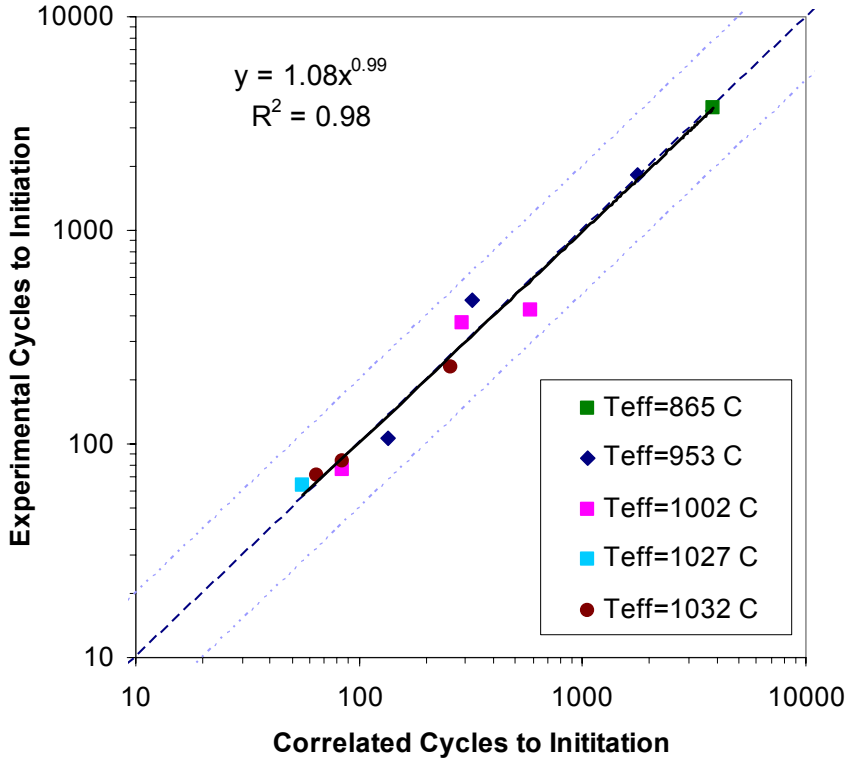

Figure 6-15 Prediction of <001> PWA 1484 at all Effective Temperatures Tested

The effective temperatures shown in Fig 6-15 result from the following test conditions (also detailed in Table 3-2):

- T_{eff}=865°C: OP BiF with T_{min}=550°C and T_{max}=900°C
- T_{eff}=953°C: OP TMF with T_{min}=550°C and T_{max}=1050°C
- T_{eff}=1002°C: OP BiF with T_{min}=550°C and T_{max}=1050°C
- T_{eff}=1027°C: OP TMF with T_{min}=550°C and T_{max}=1050°C with 5 minute high temperature hold
- T_{eff}=1032°C: OP BiF with T_{min}=550°C and T_{max}=1050°C with 5 minute high temperature hold

The model clearly does an excellent job of correlating data from tests having different waveforms (BiF and TMF), maximum temperatures and high temperature hold times. The correlated model was then used to estimate lives for all <001> oriented test results in Table 3-3 and is shown in Fig 6-16.

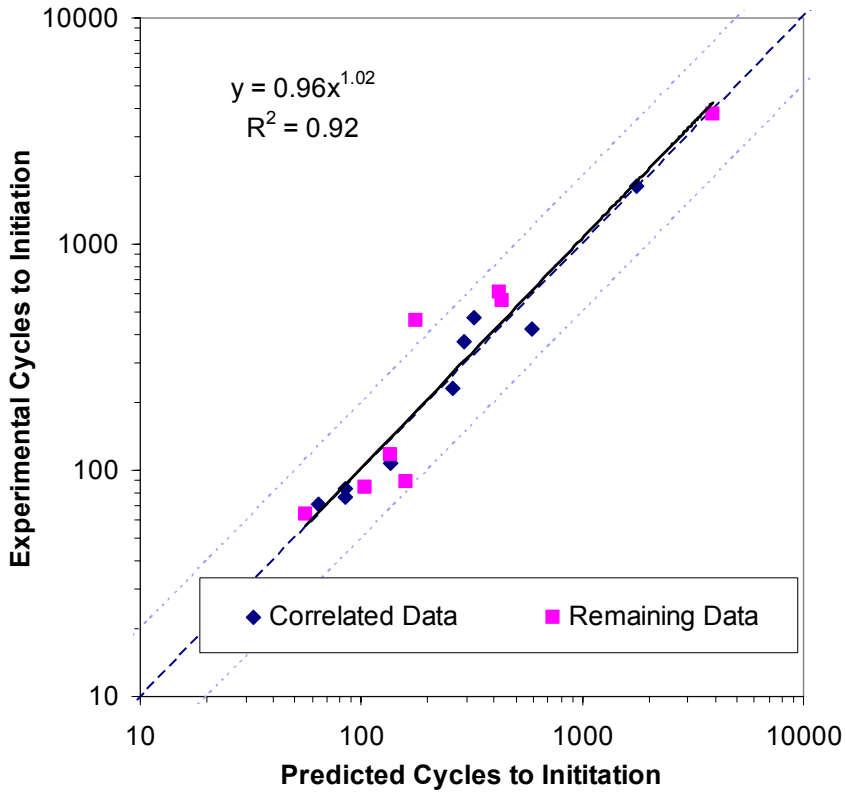

Figure 6-16 Life Prediction Using Equation 6-33 to all <001> PWA 1484 OP TMF and BiF Results- Delineated by Cycle Effective Temperature

Eq 6-33 does an excellent job of predicting <001> oriented OP TMF and BiF lives, including tests having different maximum temperature and hold times, with a correlation coefficient above 0.91. Furthermore the model predicts 94% of the experimental results within a factor of 2X. The single data point falling outside of the 2X bands is from an OP TMF test who's first 30 cycles were mistakenly conducted at $\Delta\varepsilon_{mech}$ = 0.5% and remaining cycles had $\Delta\varepsilon_{mech}$ = 1.3%. The life estimation for this TMF test,

determined using data from the normalized hysteresis loop of the half cycle (occurring in the $\Delta\varepsilon_{mech}$ = 1.3% portion of the cycle), indicates that the model does not account for varying-load history effects.

The model was then used to predict the <111> and <123> oriented specimen lives. Results for OP TMF baseline tests for all three axis are shown in Fig 6-17.

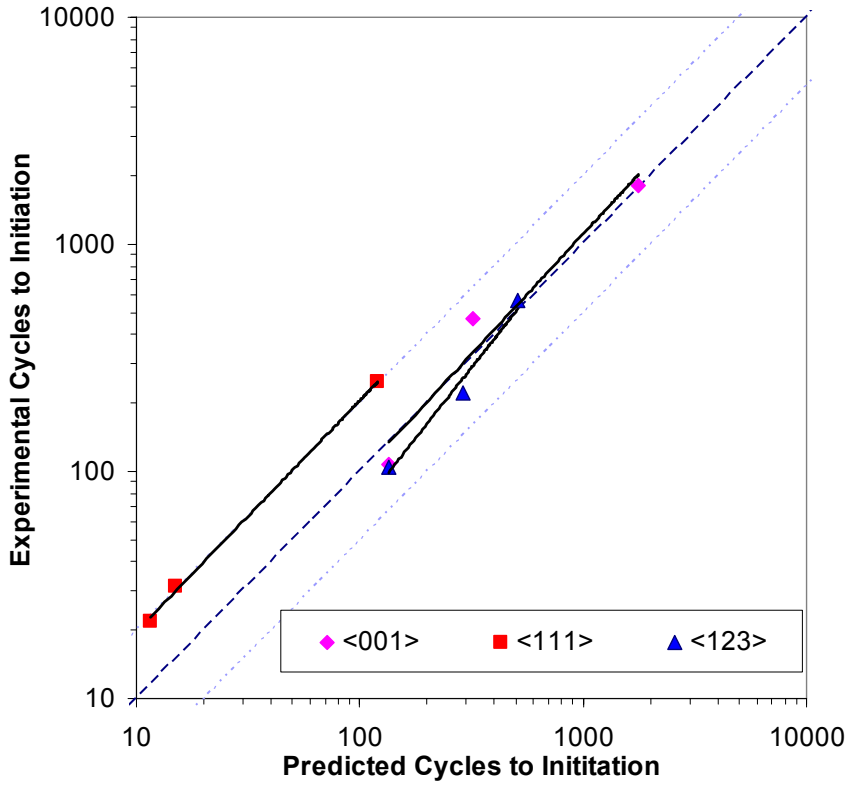

Figure 6-17 Life Prediction Using Equation 6-33 to Baseline <001>, <111> and <123> Oriented PWA 1484 OP TMF Results

As indicated by Figure 6-17 the model does an excellent job of predicting the lives of <111> and <123> oriented specimens. Having proven the capacity to account for differing number of slip systems activated, the life model should be a good starting point for fatigue crack initiation at notches. One requirement for utilizing Eq. 6-33 to predict notch-life is a crystal plasticity model which can determine the inelastic strain,

orientation with respect to <001>, maximum stress and minimum shear stress of the stabilized cycle for the area of interest in the component.

Figure 6-18 depicts the inelastic shear strain range versus experimental cycles to failure, as well as the environmental-fatigue life prediction trend, from Eq 6-33, calibrated using the values in Table 6-4 for all experiments in Table 3-3.

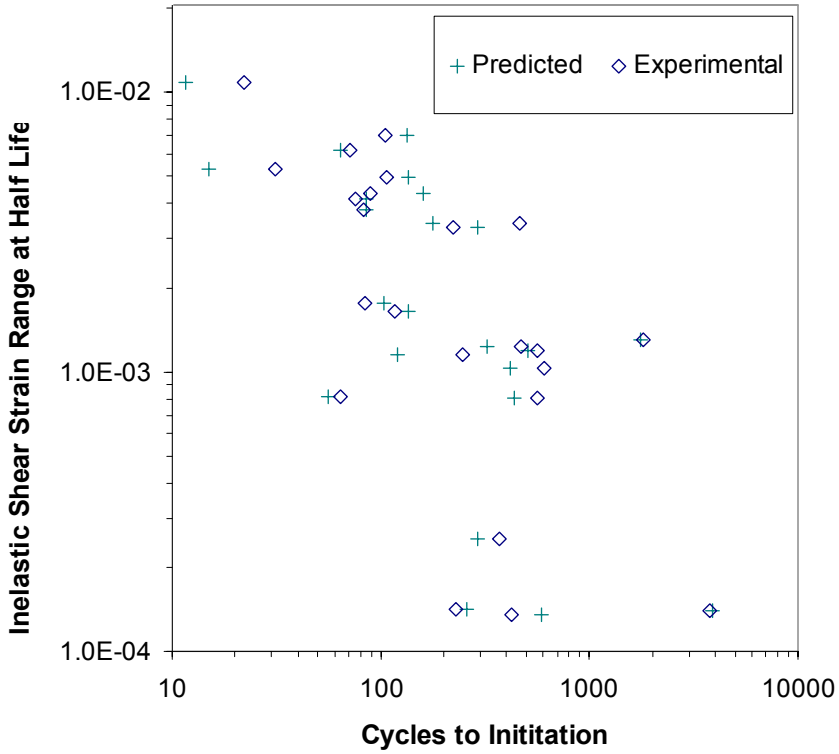

Figure 6-18 $\Delta\gamma_{in}^{sl}$ versus Cycles to Crack Initiation- Predicted Values from Eq 6-33

The data in Figure 6-18 was then delineated by material primary orientation, cycle type and effective temperature, as shown in Fig 6-19.

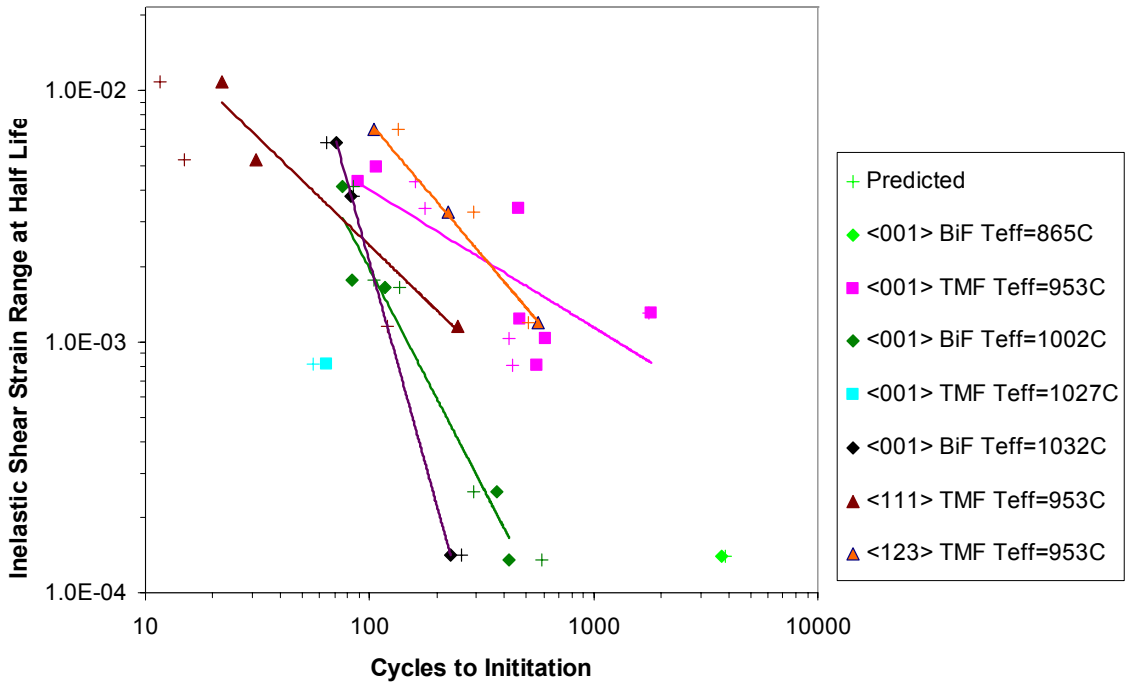

Figure 6-19 $\Delta\gamma_{in}^{sl}$ versus Cycles to Crack Initiation- Predicted Values from Eq 6-33 Delineated by Specimen Orientation, Cycle Type and Effective Temperature

6.4 Discussion

A single relationship that predicts the number of cycles to crack initiation for components experiencing BiF and TMF waveforms has been identified and modified to account for microstructural evolution and damage mechanism coupling. The original relationship is based upon independently occurring fundamental dominant damage relationships and their interactions, i.e. non-stressed γ' depletion and relatively low temperature slip spacing studies. It was shown that when combining the relationships determined for these independent mechanisms in a physics-inspired model, the interactions between these dominant damage drivers was not sufficiently accounted for. Specifically the γ' depletion kinetics as well as the relative amount of damage contributed

to by the strain were determined to be dependent upon applied stress (of some form). There are several key aspects of the model which should be discussed.

The model includes three variables that require fitting to experimental data. They are: the prefactor, A; the exponent, p; and the γ' coarsening parameter, u. Fitting of the prefactor, A, to experimental data is straight forward, however the remaining variables should be discussed. According to the fundamental slip spacing studies (Section 5.5), the exponent, p, should have the value $p = (1+.0653)^{-1} = 0.939$. However the value p = 0.27 fit the life data. This may be explained by the fact that the slip band spacing studies as a function of cycles were carried out at room temperature and then only conducted to 76 cycles. Further work on slip band spacing as a function of temperatures and cycles needs to be conducted to resolve this issue. Though the value determined for the coarsening kinetics parameter, u = 0.04, is similar to that found for Nimonic alloys (u = 0.012), the parameter should be determined from γ' coarsening studies performed on PWA 1484, as was done for the Nimonic alloy [72]. However, lack of data required the fitting of the exponent in the final stages of the life estimation correlation.

Finally the implications of the crystallographic orientation results should be quantified. A simplified life estimation model for OP TMF and BiF that accounts for crystal orientation coupled with a crystal plasticity constitutive model will greatly enhance life predictive capabilities for turbine components; resulting in far fewer up-front specimen and component tests. If implemented into the standard practice of a turbine manufacturer, this relationship will reduce upfront modeling and testing costs as well as the time required for new designs to be implemented.

CHAPTER 7. CONCLUSIONS AND RECOMMENDATIONS FOR FUTURE WORK

7.1 Conclusions

The goal of this research was to create a life-estimation model for PWA 1484 turbine components experiencing OP thermomechanical fatigue interactions. In doing so fundamental studies were undertaken to determine slip band spacing as a function of applied strain and temperature, as well as determination of oxidation kinetics as a function of surface roughness and temperature. The proposed life estimation model does an excellent job of predicting OP TMF and BiF life for various test conditions. The primary novel contributions of this work with regard to PWA 1484 are as follows:

- Utilizing both the bithermal fatigue (BiF) and thermomechanical fatigue (TMF) tests enables the isolation and subsequent determination of dominant damage mechanisms.
- A relationship was proposed between BiF and TMF inelastic strain ranges (for tests having identical lives) using an Arrhenius component. This relationship accounts for relative amounts of environmental degradation and allows the use of a single test type.
- PWA 1484 is a Group II oxide former with dominant oxides consisting of any combination of spinel, NiO and/or α-Al_2O_3.
    - Oxidation of PWA 1484 follows a sub-parabolic relationship.
    - The type of oxide produced is temperature and exposure time dependent.
    - Oxides produced at temperature above 950°C spall extensively.
- A single kinetics relationship for the oxidation of PWA 1484 between 850° and 1050°C was proposed and correlates the isothermal non-stressed data well.
- A relationship was proposed which accounts for the stress-assisted γ' depletion kinetics of PWA 1484 experiencing OP waveforms. The proposed relationship correlates experimental data well.

- Average slip band spacing can be related to inelastic strain and temperature using an Arrhenius form. The proposed relationship correlates the experimental data very well.
- Average slip band spacing occurring during OP TMF and BiF experiments is not only strain but also stress dependent.
- Crack initiation of OP TMF and BiF specimens occurring as a result of slip band-oxidation interactions can be predicted using a model which accounts for stress-assisted oxidation kinetics, temperature-dependent slip spacing kinetics and γ' coarsening.
- The proposed modification of a classic life-estimation model does an excellent job of capturing cycle type, hold time, effective temperature and orientation effects.

This research also resulted in several less novel conclusions, as listed below.

- Out-of-phase TMF and BiF specimens can experience a range of dominant damage mechanisms, from fatigue and environmental-fatigue-dominated to inclusion of a viscoplastic damage element, as indicated by Figure 3-41.
- Out-of-phase BiF specimens experience far more environmental damage than do the OP TMF specimens.
- Slip band-oxide spike (fatigue-environment) interactions produce crack initiation sites in PWA 1484 experiencing OP TMF and BiF.
- Specimens having <001> orientation have the longest OP TMF lives while <111> have the shortest.
- Utilizing the inelastic shear strain range, on the slip system having highest Schmid factor, in strain-life curves collapses life data best for <001>, <111> and <123> orientations.
- Oxidation kinetics has been shown to be surface roughness dependent, with higher roughness values yielding faster kinetics.
- Stress-enhanced oxidation occurs at a considerably faster rate (two to three times) than non-stressed oxidation.

- Average slip band spacing is dependent upon the number of cycles experienced by the specimen.
- The strain exponent in the slip band spacing relationship of single crystal superalloys is considerable more negative than that found for polycrystalline materials.
- The primary parameters controlling OP TMF life in the Neu-Sehitoglu (N-S) model are the oxidation and γ' depletion activation energies and the strain exponents in the environmental-fatigue module.
- The N-S model was found to be quite robust and relatively easily modifiable into an engineering life estimation form, requiring only three baseline TMF tests to calibrate the model for TMF data.

7.2 Recommendation for Future Work

Though a considerable amount of experimentation and analysis was performed for this work, inevitably more work can be performed. Specific suggestions for future work are provided which, when coupled with the analysis provided here, may shed more light on the underlying deformation physics resulting from OP TMF testing.

- A complete test matrix for <011> oriented specimens, as well as continued testing of <111> and <123> specimens are required to confirm the life estimation models ability to account for crystallographic orientation. Tests should include both OP BiF and TMF waveforms, as well as high temperature hold times.
- Continued testing of <001> oriented specimens to account for cycle minimum temperature effects would be beneficial. Previous work indicates that the cycle minimum temperature may severely effects TMF cycle life [113, 114]. Several OP TMF and BiF tests performed at a range of minimum temperatures would provide insight to PWA 1484's dependence upon this cycle parameter, if any.
- TMF and BiF testing which incorporate fatigue cycling within a high temperature hold time would yield a more realistic aero turbine cycle. Analysis of these

results with respect to the studies performed here may lead to a cycle counting method for aero turbine mission cycles.

- Thermogravimetric oxidation tests of PWA 1484 between 750° and 1050°C in 50°C increments would enable the determination of both the lower and higher temperature activation energy for oxidation. These tests would also allow for confirmation of the hypothesis that the oxidation and γ' depletion activation energies are the same. Furthermore, continued microscopy of oxidized specimens may result in calibration of ThermoCalc and DICTRA models to predict oxidation and γ' depletion [115]. Finally, incorporation of the effects of γ' depletion into a crystal plasticity model, as in [52], would be of great benefit to predicting material deformation response.
- Systematic studies of stress-assisted γ' depletion and oxidation should be performed to confirm the relationship proposed in Chapter 4 (Eq. 4-7).
- The calibration of the proposed life estimation equation indicates that slip band spacing is more dependent on continued cycling than was determined in the initial slip band spacing tests. Therefore cyclic slip band spacing tests at 450°, 550° and 650°C, continued to 3000 cycles, are required to confirm this finding.
- Studies to determine the kinetics of γ' coarsening in PWA 1484 is required to calibrate the microstructural evolution damage parameter used in the life estimation relationship. Furthermore, the results of these studies could be incorporated into a crystal viscoplasticity model accounting for γ' depletion similar to those of [116].
- A temperature dependent crystal viscoplasticity model needs to be developed for PWA 1484. A model of this type is required to provide the stabilized hysteresis loops needed to determine the model parameters for the life estimation model proposed (Eq. 6-33). Furthermore, calibration of a CVP would potentially allow the implementation of the proposed life estimation routine to life prediction of notches. Notch specimen tests would then need to be performed to validate the potential notched life prediction capabilities of the proposed life prediction model.

APPENDIX

A.1 Specimen Drawings

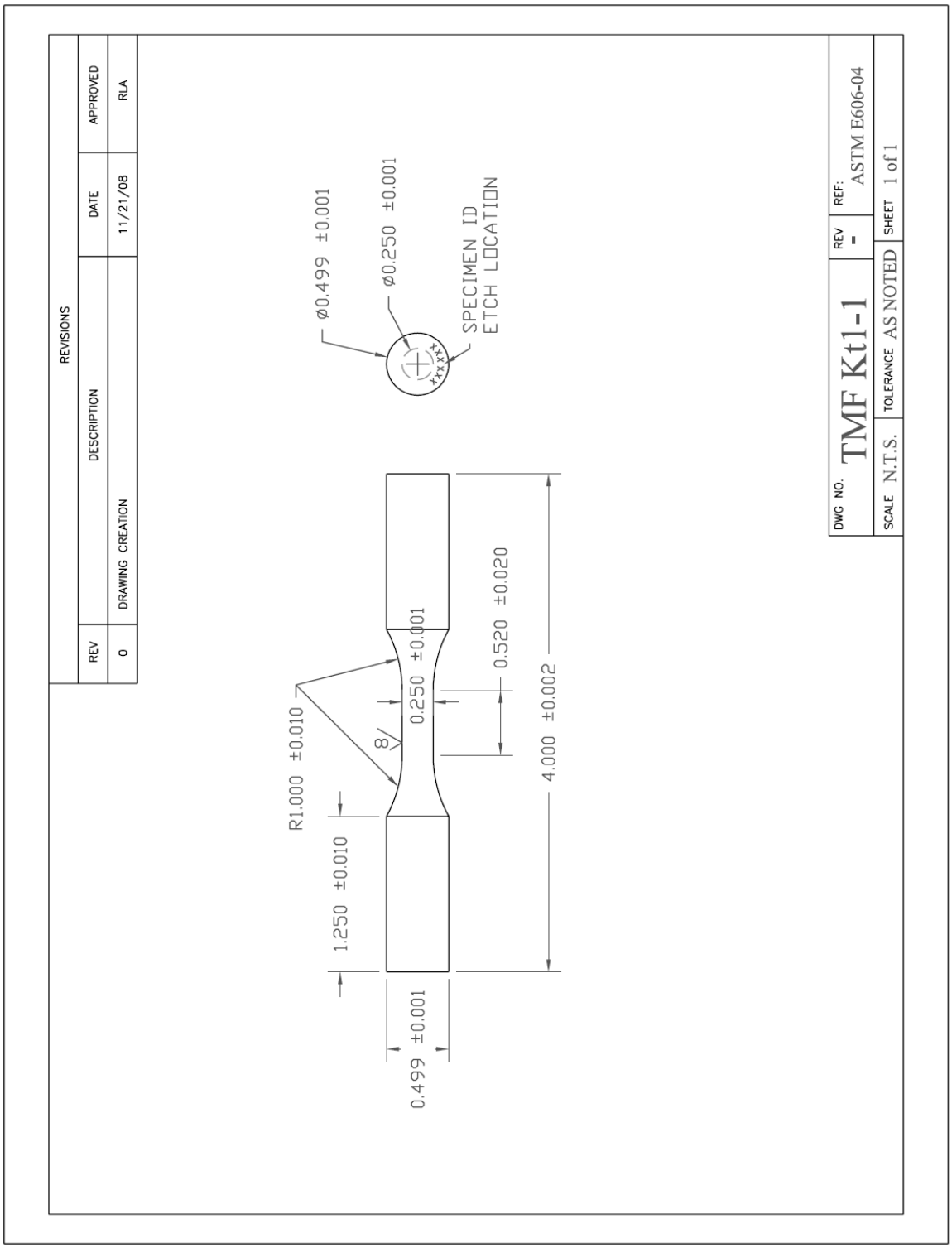

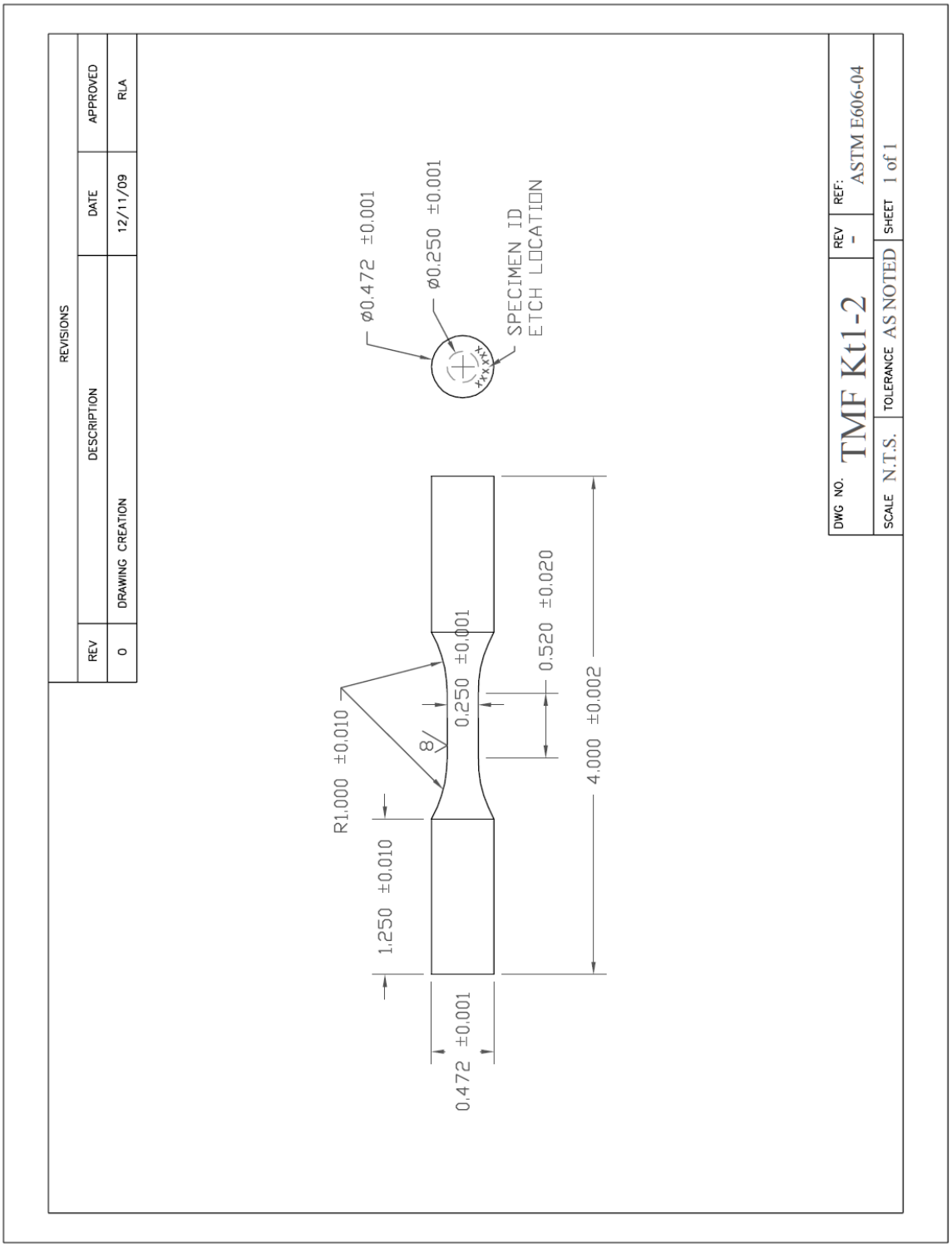
REVISIONS
REV
DESCRIPTION
DATE
APPROVED
0
DRAWING CREATION
12/11/09
RLA
Ø0.472 ±0.001
Ø0.250 ±0.001
SPECIMEN ID
ETCH LOCATION
R1.000 ±0.010
8
0.250 ±0.001
0.520 ±0.020
4.000 ±0.002
1.250 ±0.010
0.472 ±0.001
DWG NO.
TMF Kt1-2
REV
-
REF:
ASTM E606-04
SCALE N.T.S.
TOLERANCE AS NOTED
SHEET 1 of 1

A.2 Material Tracking Documents

GATech MPRL
MRDC 2340
771 Ferst Dr, Atlanta Ga, 30332-0405
404-385-7135

MATERIAL RECEIVER

Project Reference: **Thermomechanical Fatigue Crack Formation in Single-Crystal Ni-base Alloy**

Date: _____

Received by: Robert Amaro
Email:
Phone:

Received From:

Reference documents:
Drawing No:

Reference Quote:

Items received:

Item	Qty	Material	Specimen No:	Inspection Report	Orientation	Cert	Traveler	Packing List
1	1	PWA 1484						
2	1	PWA 1484						
3	1	PWA 1484						
4	1	PWA 1484						
5	1	PWA 1484						
6	1	PWA 1484						
7	1	PWA 1484						
8	1	PWA 1484						
9	1	PWA 1484						
10	1	PWA 1484						
11	1	PWA 1484						

Specific documents received with materials/items:
1.

GATech MPRL
MRDC 2340
771 Ferst Dr, Atlanta Ga, 30332-0405
404-385-7135

MATERIAL SHIPPER (page 1 of 2)

Job Reference: **Thermomechanical Fatigue Crack Formation in Ni-base Superalloys**

Contact: Robert Amaro
Email:
Phone:

Drawing No: TMF Kt1-1 Rev 0

Reference Quote: -

Ship to: -

Item	Qty	Material	Specimen No:	Dim's (as shipped)	Packed	Traveler	dwg	instructions
1	1	PWA 1484	-					
2	1	PWA 1484	-					

GATech MPRL
MRDC 2340
771 Ferst Dr, Atlanta Ga, 30332-0405
404-385-7135

MATERIAL SHIPPER (page 2 of 2)

Job Reference: **Thermomechanical Fatigue Crack Formation in Ni-base Superalloys**

Contact: Robert Amaro
Email:
Phone:

Drawing No: TMF Kt1-1 Rev 0

Reference Quote: -

Ship to: -

Instructions:
Please find enclosed 2 PWA 1484 material specimens. Please machine all specimens per drawing number TMF Kt1-1 and ASTM E606-04 $^{\epsilon 1}$, particularly Appendix X3 (enclosed). Please make 2 specimens from all bars. There should be a total of 4 specimens machined from the 2 bars provided. Please transfer/etch the specimen ID number to both ends of the finished part as indicated in the supplied dwg. Please ensure that the material travelers stay with the material specimens at all times and return all documents with the finished pieces. Additionally please enclose a certificate of conformance and a specimen inspection report detailing each of the specimens in the final return shipment. Finally, please send back any scrap that me be left after machining.

If you have any questions please contact me at _____

Thank you
Robert L. Amaro

GATech MPRL
MRDC 2340
771 Ferst Dr, Atlanta Ga, 30332-0405
404-385-7135

MATERIAL TRAVELER

Job Reference: **Thermomechanical Fatigue Crack Formation in Single-Crystal Ni-base**

Contact: Robert Amaro
Email:
Phone:

Drawing No: TMF Kt1-1 R0

Reference Quote: -

QTY	Material:	Specimen No:	Ref. Drawing:
1	PWA 1484	-	TMF Kt1-1 R0
	Dim's: (as shipped)	Primary Orientation	deviation (deg)
	-	-	-

Notes:
Machine 2 specimens from this bar

A.3 Laue Results

- Material having <123> orientation- email from Venkat Seetharaman (Pratt & Whitney) July 26 2010

Rick,

I do not have the 5/8" diameter bars with <123> orientation.

Instead, I have been able to get a couple of 1.0" diameter bars. I am arranging to send them separately by Fedex to your attention. I understand that GT TMF specimens are 0.5" in diameter and 4.0" long. I hope you can machine two specimens from each 1.0" dia x 8.75" long bar.

The orientation information for the bars is as follows:

BAR ID	deviation From <001> (degrees)	deviation from <011> (degrees)	deviation from <111> (degrees)	Approximate Miller Indices of the orientation
21141	40.7	19.5	18.7	749
21142	38.1	14.6	24.6	729

Please let me know if you have any questions

Thanks!

Venkat

- Material having <111> orientation- received the following with shipment of material from P&W 4-12-09

			Alpha
Part #			111
23816	6.2	2	6.5
23822	4.5	7.8	9.0
23824	5.8	10.3	11.8
23825	6	9.8	11.5
23828	3	3	4.2
23851	7	4	8.1
23856	1.2	1.5	1.9
23857	1.2	1.5	1.9
23858	6.5	0.7	6.5
23863	4.1	6.1	7.3
23864	4.1	4.2	5.9
23865	7.8	2.2	8.1
23866	7	3.5	7.8

Figure A-1 PWA 1484 Laue Results for <111> Oriented Bars

- Material having <001> orientation- material existing at GaTech from previous project (specimen -03)

MERL XRD OWIKLAUE ANALYSIS STEREOGRAPHIC CONVENTION

XRD NUMBER: w/o 545130-0

5-28-04

SPEC. NO.	DEVIATION OF SPEC. AXIS FROM: [001] (ALPHA)	[100]	[010]	AVE. ALPHA	LOCATION	BETA	RHO	LAUE COORDINATES [hkl] (001) X	Y	[hkl] (210) X	Y
04	2.5	87.5	89.8		TOP	-13.1	-13.1	-2.3	-.7	-7.7	+24.2
								(001)		(210)	
138X	3.2	86.8	89.8		TOP	-25.1	-25.1	-1.5	+2.8	+22.8	+14.8
								(001)		(210)	
10	1.0	89.7	89.1		TOP	-5.8	-5.8	-.9	-.4	+24.3	+2.3
								(001)		(210)	
138Y	7.6	83.3	86.6		TOP	+1.5	+1.3	-3.3	+6.8	+22.0	+6.1
								(001)		(210)	
02	4.8	88.8	85.3		TOP	+.2	+.3	-4.7	-1.2	+22.1	-1.3
								(001)		(210)	
09	1.6	88.5	89.5		TOP	-14.1	-14.1	-1.4	-.8	-7.6	+25.8
								(001)		(210)	
12	4.3	89.6	85.7		TOP	-4.3	-4.3	-.7	+4.3	+1.3	-21.7
								(001)		(210)	
08	7.6	82.5	88.5		TOP	-14.7	-14.6	+6.8	+3.4	+12.6	-22.0
								(001)		(210)	
03	8.7	89.4	81.3		TOP	-17.2	-17.1	-2.0	+8.5	+5.6	-16.7
								(001)		(210)	
05	7.9	82.9	86.5		TOP	-17.7	-17.9	+7.8	-1.2	-1.3	+25.3
								(001)		(210)	
138Z	5.5	87.6	85.1		TOP	-15.0	-15.1	+5.4	-1.1	-20.5	-8.2
								(001)		(210)	
11	6.6	86.3	84.6		TOP	+6.7	+6.5	-3.1	+5.8	-5.7	-20.0

Figure A-2 PWA 1484 Laue Results for <001> Oriented Bars-1

- Material having <001> orientation- received the following with shipment of material from P&W 12-2-09

RPCL CASTING DELIVERY TICKET

CDT 030-08-02

DATE	W.O. SERIAL NUMBER		SAP#
10/31/2008	various		
SPECIFICATION	HEAT NO.	JOB FILE NO.	
PWA1484	various	030-08	
TOTAL QTY	PART NUMBER	DESCRIPTION	
27	EXF2347	5/8" bars	
QUALITY SUPERVISOR EXT.	REQUESTOR EXT.	CASTING ENGINEER EXT.	
R. Ristau 5-4051	V. Seetharaman	K. Chittenden 5-8064	

Cast via following work order #s:

Mold #	Alloy & Heat#	QTY	Part Type
2184	PWA1484(P1115)	8	
2154	PWA1484(P1119)	4	
2249	PWA1484(P1116)	15	
	Total	27	

REMARKS: Solution-2390F/30min, Secondary-1975/4hrs, Precipitation-1600F/32hrs

Bar ID #	a<001>
215402	5.1
215406	7.2
215408	4.9
215411	8.3
218401	5.3
218408	10.4
218411	1.7
218412	14.0
218414	6.9
218415	6.6
218417	12.6
218418	2.8

Bar ID #	<001>
224902	2.7
224903	3.9
224904	1.4
224911	10.0
224912	4.1
224913	8
224914	10.4
224920	13.2
224921	4.8
224922	6.4
224923	13.4
224924	8.0

Bar ID #	<001>
224919	7.2
224910	7
224906	13.6

8.4" + Long Bars

Figure A-3 PWA 1484 Laue Results for <001> Oriented Bars-2

A.4 Test Matrices

Table A-1 Matrix of OP TMF and BiF Tests

Waveform	Nominal Orientation	$\Delta\varepsilon_{mech}$ (-)	T_{min} (deg C)	T_{max} (deg C)	High Temp hold time (s)
Thermomechanical Fatigue					
OP TMF	<001>	0.013	550	1050	0
OP TMF	<001>	0.009	550	1050	0
OP TMF	<001>	0.005	550	1050	0
OP TMF	<001>	0.013	550	1050	300
Bithermal Thermomechanical Fatigue					
OP BiF	<001>	0.013	550	1050	0
OP BiF	<001>	0.01216	550	1050	0
OP BiF	<001>	0.0106	550	1050	0
OP BiF	<001>	0.009	550	1050	0
OP BiF	<001>	0.007	550	1050	0
Effect of T_{eff}					
OP BiF	<001>	0.013	550	1050	300
OP BiF	<001>	0.009	550	1050	300
OP BiF	<001>	0.007	550	1050	300
OP BiF	<001>	0.009	550	900	0
Off-Orientation					
OP TMF	<111>	0.013	550	1050	0
OP TMF	<111>	0.009	550	1050	0
OP TMF	<111>	0.005	550	1050	0
OP TMF	<123>	0.009	550	1050	0
OP TMF	<123>	0.007	550	1050	0
OP TMF	<123>	0.005	550	1050	0

A.5 TMF/BiF Start-up-procedure

BEFORE ENTERING HIBAY

- ☐ Choose appropriate specimen (L/T)
- ☐ Record diameter of specimen and other appropriate information on sheet

AFTER ENTERING HIBAY

- ☐ Turn hydraulic pump; first to low, then to high.
- ☐ Place MARC MPRL indicator on board and test running sign
- ☐ While in specimen insertion mode, turn on test frame by turning HPS and HSM controls to low, then high
- ☐ Warm up machine
- ☐ Turn on water to induction heater, coil and grips
- ☐ Follow procedure for specimen preparation:
    - ☐ Clean specimen with acetone and ethanol
    - ☐ Dimple specimen
    - ☐ Measure and mark place the grips should be placed
    - ☐ Spot weld thermocouples to specimen
    - ☐ Plug in one thermocouple into temperature controller
    - ☐ Plug other thermocouple(s) into temperature indicators
- ☐ Install specimen into lower grip and tighten bottom grips
- ☐ Put in displacement mode and then auto zero (offset) load
- ☐ Turn on force interlock
- ☐ Change mode to specimen insertion mode and tighten top grips
- ☐ Center coil around specimen
- ☐ Zero out (make zero) load by changing the mode to force control (make less than 25 lbs but more than 10 lbs)
- ☐ Turn on displacement interlock
- ☐ Remove strain offset
- ☐ After calibrating extensometer, install extensometer on specimen
- ☐ Auto zero strain
- ☐ Record name of configuration file in TestStar
- ☐ Set and record displacement and force interlock values
- ☐ Turn on isolation amplifier
- ☐ Send temperature set point to zero
- ☐ Turn on induction heater
- ☐ Heat specimen to desired temperature (T_{mean}) under zero force
- ☐ Set control thermocouple
- ☐ Allow specimen temperature to stabilize
- ☐ Record thermal strain at T_{mean}
- ☐ Zero strain
- ☐ Enter minimum temperature
- ☐ Run thermal cycling code

- ☐ Allow thermal strain response to stabilize (if necessary, tune induction heater and record parameters)
- ☐ Stop code and turn off induction heater
- ☐ Calculate thermal strain polynomial in Excel and record coefficients on sheet
- ☐ Turn off machine and input new thermal strain polynomial
- ☐ Put machine in specimen insertion mode and turn it on
- ☐ Send temperature set point back to zero
- ☐ Turn on induction heater
- ☐ Send temperature back to T_{mean}
- ☐ Modify main TMF script for current test
- ☐ Rock and Roll

A.6 TMF/BiF Test Data Sheet

Life modeling of a Ni-base superalloy under TMF

GRA: RLA
Material: PWA 1484

Administrative:

Name	
Date	
Time Started	

Specimen info:

Specimen ID:	
Measured Dia. (in)	
Grip Placement	

Interlocks:

Displacement	
Load	
Strain	

Data Acquisition:

1-11 cycles	
>11 cycles	

Final Count:

Total Hrs.	
Total Tens	
Total Segments	
N_f	
Failure Point	

Test Details:

Test Number	
Force/Strain Control	
Predicted Life	
P tuning	
Preliminary Segments	
IP / OP	

Config File:

Name	
$\Delta\varepsilon/\Delta\sigma$	
Load (lbs)/ε_{mech} (%)	
Cycle Time	
ε_{therm} before zeroed (%)	
Data File	

ε_{therm} coefficients:

a	
b	
c	
d	

Notes:

A.7 Test Control Algorithms

- OP TMF CODE

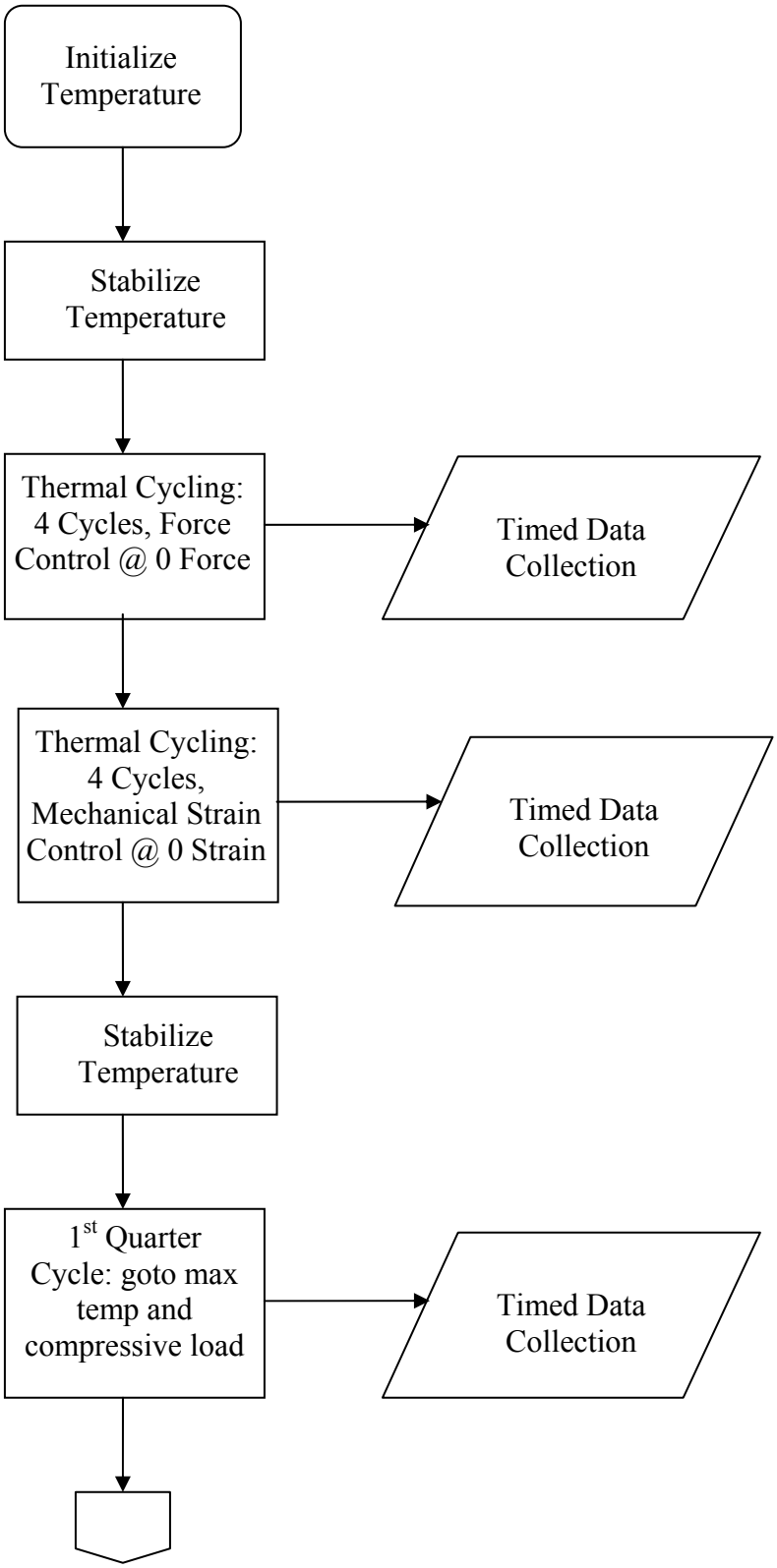

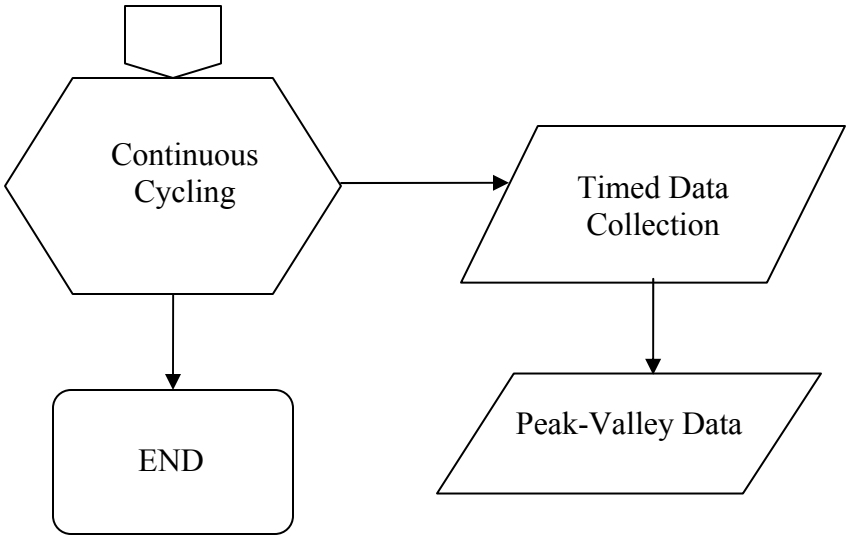

Figure A-4 Control Algorithm- OP TMF

- Screen Shots from the TestWare-SX software

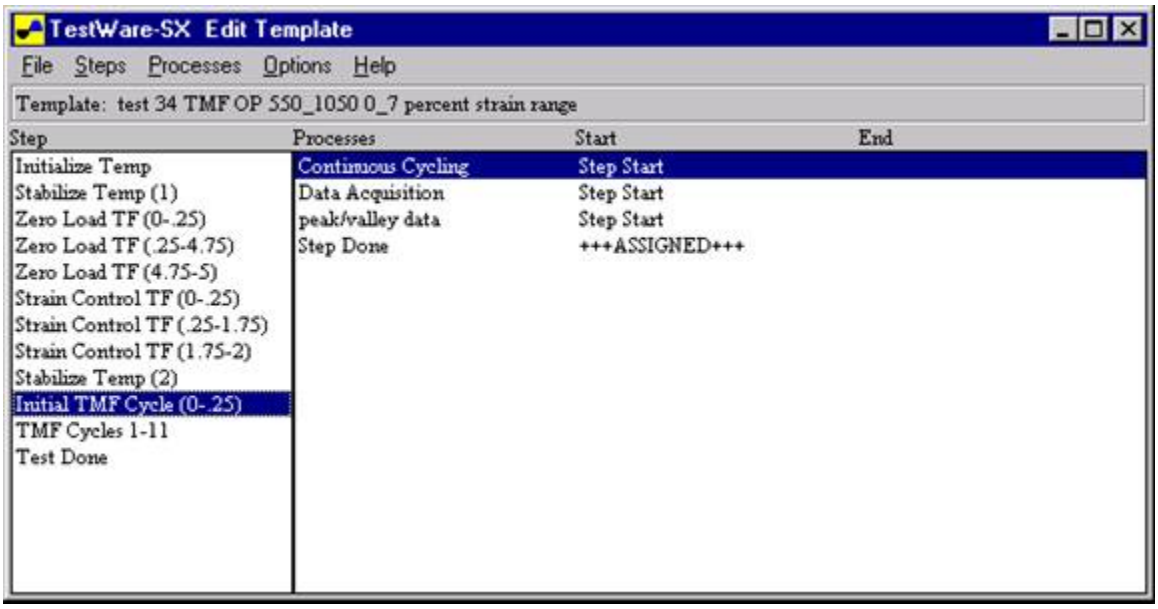

Figure A-5 Control Algorithm for OP TMF- Highlight of Initial Ramp

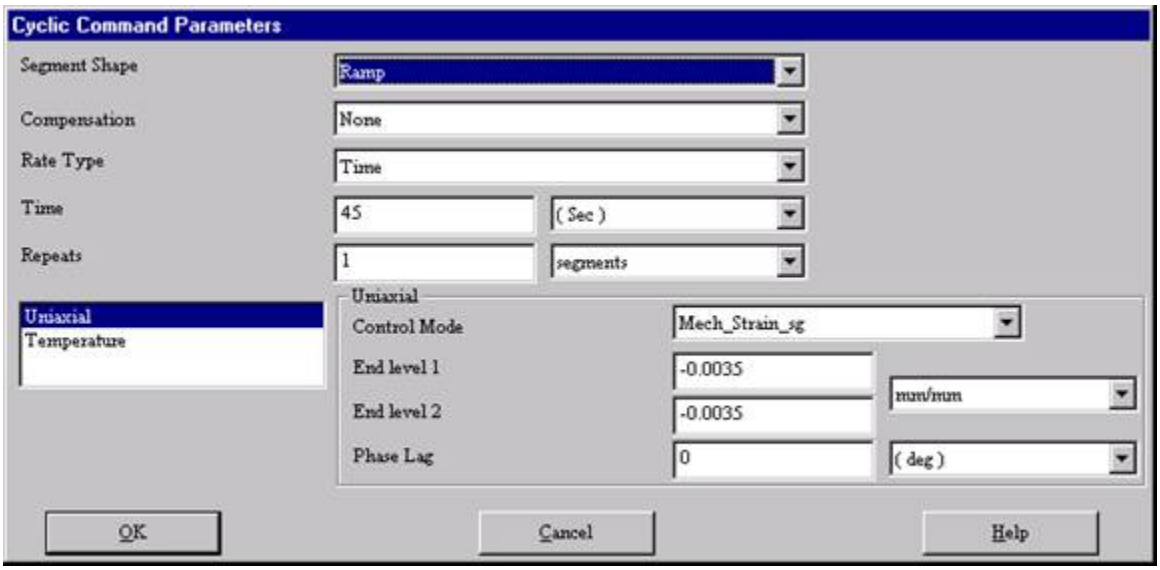

Figure A-6 OP TMF "Initial TMF Cycle (0-.25)"- Go To T_{max} and ε_{min}

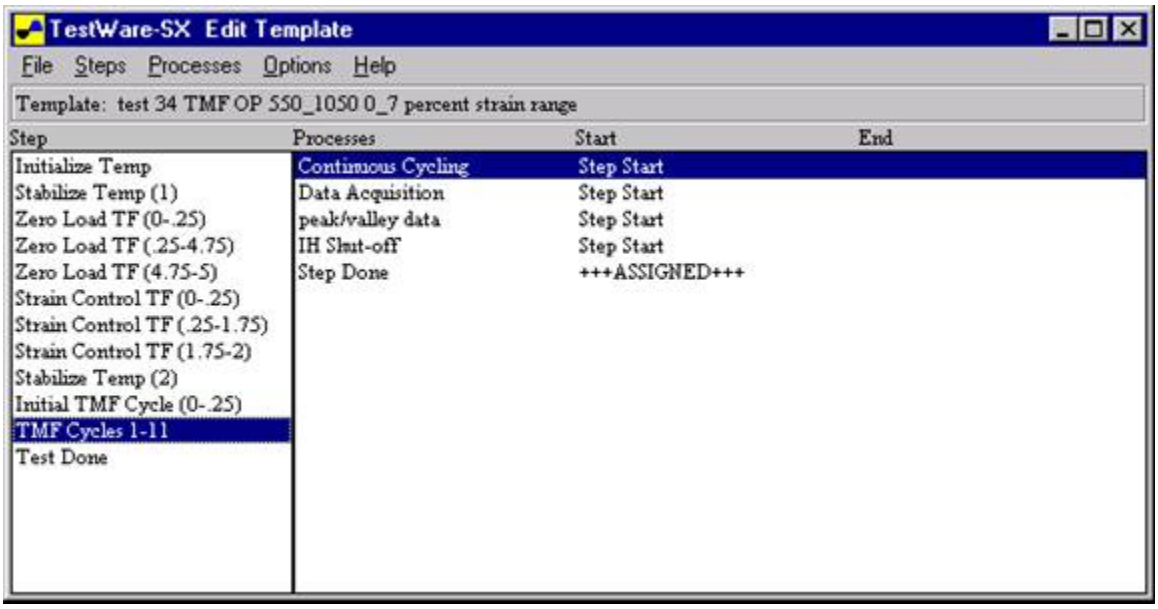

Figure A-7 Control Algorithm for OP TMF- Highlight of Continuous Cycling

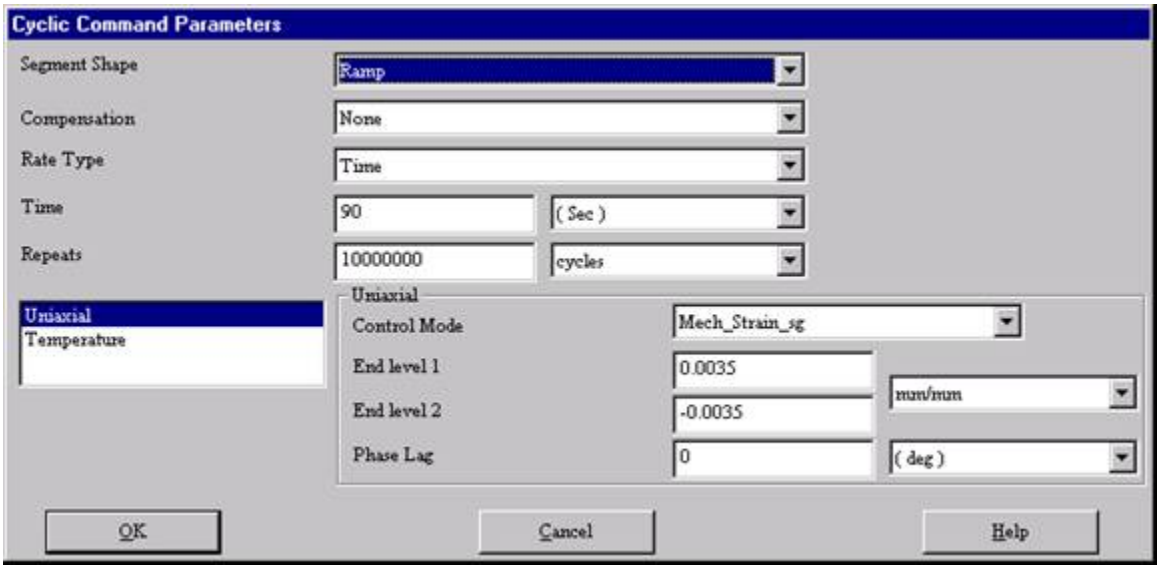

Figure A-8 OP TMF "Continuous Cycling"

OP BiF CODE

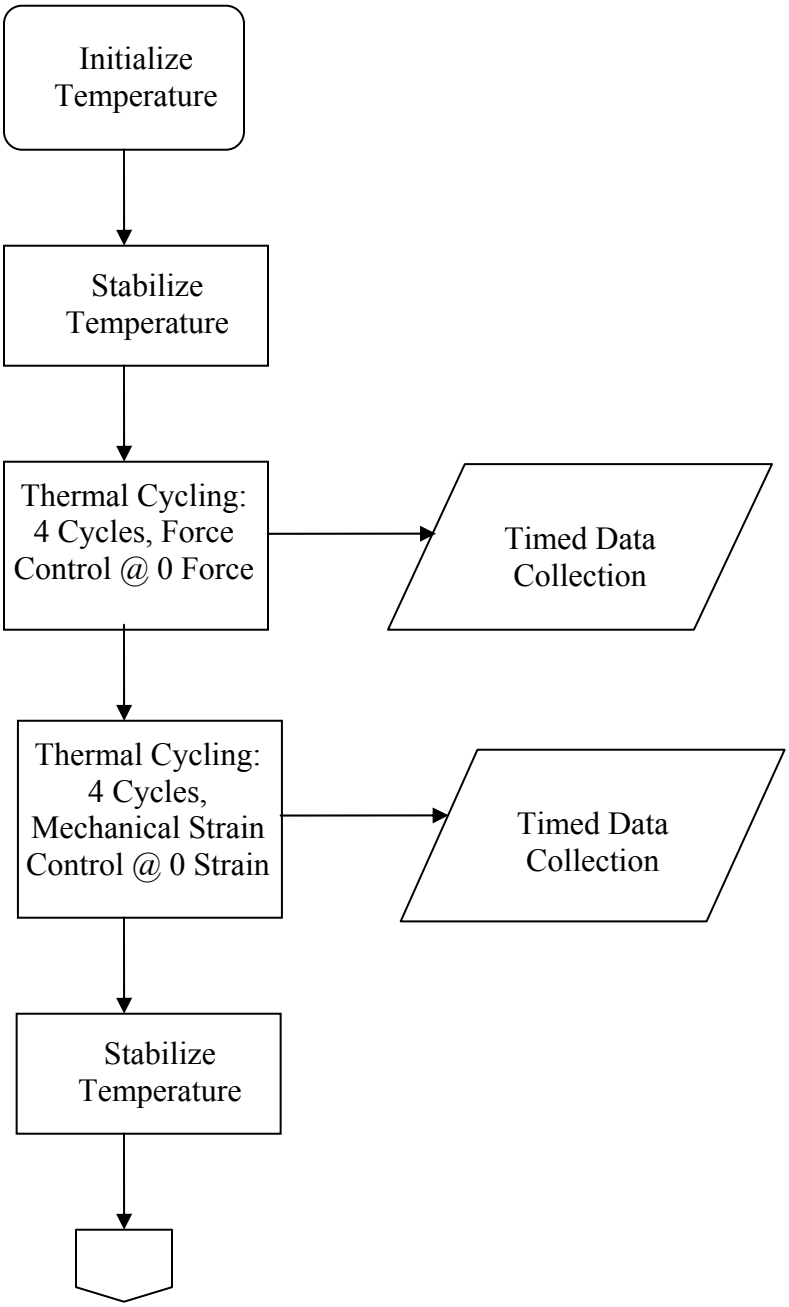
Initialize Temperature
Stabilize Temperature
Thermal Cycling: 4 Cycles, Force Control @ 0 Force
Timed Data Collection
Thermal Cycling: 4 Cycles, Mechanical Strain Control @ 0 Strain
Timed Data Collection
Stabilize Temperature

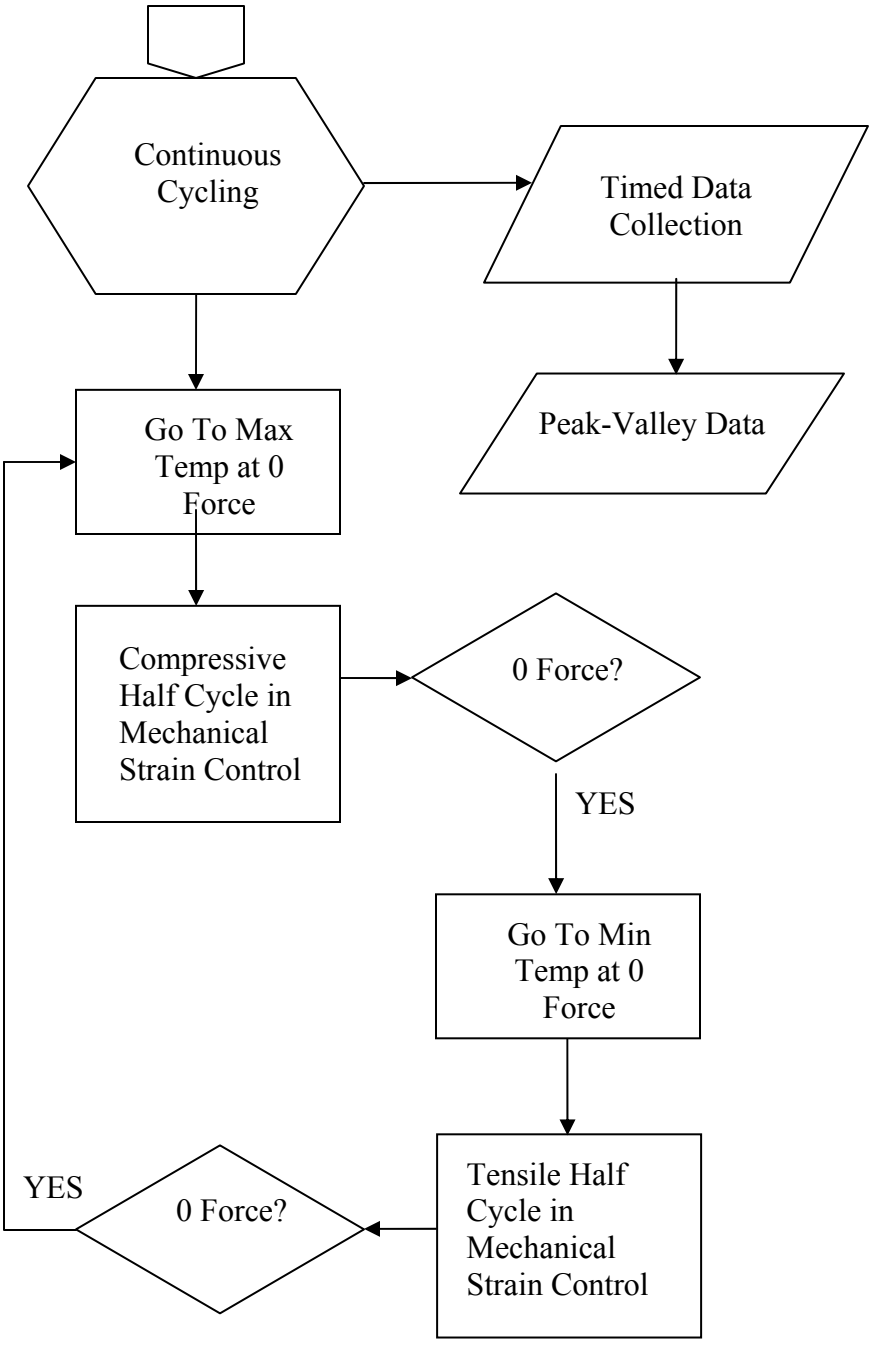

Figure A-9 Control Algorithm- OP BiF

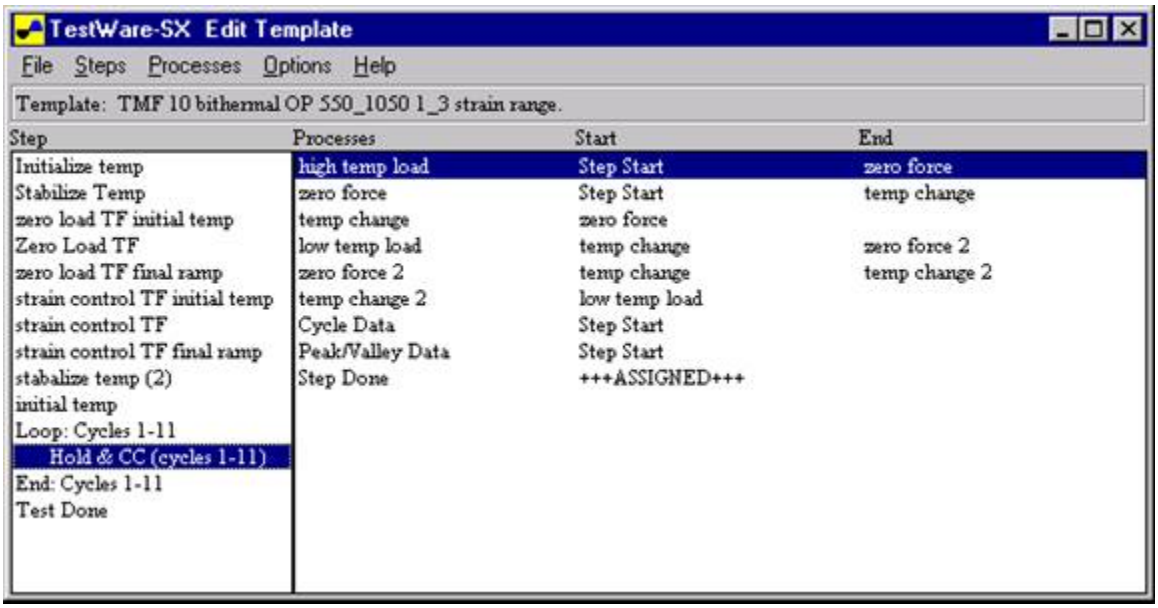

Figure A-10 Control Algorithm for OP BiF

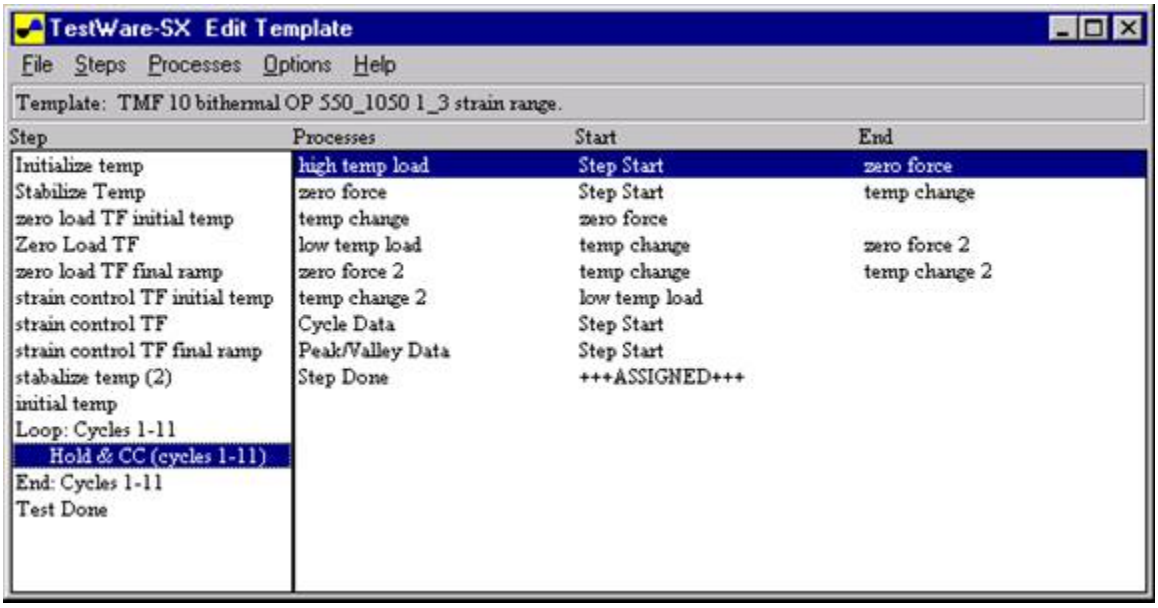

Figure A-11 OP BiF "high temp load"- Compressive Half Cycle

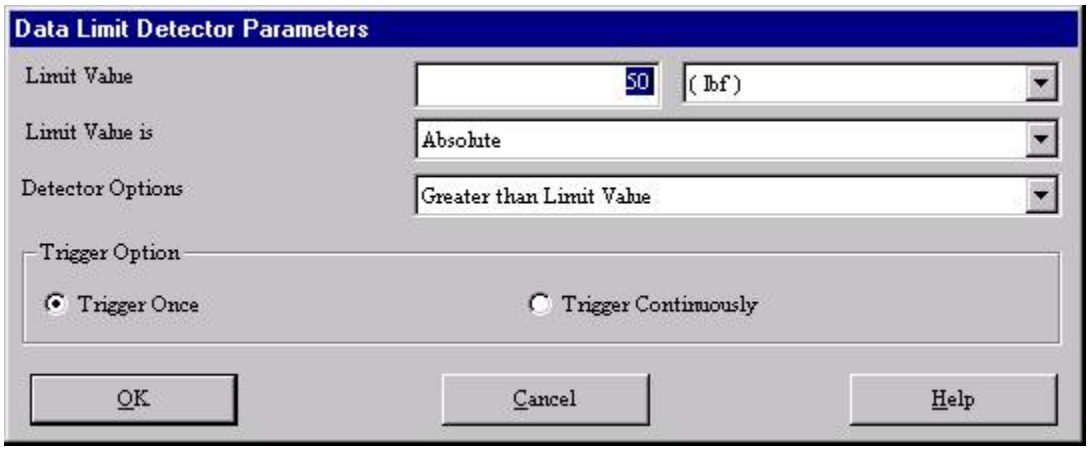

Figure A-12 OP BiF "zero force"- End Compressive Half Cycle

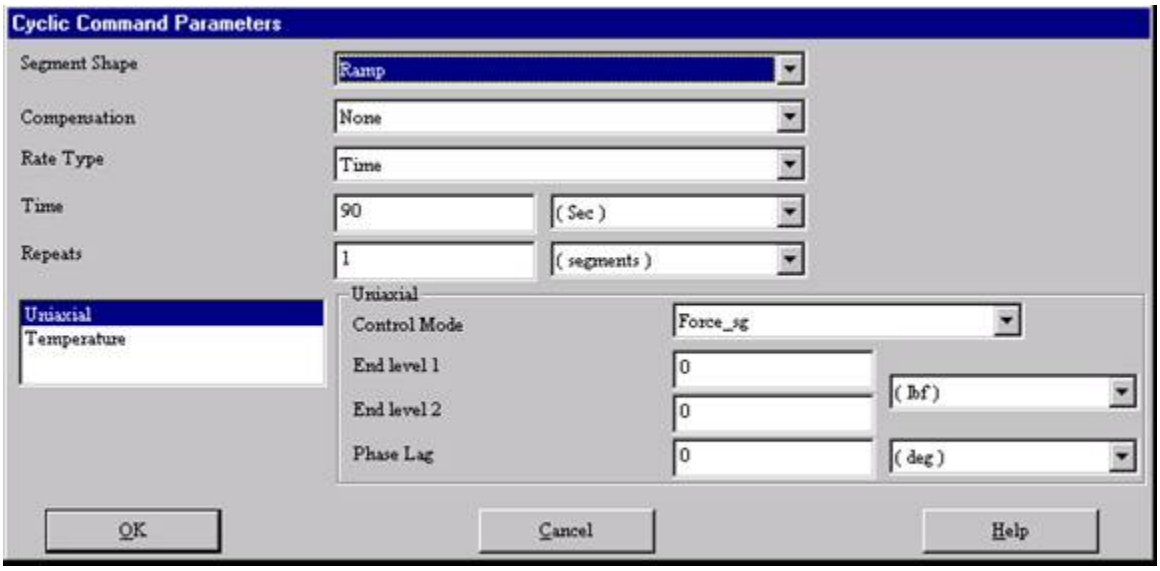

Figure A-13 OP BiF "temp change"- Transition to T_{min} at 0 Force

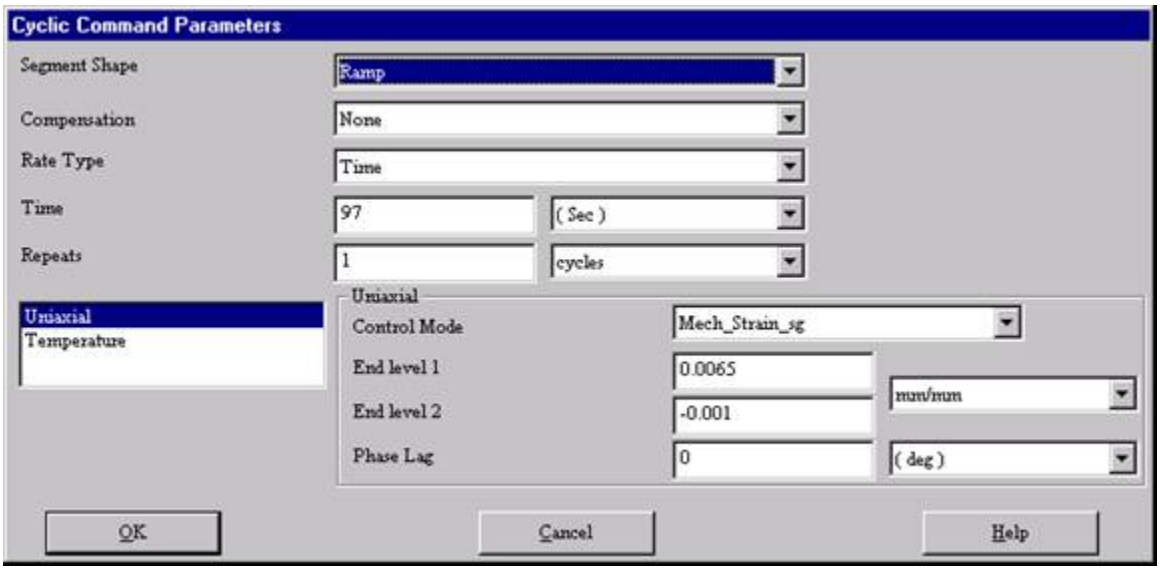

Figure A-14 OP BiF Control Loop "high temp load"- Tensile Half Cycle

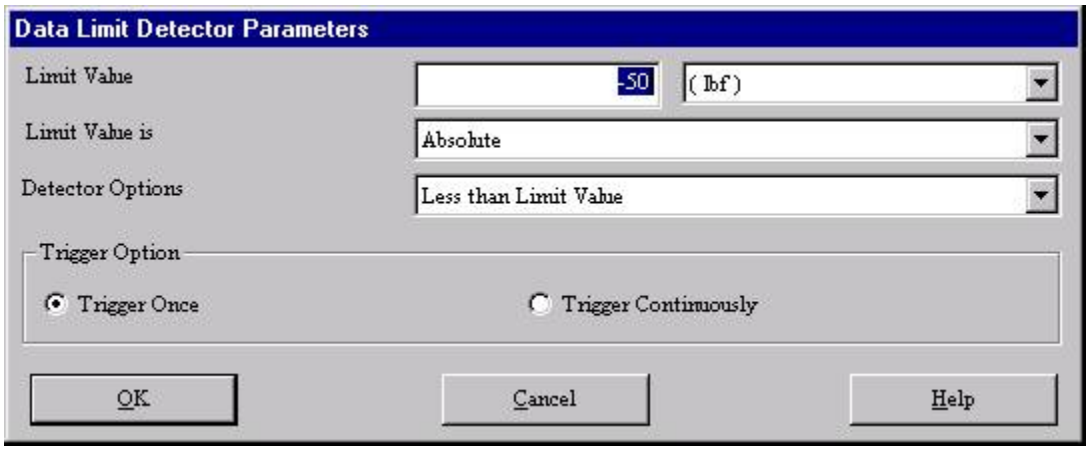

Figure A-15 OP BiF "zero force 2"- End Tensile Half Cycle

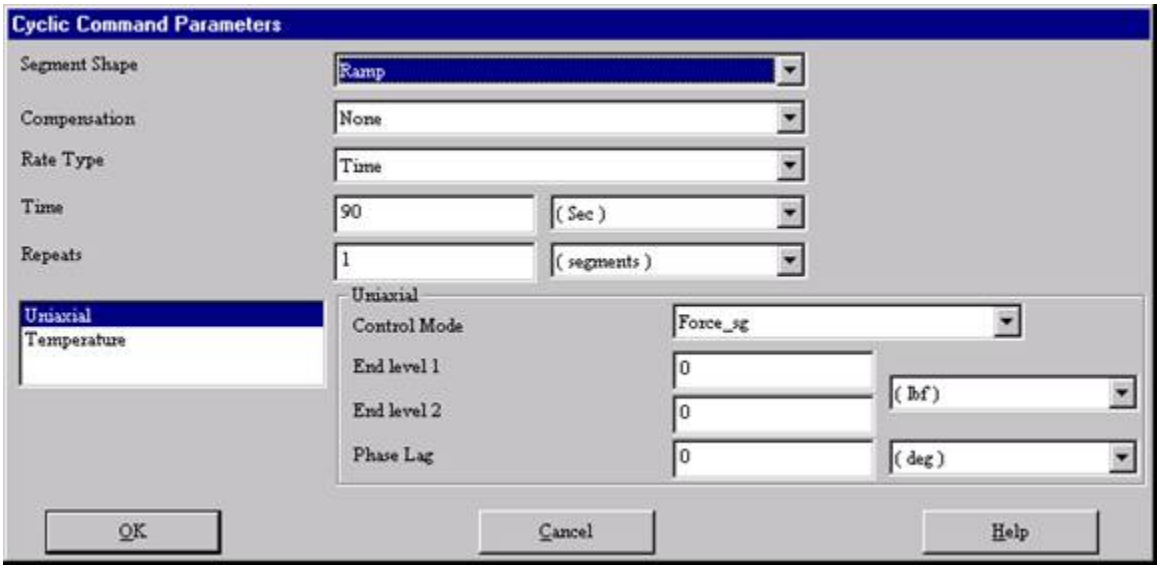

Figure A-16 OP BiF "temp change 2"- Transition to T_{max} at 0 Force

A.8 Oxide EDS Results

- Polished and Etched Cross-Section: See Fig 4-10 through 4-11 "Blue Oxide"

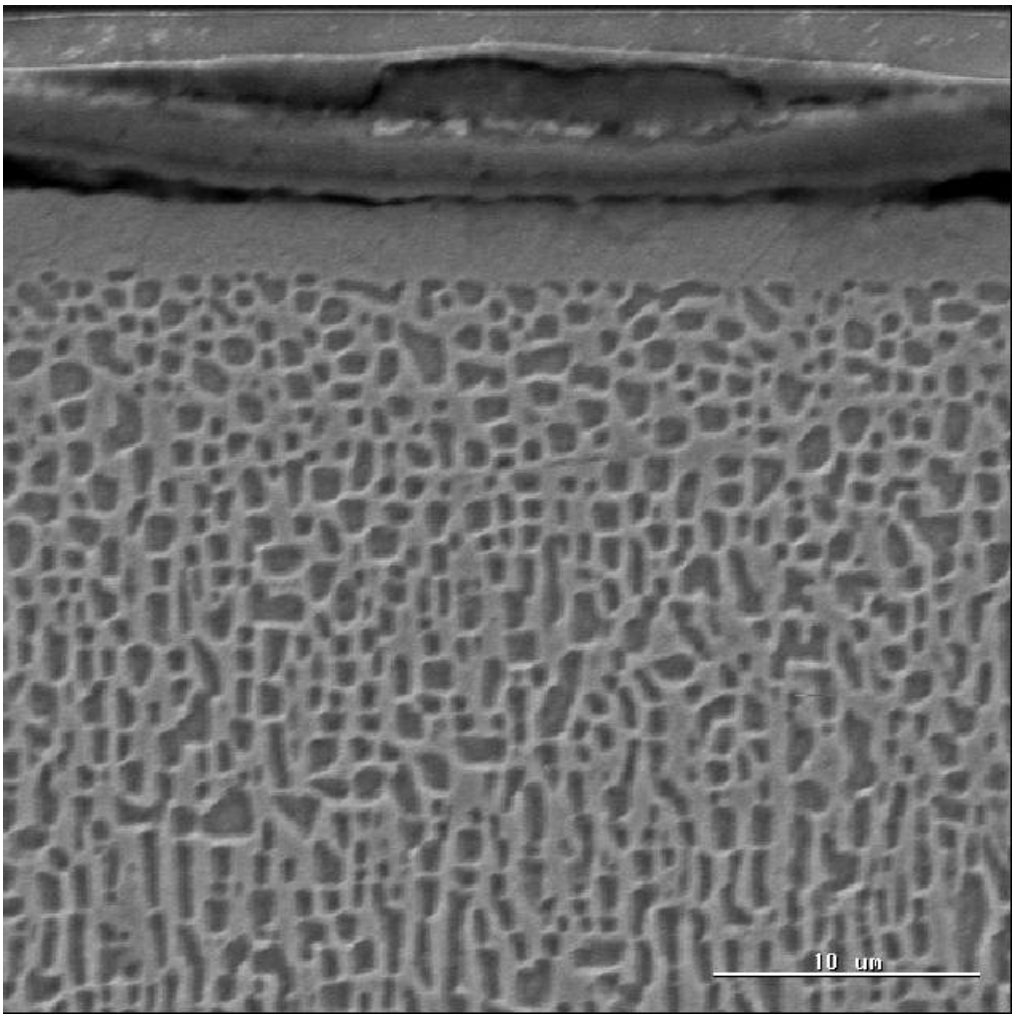

Figure A-17 Polished and Etched Cross-Section- 1050C, 300hr, "Blue Oxide", 2500X

Polished and Etched Cross-Section: See Fig 4-10 through 4-11

"Blue Oxide"- Chemical Analysis

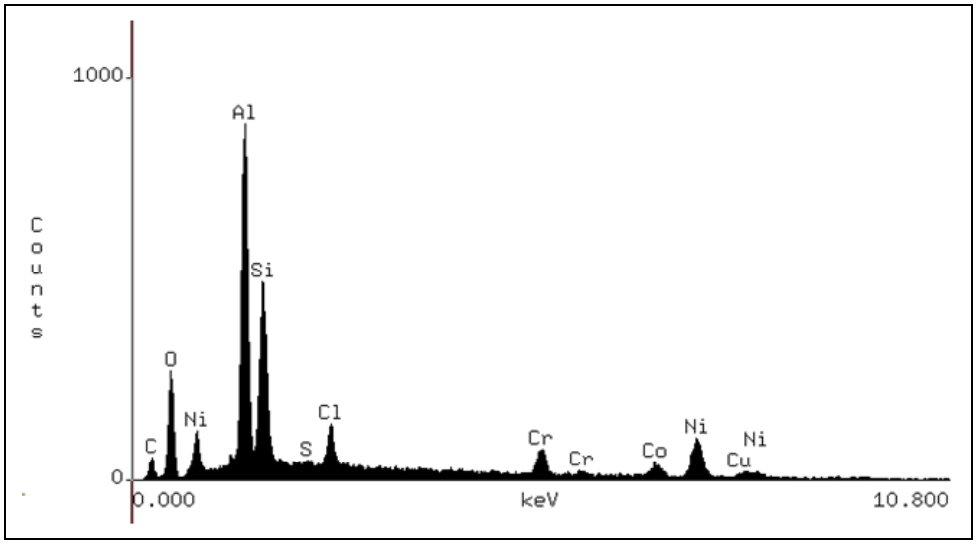

Polished and etched cross-section, 1050C, 300hr, blue oxide, eds-1

Accelerating Voltage: 15 KeV
Take Off Angle: 39.6197°
Live Time: 30 seconds
Dead Time: 13.547

Figure A-18 Polished and Etched Cross-Section- 1050C, 300hr, "Blue Oxide "- Chemical Analysis

Quantitative Analysis

Thu Sep 16 14:17:58 2010

Polished and etched cross-section, 1050C, 300hr, blue oxide, eds-1

Refit _S -K' _S -K"
Refit _Cl-K" _Co-K" _Ni-K"
Filter Fit Method
Chi-sqd = 1.27 Livetime = 30.0 Sec.
Standardless Analysis

Element	Relative k-ratio	Error (1-Sigma)	Net Counts	Error (1-Sigma)
C -K	0.02907	+/- 0.00187	389	+/- 25
Si-K	0.11362	+/- 0.00284	4963	+/- 124
O -K	0.12828	+/- 0.00312	2100	+/- 51
Al-K	0.17946	+/- 0.00277	8371	+/- 129
S -K	0.00233	+/- 0.00111	87	+/- 41
Cl-K	0.03843	+/- 0.00160	1178	+/- 49
Cr-K	0.08801	+/- 0.00686	1078	+/- 84
Co-K	0.07855	+/- 0.00746	537	+/- 51
Ni-K	0.34224	+/- 0.01318	1845	+/- 71
Ni-L	---	---	1193	+/- 58

Adjustment Factors	K	L	M
Z-Balance:	0.00000	0.00000	0.00000
Shell:	1.00000	1.00000	1.00000

PROZA Correction Acc.Volt.= 15 kV Take-off Angle=39.62 deg Tilt = 30 deg
Number of Iterations = 6

Element	k-ratio (calc.)	ZAF	Atom %	Element Wt %	Wt % Err. (1-Sigma)	No. of Cations
C -K	0.0188	5.368	21.82	10.11	+/- 0.65	17.047
Si-K	0.0736	1.505	10.23	11.08	+/- 0.28	7.989
O -K	0.0831	2.281	30.72	18.96	+/- 0.46	---
Al-K	0.1163	1.570	17.54	18.26	+/- 0.28	13.700
S -K	0.0015	1.282	0.16	0.19	+/- 0.09	0.122
Cl-K	0.0249	1.250	2.28	3.11	+/- 0.13	1.778
Cr-K	0.0570	1.122	3.19	6.40	+/- 0.50	2.493
Co-K	0.0509	1.201	2.69	6.11	+/- 0.58	2.101
Ni-K	0.2218	1.161	11.37	25.76	+/- 0.99	8.884
Total			100.00	100.00		54.114

The number of cation results are based upon 24 Oxygen atoms

- Polished and Etched Cross-Section: See Fig 4-10 through 4-11

  “Blue Oxide”- Oxide Analysis

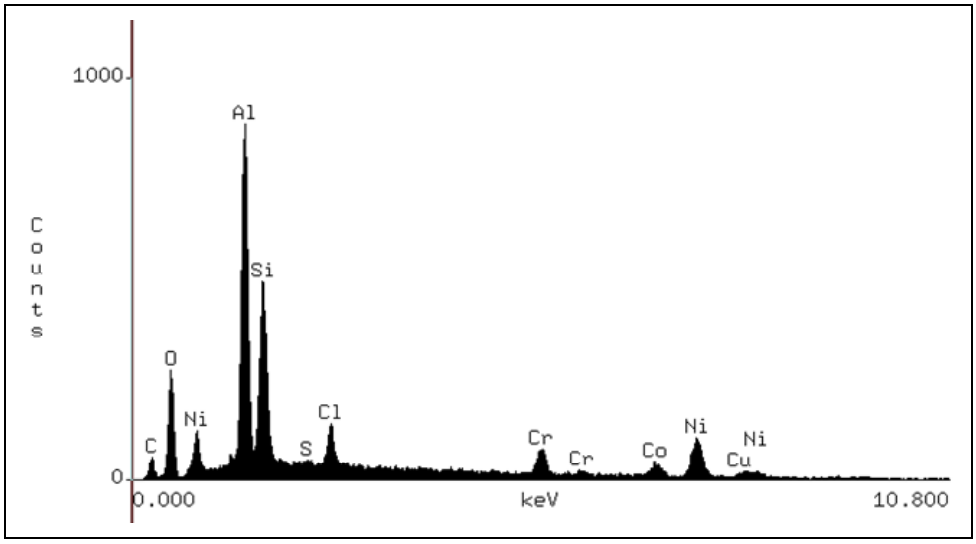

Polished and etched cross-section, 1050C, 300hr, blue oxide, eds-1b

Oxides analysis

Accelerating Voltage: 15 KeV	Take Off Angle: 39.6197°
Live Time: 30 seconds	Dead Time: 13.547

Figure A-19 Polished and Etched Cross-Section- 1050C, 300hr, “Blue Oxide “- Oxide Analysis

Quantitative Analysis

Thu Sep 16 14:21:28 2010

Polished and etched cross-section, 1050C, 300hr, blue oxide, eds-1b (oxide analysis)

Filter Fit Method
Chi-sqd = 40.65 Livetime = 30.0 Sec.
Standardless Analysis

Element	Relative k-ratio	Error (1-Sigma)	Net Counts	Error (1-Sigma)
Si-K	0.14040	+/- 0.00351	4962	+/- 124
Al-K	0.22177	+/- 0.00342	8370	+/- 129
S -K	0.01422	+/- 0.00255	425	+/- 76
Cr-K	0.10877	+/- 0.00848	1078	+/- 84
Co-K	0.09599	+/- 0.01609	531	+/- 89
Ni-K	0.41884	+/- 0.02500	1826	+/- 109
Ni-L	---	---	1470	+/- 57

Bence-Albee Analysis Acc.Volt.= 15 kV Take-off Angle= 39.62 deg

No. of Iterations 3

Oxide Formula	k-ratio (calc)	Beta Factor	Oxide Wt %	No. of Cations
SiO2	0.1652	1.3362	22.07	Si- 3.672
Al2O3	0.2458	1.3145	32.31	Al- 6.335
SO3	0.0185	1.1830	2.19	S - 0.273
Cr2O3	0.0806	1.0334	8.33	Cr- 1.095
CoO	0.0609	1.0924	6.65	Co- 0.887
NiO	0.2637	1.0789	28.45	Ni- 3.806
Total			100.00	16.067

The number of cation results are based upon 24 Oxygen atoms

- Polished and Etched Cross-Section: See Fig 4-10 through 4-11

  “Brown Oxide”

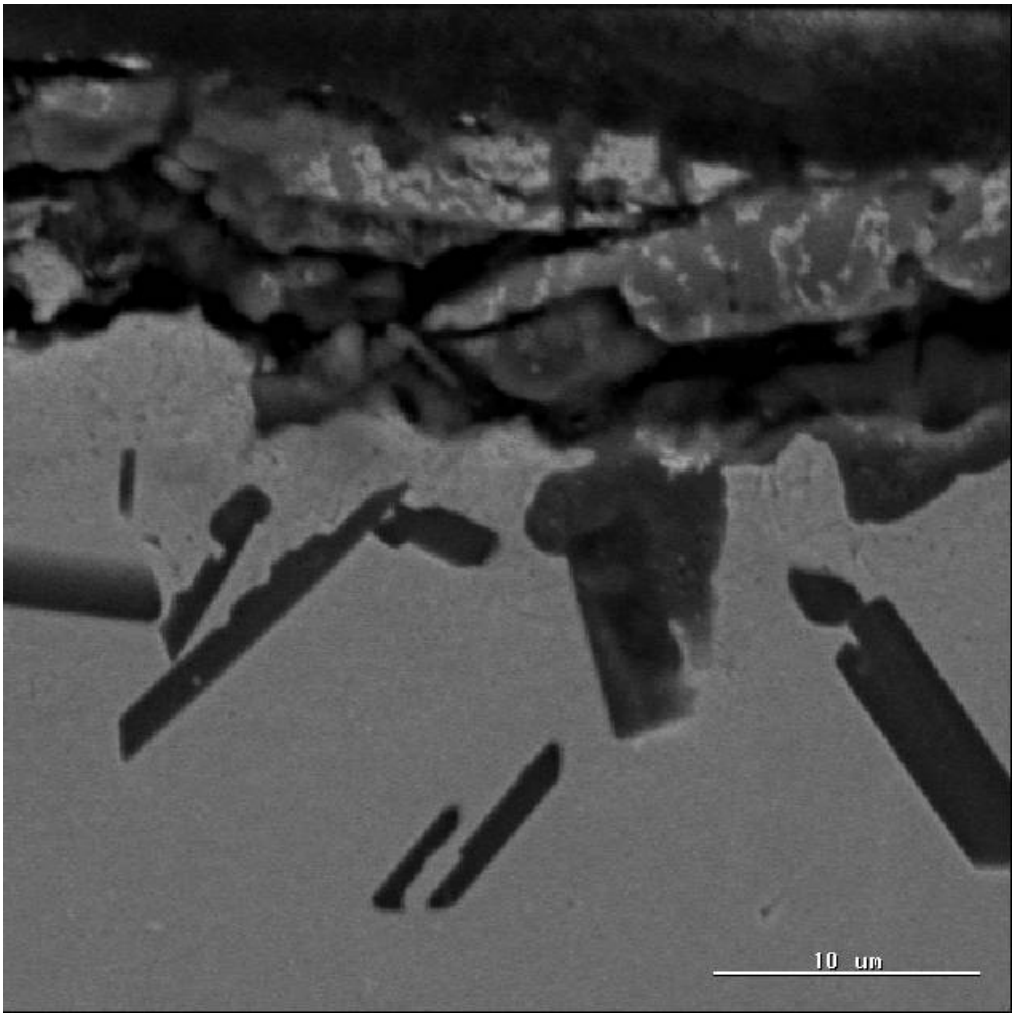

Figure A-20 Polished and Etched Cross-Section- 1050C, 300hr, “Brown Oxide”, 2500X

- Polished and Etched Cross-Section: See Fig 4-10 through 4-11

  “Brown Oxide”- Grey Phase Chemical Analysis

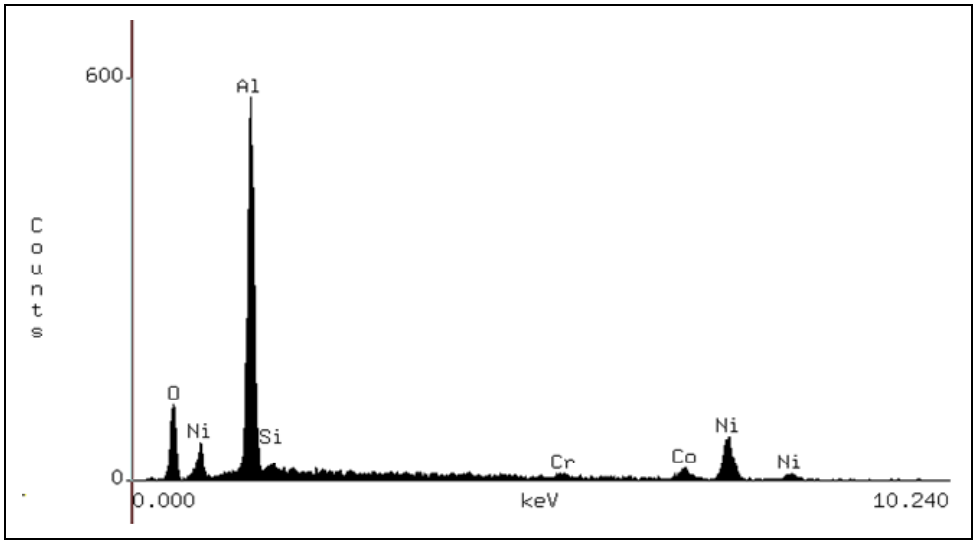

Polished and etched cross-section, 1050C, 300hr, brown oxide-grey phase, eds-1a

Accelerating Voltage: 15 KeV	Take Off Angle: 39.6197°
Live Time: 10 seconds	Dead Time: 4.867

Figure A-21 Polished and Etched Cross-Section- 1050C, 300hr, “Brown Oxide“ Grey Phase- Chemical Analysis

Quantitative Analysis

Thu Sep 16 14:45:04 2010

Polished and etched cross-section, 1050C, 300hr, brown oxide-grey phase, eds-1a

Refit _Si-K' _Si-K" _Cr-K' _Cr-K" _Co-K' _Co-K"
Filter Fit Method
Chi-sqd = 1.02 Livetime = 10.0 Sec.
Standardless Analysis

Element	Relative k-ratio	Error (1-Sigma)	Net Counts	Error (1-Sigma)
Si-K	0.00433	+/- 0.00132	82	+/- 25
Al-K	0.28145	+/- 0.00401	5688	+/- 81
Cr-K	0.01717	+/- 0.00415	92	+/- 22
Co-K	0.08441	+/- 0.01081	250	+/- 32
Ni-K	0.47170	+/- 0.03042	1102	+/- 71
Ni-L	---	---	594	+/- 37
O -K	0.14094	+/- 0.00437	1000	+/- 31

Adjustment Factors	K	L	M
Z-Balance:	0.00000	0.00000	0.00000
Shell:	1.00000	1.00000	1.00000

PROZA Correction Acc.Volt.= 15 kV Take-off Angle=39.62 deg Tilt = 30 deg
Number of Iterations = 5

Element	k-ratio (calc.)	ZAF	Atom %	Element Wt %	Wt % Err. (1-Sigma)	No. of Cations
Si-K	0.0031	1.704	0.59	0.54	+/- 0.16	0.388
Al-K	0.2042	1.652	38.47	33.72	+/- 0.48	25.432
Cr-K	0.0125	1.069	0.79	1.33	+/- 0.32	0.521
Co-K	0.0612	1.161	3.71	7.11	+/- 0.91	2.455
Ni-K	0.3422	1.123	20.14	38.42	+/- 2.48	13.317
O -K	0.1022	1.846	36.30	18.87	+/- 0.59	---
Total			100.00	100.00		42.114

The number of cation results are based upon 24 Oxygen atoms

- Polished and Etched Cross-Section: See Fig 4-10 through 4-11

"Brown Oxide"- Grey Phase Oxide Analysis

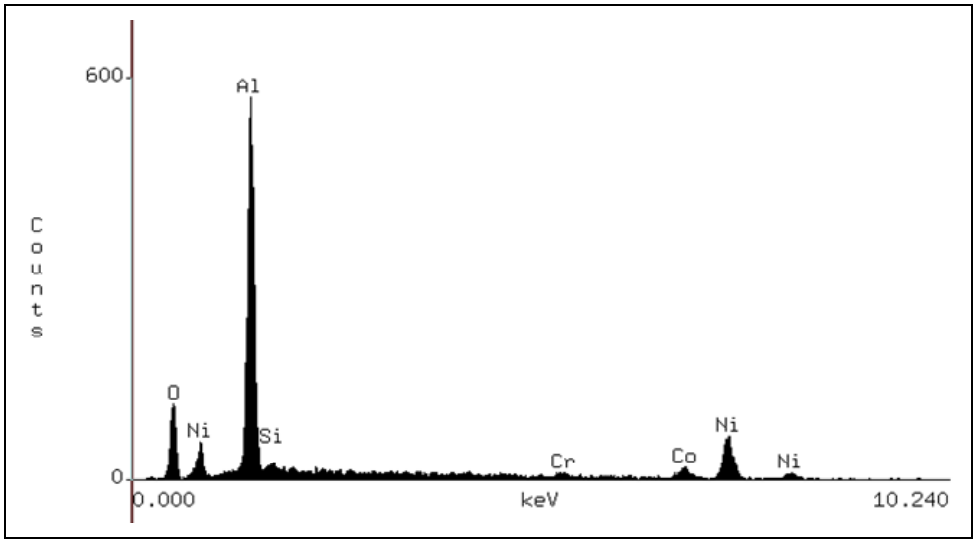

Polished and etched cross-section, 1050C, 300hr, brown oxide-grey phase, eds-1b

Oxides

Accelerating Voltage: 15 KeV
Take Off Angle: 39.6197°
Live Time: 10 seconds
Dead Time: 4.867

Figure A-22 Polished and Etched Cross-Section- 1050C, 300hr, "Brown Oxide" Grey Phase- Oxide Analysis

Quantitative Analysis

Thu Sep 16 14:47:36 2010

Polished and etched cross-section, 1050C, 300hr, brown oxide-grey phase, eds-1 (oxides)

Refit _Si-K' _Si-K" _Cr-K' _Cr-K" _Co-K' _Co-K"
Filter Fit Method
Chi-sqd = 17.87 Livetime = 10.0 Sec.
Standardless Analysis

Element	Relative k-ratio	Error (1-Sigma)	Net Counts	Error (1-Sigma)
Si-K	0.00504	+/- 0.00154	82	+/- 25
Al-K	0.32762	+/- 0.00467	5687	+/- 81
Cr-K	0.01998	+/- 0.00483	92	+/- 22
Co-K	0.09826	+/- 0.01258	250	+/- 32
Ni-K	0.54909	+/- 0.03541	1102	+/- 71
Ni-L	---	---	716	+/- 36

Bence-Albee Analysis Acc.Volt.= 15 kV Take-off Angle= 39.62 deg

No. of Iterations 4

Oxide Formula	k-ratio (calc)	Beta Factor	Oxide Wt %	No. of Cations
SiO2	0.0062	1.4742	0.92	Si- 0.167
Al2O3	0.3806	1.3625	51.85	Al-11.105
Cr2O3	0.0155	1.0165	1.58	Cr- 0.227
CoO	0.0653	1.0742	7.01	Co- 1.022
NiO	0.3623	1.0666	38.64	Ni- 5.648
Total			100.00	18.168

The number of cation results are based upon 24 Oxygen atoms

- Polished and Etched Cross-Section: See Fig 4-10 through 4-11

  “Brown Oxide”- White Phase Chemical Analysis

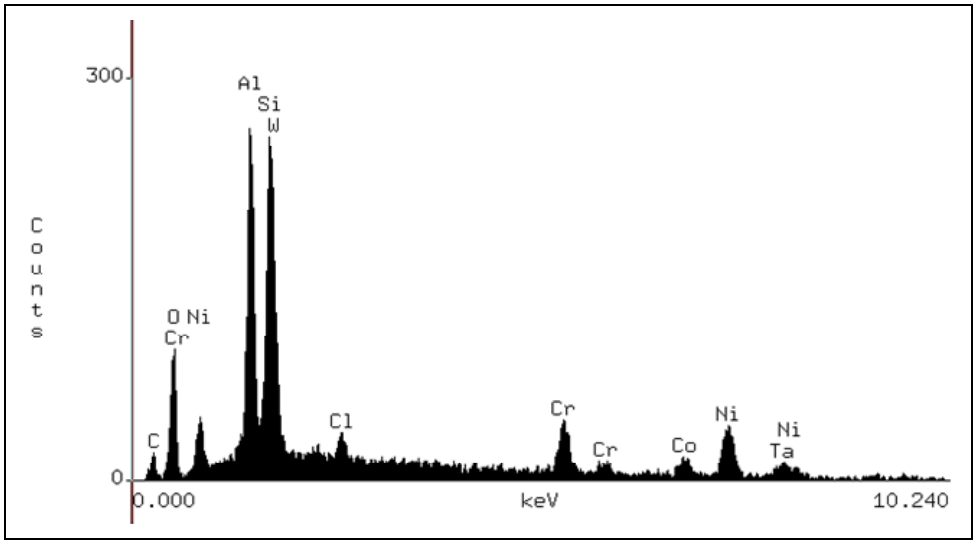

Polished and etched cross-section, 1050C, 300hr, brown oxide-white, eds-1a

Accelerating Voltage: 15 KeV	Take Off Angle: 39.6197°
Live Time: 10 seconds	Dead Time: 5.632

Figure A-23 Polished and Etched Cross-Section- 1050C, 300hr, “Brown Oxide“ White Phase-Chemical Analysis

Quantitative Analysis

Thu Sep 16 14:56:21 2010

Polished and etched cross-section, 1050C, 300hr, brown oxide-white, eds-1a

Refit _Si-K' _Si-K" _Co-K' _Co-K" _Cl-K' _Cl-K" _W -M' _W -M" _Ta-L' _Ta-L"
Refit _Al-K" _Cr-K" _Ni-K" _C -K'
Filter Fit Method
Chi-sqd = 1.06 Livetime = 10.0 Sec.
Standardless Analysis

Element	Relative k-ratio	Error (1-Sigma)	Net Counts	Error (1-Sigma)
Si-K	0.09345	+/- 0.00289	1975	+/- 61
Al-K	0.09092	+/- 0.00208	2053	+/- 47
Cr-K	0.09779	+/- 0.00608	580	+/- 36
Co-K	0.07044	+/- 0.00998	234	+/- 33
Ni-K	0.28041	+/- 0.01726	731	+/- 45
Ni-L	---	---	511	+/- 38
C -K	0.02502	+/- 0.00216	163	+/- 14
O -K	0.09890	+/- 0.00379	784	+/- 30
Cl-K	0.01591	+/- 0.00189	237	+/- 28
W -M	0.04860	+/- 0.00660	524	+/- 71
Ta-L	0.17855	+/- 0.03586	240	+/- 48

Adjustment Factors	K	L	M
Z-Balance:	0.00000	0.00000	0.00000
Shell:	1.00000	1.00000	1.00000

PROZA Correction Acc.Volt.= 15 kV Take-off Angle=39.62 deg Tilt = 30 deg
Number of Iterations = 5

Element	k-ratio (calc.)	ZAF	Atom %	Element Wt %	Wt % Err. (1-Sigma)	No. of Cations
Si-K	0.0648	1.363	10.31	8.84	+/- 0.27	7.424
Al-K	0.0631	1.474	11.28	9.30	+/- 0.21	8.127
Cr-K	0.0679	1.069	4.57	7.25	+/- 0.45	3.290
Co-K	0.0489	1.080	2.93	5.28	+/- 0.75	2.113
Ni-K	0.1946	1.061	11.51	20.64	+/- 1.27	8.291
C -K	0.0174	4.344	20.56	7.54	+/- 0.65	14.808
O -K	0.0686	2.373	33.32	16.28	+/- 0.62	---
Cl-K	0.0110	1.282	1.31	1.42	+/- 0.17	0.941
W -M	0.0337	1.548	0.93	5.22	+/- 0.71	0.670
Ta-L	0.1239	1.471	3.30	18.23	+/- 3.66	2.375
Total			100.00	100.00		48.039

The number of cation results are based upon 24 Oxygen atoms

- Polished and Etched Cross-Section: See Fig 4-10 through 4-11

"Brown Oxide"- White Phase Oxide Analysis

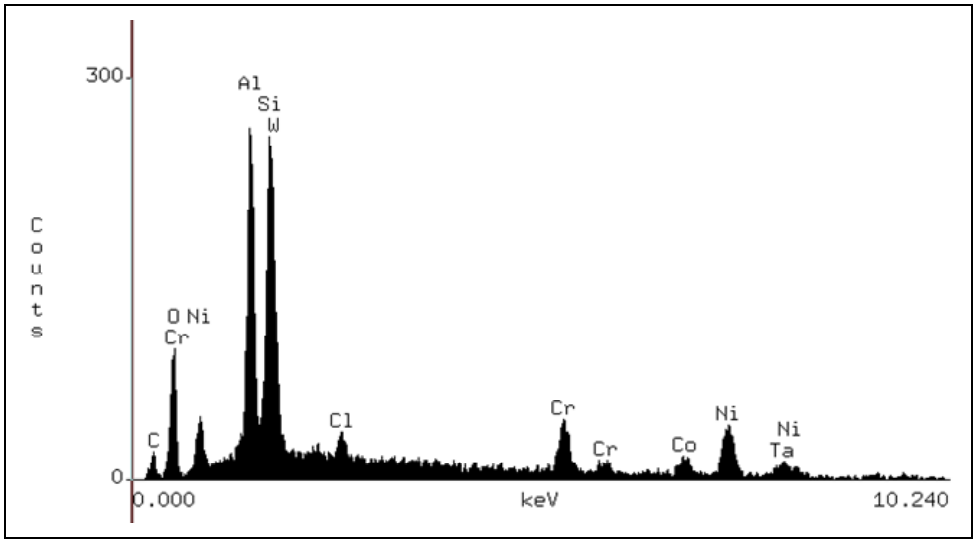

Polished and etched cross-section, 1050C, 300hr, brown oxide-white phase, eds-1b

oxides

Accelerating Voltage: 15 KeV
Take Off Angle: 39.6197°
Live Time: 10 seconds
Dead Time: 5.632

Figure A-24 Polished and Etched Cross-Section- 1050C, 300hr, "Brown Oxide" White Phase- Oxide Analysis

Quantitative Analysis

Thu Sep 16 15:00:15 2010

Polished and etched cross-section, 1050C, 300hr, brown oxide-white, eds-1b (oxides)

Refit _Co-K' _Co-K" _Ta-L' _Ta-L" _W -L' _W -L"
Refit _Cr-K" _Ni-K" _Ni-L'
Filter Fit Method
Chi-sqd = 11.78 Livetime = 10.0 Sec.
Standardless Analysis

Element	Relative k-ratio	Error (1-Sigma)	Net Counts	Error (1-Sigma)
Si-K	0.13243	+/- 0.00440	2737	+/- 91
Al-K	0.10094	+/- 0.00340	2227	+/- 75
Cr-K	0.10003	+/- 0.00622	580	+/- 36
Co-K	0.07205	+/- 0.01021	234	+/- 33
Ni-K	0.29036	+/- 0.01766	741	+/- 45
Ni-L	---	---	622	+/- 37
Ta-L	0.19181	+/- 0.03745	252	+/- 49
W -L	0.11237	+/- 0.03893	128	+/- 44

Bence-Albee Analysis Acc.Volt.= 15 kV Take-off Angle= 39.62 deg

No. of Iterations 3

Oxide Formula	k-ratio (calc)	Beta Factor	Oxide Wt %	No. of Cations
SiO2	0.1785	1.1780	21.03	Si- 4.175
Al2O3	0.1282	1.2021	15.41	Al- 3.605
Cr2O3	0.0849	0.9555	8.11	Cr- 1.274
CoO	0.0523	0.9780	5.12	Co- 0.815
NiO	0.2094	0.9686	20.28	Ni- 3.239
Ta2O5	0.1422	1.3098	18.63	Ta- 1.006
WO3	0.0879	1.2992	11.42	W - 0.588
Total			100.00	14.701

The number of cation results are based upon 24 Oxygen atoms

- Polished and Etched Cross-Section: See Fig 4-10 through 4-11

  “Brown Oxide”- Internal Spike Chemical Analysis

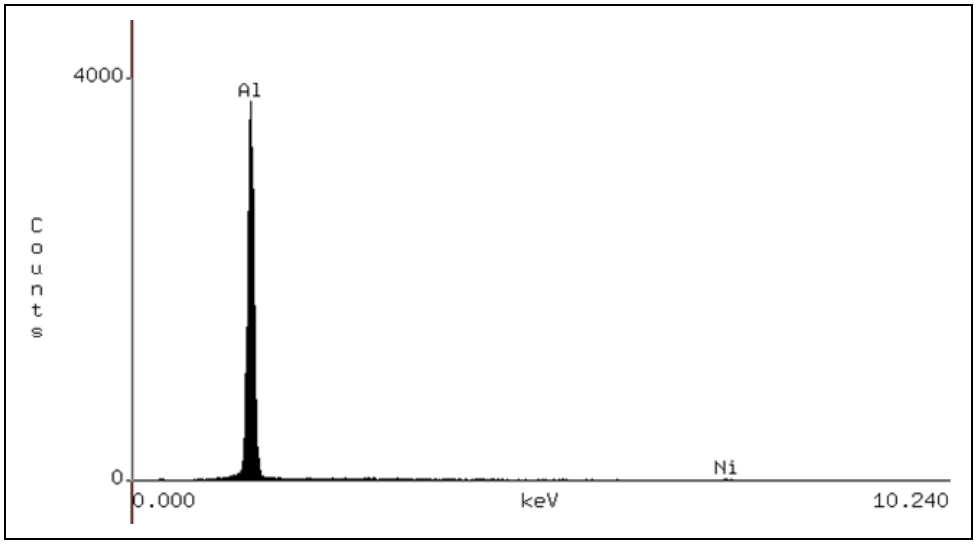

Polished and etched cross-section, 1050C, 300hr, internal spikes, eds-1

Accelerating Voltage: 15 KeV	Take Off Angle: 39.6197°
Live Time: 20 seconds	Dead Time: 15.61

Figure A-25 Polished and Etched Cross-Section- 1050C, 300hr, “Brown Oxide“ Internal Spikes- Chemical Analysis

Quantitative Analysis

Thu Sep 16 15:10:53 2010

Polished and etched cross-section, 1050C, 300hr, internal spikes, eds-1

Refit _Ni-K' _Ni-K"
Filter Fit Method
Chi-sqd = 1.45 Livetime = 20.0 Sec.
Standardless Analysis

Element	Relative k-ratio	Error (1-Sigma)	Net Counts	Error (1-Sigma)
Al-K	0.96401	+/- 0.00591	37337	+/- 229
Ni-K	0.03599	+/- 0.00648	162	+/- 29

Adjustment Factors	K	L	M
Z-Balance:	0.00000	0.00000	0.00000
Shell:	1.00000	1.00000	1.00000

PROZA Correction Acc.Volt.= 15 kV Take-off Angle=39.62 deg Tilt = 30 deg
Number of Iterations = 4

Element	k-ratio (calc.)	ZAF	Atom %	Element Wt %	Wt % Err. (1-Sigma)
Al-K	0.9049	1.062	98.15	96.07	+/- 0.59
Ni-K	0.0338	1.164	1.85	3.93	+/- 0.71
Total			100.00	100.00	

- Surface Oxidation 850˚C- 300 hours

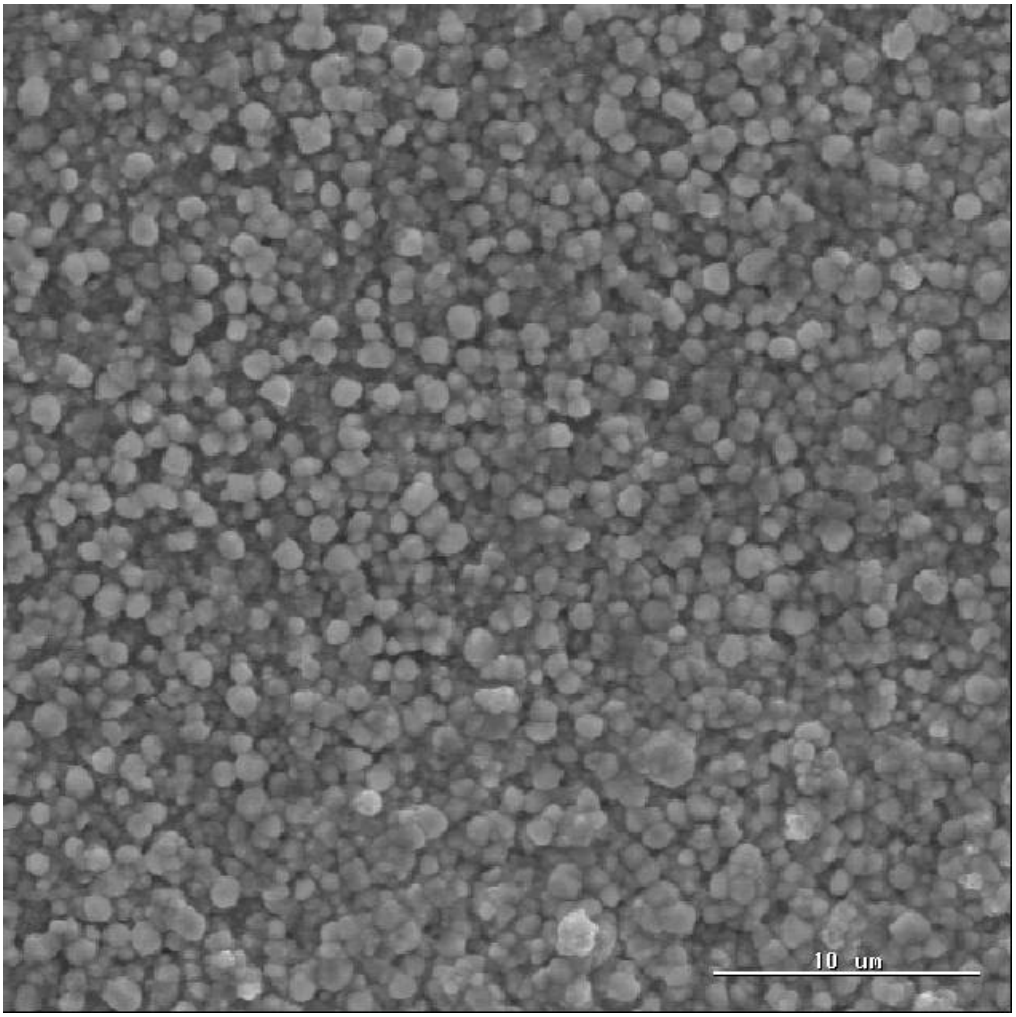

Figure A-26 Oxidized Surface: PWA 1484, 850°C, 300 hours, 2500X

- Surface Oxidation 850˚C- 300 hours
  Chemical Analysis

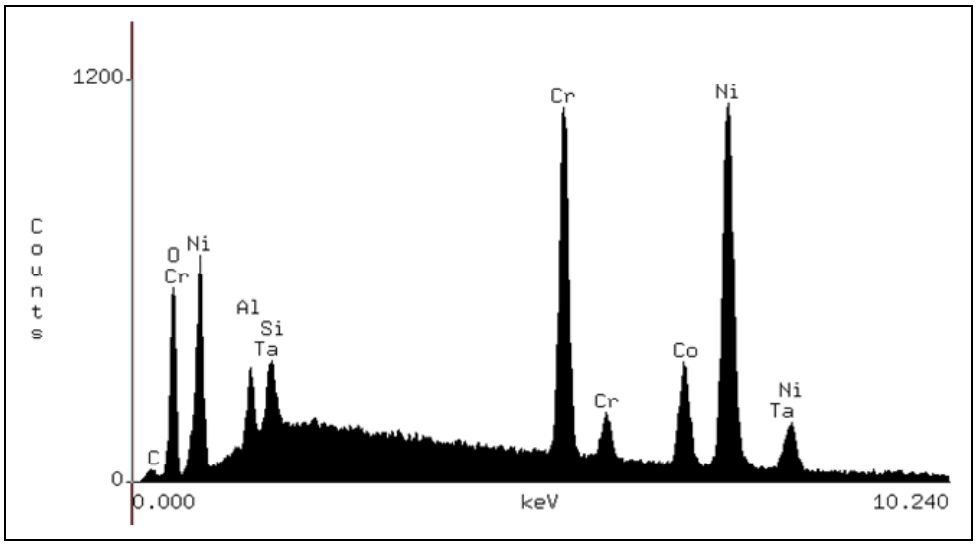

PWA 1484, 850C, 300hr, oxides, eds-1a

Accelerating Voltage: 15 KeV
Take Off Angle: 39.6197°
Live Time: 90 seconds
Dead Time: 45.061

Figure A-27 Oxidized Surface: PWA 1484, 850°C, 300 hours, 2500X- Chemical Analysis

Quantitative Analysis

Thu Sep 16 15:41:11 2010

PWA 1484, 850C, 300hr, oxides, eds-1a

Refit _Cr-L' _Cr-L" _Ta-L' _Ta-L" _O -K' _O -K"
Refit _Ni-L' _Al-K' _Cr-K" _Co-K'
Filter Fit Method
Chi-sqd = 2.55 Livetime = 90.0 Sec.
Standardless Analysis

Element	Relative k-ratio	Error (1-Sigma)	Net Counts	Error (1-Sigma)
Cr-L	---	---	871	+/- 176
Ni-L	---	---	7823	+/- 120
Al-K	0.00707	+/- 0.00036	2132	+/- 107
Si-K	0.00916	+/- 0.00046	2584	+/- 129
Cr-K	0.21081	+/- 0.00209	16660	+/- 165
Co-K	0.12084	+/- 0.00494	5335	+/- 218
Ni-K	0.58559	+/- 0.00879	20376	+/- 306
Ta-L	0.02535	+/- 0.00851	454	+/- 152
C -K	0.00283	+/- 0.00035	245	+/- 30
O -K	0.03834	+/- 0.00099	4052	+/- 105

Adjustment Factors	K	L	M
Z-Balance:	0.00000	0.00000	0.00000
Shell:	1.00000	1.00000	1.00000

PROZA Correction Acc.Volt.= 15 kV Take-off Angle=39.62 deg Tilt = 30 deg
Number of Iterations = 4

Element	k-ratio (calc.)	ZAF	Atom %	Element Wt %	Wt % Err. (1-Sigma)	No. of Cations
Al-K	0.0065	1.926	2.24	1.26	+/- 0.06	3.115
Si-K	0.0084	1.527	2.21	1.29	+/- 0.06	3.071
Cr-K	0.1944	0.989	17.77	19.21	+/- 0.19	24.718
Co-K	0.1114	1.078	9.80	12.01	+/- 0.49	13.629
Ni-K	0.5399	1.041	46.02	56.18	+/- 0.84	64.011
Ta-L	0.0234	1.439	0.89	3.36	+/- 1.13	1.244
C -K	0.0026	3.639	3.81	0.95	+/- 0.12	5.297
O -K	0.0353	1.624	17.26	5.74	+/- 0.15	---
Total			100.00	100.00		115.085

The number of cation results are based upon 24 Oxygen atoms

- Surface Oxidation 850˚C- 300 hours
  Oxide Analysis

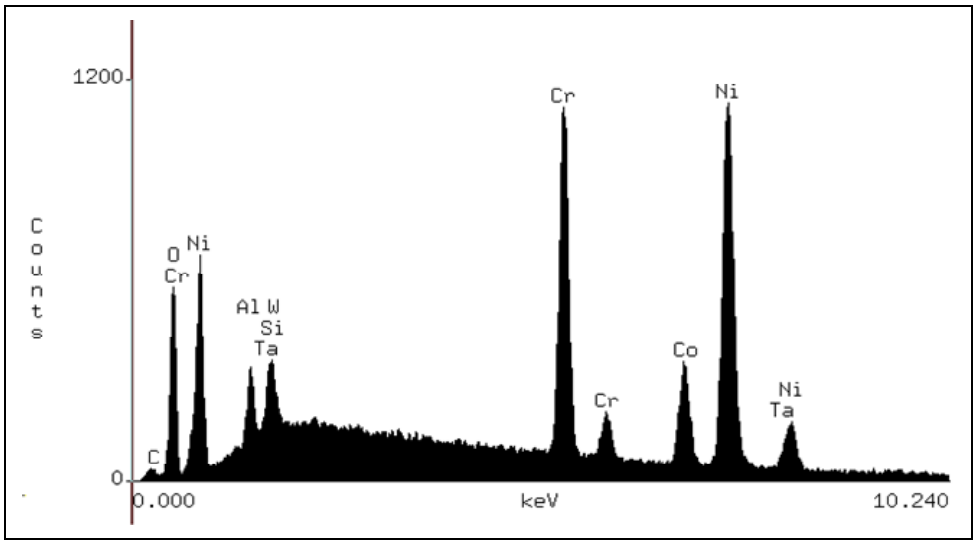

PWA 1484, 850C, 300hr, oxides, eds-1b

oxides

Accelerating Voltage: 15 KeV
Take Off Angle: 39.6197°
Live Time: 90 seconds
Dead Time: 45.061

Figure A-28 Oxidized Surface: PWA 1484, 850°C, 300 hours, 2500X- Oxide Analysis

Quantitative Analysis

Thu Sep 16 15:38:55 2010

PWA 1484, 850C, 300hr, oxides, eds-1 (oxides)

Refit _Ta-L' _Ta-L"
Refit _Al-K' _Cr-K" _Co-K'
Filter Fit Method
Chi-sqd = 10.17 Livetime = 90.0 Sec.
Standardless Analysis

Element	Relative k-ratio	Error (1-Sigma)	Net Counts	Error (1-Sigma)
Cr-L	---	---	6778	+/- 129
Ni-L	---	---	7345	+/- 121
Al-K	0.00738	+/- 0.00037	2133	+/- 107
Si-K	0.00955	+/- 0.00048	2584	+/- 129
Cr-K	0.21987	+/- 0.00218	16660	+/- 165
Co-K	0.12603	+/- 0.00515	5335	+/- 218
Ni-K	0.61073	+/- 0.00917	20376	+/- 306
Ta-L	0.02644	+/- 0.00887	454	+/- 152

Bence-Albee Analysis Acc.Volt.= 15 kV Take-off Angle= 39.62 deg

No. of Iterations 2

Oxide Formula	k-ratio (calc)	Beta Factor	Oxide Wt %	No. of Cations
Al2O3	0.0122	1.6207	1.97	Al- 0.599
SiO2	0.0167	1.3518	2.26	Si- 0.582
Cr2O3	0.2425	0.9332	22.63	Cr- 4.608
CoO	0.1189	1.0065	11.97	Co- 2.471
NiO	0.5724	1.0087	57.74	Ni-11.956
Ta2O5	0.0255	1.3414	3.42	Ta- 0.239
Total			100.00	20.456

The number of cation results are based upon 24 Oxygen atoms

- Surface Oxidation 950˚C- 150 hours

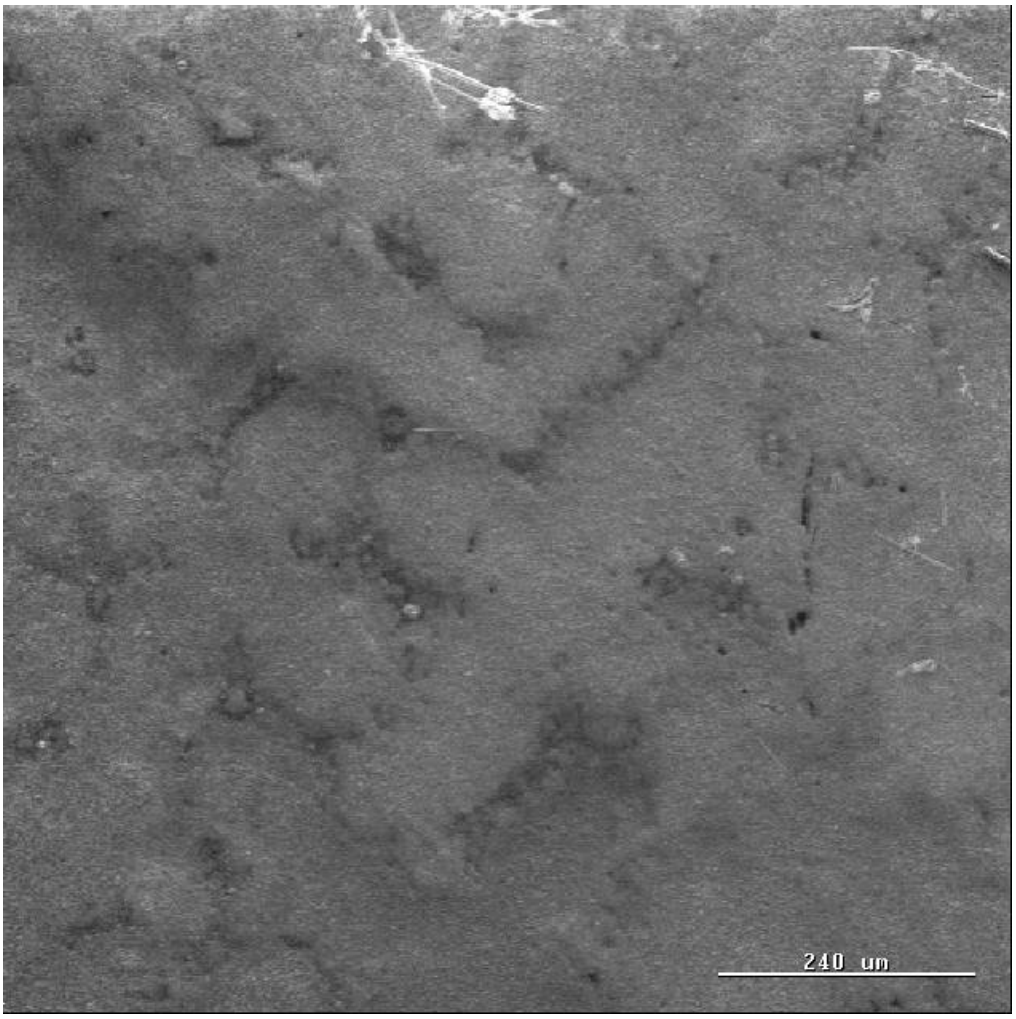

Figure A-29 Oxidized Surface: PWA 1484, 950°C, 150 hours, 100X

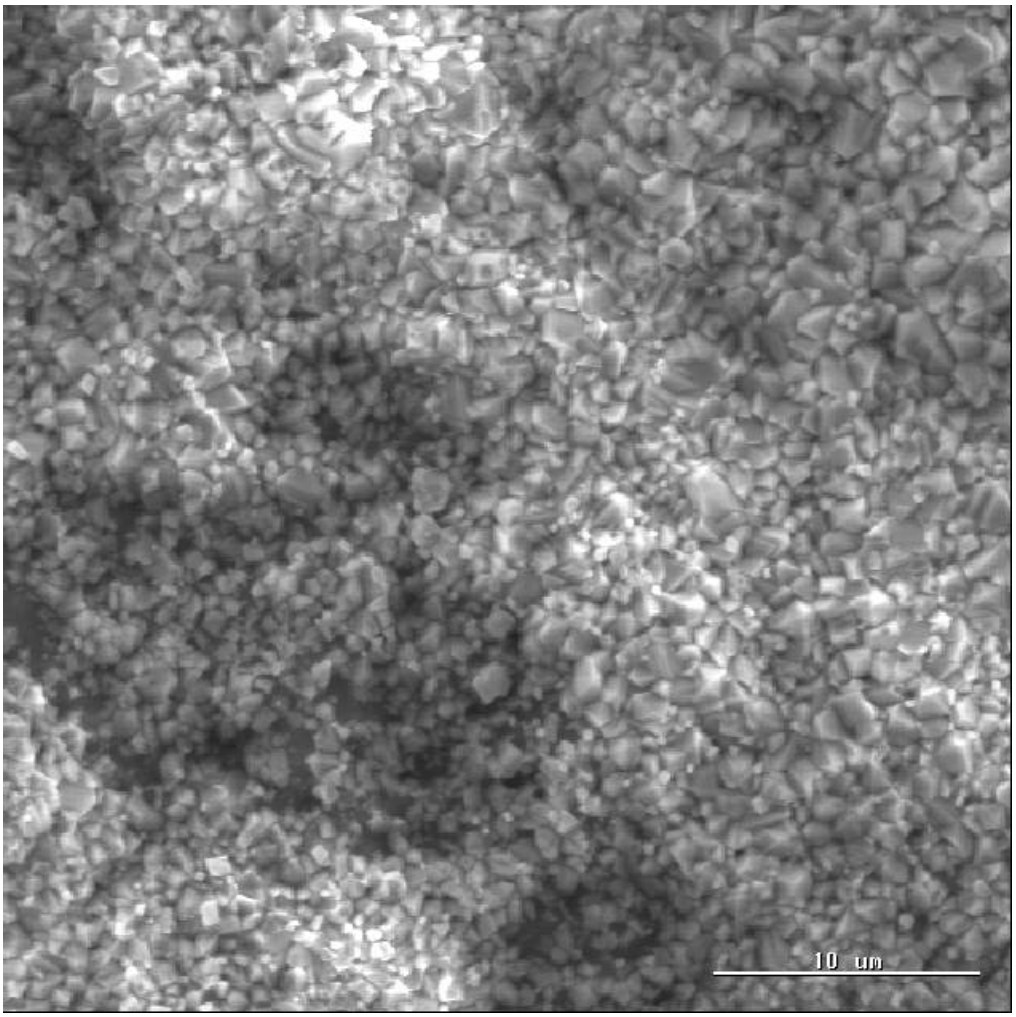

Figure A-30 Oxidized Surface: PWA 1484, 950°C, 150 hours, 2500X

- Surface Oxidation 950˚C- 150 hours
  Dendrites- Chemical Analysis

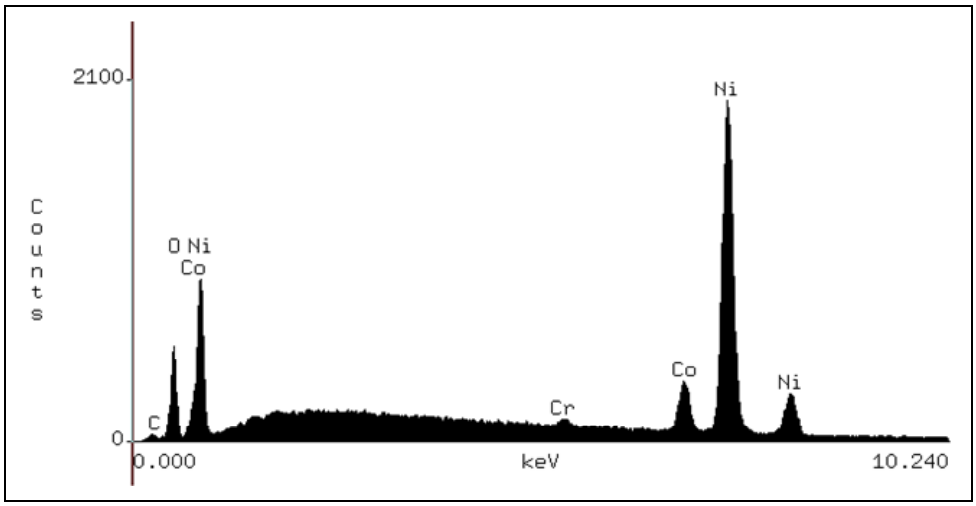

PWA 1484, 950C, 150hr, dendrites, eds-1a

Accelerating Voltage: 15 KeV	Take Off Angle: 39.6197°
Live Time: 90 seconds	Dead Time: 48.025

Figure A-31 Oxidized Surface: PWA 1484, 950°C, 150 hours- Dendrite Chemical Analysis

Quantitative Analysis

Thu Sep 16 16:24:12 2010

PWA 1484, 950C, 150hr, dendrites, eds-1a

Refit _Co-L' _Co-L" _Cr-K' _Cr-K"
Refit _Co-K'
Filter Fit Method
Chi-sqd = 1.58 Livetime = 90.0 Sec.
Standardless Analysis

Element	Relative k-ratio	Error (1-Sigma)	Net Counts	Error (1-Sigma)
O -K	0.03563	+/- 0.00065	4520	+/- 83
Co-L	---	---	243	+/- 139
Ni-L	---	---	11200	+/- 140
Co-K	0.10184	+/- 0.00443	5397	+/- 235
Ni-K	0.85347	+/- 0.00912	35646	+/- 381
C -K	0.00212	+/- 0.00030	220	+/- 31
Cr-K	0.00694	+/- 0.00089	658	+/- 84

Adjustment Factors	K	L	M
Z-Balance:	0.00000	0.00000	0.00000
Shell:	1.00000	1.00000	1.00000

PROZA Correction Acc.Volt.= 15 kV Take-off Angle=39.62 deg Tilt = 30 deg
Number of Iterations = 4

Element	k-ratio (calc.)	ZAF	Atom %	Element Wt %	Wt % Err. (1-Sigma)	No. of Cations
O -K	0.0334	1.659	17.24	5.53	+/- 0.10	---
Co-K	0.0953	1.075	8.67	10.25	+/- 0.45	12.065
Ni-K	0.7990	1.037	70.33	82.84	+/- 0.89	97.894
C -K	0.0020	3.852	3.17	0.76	+/- 0.11	4.418
Cr-K	0.0065	0.944	0.59	0.61	+/- 0.08	0.818
Total			100.00	100.00		115.195

The number of cation results are based upon 24 Oxygen atoms

- Surface Oxidation 950˚C- 150 hours
  Dendrites- Oxide Analysis

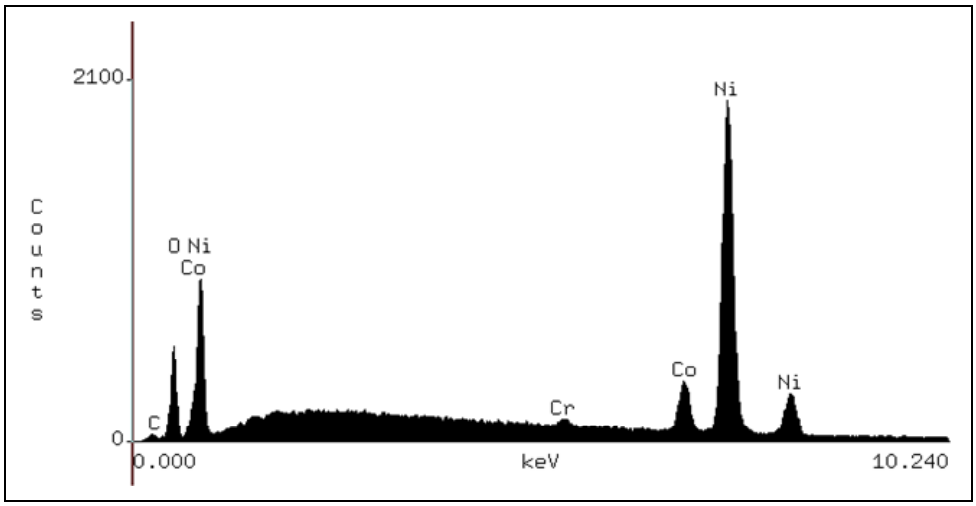

PWA 1484, 950C, 150hr, dendrites, eds-1b (oxides)

Accelerating Voltage: 15 KeV	Take Off Angle: 39.6197°
Live Time: 90 seconds	Dead Time: 48.025

Figure A-32 Oxidized Surface: PWA 1484, 950°C, 150 hours- Dendrite Oxide Analysis

Quantitative Analysis

Thu Sep 16 16:25:20 2010

PWA 1484, 950C, 150hr, dendrites, eds-1b (oxides)

Refit _Co-L' _Co-L" _Cr-K' _Cr-K"
Refit _Co-K'
Filter Fit Method
Chi-sqd = 79.25 Livetime = 90.0 Sec.
Standardless Analysis

Element	Relative k-ratio	Error (1-Sigma)	Net Counts	Error (1-Sigma)
Co-L	---	---	222	+/- 134
Ni-L	---	---	11963	+/- 138
Co-K	0.10584	+/- 0.00461	5397	+/- 235
Ni-K	0.88695	+/- 0.00948	35646	+/- 381
Cr-K	0.00721	+/- 0.00092	658	+/- 84

Bence-Albee Analysis Acc.Volt.= 15 kV Take-off Angle= 39.62 deg

No. of Iterations 2

Oxide Formula	k-ratio (calc)	Beta Factor	Oxide Wt %	No. of Cations
CoO	0.1068	0.9804	10.47	Co- 2.498
NiO	0.8892	0.9981	88.75	Ni-21.229
Cr2O3	0.0085	0.9109	0.77	Cr- 0.182
Total			100.00	23.909

The number of cation results are based upon 24 Oxygen atoms

- Surface Oxidation 950˚C- 150 hours
  Interdendritic Region- Chemical Analysis

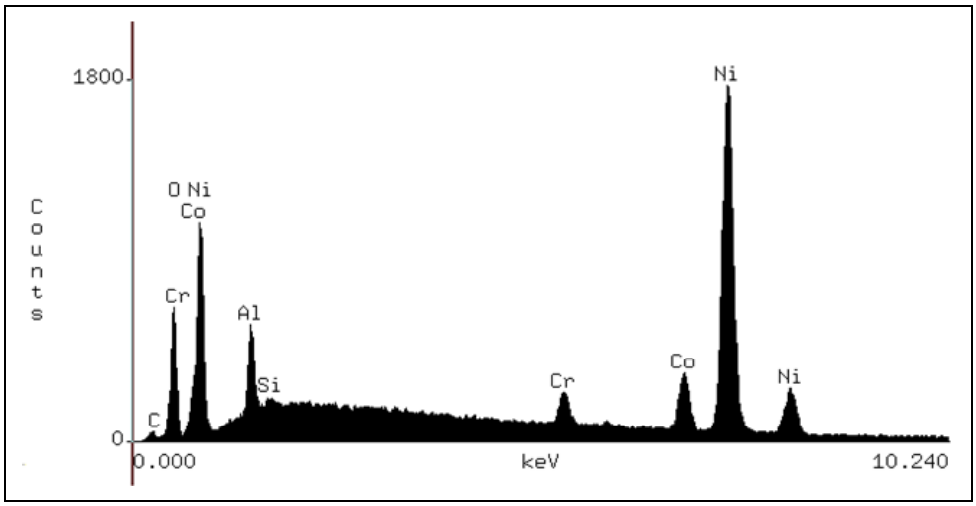

PWA 1484, 950C, 150hr, interdendritic region, eds-1a

Accelerating Voltage: 15 KeV
Take Off Angle: 39.6197°
Live Time: 90 seconds
Dead Time: 50.182

Figure A-33 Oxidized Surface: PWA 1484, 950°C, 150 hours- Inter-Dendrite Chemical Analysis

Quantitative Analysis

Thu Sep 16 16:29:18 2010

PWA 1484, 950C, 150hr, interdendritic region, eds-1a

Refit _Co-L' _Co-L" _O -K' _O -K" _Si-K' _Si-K" _Cr-L' _Cr-L"
Refit _Co-K' _Cr-K"
Filter Fit Method
Chi-sqd = 1.96 Livetime = 90.0 Sec.
Standardless Analysis

Element	Relative k-ratio	Error (1-Sigma)	Net Counts	Error (1-Sigma)
Co-L	---	---	660	+/- 161
Ni-L	---	---	12635	+/- 151
Co-K	0.10157	+/- 0.00456	5123	+/- 230
Ni-K	0.82017	+/- 0.00918	32597	+/- 365
Cr-K	0.02775	+/- 0.00107	2505	+/- 97
C -K	0.00318	+/- 0.00032	314	+/- 32
O -K	0.03442	+/- 0.00106	4154	+/- 128
Al-K	0.01174	+/- 0.00033	4040	+/- 115
Si-K	0.00118	+/- 0.00023	379	+/- 73
Cr-L	---	---	1851	+/- 222

Adjustment Factors	K	L	M
Z-Balance:	0.00000	0.00000	0.00000
Shell:	1.00000	1.00000	1.00000

PROZA Correction Acc.Volt.= 15 kV Take-off Angle=39.62 deg Tilt = 30 deg
Number of Iterations = 4

Element	k-ratio (calc.)	ZAF	Atom %	Element Wt %	Wt % Err. (1-Sigma)	No. of Cations
Co-K	0.0934	1.080	8.26	10.09	+/- 0.45	12.360
Ni-K	0.7544	1.042	64.54	78.59	+/- 0.88	96.621
Cr-K	0.0255	0.956	2.26	2.44	+/- 0.09	3.386
C -K	0.0029	3.930	4.62	1.15	+/- 0.12	6.909
O -K	0.0317	1.680	16.03	5.32	+/- 0.16	---
Al-K	0.0108	2.068	3.99	2.23	+/- 0.06	5.975
Si-K	0.0011	1.620	0.30	0.18	+/- 0.03	0.450
Total			100.00	100.00		125.702

- Surface Oxidation 950˚C- 150 hours
  Interdendritic Region- Oxide Analysis

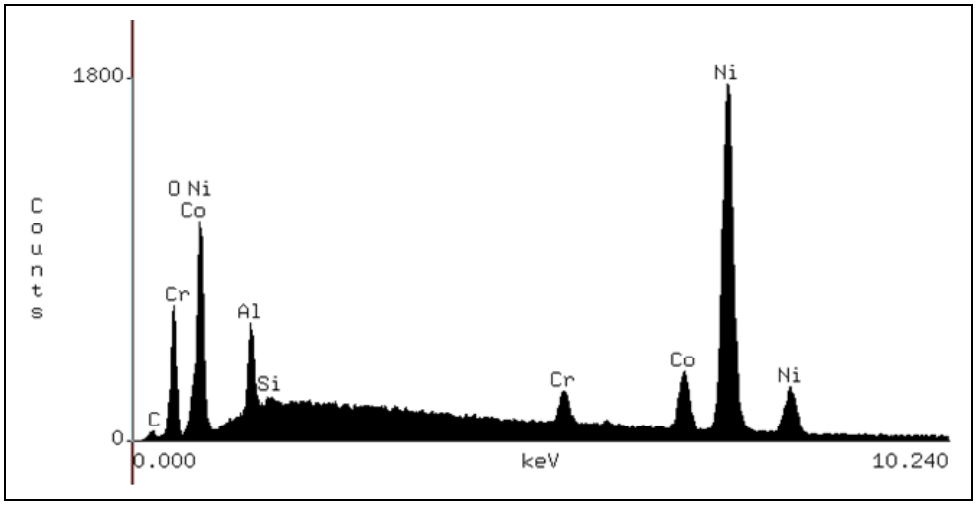

PWA 1484, 950C, 150hr, interdendtritic region, eds-1b (oxides)

Accelerating Voltage: 15 KeV
Live Time: 90 seconds
Take Off Angle: 39.6197°
Dead Time: 50.182

Figure A-34 Oxidized Surface: PWA 1484, 950°C, 150 hours- Inter-Dendrite Oxide Analysis

Quantitative Analysis

Thu Sep 16 16:31:00 2010

PWA 1484, 950C, 150hr, interdendritic, eds-1b (oxides)

Refit _Co-L' _Co-L" _Si-K' _Si-K"
Refit _Co-K' _Cr-K"
Filter Fit Method
Chi-sqd = 10.75 Livetime = 90.0 Sec.
Standardless Analysis

Element	Relative k-ratio	Error (1-Sigma)	Net Counts	Error (1-Sigma)
Co-L	---	---	1947	+/- 163
Ni-L	---	---	12049	+/- 150
Co-K	0.10554	+/- 0.00474	5123	+/- 230
Ni-K	0.85220	+/- 0.00954	32597	+/- 365
Cr-K	0.02884	+/- 0.00112	2505	+/- 97
Al-K	0.01221	+/- 0.00035	4042	+/- 115
Si-K	0.00122	+/- 0.00024	380	+/- 73
Cr-L	---	---	8564	+/- 150

Bence-Albee Analysis Acc.Volt.= 15 kV Take-off Angle= 39.62 deg
No. of Iterations 2

Oxide Formula	k-ratio (calc)	Beta Factor	Oxide Wt %	No. of Cations
CoO	0.1028	0.9902	10.18	Co- 2.294
NiO	0.8247	1.0047	82.85	Ni-18.720
Cr2O3	0.0328	0.9208	3.02	Cr- 0.672
Al2O3	0.0208	1.7434	3.63	Al- 1.200
SiO2	0.0022	1.4355	0.32	Si- 0.089
Total			100.00	22.975

The number of cation results are based upon 24 Oxygen atoms

- Surface Oxidation 1050˚C- 150 hours

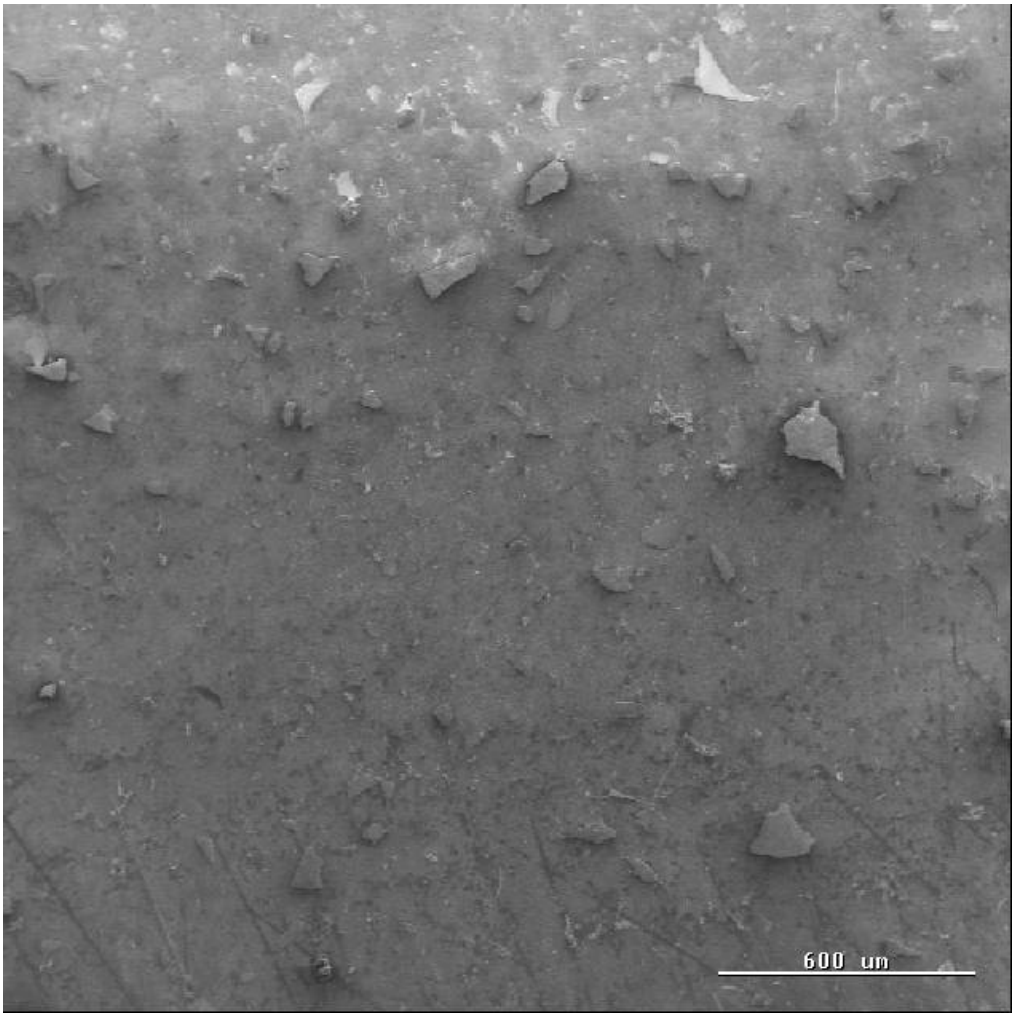

Figure A-35 Oxidized Surface: PWA 1484, 1050°C, 150 hours, 40X

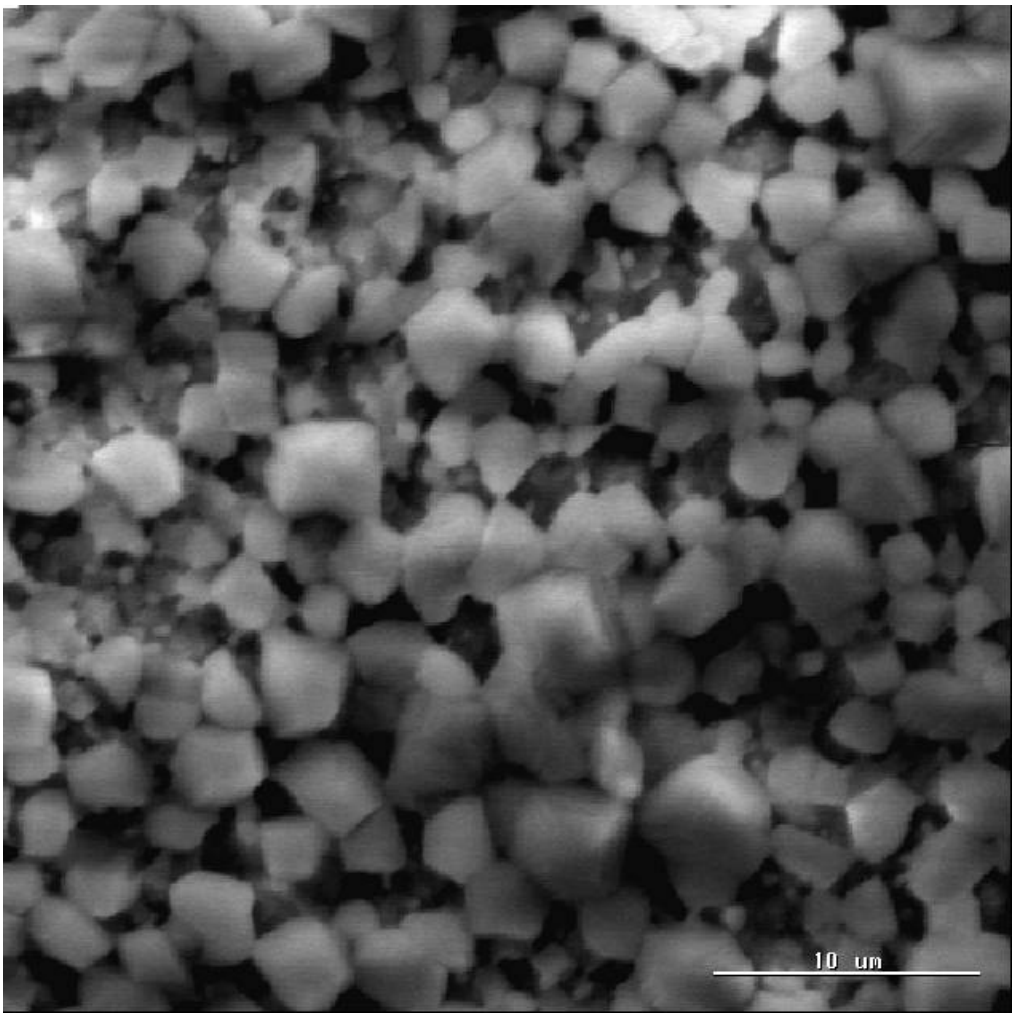

Figure A-36 Oxidized Surface: PWA 1484, 1050°C, 150 hours, 2500X

- Surface Oxidation 1050˚C- 150 hours
  Chemical Analysis

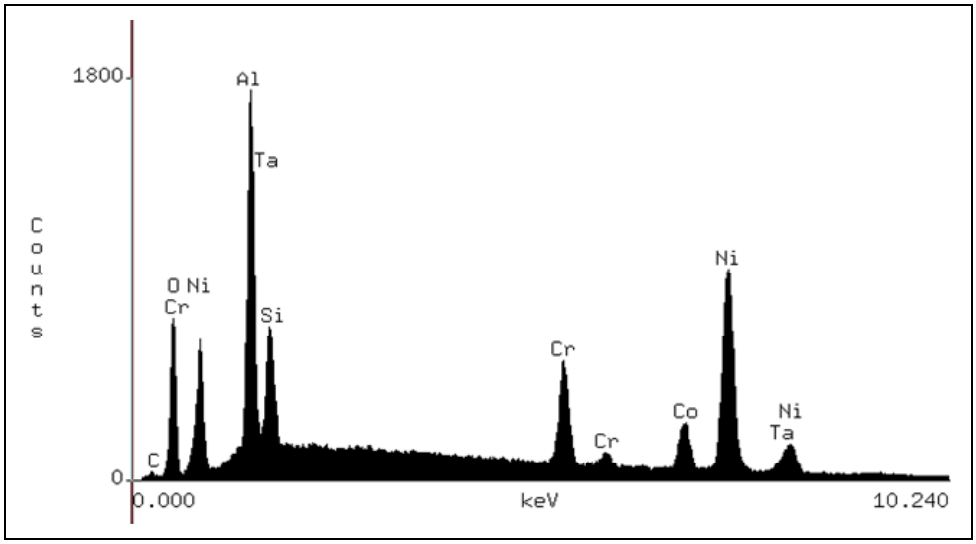

PWA 1484, 1050C, 150hr, oxides, eds-1a

Accelerating Voltage: 15 KeV
Take Off Angle: 39.6197°
Live Time: 90 seconds
Dead Time: 46.192

Figure A-37 Oxidized Surface: PWA 1484, 1050°C, 150 hours- Chemical Analysis

Quantitative Analysis

Thu Sep 16 16:01:25 2010

PWA 1484, 1050C, 150hr, oxides, eds-1a

Refit _Cr-L' _Cr-L" _Ta-L' _Ta-L" _C -K' _C -K" _O -K' _O -K"
Refit _Co-K'
Filter Fit Method
Chi-sqd = 3.10 Livetime = 90.0 Sec.
Standardless Analysis

Element	Relative k-ratio	Error (1-Sigma)	Net Counts	Error (1-Sigma)
Cr-L	---	---	1320	+/- 186
Ni-L	---	---	7242	+/- 121
Al-K	0.06165	+/- 0.00073	15997	+/- 189
Si-K	0.02695	+/- 0.00071	6550	+/- 173
Cr-K	0.11196	+/- 0.00297	7622	+/- 202
Co-K	0.09991	+/- 0.00542	3800	+/- 206
Ni-K	0.57664	+/- 0.00974	17286	+/- 292
Ta-L	0.06874	+/- 0.01033	1059	+/- 159
C -K	0.00180	+/- 0.00027	134	+/- 20
O -K	0.05236	+/- 0.00124	4767	+/- 113

Adjustment Factors	K	L	M
Z-Balance:	0.00000	0.00000	0.00000
Shell:	1.00000	1.00000	1.00000

PROZA Correction Acc.Volt.= 15 kV Take-off Angle=39.62 deg Tilt = 30 deg
Number of Iterations = 5

Element	k-ratio (calc.)	ZAF	Atom %	Element Wt %	Wt % Err. (1-Sigma)	No. of Cations
Al-K	0.0523	1.796	15.20	9.40	+/- 0.11	16.494
Si-K	0.0229	1.539	5.47	3.52	+/- 0.09	5.937
Cr-K	0.0950	1.006	8.02	9.56	+/- 0.25	8.707
Co-K	0.0848	1.075	6.75	9.12	+/- 0.49	7.325
Ni-K	0.4895	1.046	38.05	51.20	+/- 0.86	41.292
Ta-L	0.0584	1.446	2.04	8.44	+/- 1.27	2.208
C -K	0.0015	4.231	2.35	0.65	+/- 0.10	2.548
O -K	0.0444	1.825	22.12	8.11	+/- 0.19	---
Total			100.00	100.00		84.511

The number of cation results are based upon 24 Oxygen atoms

- Surface Oxidation 1050˚C- 150 hours
  Oxide Analysis

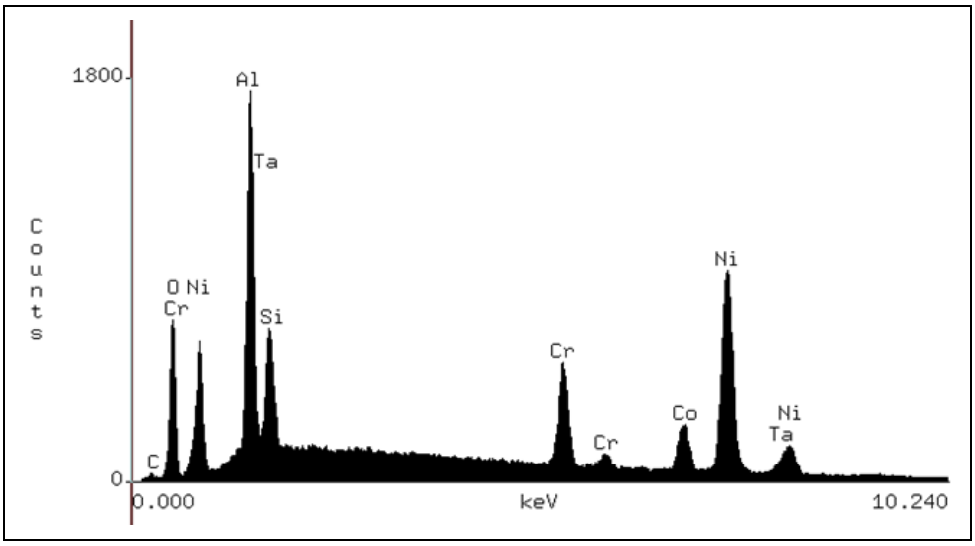

PWA 1484, 1050C, 150hr, oxides, eds-1b (oxides)

Accelerating Voltage: 15 KeV
Take Off Angle: 39.6197°
Live Time: 90 seconds
Dead Time: 46.192

Figure A-38 Oxidized Surface: PWA 1484, 1050°C, 150 hours- Oxide Analysis

Quantitative Analysis

Thu Sep 16 16:03:15 2010

PWA 1484, 1050C, 150hr, oxides, eds-1b (oxides)

Refit _Ta-L' _Ta-L"
Refit _Co-K'
Filter Fit Method
Chi-sqd = 12.83 Livetime = 90.0 Sec.
Standardless Analysis

Element	Relative k-ratio	Error (1-Sigma)	Net Counts	Error (1-Sigma)
Cr-L	---	---	8102	+/- 135
Ni-L	---	---	6696	+/- 121
Al-K	0.06518	+/- 0.00077	15998	+/- 189
Si-K	0.02849	+/- 0.00075	6548	+/- 173
Cr-K	0.11837	+/- 0.00314	7622	+/- 202
Co-K	0.10563	+/- 0.00573	3800	+/- 206
Ni-K	0.60966	+/- 0.01030	17286	+/- 292
Ta-L	0.07268	+/- 0.01092	1059	+/- 159

Bence-Albee Analysis Acc.Volt.= 15 kV Take-off Angle= 39.62 deg

No. of Iterations 3

Oxide Formula	k-ratio (calc)	Beta Factor	Oxide Wt %	No. of Cations
Al2O3	0.0956	1.5028	14.36	Al- 3.884
SiO2	0.0443	1.3551	6.01	Si- 1.379
Cr2O3	0.1160	0.9498	11.02	Cr- 1.999
CoO	0.0886	1.0072	8.92	Co- 1.642
NiO	0.5077	1.0103	51.30	Ni- 9.467
Ta2O5	0.0622	1.3490	8.39	Ta- 0.524
Total			100.00	18.894

The number of cation results are based upon 24 Oxygen atoms

References

1. Pineau, A., Antolovich, S. D., *High Temperature Fatigue of Nickel-base Superalloys - A Review With Special Emphasis on Deformation Modes and Oxidation.* Engineering Failure Analysis, 2010. **16**(8): pp. 2668-2697.
2. Reed, R.C., *The superalloys : fundamentals and applications*. 2008, Cambridge: Cambridge University Press.
3. Arakere, N.K., *High-temperature fatigue properties of single crystal superalloys in air and hydrogen.* Journal of Engineering for Gas Turbines and Power, 2004. **126**(3): pp. 590-603.
4. Arakere, N.K., Moroso, J., *Fatigue Failure in High-Temperature Single Crystal Superalloy Turbine Blades.* High Temperature Materials and Processes, 2001. **20**(2): pp. 117-136.
5. Arakere, N.K., Orozco, E., *Analysis of Low Cycle Fatigue Properties of Single Crystal Nickel-Base Turbine Blade Superalloys.* High Temperature Materials and Processes, 2001. **20**(5-6): pp. 403-419.
6. Arakere, N.K., Swanson, G., *Effect of Crystal Orientation on Fatigue Failure of Single Crystal Nickel Base Turbine Blade Superalloys.* Journal of Engineering for Gas Turbines and Power, 2002. **124**(1): pp. 161-176.
7. Cetel, A.D., Duhl, D.N., *Second Generation Nickel-Base Single Crystal Superalloy.* Superalloys, 1988: pp. 235-244.
8. Gayda, J., Gabb, T. P., Miner, R. V., Halford, G. R., *Isothermal and "Bithermal" Thermomechanical Fatigue Behavior of a NiCoCrAlY-Coated Single Crystal Superalloy*, in *Superalloys 1988*, S. Reichman, Duhl, D., N., Maurer, G., Antolovich, S., D., Lund, C., Editor. 1988, The Metallurgical Society. pp. 575-584.
9. Okazaki, M., Sakaguchi, M., *Thermo-Mechanical Fatigue Failure of a Single Crystal Ni-Based Superalloy.* International Journal of Fatigue, 2008. **30**(2): pp. 318-323.
10. Nissley, D.M., *Thermomechanical fatigue life prediction in gas turbine superalloys: a fracture mechanics approach.* AIAA Journal, 1995. **33**(6): pp. 1114-1120.
11. Huang, Z.W., Wang, Z. G., Zhu, S. J., Yuan, F. H., Wang, F. G., *Thermomechanical fatigue behavior and life prediction of a cast nickel-based superalloy.* Materials Science and Engineering A, 2006. **432**(1-2): pp. 308-316.
12. Matan, N., Cox, D. C., Carter, P., Rist, M. A., Rae, C. M. F., Reed, R. C., *Creep of CMSX-4 superalloy single crystals: effects of misorientation and temperature.* Acta Materialia, 1999. **47**(5): pp. 1549-63.
13. Sass, V., U. Glatzel, and M. Feller-Kniepmeier, *Anisotropic creep properties of the nickel-base superalloy CMSX-4.* Acta Materialia, 1996. **44**(5): pp. 1967-77.
14. Gabb, T.P., J. Gayda, and R.V. Miner, *Orientation and Temperature Dependence of Some Mechanical Properties of the Single-Crystal Nickel-Base Superalloy RENE-N4: Part II. Low Cycle Fatigue Behavior.* Metallurgical Transactions A (Physical Metallurgy and Materials Science), 1986. **17A**(3): pp. 497-505.

15. Miner, R.V., Gabb, T. P., Gayda, J., Hemker, K. J., *Orientation and Temperature Dependence of Some Mechanical Properties of the Single-Crystal Nickel-Base Superalloy RENE N4: Part III. Tension-Compression Anisotropy.* Metallurgical transactions. A, Physical metallurgy and materials science, 1986. **17 A**(3): pp. 507-512.
16. Miner, R.V., Voigt, R. C., Gayda, J., Gabb, T. P., *Orientation and Temperature Dependence of Some Mechanical Properties of the Single-Crystal Nickel-Base Superalloy RENE-N4: Part I. Tensile Behavior.* Metallurgical Transactions A (Physical Metallurgy and Materials Science), 1986. **17A**(3): pp. 491-496.
17. Erickson, G.L. *Ni-Based Superalloy Developments*. 1993. Warrendale, PA, USA: Publ by Minerals, Metals & Materials Soc (TMS).
18. McDowell, D.L., Antolovich, S. D., Oehmke, R. L. T., *Mechanistic considerations for TMF life prediction of nickel-base superalloys.* Nuclear Engineering and Design, 1992. **133**(3): pp. 383-399.
19. Kamaraj, M., *Rafting in single crystal nickel-base superalloys — An overview.* Sadhana, 2003. **28**(1): pp. 115-128.
20. Li, J., Tang, Dingzhong, Lao, Riling, Liu, Shizhong, Wu, Zhongtang, *Effects of rhenium on creep rupture life of a single crystal superalloys.* Journal of Materials Science and Technology, 1999. **15**(1): pp. 53-57.
21. Prasad, S.C., Constitutive Modeling of Creep of Singe Crystal Superalloys, PhD in Mechanical Engineering, 2005, Texas A&M
22. Harvey, S.E., P.G. Marsh, and W.W. Gerberich, *Atomic force microscopy and modeling of fatigue crack initiation in metals.* Acta metallurgica et materialia, 1994. **42**(10): pp. 3493-3502.
23. Schaffer, J., P., Saxena, A., Antolovich, S., D., Sanders, T., H., Warner, *The science and design of engineering materials*. 2nd ed. ed, ed. J.P. Schaffer. 1999, Boston :: WCB McGraw-Hill.
24. Dowling, N.E., *Mechanical behavior of materials : engineering methods for deformation, fracture, and fatigue*. 2nd ed. ed. 1999, Upper Saddle River, NJ :: Prentice Hall.
25. Frost, H.J., Ashby, M. F., *Deformation-Mechanism Maps The Plasticity and Creep of Metals and Ceramics*. 1982: Pergamon Press.
26. Shyam, A., Milligan, W. W., *Effects of deformation behavior on fatigue fracture surface morphology in a nickel-base superalloy.* Acta Materialia, 2004. **52**(6): pp. 1503-1513.
27. Diederich, D., Lerch, B., Antolovich, S.D., *Observations of Low Cycle Fatigue and Fatigue Crack Propagation Substructures in Waspaloy*, in *8th Inter-American Conference on Materials Technology*. 1985: San Juan, Puerto Rico. pp. 7.1-7.6.
28. Venkataraman, G., Chung, Y., W., Mura, T., *Application of minimum energy formalism in a multiple slip band model for fatigue -- I. Calculation of slip band spacings.* Acta metallurgica et materialia, 1991. **39**(11): pp. 2621-2629.
29. Thompson, A., W., Baskes, M., I., Flanagan, W., F., *The dependence of polycrystal work hardening on grain size.* Acta Metallurgica, 1973. **21**(7): pp. 1017-1028.

30. Margolin, H., Stefan Stanescu, M., *Polycrystalline strengthening.* Acta Metallurgica, 1975. **23**(12): pp. 1411-1418.
31. Shyam, A., Milligan, W. W., *A model for slip irreversibility, and its effect on the fatigue crack propagation threshold in a nickel-base superalloy.* Acta Materialia, 2005. **53**(3): pp. 835-844.
32. Betteridge, W., *The Nimonic alloys, and other nickel-base high-temperature alloys*. [2nd ed.] ed, ed. J. Heslop. 1974, New York: Crane, Russak.
33. Milligan, W.W., Antolovich, S., D., *Yielding and Deformation Behavior of the Single Crystal Superalloys PWA 1480.* Metallurgical transactions. A, Physical metallurgy and materials science, 1987. **18 A**(1): pp. 85-95.
34. Yablinsky, C.A., Flores, K.M., Mills, M.J., Williams, J.C., Rigney, Joe, *Fatigue Behavior in Monocrystalline Ni-Based Superalloys for Blade Applications*, in *Superalloys 2008*, M.M.S. The Minerals, Editor. 2008: Champion, Pennsylvania. pp. 6.
35. Sims, C.T., Stoloff, N. S., Hagel, W. C., *Superalloys II*. 1987, New York: Wiley.
36. Li, S.X., Smith, D., J., *Development of an anisotropic constitutive model for single-crystal superalloy for combined fatigue and creep loading.* International Journal of Mechanical Sciences, 1998. **40**(10): pp. 937-948.
37. Arakere, N.K., Siddiqui, S., Magnan, S., Ebrahimi, F., Forero, L.E., *Investigation of Three-Dimensional Stress Fields and Slip Systems for FCC Single-Crystal Superalloy Notched Specimens.* Journal of Engineering for Gas Turbines and Power, 2005. **127**(3): pp. 629-637.
38. Oesterle, W., Bettge, D., Fedelich, B., Klingelhoeffer, H., *Modelling the Orientation and Direction Dependence of the Critical Resolved Shear Stress of Nickel-Base Superalloy Single Crystals.* Acta Materialia, 2000. **48**(3): pp. 689-700.
39. Bettge, D., Oesterle, W., *`Cube slip' in near-[111] oriented specimens of a single-crystal nickel-base superalloy.* Scripta Materialia, 1999. **40**(4): pp. 389-395.
40. Kandil, F.A., Brown, M. W., Miller, K. J. *Biaxial Low Cycle Fatigue Failure of 316 Stainless Steel at Elevated Temperatures*. 1981. Varese, Italy.
41. Socie, D.F., Kurath, P., Koch, J., *A Multiaxial Fatigue Damage Parameter*, in *Second International Symposium on Multiaxial Fatigue*. 1985: Sheffield, U.K.
42. Fatemi, A., Socie, D. F., *A critical plane approach to multiaxial fatigue damage including out-of-phase loading.* Fatigue & Fracture of Engineering Materials & Structures, 1988. **11**(3): pp. 149-65.
43. Smith, K.N., P. Watson, and T.H. Topper, *A stress-strain function for the fatigue of metals.* Journal of Materials, 1970. **5**(4): pp. 767-78.
44. Fleury, E., Remy, L., *Behavior of nickel-base superalloy single crystals under thermal-mechanical fatigue.* Metallurgical and Materials Transactions A: Physical Metallurgy and Materials Science, 1994. **25 A**(1): pp. 99-109.
45. Auerswald, J., Mukherji, D., Chen, W., Wahi, R.P., *Estimation of the Critical Stress for Gamma Prime Shearing in a Single Crystal Superalloy From LCF Data*, in *Fourth International Conference on Low Cycle Fatigue and Elasto-Plastic Behaviour of Materials*, K.-T. Rie, Portella, P. D., Editor. 1998, Elsevier: Garmisch-Partenkirchen, Germany. pp. 351-356.

46. Lukas, P., Preclk, P., Cadek, J., *Notch Effects on Creep Behaviour of CMSX-4 Superalloy Single Crystals.* Materials Science and Engineering: A, 2001. **298**: pp. 84-89.
47. Nutzel, R., Affeldt, E., Goken, M., *Damage Evolution During Thermo-Mechanical Fatigue of a Coated Monocrystalline Nickel-Base Superalloy.* International Journal of Fatigue, 2008. **30**(2): pp. 313-317.
48. Okazaki, M., *High-temperature strength of Ni-base superalloy coatings.* Science and Technology of Advanced Materials, 2001. **2**(2): pp. 357-366.
49. Verrilli, M.J., *Bithermal Fatigue of a Nickel-Base Superalloy Single Crystal*. 1988, NASA Technical Memorandum 100885: Cleveland, Ohio. pp. 13.
50. Giggins, C.S., Pettit, F. S., *Oxidation of Ni-Cr-Al alloys between 1000 and 1200C.* Journal of the Electrochemical Society, 1971. **118**(11): pp. 1782-90.
51. Akhtar, A., Hegde, S., Reed, R., C., *The oxidation of single-crystal nickel-based superalloys.* JOM, 2006. **58**(1): pp. 37-42.
52. Zhao, L.G., O'Dowd, N. P., Busso, E. P., *A coupled kinetic-constitutive approach to the study of high temperature crack initiation in single crystal nickel-base superalloys.* Journal of the Mechanics and Physics of Solids, 2006. **54**(2): pp. 288-309.
53. Das, D.K., Singh, V., Joshi, S., V., *High temperature oxidation behaviour of directionally solidified nickel base superalloy CM - 247LC.* Materials Science and Technology, 2003. **19**(6): pp. 695-708.
54. Levy, M., Farrell, P., Pettit, F., *Oxidation of Some Advance Single-Crystal Nickel-Base Superalloys in Air at 2000 F(1093 C).* Corrosion, 1986. **42**(12): pp. 708-717.
55. Levy, M., R. Huie, and F. Pettit, *Oxidation and hot corrosion of some advanced superalloys at 1300 to 2000 F (704 to 1093 C).* Corrosion, 1989. **45**(8): pp. 661-674.
56. Bouhanek, K., Oquab, D., Pieraggi, B., *High temperature oxidation of single-crystal Ni-base superalloys.* Materials Science Forum, 1997. **251-254**(part 1): pp. 33-40.
57. Nychka, J.A., Clarke, D., R., Meier, G., H., *Spallation and transient oxide growth on PWA 1484 superalloy.* Materials Science and Engineering: A, 2008. **490**(1-2): pp. 359-368.
58. Li, M.H., Sun, X. F., Li, J. G., Zhang, Z. Y., Jin, T., Guan, H. R., Hu, Z. Q., *Oxidation behavior of a single-crystal Ni-base superalloy in air. I. At 800 and 900C.* Oxidation of Metals, 2003. **59**(5-6): pp. 591-605.
59. Li, M.H., Sun, X. F., Jin, T., Guan, H. R., Hu, Z. Q., *Oxidation behavior of a single-crystal Ni-base superalloy in air-II: At 1000, 1100, and 1150C.* Oxidation of Metals, 2003. **60**(1-2): pp. 195-210.
60. Peraldi, R., Monceau, D., Pieraggi, B., *Correlations between growth kinetics and microstructure for scales formed by high-temperature oxidation of pure nickel. II. Growth kinetics.* Oxidation of Metals, 2002. **58**(3-4): pp. 275-295.
61. Peraldi, R., Monceau, D., Pieraggi, B., *Correlations between growth kinetics and microstructure for scales formed by high-temperature oxidation of pure nickel. I. Morphologies and microstructures.* Oxidation of Metals, 2002. **58**(3-4): pp. 249-273.

62. Gordon, A.P., Trexler, M. D., Neu, R. W., Sanders Jr, T. J., McDowell, D. L., *Corrosion kinetics of a directionally solidified Ni-base superalloy.* Acta Materialia, 2007. **55**(10): pp. 3375-3385.
63. Krupp, U. and H.J. Christ, *Selective oxidation and internal nitridation during high-temperature exposure of single-crystalline nickel-base superalloys.* Metallurgical and Materials Transactions A: Physical Metallurgy and Materials Science, 2000. **31**(1): pp. 47-56.
64. Esmaeili, S., Engler-Pinto, C. C., Ilschner, B., Rézaï-Aria, F., *Interaction between oxidation and thermo-mechanical fatigue in IN738LC superalloy -- I.* Scripta Metallurgica et Materialia, 1995. **32**(11): pp. 1777-1781.
65. Wright, P.K. *Oxidation-Fatigue Interactions in a Single-Crystal Superalloy*. 1987. Bolton Landing, NY, USA: ASTM.
66. Dumoulin, S., Busso, E. P., O'Dowd, N. P., Allen, D. *A Multiscale Approach for Coupled Phenomena in FCC Materials at High Temperatures*. 2003: Taylor and Francis Ltd.
67. Kupkovits, R., Thermomechanical Fatigue Behavior of the Directionally-Solidified Nickel-Base Superalloy CM247LC, Masters in Mechanical Engineering, 2009, Georgia Institute of Technology
68. Zhao, L.G., Busso, E. P., O'Dowd, N. P. *Computational modelling of crack initiation in a single crystal superalloy under fatigue-oxidation conditions*. 2007. Suite 1C, Joseph's Well, Hanover Walk, Leeds, LS3 1AB, United Kingdom: Maney Publishing.
69. Busso, E.P., O'Dowd, N. P., Nikbin, K., *Mechanistic studies of high-temperature crack initiation in single crystal materials.* Journal of ASTM International, 2006. **3**(7).
70. Sehitoglu, H., Boismier, D. A., *Thermo-mechanical fatigue of Mar-M247. Part 2. Life prediction.* Journal of Engineering Materials and Technology, Transactions of the ASME, 1990. **112**(1): pp. 80-89.
71. Reuchet, J., Remy, L., *Fatigue Oxidation Interaction in a Superalloy - Application to Life Prediction in Hight Temperature Low Cycle Fatigue.* Metallurgical transactions. A, Physical metallurgy and materials science, 1983. **14 A**(1): pp. 141-149.
72. Manonukul, A., Dunne, F. P. E., Knowles, D., *Physically-based model for creep in nickel-base superalloy C263 both above and below the gamma solvus.* Acta Materialia, 2002. **50**(11): pp. 2917-2931.
73. Wagner, C., *Theory of Precipitate Change by Redissolution (Ostwald Ripening).* Z. Elektrochem, 1961. **65**: pp. 581-591.
74. Lifshitz, I.M. and V.V. Slyozov, *The kinetics of precipitation from supersaturated solid solutions.* Journal of Physics and Chemistry of Solids, 1961. **19**(1-2): pp. 35-50.
75. Malpertu, J.L., Remy, L. *Thermal-Mechanical fatigue Behaviour of IN100 Superalloy*. in *High Temperature Alloys for Gas Turbines and Other Applications*. 1986. Li'ege, Belgium: D. Reidel Publishing Co.
76. Hunsche, A. and P. Neumann, *Quantitative measurement of persistent slip band profiles and crack initiation.* Acta Metallurgica, 1986. **34**(2): pp. 207-217.

77. Francois, M., Remy, L., *Thermal-Mechanical Fatigue of MAR-M 509 Superalloy. Comparison With Low-Cycle Fatigue Behaviour.* Fatigue & Fracture of Engineering Materials & Structures, 1991. **14**(1): pp. 115-129.
78. Gallerneau, F., Nouailhas, D., Chaboche, J., L. *A Fatigue Damage Model Including Interaction Effects With Oxidation and Creep Damages*. in *Sixth International Fatigue Congress*. 1996. Berlin, Germany: Pergamon.
79. *ASTM Standard E 2368-04, "Standard Practice for Strain Controlled Thermomechanical Fatigue Testing"*. 2004: West Conshohocken, PA.
80. Brendel, T., Affeldt, E., Hammer, J., Rummel, C., *Temperature gradients in TMF specimens. Measurement and influence on TMF life.* International Journal of Fatigue, 2008. **30**(2): pp. 234-240.
81. Halford, G.R., *Low-Cycle Thermal Fatigue*. 1986, NASA Technical Memorandum 87225: Cleveland, Ohio.
82. Halford, G.R., MCGaw, M. A., Bill, R. C., Fanti, P. D., *Bithermal Fatigue: A link Between Isothermal and Thermomechanical Fatigue; Low cycle fatigue : A Symposium*. Special technical publication, ed. H.D. Solomon. 1987, Philadelphia, Pa.: ASTM STP 942.
83. Halford, G.R., Meyer, T., G., Nelson, R., S., Nissley, D., M., Swanson, G., A., *NASA Technical Memorandum 100291, Fatigue Life Prediction Modeling for Turbine Hot Section Materials*, in *33rd International Gas Turbine and Aeroengine Congress and Exposition*. 1988, NASA: Amsterdam, The Netherlands. pp. 18.
84. Gayda, J., Gabb, T., P., Miner, R., V., Halford, G., R.,, *Bithermal Low-Cycle Fatigue Behavior of a NiCoCrAlY-Coated Single Crystal Superalloy*. 1987, NASA Technical Memorandum 89831: NASA Glenn Ressearch Center. pp. 25.
85. Malpertu, J.L., Remy, L., *Influence of Test Parameters on the Thernal-Mechanical Fatigue Behavior of a Superalloy.* Metallurgical Transactions A (Physical Metallurgy and Materials Science), 1990. **21**(1).
86. Gordon, A.P., Crack Initiation Modeling of a Directionally-Solidified Ni-base Superalloy, PhD in Mechanical Engineering, 2006, Georgia Institute of Technology
87. Antolovich, S.D., Liu, S., Bauer, R., *Low Cycle Fatigue Behavior of Rene 80 at Elevated Temperature.* Metallurgical transactions. A, Physical metallurgy and materials science, 1981. **12 A**(3): pp. 473-481.
88. Neu, R.W., Sehitoglu, H., *Thermomechanical fatigue, oxidation, and creep. Part I. Damage mechanisms.* Metallurgical transactions. A, Physical metallurgy and materials science, 1989. **20 A**(9): pp. 1755-1767.
89. Neu, R.W., Sehitoglu, H., *Thermomechanical fatigue, oxidation, and creep. Part II. Life prediction.* Metallurgical transactions. A, Physical metallurgy and materials science, 1989. **20 A**(9): pp. 1769-1783.
90. Boismier, D.A., Sehitoglu, H., *Thermo-mechanical fatigue of Mar-M247. Part 1. Experiments.* Journal of Engineering Materials and Technology, Transactions of the ASME, 1990. **112**(1): pp. 68-79.
91. Sehitoglu, H. *Thermo-mechanical fatigue life prediction methods*. 1992. San Francisco, CA, USA: Publ by ASTM.

92. Cai, C., Liaw, P. K., Ye, M., Yu, J., *Recent Developments in the Thermomechanical fatige Life Prediction of Superalloys.* JOM-e, 1999. **51 (4)**.
93. Manson, S.S., Halford, G., R., *Fatigue and durability of metals at high temperatures*, ed. G.R. Halford. 2009, Materials Park, Ohio :: ASM International.
94. Naik, R., A. , DeLuca, D., P. , Shah, D., M. , *Critical Plane Fatigue Modeling and Characterization of Single Crystal Nickel Superalloys.* Journal of Engineering for Gas Turbines and Power, 2004. **126**(2): pp. 391-400.
95. Stouffer, D.C., *Inelastic deformation of metals : models, mechanical properties, and metallurgy*, ed. L.T. Dame. 1996, New York :: J. Wiley.
96. Antolovich, S.D., Baur, R., Liu, S., *A Mechanistically Based Model for High Temperature LCF of Ni Base Superalloys*, in *Superalloys 1980*, J.K. Tien, Wlodek, S. T., Morrow, H., Gell, M., Mauer, G. E., Editor. 1980, The Metallurgical Society. pp. 605-613.
97. Pilling, N.B., Bedworth, R E., *The Oxidation of Metals at high Temperatures.* Journal Institute of Metals, 1923. **29**: pp. 529.
98. Rezai-Aria, F., Remy, L., *Oxidation fatigue interaction damage model for thermal fatigue crack growth.* Engineering Fracture Mechanics, 1989. **34**(2): pp. 283-294.
99. Tammann, G., *Über Anlauffarben von Metallen.* Zeitschrift für anorganische und allgemeine Chemie, 1920. **111**(1): pp. 78-89.
100. Wagner, C. *Diffusion and High-Temperature Oxidation of Metals*. in *Atom Movements*. 1951. Cleveland, OH: American Society of Metals.
101. Göbel, M., A. Rahmel, and M. Schütze, *The isothermal-oxidation behavior of several nickel-base single-crystal superalloys with and without coatings.* Oxidation of Metals, 1993. **39**(3): pp. 231-261.
102. Gross, M., et al., *Oxidation of the turbine blade material CMSX4 studied by X-ray diffraction.* J. Phys. IV France, 1998. **08**(PR5): pp. Pr5-505-Pr5-510.
103. Fisher, J.C., *Calculation of diffusion penetration curves for surface and grain boundary diffusion.* Journal of Applied Physics, 1951. **22**: pp. 74-77.
104. Tinga, T., W.A.M. Brekelmans, and M.G.D. Geers, *Time-incremental creep-fatigue damage rule for single crystal Ni-base superalloys.* Materials Science and Engineering A, 2009. **508**(1-2): pp. 200-208.
105. Yeh, N.-M. and E. Krempl. *Incremental life prediction law for multiaxial creep-fatigue interaction and thermomechanical loading*. 1993. San Diego, CA, USA: Publ by ASTM.
106. Suresh, S., *Fatigue of materials*. 2nd ed. ed. 1998, Cambridge: Cambridge University Press.
107. Ganesh Sundara Raman, S. and K.A. Padmanabhan, *Room-temperature low-cycle fatigue behaviour of a Ni-base superalloy.* International Journal of Fatigue, 1994. **16**(3): pp. 209-215.
108. Stoltz, R.E., Pineau, A. G., *Dislocation-precipitate interaction and cyclic stress-strain behavior of a γ′ strengthened superalloy.* Materials Science and Engineering, 1978. **34**(3): pp. 275-284.
109. *ASTM Standard E 606-04 E1 "Standard Practice for Strain-Controlled Fatigue Testing"*. 2004: West Conshohocken, PA.
110. Thompson, A.W. and W.A. Backofen, *The effect of grain size on fatigue.* Acta Metallurgica, 1971. **19**(7): pp. 597-606.

111. Amaro, R.L., Antolovich, S. D., Neu, R. W., Staroselsky, A., *On thermo-mechanical fatigue in single crystal Ni-base superalloys.* Procedia Engineering, 2010. **2**(1): pp. 815-824.
112. McLean, M., Dyson, B. F., *Modeling the Effects of Damage and Microstructural Evolution on the Creep Behavior of Engineering Alloys.* Journal of Engineering Materials and Technology, 2000. **122**(3): pp. 273-278.
113. Arrell, D., Hasselqvist, M., Sommer, C., Moverare, J. *On TMF Damage, Degradation Effects, and the Associated Tmin Influence on TMF Test Results in gamma/gamma-prime Alloys*. 2004. Warrendale, PA 15086, United States: Minerals, Metals and Materials Society.
114. Kupkovits, R., A., Smith, D., J., Neu, R., W., *Influence of minimum temperature on the thermomechanical fatigue of a directionally-solidified Ni-base superalloy.* Procedia Engineering, 2010. **2**(1): pp. 687-696.
115. Bensch, M., PreuBner, J., Huttner, R., Obigodi, G., Virtanen, S., Gabel, J., Glatzel, U., *Modelling and analysis of the oxidation influence on creep behaviour of thin-walled structures of the single-crystal nickel-base superalloy Rene N5 at 980°C.* Acta Materialia, 2009. **58**(5): pp. 1607-1617.
116. Meissonnier, F.T., Busso, E. P., O'Dowd, N. P., *Finite Element Implementation of a Generalised Non-Local Rate-Dependent Crystallographic Formulation for Finite Strains.* International Journal of Plasticity, 2001. **17**(4): pp. 601-640.